Modelling the effects of structure degradation in geotechnical problems

Stylianos Panayides MEng (Hons) MSc

A thesis submitted for the degree of Doctor of Philosophy (PhD) at Newcastle University

School of Civil Engineering and Geosciences

Newcastle University

Newcastle

NE1 7RU

September 2012

Abstract

Bond degradation is an irreversible phenomenon that, experimentally, appears to be controlled by plastic strain accumulation. Conventional constitutive soil models do not capture the effects of small strain non-linearity, recent stress history as well as material structure and its consequent reduction due to bond degradation. The aim of this thesis is to investigate the behaviour of a constitutive model that describes the initial structure, on various geotechnical problems. The kinematic hardening structured constitutive model (Rouainia and Muir Wood, 2000) ,formulated within a framework of kinematic hardening and bounding surface plasticity, was implemented into the PLAXIS Finite Element Analysis software package and was used to simulate a variety of boundary value problems.

The implementation of the model was validated through a number of single finite element analyses of laboratory tests on natural clay from the Vallericca valley in Italy. The model was further adopted in the finite element analyses of geotechnical problems. The first of these simulated the Self Boring Pressuremeter test in London Clay, with the main focus being the characterisation of the degree of initial structure of London clay, as well as identifying the effect of structure related parameters. The premise that the SBPM is installed without damage was also investigated. The second boundary value problem involved the 2D and 3Danalysis of an embankment situated on soft structured clay in Saint Alban, Canada. The numerical predictions of pore-water pressures and settlements are also compared with field measurements. The model developed in this work was then adopted in the study of the behaviour of a deep excavation located in Boston, Massachusetts, USA. The numerical simulations were aimed to demonstrate that the added features of the model implemented in this work such as small strain stiffness, structure and anisotropy are vital components to give a good prediction. Comparison of the predicted wall profiles, time dependent dissipation of excess pore water pressures and associated ground heave with field data are provided.

Dedication

This thesis is dedicated to the two angels watching over me. In loving memory of my mother Maro Panayides who passed away in October 5th, 2006. May she rest in peace and watch over me as she had done for so many years. Thank you for being my guardian angel. My mother did not only raise and nurture me but also taxed herself dearly over the years for my education and intellectual development.

A special feeling of gratitude goes to my other angel, my understanding and patient wife Michelle, who came into my life just when I needed her. Her continual love and support throughout my work was vital, Thank you for always watching over me and for being who you are.

Acknowledgements

My sincere gratitude goes to my supervisor Dr. M. Rouainia for initially giving me the chance to do research and then continual support and encouragement throughout the preparation of this Thesis.

The research presented in this thesis was partly funded by Buro Happold. Their support is gratefully acknowledged. Special thanks go to Mr Peter Scott, Mr Alex Nikolic and Mr Angelo Fasano from Buro Happold, London for their useful discussions and advice during this work.

Thanks also to Mr Rob Hiley for his help and advice during the model development stage of this work

I would like to thank all the people that made the environment friendly and lively. Special thanks are due to Ross, Chris and Ini, for not only being friends, but also helping me in my work in numerous ways.

Finally, my last thanks go to my family, for loving me, supporting me and encouraging me in everything I have done in life, and giving me the strength to chase my dreams.

Table of contents

List of figures

List of tables

Chapter 1: Introduction

1.1 Introduction

Numerical analyses have proved a powerful tool in analysing complex soil-structure interaction problems. However, the predictions obtained are heavily influenced by the constitutive soil models adopted in each case. Clearly, the use of appropriate soil models that can describe satisfactorily the observed soil behaviour is necessary in order to obtain realistic predictions.

The analysis of geotechnical problems requires constitutive models which can capture characteristics that the natural soils exhibit, with adequate precision. It is now evident that natural soils have components of stiffness and strength which cannot be accounted for by classical soil mechanics and originate from the influence of structure caused by cementation, ageing or even overconsolidation. Upon increase of the applied loads, the stresses at certain inter-particle contacts are presumed to reach and surpass the bond strength, resulting in the initiation of the mechanical bond degradation process. Bond degradation is an irreversible phenomenon that, experimentally, appears to be controlled by plastic strain accumulation. Conventional constitutive soil models which are based on experimental studies of reconstituted soils and the classical principles of soil mechanics are not able to describe the effects of small strain non-linearity, recent stress history as well as material structure and its consequent reduction due to bond degradation.

To model such behaviour, it is reasonable to extend a model which is already capable of describing the behaviour of the reconstituted material, such as the Modified Cam Clay by assigning additional characteristics to it. Recent developments in modelling saw a family of elasto-plastic soil models, the kinematic hardening models, developed to address some of these limitations. Kinematic hardening models are advantageous in the way that they permit the retention of some information concerning the recent stress history. The kinematic hardening models allow for plasticity and non-linearity to be invoked within the conventionally defined yield surface, through the introduction of kinematic

surfaces. The kinematically hardening bubble is the yield surface separating regions of elastic and plastic response and moving with the current stress. In order

to capture the effects of initial structure of natural soil, another surface is introduced, which acts as a bounding surface and contains information about the current magnitude and anisotropy of structure. As plastic straining occurs, the structure surface subsides towards a third reference surface, which represents the behaviour of the reconstituted or completely remoulded soil in the same way as the outer surface in the bubble model.

1.2 Research Objectives

The main aim of the thesis was to implement, validate and apply a family of advanced constitutive models based on the kinematic hardening concept, to a variety of geotechnical problems .To achieve this aim the following objectives were identified:

1. Conduct a comprehensive literature review of existing constitutive models that are based on this concept and can describe important features of the behaviour of natural soils and make a decision which one to adopt for this study.

2. Implement the constitutive model into a finite element program, which is capable of analysing geotechnical problems and validate them through comparison of experimental data.

3. Apply the proposed model in the finite element analysis of a number of boundary value problems and assess its relative strengths and weaknesses.

4. Analyse and discuss the findings of this research and provide recommendations to advance this research in future work.

1.3 Layout of the thesis

1.3.1 Chapter 2

This chapter presents a literature review which covers 'Constitutive models of soil', The Bubble model and several other most relevant soil constitutive models are reviewed and the main differences between them are discussed.

1.3.2 Chapter 3:

The work in this chapter presents the main features of the Kinematic Hardening Structured model (KHSM) (Rouainia & Muir Wood, 2000). It also includes a demonstration of its stress-strain behaviours, with comparison with the modified Cam-clay model as well as a validation on triaxial test from Vallericca clay. Modifications to the model are proposed and discussed. Some key aspects of the model are also discussed. The implementation of the Bubble model in PLAXIS is explained and the derivatives of the yield function and the plastic potential are given in Appendix B.

1.3.3 Chapter 4:

This chapter contains the simulation of self-boring pressuremeter (SBPM) tests in London clay. The motivation for this work was the characterisation of the degree of initial structure of London clay. A total of three self-boring pressuremeter tests have been analysed at various depths, and specific parameters for the KHSM model have been calibrated and presented. A sensitivity study was conducted on the key parameters of the proposed model which control the destructuration process. One hypothesis whose influence on the results was investigated was that the SBPM is installed without damage. The results demonstrate the potential of the proposed model and also give a general indication of the influence r_0 and k have on the model's response during the course of a SBPM test.

1.3.4 Chapter 5

This chapter investigates the behaviour of a full scale embankment, constructed at Saint Alban, Quebec. The soft clay foundation was modelled with the kinematic hardening model for structured soils (KHSM) described in Chapter 3. The chapter is divided into two parts. The first part deals with the pre-failure behaviour of the embankment in a two-dimensional analysis. It presents a comparison of the deformational behaviour predicted by the three-surface model (KHSM) and the standard two-surface bubble model (KHM) when the same undrained strength is assigned to both models. The numerical predictions of pore-water pressures and settlements are also compared with field measurements. The second part of the chapter studies the three dimensional effects on the pre-failure response of the embankment. Comparisons between the two and three dimensional analyses are made with emphasis paid on the aspects that could not be modelled correctly with the two dimensional plane stain models in the past.

1.3.5 Chapter 6

This chapter analyses the behaviour of a deep excavation which forms part of a 100m wide basement excavation located in Boston, Massachusetts, USA. The glacial marine clay foundation was modelled with the kinematic hardening model for structured soils (KHSM) described in Chapter 3, the reduced version of the bubble model (KHM) and the very well-known Modified Cam Clay models. The aim of the work conducted in this chapter is to demonstrate that structure, anisotropy and history are essential components to give a good prediction.

1.3.6 Chapter 7

The thesis concludes with an outline of the findings of the study. The relative strengths and weaknesses of all findings are discussed and recommendations made to further this research. This chapter also discusses recent developments in the constitutive model under study, that were introduced in order to include the

effects of rotational hardening, as well as predict a smooth transition between the elastic and elasto-plastic state, with the introduction of subloading. The chapter also present a validation of the constitutive model through a series of simulations of the triaxial test data adopted in Chapter 3.

1.4 Definitions of stress and strain invariants

The state of stress for a three-dimensional point is defined by a matrix containing nine stress components shown in figure 1.1.

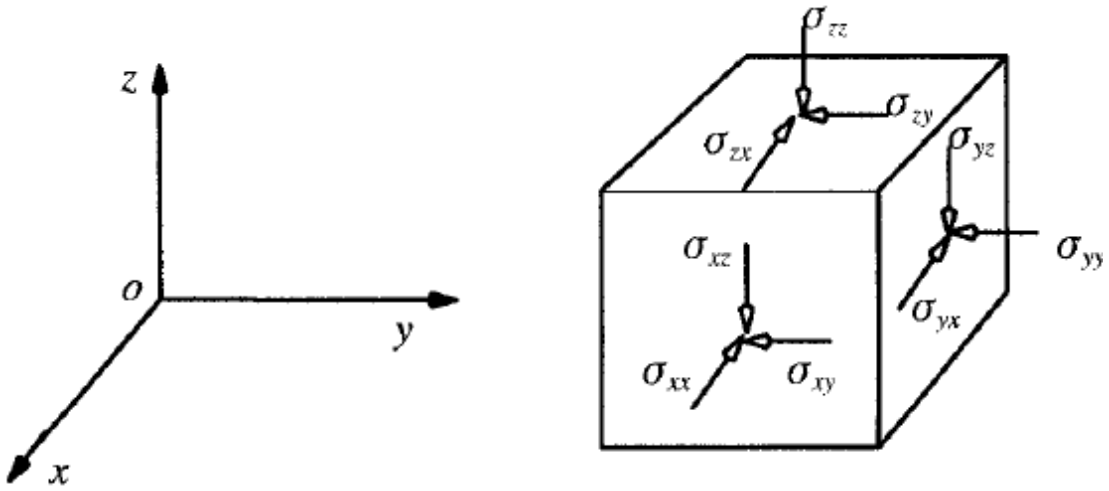

Figure 1.1: Stress components on a cubic soil element

The nine components of the stress at any point form a second order tensor, known as the stress tensor σ_{ij}, where *i* and *j* take integral values 1, 2 and 3:

$$\boldsymbol{\sigma} = \begin{bmatrix} \sigma_{xx} & \sigma_{xy} & \sigma_{xz} \\ \sigma_{yx} & \sigma_{yy} & \sigma_{yz} \\ \sigma_{zx} & \sigma_{zy} & \sigma_{zz} \end{bmatrix} = \begin{bmatrix} \sigma_{11} & \sigma_{12} & \sigma_{13} \\ \sigma_{21} & \sigma_{22} & \sigma_{23} \\ \sigma_{31} & \sigma_{32} & \sigma_{33} \end{bmatrix} = \sigma_{ij} \tag{1.1}$$

where the following relationships on shear stresses (τ) exists:

$$\sigma_{xy} = \sigma_{yx},\ \sigma_{xz} = \sigma_{zx} \text{ and } \sigma_{yz} = \sigma_{zy} \tag{1.2}$$

As a result there are only six independent stress components: three normal stresses, σ_{xx}, σ_{yy}, σ_{zz} and three shear stresses σ_{xy}, σ_{yz} σ_{xz}.

1.4.1 Principal stresses

The state of stress at a point in three dimensions can also be defined by three principal stresses σ_1, σ_2 and σ_3. These principal stresses are linked to the components of the stress tensor by the following equation:

$$\sigma^3 + I_1\sigma + I_1\sigma + I_3 = 0 \tag{1.3}$$

where I_1, I_2 and I_3 are known as the first, second and third stress invariant respectively and are defined as follows:

$$I_1 = \sigma_{xx} + \sigma_{yy} + \sigma_{zz} \tag{1.4}$$

$$I_2 = \sigma_{xx}\sigma_{yy} + \sigma_{yy}\sigma_{yy} + \sigma_{zz}\sigma_{xx} - {\sigma_{xy}}^2 - {\sigma_{yz}}^2 - {\sigma_{xz}}^2 \tag{1.5}$$

$$I_3 = \sigma_{xx}\sigma_{yy}\sigma_{zz} - \sigma_{xx}{\sigma_{yz}}^2 - \sigma_{yy}{\sigma_{xz}}^2 - \sigma_{zz}{\sigma_{xy}}^2 + 2\sigma_{xy}\,\sigma_{yz}\sigma_{xz} \tag{1.6}$$

Subsequently the stress tensor from equation 1.1 takes the following form

$$\begin{bmatrix} \sigma_1 & 0 & 0 \\ 0 & \sigma_2 & 0 \\ 0 & 0 & \sigma_3 \end{bmatrix} = \sigma_{ij} \tag{1.7}$$

In this case the stress invariants are linked to the principal stresses as follows:

$$I_1 = \sigma_1 + \sigma_2 + \sigma_3 \tag{1.8}$$

$$I_2 = \sigma_1\sigma_2 + \sigma_2\sigma_3 + \sigma_3\sigma_1 \tag{1.9}$$

$$I_3 = \sigma_1\,\sigma_2\sigma_3 \tag{1.10}$$

1.4.2 Mean and deviatoric stresses

The first invariant of the stress tensor is the mean stress of a point and is defined as the average of normal stresses in three directions, which can be expressed as follows:

$$p = \frac{\sigma_{xx} + \sigma_{yy} + \sigma_{zz}}{3} = \frac{1}{3}I_1 \tag{1.11}$$

The deviatoric components of the stress are defined by the following equation:

$$s_{ij} = \sigma_{ij} - p\delta_{ij} \tag{1.12}$$

where δ_{ij} is the *Kronecker delta* whose value is 1 when $i = j$ and is equal to 0 otherwise.

The second invariant of the deviatoric stress tensor is given by the following equation:

$$J_2 = s_{ij}s_{ij} = \frac{1}{2}[(\sigma_{11} - \sigma_{22})^2 + (\sigma_{11} - \sigma_{33})^2 + (\sigma_{22} - \sigma_{33})^2] + \sigma_{12}^2 + \sigma_{13}^2 + \sigma_{23}^2$$

$$J_2 = \frac{1}{3}(I_1^2 + 2I_3)$$

$$J_2 = \frac{1}{6}[(\sigma_1 - \sigma_2)^2 + (\sigma_2 - \sigma_3)^2 + (\sigma_3 - \sigma_1)^2] \tag{1.13}$$

The square root of the second invariant of deviatoric stress tensor is defined by:

$$J = \sqrt{J_2} \tag{1.14}$$

The third invariant of the deviator stress tensor is defined by the following equation:

$$J_3 = \frac{1}{3} s_{ij} s_{jk} s_{kl}$$

$$J_3 = \frac{1}{27} (2I_1^3 + 9I_1 I_2 + 27I_3) \tag{1.15}$$

The three principal stresses are related to the stress invariants by Lode's angle θ (figure 1.2), which is defined by the following equation:

$$\theta = \frac{1}{3} \sin^{-1}\left(\frac{-3\sqrt{3}J_3}{2J^3}\right) \tag{1.16}$$

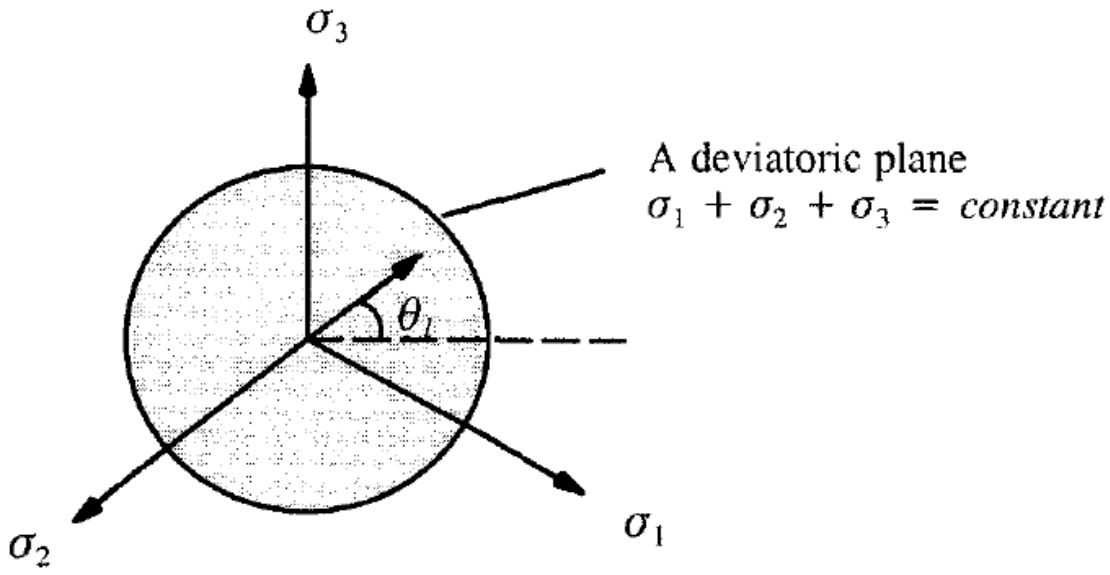

Figure 1.2: Lode angle on the deviatoric plane

1.4.3 Strain invariants

Similarly to the stress, the strain is a second order tensor given by the equation below:

$$\varepsilon_{ij} = \varepsilon_v \delta_{ij} + e_{ij} \tag{1.17}$$

It is defined by the six components provided below:

$$\varepsilon = \begin{bmatrix} \varepsilon_x & {}^1/_2\,\varepsilon_{xy} & {}^1/_2\,\varepsilon_{xz} \\ {}^1/_2\,\varepsilon_{yx} & \varepsilon_y & {}^1/_2\,\varepsilon_{yz} \\ {}^1/_2\,\varepsilon_{zx} & {}^1/_2\,\varepsilon_{zy} & \varepsilon_z \end{bmatrix} \tag{1.18}$$

where the following relationships on shear strain (γ) exists:

$$\varepsilon_{xy} = \varepsilon_{yx},\ \varepsilon_{xz} = \varepsilon_{zx} \text{ and } \varepsilon_{yz} = \varepsilon_{zy} \tag{1.19}$$

The strains tensor can be decomposed to two parts, the deviatoric strain tensor, and the volumetric strain, which are defined by equations 1.21 and 1.22:

$$\varepsilon = \begin{bmatrix} \varepsilon_v & 0 & 0 \\ 0 & \varepsilon_v & 0 \\ 0 & 0 & \varepsilon_v \end{bmatrix} + \begin{bmatrix} \varepsilon_x - \varepsilon_v & {}^1/_2\,\varepsilon_{xy} & {}^1/_2\,\varepsilon_{xz} \\ {}^1/_2\,\varepsilon_{yx} & \varepsilon_y - \varepsilon_v & {}^1/_2\,\varepsilon_{yz} \\ {}^1/_2\,\varepsilon_{zx} & {}^1/_2\,\varepsilon_{zy} & \varepsilon_z - \varepsilon_v \end{bmatrix} \tag{1.20}$$

$$e_{ij} = \varepsilon_{ij} - \varepsilon_v \delta_{ij} \tag{1.21}$$

$$\varepsilon_v = \varepsilon_{11} + \varepsilon_{22} + \varepsilon_{33} \tag{1.22}$$

1.4.4 Triaxial stress space

It is common in geotechnical engineering to work in the triaxial stress space, where the stress and strain invariants that are frequently applied are the mean effective stress *p'*, shear stress *q*, the volumetric strain ε_v and the shear strain ε_q. In this case the stress and strain invariants are expressed as follows:

$$p' = \frac{1}{3}(\sigma'_{11} + 2\sigma'_{33}) \tag{1.23}$$

$$q = \sigma'_{11} - \sigma'_{33} \tag{1.24}$$

$$\varepsilon_v = \varepsilon_{11} + 2\varepsilon_{33} \tag{1.25}$$

$$\varepsilon_q = \frac{2}{3}(\varepsilon_{11} - \varepsilon_{33}) \tag{1.26}$$

Chapter 2: Literature review

The aim of this chapter is to summarize the theoretical background for the development of the KHSM model and to provide an outline of the most relevant constitutive models that have been developed in recent years.

The literature review comprises of two parts. The first part covers the Critical State theory and describes the basic concepts associated with the various constitutive soil models that have been developed based on the Critical State framework. A brief description of the models that have been published through the years is given. The second part provides an overview of the notion of structure that is present in natural deposits and presents the constitutive models that have been developed in order to capture this attribute of the soil. A brief discussion of the similarities and differences between the models is provided while a detailed description of the proposed model is presented in the following chapter.

2.1. Critical State Soil Mechanics

The approach to plasticity in soil mechanics originated from theories on conventional engineering materials such as metal. For that reason, the first soil constitutive models were fundamentally flawed in describing the true behaviour of natural soils since they made use of unrealistic stress-strain relationships, disregarding phenomena such as non- linearity, strain hardening, strain softening and strength anisotropy. With the introduction of Critical State soil mechanics a more realistic description of the soil's volumetric behaviour during loading was achieved.

The Critical state framework was proposed by Roscoe, Schofield and Wroth (1958) at Cambridge University and brought together the work carried out on normally consolidated clays by Rendulic (1937) and that of Hvorslev (1937) which comprised of work on overconsolidated soils. The theory was founded on observations from triaxial compression tests on saturated clays which revealed behavioural patterns that indicated the relation between shear strength and deformation. The critical state of soil was defined as the stress state at which all clays would in due course reach under continuous loading. At this state, plastic shearing could continue indefinitely without any variations in volume and effective stresses. This perfectly plastic state is given by the following equation:

$$\frac{dp'}{d\varepsilon_q} = \frac{dq}{d\varepsilon_q} = \frac{dv}{d\varepsilon_q} = 0 \qquad (2.1)$$

Roscoe and his colleagues postulated that a characteristic surface exists in *p', q, v* space which contains all possible stress states of the soil (Figure 2.1). It should be noted that p', is the effective mean stress, q is the deviator stress defined as the difference between major and minor principal stresses and v is the specific volume of the soil and ε_q is the deviatoric strain as defined in the previous chapter .

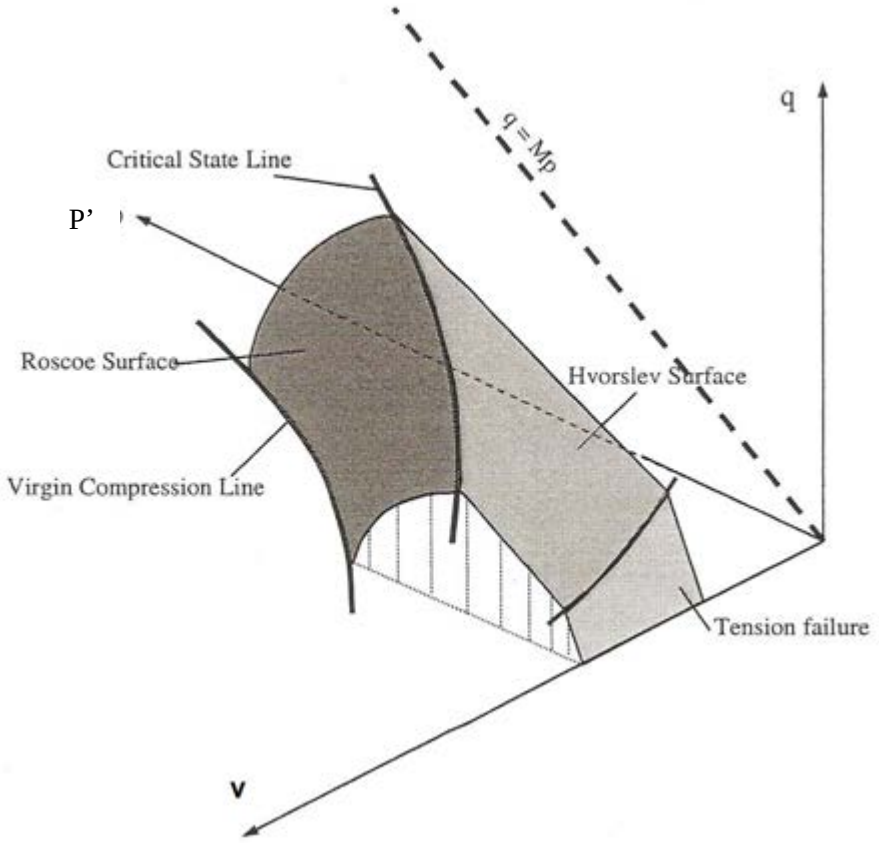

Figure 2.1 State boundary surface of the critical state framework in p'-q -v space

Upon loading of a soil specimen the stress path followed-irrespective of the stress history or mode of loading- will approach and consequently converge to a point on that surface which defines the critical state. It was assumed that the behaviour of the soil while it is located inside the state boundary surface was purely elastic and hence only recoverable deformations were predicted. On contact with the bounding surface, the behaviour became elasto-plastic, with a portion of the strains being plastic and therefore irrecoverable. When the critical state was reached, the stress state for a given soil formed a distinctive line in p'-q- v space referred to as the critical state line (CSL), which had the following equation:

$$\frac{q}{p'} = M \tag{2.2}$$

The earliest suggestions for using the theory of elasto-plasticity to produce constitutive models, replicating soil behaviour came in the 1950's when Drucker *et al.* (1957) hypothesised that a spherical cap could be added on the Druker-Prager

cone. This modified yield surface was controlled by the volume change. In addition, the emergence of the critical state framework by Roscoe *et al.*, as it was explained previously, provided the theoretical basis for the development of the first critical state soil models.

For a formulation of elasto-plastic constitutive model to be valid, four fundamental elements need to be specified; Firstly, the equation describing the yield surface, a definition for the flow rule and hardening rule and lastly a definition describing the elastic response of the model. A brief summary of the above elements is provided below (Wood, 1990).

.

- *Yield surface*

In conventional plasticity, a yield surface provides the criterion that needs to be satisfied in order for any plastic strains to develop. The equation for the yield surface, F, is dependent on the current stress state, $\boldsymbol{\sigma'}$, and the hardening (or internal) parameters, $\boldsymbol{k}$. Consequently, the size of the yield surface changes corresponding to variation of these two parameters:

$$F(\boldsymbol{\sigma'}, \boldsymbol{k}) = 0 \qquad (2.3)$$

In the event a stress state is contained inside the yield surface, implying $F < 0$, purely elastic behaviour is assumed to occur; otherwise the behaviour is elasto-plastic and the mathematical response is described by $F=0$.

- *Elastic part*

This particular element of the model describes the pure elastic behaviour, and in addition, the elastic strains which develop due to the elasto-plastic behaviour, (in the event the stress state is in contact with the yield surface)

- *Flow rule*

The flow rule is introduced to manage the direction of the plastic strain increments. Von Mises (1928) firstly introduced the concept of a plastic potential surface, for which the outward normal vector at the present stress state denotes the direction of the plastic strain vector. The flow rule can be described by the following:

$$d\varepsilon^p = \Lambda \frac{dP(\boldsymbol{\sigma'}, \boldsymbol{m})}{d\boldsymbol{\sigma'}} \tag{2.4}$$

In equation 2.4, variable $d\varepsilon^p$ describes the plastic strain increment vector, whereas $P(\boldsymbol{\sigma'},\boldsymbol{m}) = 0$, represents the plastic potential equation and finally variable Λ is defined as a scalar multiplier. Following that work, Drucker *et al.* (1957) postulated that for work hardening materials, the plastic potential function P has to be identical to the yield function F, giving an associated flow rule. In the event the plastic potential equation differs from the yield function, $P(\boldsymbol{\sigma'},\boldsymbol{m}) \neq F(\boldsymbol{\sigma'},\boldsymbol{k})$, the flow rule is considered as non-associated.

The absolute magnitudes of the components of vector $\boldsymbol{m}$ are irrelevant in this particular condition, due to the fact that only the results from differentiation of the plastic potential equation corresponding to the stress components are essential for the flow rule formulation.

In Equation 2.4 the normal vector of the plastic potential equation is responsible for describing the relative amounts of the plastic strain components and it is the scalar parameter, Λ, which quantifies their actual value.

- *Hardening rule*

The hardening rule determines the progression of the yield surface during the development of plastic deformation and is the last ingredient used to describe the plastic response. It defines the scalar parameter, Λ and consequently how the hardening parameters $\boldsymbol{k=m}$ (for an associated rule) change with plastic straining.

If the elasto-plastic formulation is considered to be purely plastic, it can be extrapolated that the hardening parameters $\boldsymbol{k}$ are continuous and therefore no hardening rule is required. More generally the hardening parameters are thought to be dependent one of the two following elements: the plastic work or the plastic strains.

In the case where the yield criterion is $F(\boldsymbol{\sigma},\boldsymbol{k})=0$, the consistency condition necessitates that the stress state maintains its position on the yield function ($F=0$) during small increments so that:

$$dF = \left\{\frac{dF}{d\boldsymbol{\sigma}'}\right\}^T d\boldsymbol{\sigma}' + \left\{\frac{dF}{dk}\right\} dk = 0 \tag{2.5}$$

In the event where a stress increment $d\boldsymbol{\sigma}'$ engages and consequently moves the yield surface, the hardening parameters $\boldsymbol{k}$ evolves according to equation 2.3 above. In strain hardening materials it is reasonable to assume that the amounts of plastic strains are undoubtedly correlated to the hardening parameters by the following equations.

$$dk = \left[\frac{dk}{d\varepsilon^p}\right] d\varepsilon^p \tag{2.6}$$

And therefore the relationship stemming from the consistency conditions (equation 2,5) can be re-written as:

$$dF = \left\{\frac{dF}{d\boldsymbol{\sigma}'}\right\}^T d\boldsymbol{\sigma}' + \left\{\frac{dF}{dk}\right\} \left[\frac{dk}{d\varepsilon^p}\right] d\varepsilon^p = 0 \tag{2.7}$$

By substituting equation 2.7 in the flow rule (equation 2.4)

$$dF = \left\{\frac{dF}{d\boldsymbol{\sigma}'}\right\}^T d\boldsymbol{\sigma}' + \left\{\frac{dF}{dk}\right\} \left[\frac{dk}{d\varepsilon^p}\right] \Lambda \frac{dP(\boldsymbol{\sigma}', \boldsymbol{m})}{d\boldsymbol{\sigma}'} = 0 \tag{2.8}$$

A simple rearrangement of the equation above provides the scalar quantity Λ as:

$$\Lambda = \frac{1}{A}\left\{\frac{dF}{d\boldsymbol{\sigma}'}\right\}^{T} d\boldsymbol{\sigma}' \tag{2.9}$$

Where A is defined as the hardening or plastic modulus and is described by the following equation termed hardening function:

$$A = -\left\{\frac{dF}{dk}\right\}\left[\frac{dk}{d\varepsilon^{p}}\right]\left\{\frac{dP(\boldsymbol{\sigma}', \boldsymbol{m})}{d\boldsymbol{\sigma}'}\right\} = 0 \tag{2.10}$$

2.1.1 *Original Cam clay*

The original Cam clay formulation was firstly proposed by Roscoe and Schofield (1963) and assumed a yield locus for the soil in the form of a logarithmic curve in p'-q stress space (figure 2.2). This surface was drawn symmetrically about the hydrostatic (i.e isotropic) axis (p') and marked the boundary between elastic and elasto-plastic material behaviour. The description of the yield surface is mathematical terms is given by the equation below:

$$F = \frac{q}{p'M} + ln\left(\frac{p'}{p'_0}\right) = 0 \tag{2.11}$$

Where p' is the mean effective stress, q is the deviatoric stress, M is a soil constant defined as the critical state ratio and p'_0 is the value of the mean stress variable that controls the size of the yield surface and thus the hardening parameters (**k=p$_0$'**) as defined previously.

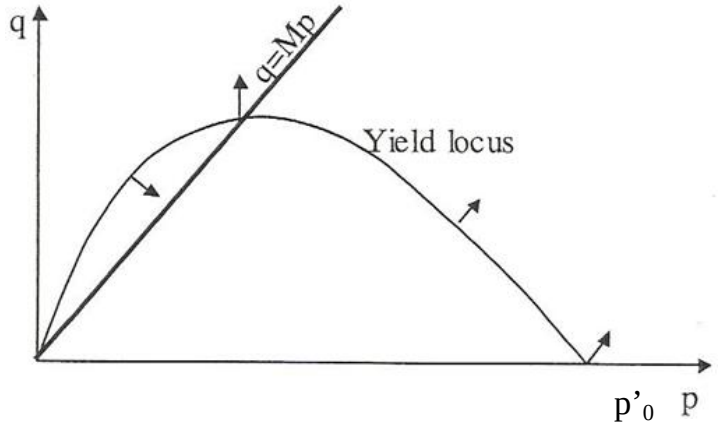

Figure 2.2 Projection of the yield surface for the original Cam clay model in *p'-q* space

2.1.2 *Modified Cam clay*

Some difficulties which became evident with the original formulation of the Cam clay model, lead to the development of the modified Cam clay model by Roscoe and Burland (1968). Specifically, the singularity of the logarithmic curve at the point where *q=0*, produced practical and theoretical difficulties. An infinite number of points normal to the surface are produced and thus an infinite number of flow directions could be defined this point. Furthermore, with the associated flow rule that was assumed for the original formulation, any isotropic stress changes lead to the development of non-zero shear strains.

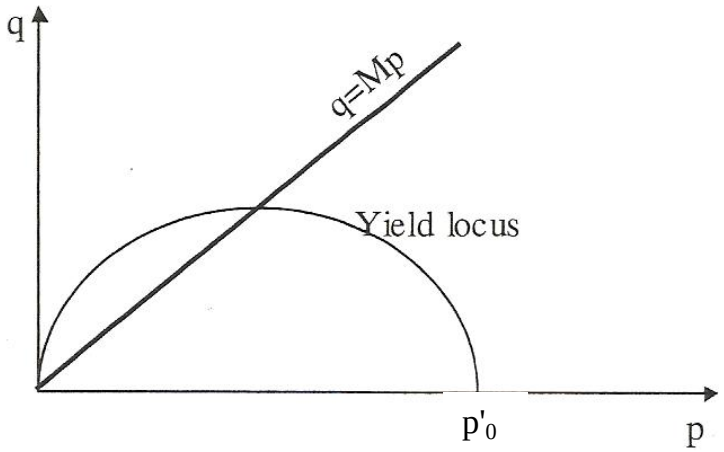

Figure 2.3 Projection of the yield surface for the modified Cam clay model in *p'-q* space

In order to alleviate these complications, Roscoe and Burland suggested a modification to the yield surface expression, so that in the modified Cam clay model the surface plots as an ellipse in the p' and q stress space(figure 2.3). It was clear that through adopting a smooth ellipsoid the issue with the discontinuity at q=0 was resolved. This change also enabled the shape of the yield surface to be described by just one shape parameter providing greater simplicity within analytical description (Wood, 1990). The soil was assumed to obey the normality condition, so that the mathematical expression for the yield surface coincided with the expression for the plastic potential surface.

$$F = g = \ q^2 - \ M^2 \left[p'\left(p'_0 - p'\right)\right] = 0 \tag{2.12}$$

It was assumed that any changes in mean effective stress p' would be followed by recoverable i.e. elastic changes in volume according to the following expression, provided that the stress state was situated inside the yield surface:

$$d\varepsilon_p^e = \kappa \frac{dp'}{vp'} \tag{2.13}$$

The elastic shear strains that ensue after any changes of the deviator stress were described by the following equation:

$$d\varepsilon_q^e = \frac{dq}{3G'} \tag{2.14}$$

This model assumed that the yield surface expanded or contracted keeping its initial shape, with the size of the surface dependent on the preconsolidation stress p'_0. The isotropic hardening or softening of the yield surface was linked to the specific volume of the soil by the following equation:

$$\frac{dp'_0}{p'_0} = d\varepsilon_p^{\mathrm{p}} \frac{v}{\lambda - \kappa} \tag{2.15}$$

Since the hardening /softening of the yield surface was made to depend only on the volumetric behaviour of the soil, there was no change of the yield surface associated with the deviatoric plastic strains and therefore:

$$\frac{dp'_0}{d\varepsilon_q^{\mathrm{p}}} = 0 \tag{2.16}$$

The above equations provide a description of all the elements that are required to define an elasto-plastic soil constitutive model. For stress states that remained within the yield surface the elastic response of the model is summarized in the following matrix equation:

$$\begin{bmatrix} d\varepsilon_p^{\mathrm{e}} \\ d\varepsilon_q^{e} \end{bmatrix} = \begin{bmatrix} \kappa/vp' & 0 \\ 0 & 1/3G' \end{bmatrix} \begin{bmatrix} dp' \\ dq \end{bmatrix} \tag{2.17}$$

Once the yield surface is engaged, plastic strains began to occur and the plastic stress-strain response is given by the following matrix equation:

$$\begin{bmatrix} d\varepsilon_p^{\mathrm{p}} \\ d\varepsilon_q^{p} \end{bmatrix} = \frac{(\lambda-\kappa)}{vp(M^2+\eta^2)} \begin{bmatrix} (M^2-\eta^2) & 2\eta \\ 2\eta & 4\eta^2/(M^2-\eta^2) \end{bmatrix} \begin{bmatrix} dp' \\ dq \end{bmatrix} \tag{2.18}$$

The development of the Cam clay models marked significant progress in the field of elasto-plastic constitutive models. The models managed to capture the existence of experimentally observed yield loci and were able to simulate the behaviour of normally and lightly overconsolidated clays in a reasonable manner.

However some limitations of these initial critical state models were identified. The assumption that the existing yield surface bounds the area in which the stress states instigate elastic and therefore recoverable deformations was called into question. As described earlier, upon contact with the yield surface the strain response was assumed to become elasto-plastic leading to a sudden, sharp drop in the stiffness of the material. Furthermore, any subsequent changes of the loading direction such as unload-reload cycles, within the yield surface, produced only purely elastic strains and constant excess pore pressure response after the first

loading cycle. These characteristics were not consistent with observations of real soil behaviour, as yielding of soils was a far more gradual process, with the transition in stiffness occurring in a much smoother manner as the soil moved from the elastic to the elasto-plastic phase. In addition, soil specimens that were subjected to cyclic loading exhibited gradual accumulation of irrecoverable plastic strains that implied energy dissipation, associated with hysteretic behaviour, as well as accumulation of excess pore water pressures.

The Cam clay models were developed based on the assumption isotropic behaviour. However, most natural soils exhibit anisotropic characteristics due to a variety of reasons. The mode of deposition, anisotropic consolidation, and subsequent stress history of the soil deposits influence behaviour of the soil and- in modelling terms- the orientation of the yield loci. In many cases soils were deposited over large areas, and therefore the deformations they have experienced during and after deposition have been essentially one-dimensional. As shown in figure 2.4, the shape of the experimental yield loci could be approximated by an ellipse for modelling purposes. However, the yield loci were found to be rotated from the isotropic axis and centred on the K_0-line. This anisotropic state of the yield surfaces was not a feature that the initial the Cam clay models were initially designed to capture.

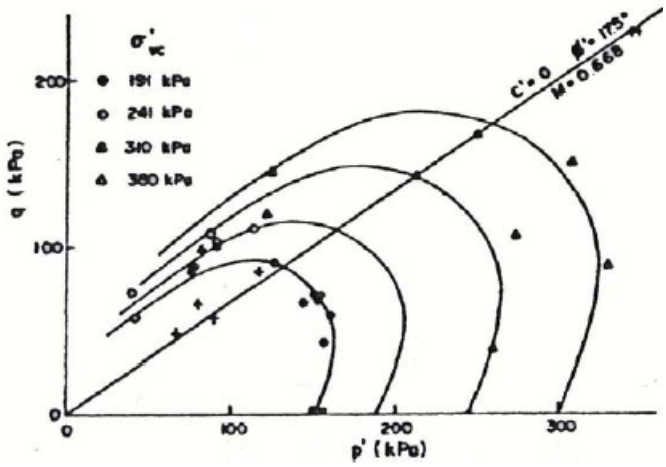

Figure 2.4: Yield curves observed from triaxial tests on undisturbed Winnipeg clay (Wood, 1990 after Graham et al., 1983).

2.2 Extensions of the critical state models

As detailed earlier, the classical theory of elasto-plasticity does not allow for any plastic deformations to take place inside the yield surface and therefore the real behaviour of soils was not correctly replicated. Various techniques have been suggested, by means of which the observed soil response may be incorporated into numerical models.

2.2.1 *Bounding surface plasticity theory*

The '*bounding surface*' plasticity theory, (Dafalias and Herrmann, 1982) and the associated models that have been developed, make allowances for plastic deformations to occur within the nominal yield surface. Furthermore, the theory treats the stiffness as dependent on the distance of the current effective stress state from the yield surface. As a result the stiffness gradually decreases as the yield surface is approached. Figure 2.5 provides a schematic illustration of the principles behind the bounding surface theory.

This type of models have their origins in conventional critical state model principles, with a plastic potential and a hardening law associated with the bounding surface, which acts in similar way to the conventional yield surface that was described earlier. Where this theory diverges from the conventional framework, is in the response of the models when the soil element occupies a stress state that places it inside the yield surface. In this case, the behaviour of the soil in the event of loading becomes elasto-plastic and hence irrecoverable deformations would take place. The response remains elastic in the event the soil is further unloaded, leading to elastic and hence recoverable deformations developing. As with all the critical state models, the elasto-plastic behaviour of soil is evaluated with the combination of the hardening modulus equation and the plastic potential rule, which are derived from the consistency condition as shown previously. The magnitude of the plastic deformations as well as the stiffness of the soil, are made to depend on the distance of the present stress state to a reciprocate point on the bounding surface. It should be noted that the theory allows for the

size and the orientation of the bounding surface to change during the elasto-plastic response of the models.

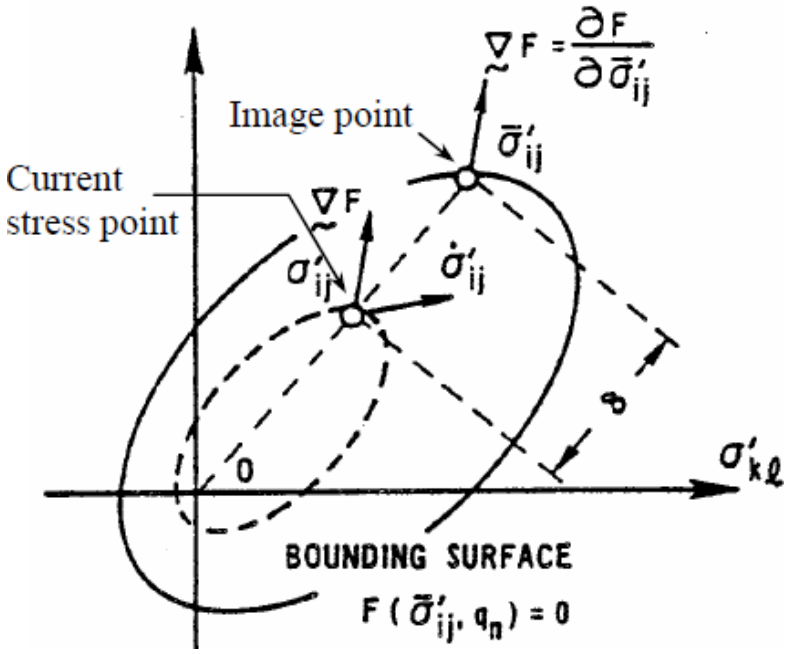

Figure 2.5: Illustration of the bounding surface plasticity theory (Dafalias and Herrmann (1982))

A number of soil constitutive models have been developed within the framework of the bounding surface plasticity, most notable the collection of MIT soil models that were developed in the Massachusetts Institute of Technology (Whittle, 1993). The MIT-E3 model was developed based on the modified Cam clay principles; however salient characteristics of the two models were distinctively different. Firstly, the isotropic elliptical shape of the modified Cam-clay yield surface was replaced by a rotated version of it. The unsymmetrical critical state boundaries were described using two different values of compression and extension Mohr- Coulomb's friction angles. These two modifications enabled the model to replicate the anisotropic behaviour of soils relatively well, however the formulation describing the change of orientation of the yield surface, had to be carefully defined. The MIT-E3 model made use of a non-associated flow rule which entails the introduction of another arbitrary function to describe the plastic flow potential.

In addition further two hardening rules, one describing the variation in size and the second the variation in orientation of the yield surface were also dictated. One drawback of the MIT-E3 model is that could not portray the accumulated strains

observed in each loading cycle. This drawback was attributed to the formulation of the hysteretic behaviour since only one point of stress reversal state was defined to address the complicated stress paths occurring during cyclic loading. The MIT-E3 bounding surface model proved to be cumbersome for day-to-day use since it made use of multiple intricate mathematical expressions and in addition requires an array of input parameters.

2.2.2 *Kinematic hardening concept*

The bounding surface plasticity theory was a significant improvement in the development on constitutive models. The concept made allowances for features of the soil behaviour, such as anisotropy of the yield surface, as well as plastic deformation occurrence within the yield surface, that could not captured by conventional critical state models. However, it still lacked the capacity to correctly portray some fundamental features of the soil's response. During unloading of a soil element it was assumed that the soil responded in an entirely elastic manner and therefore features such as energy dissipation which lead to hysteretic behaviour, as well as accumulation of excess pore water pressures under cyclic loading were not correctly addressed.

An alternative strategy which intended to address those issues was the supposition that a small, internal yield surface was present. This newly introduced surface translated inside the conventional yield surface, corresponding to the existing stress state, according to a kinematic hardening rule. This small region defined the extent of the truly elastic zone of the soil. The translation of the small elastic region gave the designation *'kinematic hardening'* to these models. Kinematic hardening models are expedient since they are able to retain information relating to the recent stress history of the material. The inelastic behaviour was treated within the framework of plasticity theory, with the usual ingredients such as a yield surface which bounds the region of elastically accessible stress states, a flow rule which described the mechanism of plastic deformation and finally hardening expressions which controlled the value of plastic strains. Figure 2.6, provides a schematic diagram on the kinematic hardening theory.

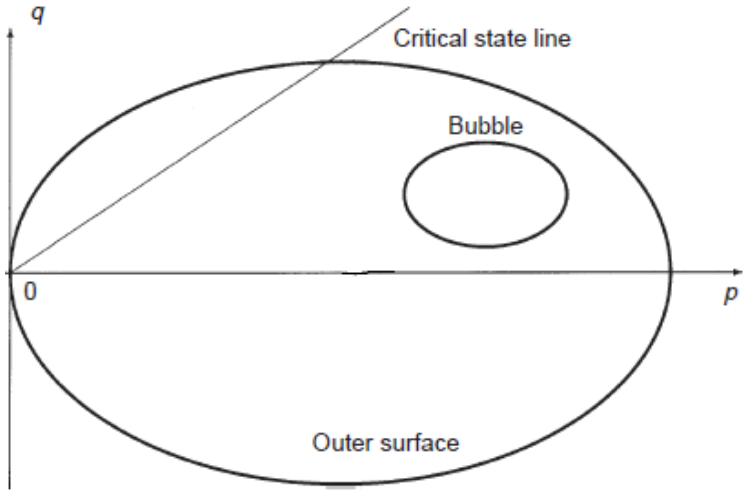

Figure 2.6: Conceptual illustration of a kinematic hardening model (after Rouainia and Muir Wood, 2000)

In order to develop a kinematic hardening constitutive model, some necessary elements need to be specified. The novel aspect relative to the bounding surface plasticity, is the small region herein referred to as the '*bubble'*. The *'bubble'* has all the attributes of a conventional yield surface and therefore equations dictating the behaviour of the bubble are required. Purely elastic behaviour is predicted if the stress state is situated inside the bubble. Once the yield surface is engaged there is a transition to the elasto-plastic state and the predicted response is directed by the plastic potential and hardening laws attributed to the bubble. The elastic domain then follows the stress path until the bubble and the external bounding make contact. In that occasion, the external surface assumes the role of a conventional yield point and the behaviour is dictated by the laws describing the outer surface. It should be noted that the formulations are such, so that the two yield surfaces never intersect.

2.2.2.1 *Two surface model (Mroz et al., 1979)*

The first one to propose a model based on the kinematic hardening concept was Mroz (1967), who developed a multi surface kinematic hardening model for metals. In order to simulate the changing magnitude of the hardening modulus which leads to the gradual decrease of the stiffness, Mroz formulated a model that contained multiple surfaces enclosed within the conventional yield surface. A distinct value of the hardening modulus was assigned to each of the surfaces. When the stress state was inside the first surface, elastic response was assumed. Upon loading, the stress path moved towards the first yield surface and once it was engaged, elasto-plastic behaviour -which was quantified by the hardening modulus associated with that surface - ensued. Continued loading dragged the first yield surface along a path that engaged the second yield surface, with the behaviour now controlled by the hardening modulus attributed to the second one. Further work was carried out to develop multi surface models for soil, which eventually lead to the work by Mroz *et al.* (1979) that reduced number of yield surfaces to only two (figure 2.7).

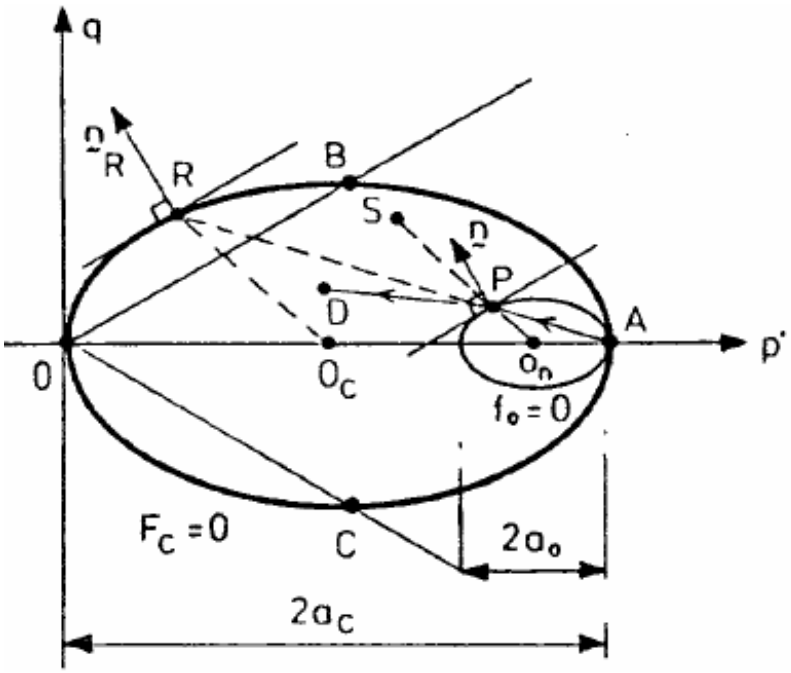

Figure 2.7: The simplified two surface kinematic hardening model (Mroz *et al.,* 1979)

The outer surface (F_c=0) was termed the '*consolidation'* surface and was expressed in terms of information from previous peak stresses in conjunction with the soil's density. The '*consolidation'* surface was allowed to increase in size, contract and even change position, upon adequate loading. The description of the outer surface is mathematical terms is given by the equation below:

$$F_c = (p' - \alpha_c)^2 + \frac{q^2}{M^2} - {\alpha_c}^2 = 0 \tag{2.19}$$

Where α_c is the major semi-diameter of ellipse (the distance from the origin to the centre of the consolidation surface on *p* axis) and *M* is the slope of the critical state line. The bubble yield surface provides a criterion for determining whether or not plastic strains accompany a particular stress increment and was expressed by the following equation:

$$f_0 = \left(p' - \alpha_p\right)^2 + \frac{\left(q - \alpha_q\right)^2}{M^2} - {\alpha_0}^2 = 0 \tag{2.20}$$

Where a_0 is the semi-diameter of the ellipse and $\boldsymbol{\alpha}$ = (α_p, α_q) is the centre of the yield surface in *p*, *q* space. The magnitude of the strains is calculated using an assumed flow rule and a hardening rule, resulting in the plastic stress-strain response (associated with the bubble surface) is given by the following matrix equation:

$$\begin{bmatrix} d\varepsilon_p^{\mathrm{p}} \\ d\varepsilon_q^{p} \end{bmatrix} = \frac{1}{K} \begin{bmatrix} \frac{p - \alpha_p}{G_f} \\ \frac{q - \alpha_q}{M^2 G_f} \end{bmatrix} [d\sigma] \tag{2.21}$$

G_f is the shear modulus of the soil and the plastic modulus in the above equation (K), was made to depend on the distance between the current stress, point P (figure 2.7) and the conjugate point R on the consolidation surface and was given by the following equation:

$$K = K_R + (K_P - K_R)\left(\frac{b}{b_0}\right)^{\gamma} \tag{2.22}$$

Where term *b,* is the distance from point *P* on the yield surface, to the conjugate point *R* on the consolidation surface. Similarly b_0 is the maximum distance which is obtained when the bubble is touching the consolidation yield surface at a point diametrically opposite to the conjugate point *R*. As it is evident from the above expression, the value of *K* is equal to the plastic modulus K_R at the conjugate point when the bubble and the structure surface are in contact at the current stress, i.e. b=0. The exponent γ described the parameter governing the reduction rate of the plastic modulus.

The translation rule of the bubble i.e. the kinematic hardening component of the model was formulated in a way which ensured a smooth transition as the bubble approaches the consolidation surface. This was necessary in order to satisfy the criterion for non- intersection of the two surfaces and it was achieved by considering that for any stress point, σ_p, on the bubble f $_0$, there is a conjugate point, $\sigma_{R,}$ on the consolidation surface F_c that has the same direction of the outward normal (figure 2.7) . The mathematical expression for the above hypothesis is provided in equation 2.23:

$$\frac{\sigma_P - \alpha}{\alpha_0} = \frac{\sigma_R - \alpha_c}{\alpha} \tag{2.23}$$

And therefore the two surfaces have the same shape.

2.2.2.2 *Kinematic hardening models (Hashiguchi, 1985, 1989)*

Treading in a similar path with Mroz, Hashiguchi formulated a two surface kinematic hardening model, (1985), for generalized stress space (figure 2.8). The general components of the model complied with the principles of the kinematic hardening model formulations. The salient feature of the model was the proposal of a new form for the kinematic hardening rule. This included a term that correlated the rule to the translation along the line connecting the centres of the surfaces whereas in previous formulations of kinematic hardening rules (Mroz, 1979 etc.) the translation was associated with the line connecting the surface of the bubble and the conjugate stress point.

Further work (Hashiguchi, 1989) saw the introduction of a third surface, located inside the sub-yield surface (i.e bubble).This new surface was labelled 'subloading *surface'* and was con-centric with the inner bubble (sub-yield surface). It must be noted that the newly introduced surface passed always through the current stress point during either loading or unloading conditions. The purpose of the new development was to eradicate the abrupt change in the stress-strain relationship predicted by the two surface models, and provided instead a smooth transition from the elastic to the plastic domain.

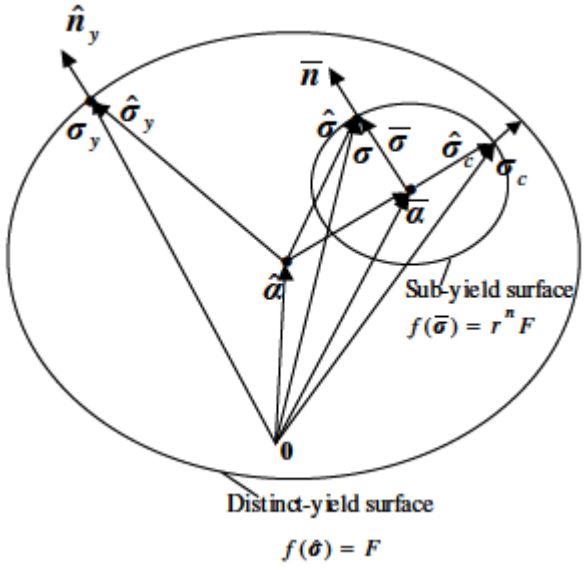

Figure 2.8: Hashiguchi kinematic hardening model (Hashiguchi, 1985)

2.2.2.3 *Bubble model (Al-Tabbaa and Wood, 1989)*

Following experimental work on speswhite kaolin, (Al-Tabbaa, 1987), Al-Tabbaa and Wood (1989), proceeded in the introduction of a two surface kinematic hardening 'bubble' model. It was an extension of the Cam clay and had many similarities with previous models proposed by Mroz et al. (1979) and Hashiguchi (1985, figure 2.9). Similarly to the previous two models, a kinematic yield surface (bubble) was assumed, which bounded the truly elastic region and was positioned within the modified Cam Clay yield surface. It had the same shape as the Cam clay yield surface and its relative size was dictated by parameter *R*. A more detailed description of the model is provided below. In the 1989 model, the conventional Cam clay yield surface assumed the role of the bounding surface. The behaviour within the kinematic yield surface obeyed the rules of isotropic elasticity. The hardening modulus was contingent on the distance between the two surfaces. The model was able to reduce to the modified Cam Clay model for monotonic loading and for continuous yielding. Al-Tabbaa (1987) showed that the model was capable of predicting satisfactorily the cyclic behaviour of speswhite kaolin.

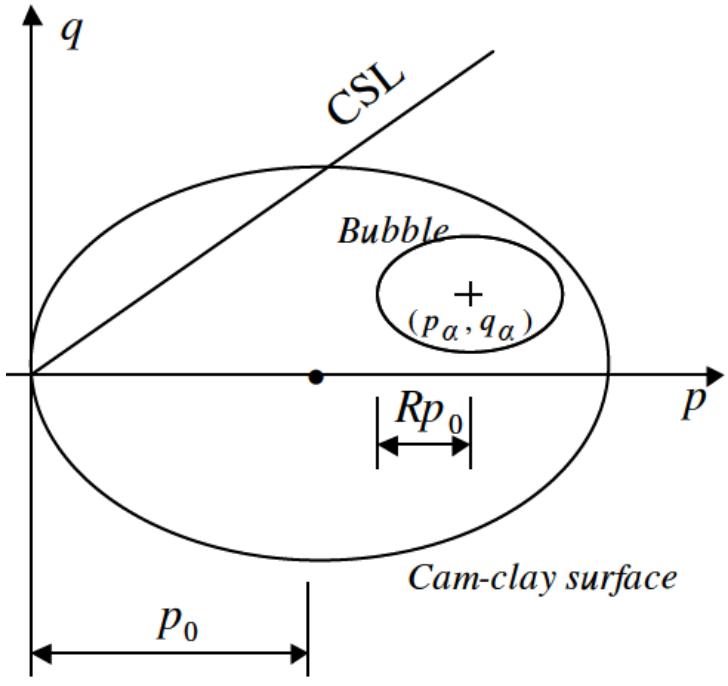

Figure 2.9: The two surface kinematic hardening 'bubble' model (Al-Tabbaa and Muir Wood, 1989)

The shape of the soil yield loci was assumed to be elliptical and the size was controlled by parameter p_0. The mathematical expression below was used to describe the yield surface:

$$F = (p - p_0)^2 + \frac{q}{M^2} - p_0^2 = 0 \tag{2.24}$$

As stated previously the elastic bubble assumed an elliptical shape (as the Cam clay yield surface) and its size was dictated by parameter *R*, which is described as the ratio of the two surfaces. The *'bubble'* equation is written as:

$$f_b = (p - p_a)^2 + \frac{(q - q_a)^2}{M^2} - Rp_0^2 = 0 \tag{2.25}$$

It was well documented earlier, that a fundamental requirement of the kinematic hardening models is that the rule of translation ensures that the bubble and the outer-Cam clay- surface engage at a common point but under no circumstances they are permitted to intersect. This was made possible by associating each point on the bubble surface with the corresponding conjugate points on the Cam clay surface (Mroz, 1967; Hashiguchi, 1985), so that the outward normal of the bubble and conjugate points faced in the same direction. The kinematic hardening principle prescribed for the bubble model comprised of two parts. The first part dealt with the variation of the size of the yield loci resulting from the development of plastic strains. The second component described the change of the bubble surface, associated with the positional variation within the Cam clay bounding surface. The movement through the stress space had to occur in the direction of the vector that joined the current and conjugate stress points, a feature which ensured that the yield locus and the bounding surface would not intersect at any time.

The equation required to describe the kinematic hardening rule then became:

$$\frac{dp'_a}{dq_a} = \frac{dp_0}{p_0}\begin{bmatrix} p'_a \\ q_a \end{bmatrix} + S\begin{bmatrix} \frac{p'-p'_a}{R} - & (p'-p_0) \\ \frac{q-q_a}{R} - & q \end{bmatrix} \tag{2.26}$$

The first term in the equation above corresponded to the change in p_0, and therefore the size of the bubble surface, whereas the second term expressed the assumed movement along the vector that joined the current and conjugate stress points.

The scalar quantity *S* was described by the following equation:

$$S = \frac{(p'-p'_a)\left[dp' - \frac{dp_0}{p_0}p'\right] + \frac{(q-q_a)}{M^2}\left[dq - \frac{dp_0}{p_0}q\right]}{(p'-p'_a)\left[\frac{p'-p'_a}{R} - (p'-p'_0)\right] + \frac{(q-q_a)}{M^2}\left[\frac{q-q_a}{R} - q\right]} \tag{2.27}$$

The isotropic hardening rule assumed the same form as that of the modified Cam-clay model, with the solitary difference being, that λ, κ were substituted by λ^*, κ^*. Parameter λ^* is the slope of normal compression lines in *lnv*:*lnp* compression plane and κ^* is the initial slope of the unloading lines in the *lnv*:*lnp* compression plane.

$$dp_0 = \frac{p_0}{(\lambda * - \kappa *)}\ d\varepsilon_p^{\mathrm{p}} \tag{2.28}$$

The hardening modulus has a form that comprises of two parts. The first part determines the plastic strain increments in conditions where the bubble and bounding surfaces interact and the second, the response of the model when plastic strains occur irrespective of the position of the bubble relative to the Cam clay surface. Therefore the hardening function expression takes the following form:

$$h = h_0 + H \tag{2.29}$$

Where h_0 describes the hardening modulus in the event the two surfaces are in contact, and is given by the following expression:

$$h_0 = \frac{(p' - p'_a)}{(\lambda * - \kappa *)} \left[p'(p' - p'_a) + \frac{q(q - q_a)}{M^2} \right] \tag{2.30}$$

The scalar quantity *H*, which was a function of the stress state, may take various forms. The sole constraint is that the proposed expression must ensure smooth reduction of the stiffness, as the bubble advances towards the bounding surface. As stated by Al-Tabbaa and Wood any form which corresponds to acceptable calibration with a set of experimental data under consideration is considered adequate for use within the same framework. For the particular model, Al-Tabbaa and Wood considered a number of features that may impact on the form of the hardening expression, before proposing the following:

$$H = \left[\frac{p_0^3}{(\lambda * - \kappa *)} \right] \left(\frac{b}{b_{max}} \right)^{\psi} \tag{2.31}$$

As it is evident in the above expression, It was assumed that the plastic modulus, *H,* was a dependent on distace *b*, which is the component of the vector joining the current and conjugate stresses, in the direction normal to the bubble at the current stress state. Furthermore, an interpolation exponent ψ was introduced. This parameter was a positive, real exponent, and was dependent on the type of soil under consideration. Determination of the value of parameter ψ was based on experimental results using a trial and error method. The mathematical expression for *b* and b_{max} are given in equations 2.32 and 2.33 respectively.

$$b = \frac{1}{Rp_0} \left[(p' - p'_a) \left[\frac{p' - p'_a}{R} - (p' - p_0) \right] + \frac{(q - q_a)}{M^2} \left[\frac{q - q_a}{M^2} - q \right] \right] \tag{2.32}$$

$$b_{max} = 2p_0(1 - R) \tag{2.33}$$

2.2.2.4 *Three surface kinematic hardening model 3-SKH (Stallebrass, 1990)*

The three-surface kinematic hardening (3-SKH) soil model was proposed in an effort to better simulate the behaviour of clays in overconsolidated states during early stages of loading. The new development provided an enhancement of the 'bubble' model of Al Tabbaa and Wood (1989), so that the effect of immediate stress history and yield at small strains or changes in the stresses were captured. This was achieved with the introduction of a new yield surface, nested within the conventional Cam clay surface of the bubble model. The model is illustrated in *p'-q* stress space in Figure 2.10. The conventional modified Cam-clay acted as the bounding surface. In similar fashion to the two surface models, the yield surface marked the onset of plastic deformations, whereas the newly introduced history surfaces, captured the effects of recent stress history. All three surfaces were described by the same elliptical geometry.

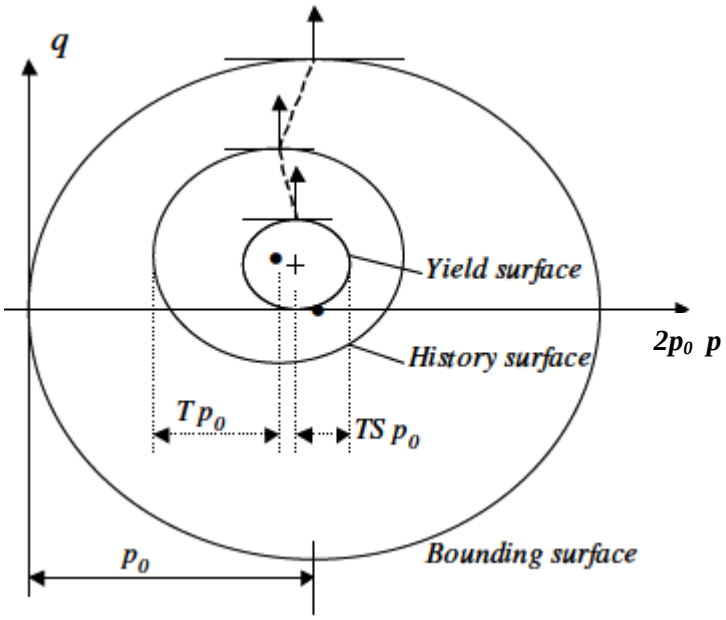

Figure 2.10: Schematic diagram of the three-surface kinematic hardening model 3-SKH (Stallebrass and Taylor, 1997)

The bounding surface was defined with the conventional expression for the modified Cam clay model:

$$F = (p' - p'_0)^2 + \frac{q}{M^2} - p'^2_0 = 0 \tag{2.34}$$

where (p_0,0), are the coordinates of the centre of the bounding surface and represented as half the preconsolidation pressure in the modified Cam clay model. As it can be seen the bounding surface is centred on the mean stress axis and therefore no anisotropy of the bounding surface is considered in this model.

The two internal kinematic surfaces are described by the same shape as the bounding surface, with reduced dimensions which are controlled by constant ratios. The equation of the history surface, which contains the extent of recent stress variations, is provided by:

$$f_h = (p' - p'_a)^2 + \frac{(q - q_a)^2}{M^2} - T^2 p'^2_0 = 0 \tag{2.35}$$

In equation 2.35, T represents the ratio of the history surface size to the bounding surface size, and in similar fashion to equation 2.34 (p_a, q_a) describe the centre of the history surface.

The yield surface, describing the elastic domain in generalised stress space, is provided by the following expression:

$$f_y = (p' - p'_b)^2 + \frac{(q - q_b)^2}{M^2} - T^2 S^2 p'^2_0 = 0 \tag{2.36}$$

where S represents the ratio of the size of the yield surface to that of the history surface and (p_b, q_b) is the centre of the yield surface in stress space.

The model assumed an associated flow rule and consequently the plastic potential equation is identical to the yield surface expression. The hardening rules for three the surfaces were a combination of isotropic and kinematic hardening and

controlled the model's response according to the position and size of the kinematic surfaces.

The bounding surface was allowed to only expand and contract with plastic strains in similar fashion to the conventional bubble model and therefore only isotropic hardening was considered (see equation 2.20). As in the two-surface model, the parameters λ^* and κ^* represented the slope of the isotropic normal compression line and the slope of the swelling line, for an unloading path lying entirely within the kinematic yield surface, in ln$v$-lnp' space.

The translational rules for the two kinematic surfaces comprised of the isotropic hardening component and the kinematic part as in the bubble model. The formulation of the 3-SKH model gave rise to three distinct responses for the behaviour of the soil. First of all, pure elastic behaviour was predicted when the stress state was situated inside the yield surface. The response continued to be elastic for any stress path that did not engage the surface. Otherwise, the stress-strain behaviour predicted was elasto-plastic with the associated flow rule on all surfaces. The appropriate hardening rule was invoked, depending which surface was engaged at the time. As with the bubble model, the case where all three surfaces are in contact was the starting point for the formulation of the hardening modulus. The constitutive equation of the plastic strain response is given below.

$$\begin{bmatrix} d\varepsilon_p^{\mathrm{p}} \\ d\varepsilon_q^{p} \end{bmatrix} = \frac{1}{h} \begin{bmatrix} (p' - p'_b)^2 & (p' - p'_b)\dfrac{q - q_b}{M^2} \\ (p' - p'_b)\dfrac{q - q_b}{M^2} & \left(\dfrac{q - q_b}{M^2}\right)^2 \end{bmatrix} \begin{bmatrix} dp' \\ dq \end{bmatrix} \tag{2.37}$$

Similarly to the bubble model, the hardening modulus h_0 is given by the following expression for the case when all the surfaces are in contact ($h = h0$):

$$h_0 = \frac{(p' - p'_b)}{(\lambda * - \kappa *)} \left[p'(p' - p'_b) + \frac{q(q - q_b)}{M^2} \right] \tag{2.38}$$

However, the hardening modulus function needed to be modified for the general case where plastic deformations occur without the surfaces being in contact. Therefore, it was a requirement for the function to include two more terms that associated the plastic response of the model with the position of the history and yield surfaces. These terms are denoted as H_1 and H_2 respectively in the generalised hardening modulus expression below.

$$h = h_0 + H_1 + H_2 \tag{2.39}$$

H_1 was made to depend of the relative distance of the history surface to the bounding surface and similarly H_2 was dependent on the relative distance of the yield surface to the history surface and are given by equations 2.40 and 2.41 respectively.

$$H_1 = \left[\frac{S^2 p_0^3}{(\lambda * - \kappa *)}\right] \left(\frac{b_1}{b_{1max}}\right)^{\psi} \tag{2.40}$$

$$H_2 = \left[\frac{p_0^3}{(\lambda * - \kappa *)}\right] \left(\frac{T b_2}{b_{2max}}\right)^{\psi} \tag{2.41}$$

where b_1 is the distance of the normal vector at the current stress point on the history surface and its image point on the bounding surface. Similarly, b_2 is the distance of the normal vector between the stress points situated on the yield surface and the reciprocal conjugate point on the history surface.

It should be noted that in the event the yield and history surfaces are in contact, and therefore $b_2 = 0$ it follows that $H_2 = 0$ and the model portrays the same behaviour as the Al-Tabbaa and Wood (1989) bubble model for the case that the kinematic surface moves within the bounding surface.

2.3 Elasticity models

In the 1970s, it was noted in several studies that back-calculated values of soil stiffness from observed ground movements around structures were higher than those measured by laboratory triaxial tests e.g. Cole and Burland (1972), St John (1975). Baldi *et al*. (1988) noted that significant errors occurred in standard triaxial tests due to uneven stress distribution in the sample as a result of incorrectly aligned loading rams and platens. As a result, strains of less than 0.1% (small strains) were not measured accurately using standard triaxial equipment. Figure 2.11 illustrates typical strain ranges for structures in comparison to standard laboratory tests. Although large strains will occur close to a structure in the ground, they will dissipate to zero at a distance from the structure (Atkinson 2000). It is therefore essential to take into account small strain behaviour in order to accurately predict ground movements, which can extend some distance from the structure.

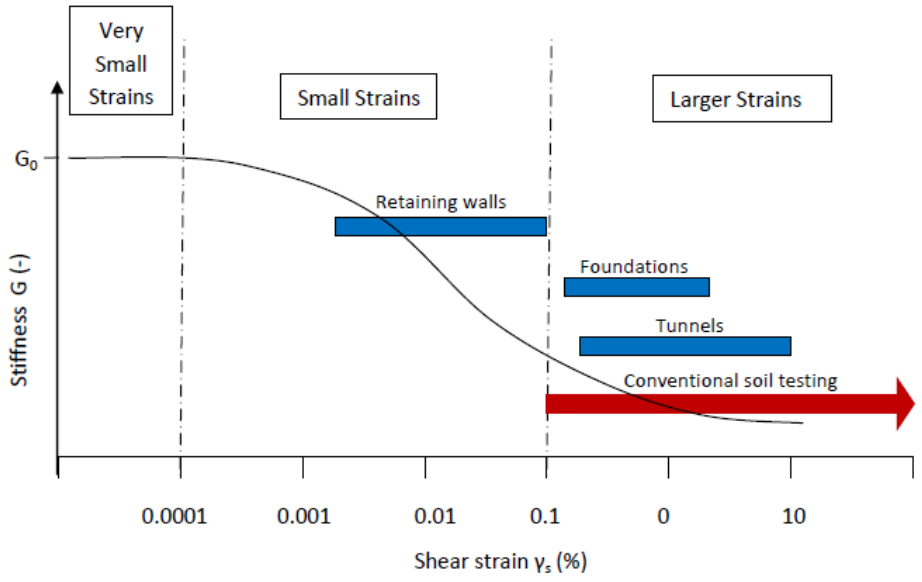

Figure 2.11: Stiffness-strain plot with typical strain ranges for structures in comparison to the range provided by standard laboratory tests (after Atkinson 2000).

In the 1980s, Clayton and Khatrush (1986) developed "Hall effect local strain gauges" which could be mounted directly onto a triaxial sample. These eliminated problems associated with uneven loading and allowed strains to be measured down to 10^{-3} %. More recently, displacement transducers have been developed which were capable of resolving stiffness at strains down to 10^{-4} %. Dynamic methods have also been developed to measure soil stiffness at small strain, which were easier to apply than the displacement transducers. The process involved passing shear waves through the samples which generate very small strains- usually less than 10^{-3} % (Dyvik and Madshus 1985).

2.3.1 Elasticity Principles

The principle of hypoelasticity is commonly used in elastic-plastic constitutive models to describe materials that exhibit nonlinear, but reversible, stress strain behaviour even at small strains. A common method used in constitutive modelling is the definition of a pressure dependent equation for the bulk modulus *K*. The shear modulus *G* is then described by means of a constant Poisson's ratio.

Hypoelastic formulations however have some deficiencies when modelling the cyclic behaviour of soils. The formulations could potentially lead to unconservative results since they imply production of energy during multiple cycles of loading as shown by Zytynski *et al.*, (1978), rather than dissipation. This is a clear violation of the First Law of Thermodynamics (Houlsby *et al.,* 2005).

The solution to this problem could be provided by the adoption of hyperelastic formulations. This principle is based on the fact that the response function is derived from a potential energy function, which is in line with the First Law of Thermodynamics. A number of models have been proposed to tackle the shortcomings of the hypoelastic models while ensuring thermodynamic acceptability. Examples include models by Vermeer, (1978); Boyce, (1980); Houlsby,(1985); *Borja et al.*,(1997), and many others.

During the implementation of the KHSM model by Dr. M. Rouainia, modifications to the original elastic formulation were included. Two new elasticity models were implemented; one adhering to the principle of hypoelasticity (see Section 2.3.2) and the other to the principle of hyperlasticity. (Section 2.3.3). A description of each elastic formulation is provided in the following sections.

2.3.2 Viggian and Atkinson elastic model

Several mathematical expressions have been proposed to model this small strain behaviour. Efforts have been directed towards empirical formulations in order to reproduce the variation of stiffness at very small strains, as it has been observed in laboratory test. The idealisation of the soil as an assembly of elastic spheres implies that the response upon loading is essentially frictional. If this hypothesis was to be taken into account, the proposition that the strength and stiffness had to be directly proportional to the mean effective stress, p' had to be made. Following this hypothesis, theoretical work which suggested that the soil stiffness varies with the mean effective stress, p', raised to the power of n which was equal to 1/3. More recently, Viggiani and Atkinson (1995) suggested that at very small strains the soil is expected to follow the theory of the elastic spheres while at large strains the purely frictional case is expected to apply. Based on the results of bender element tests on reconstituted samples of a number of clays, the authors proposed the following equation for the small strain shear modulus, which was depended on two variable terms, the mean effective stress, p', and the isotropic over-consolidation ratio R_o.

$$\frac{G_0}{p_r} = A_G \left(\frac{p'}{p_r}\right)^n R_0^m \tag{2.42}$$

where A_G, n, and m are dimensionless parameters that can be estimated using the plasticity index (see figure 3.4); p_r was a reference pressure which is usually taken equal to 1 KPa; and $R_0 = p_c / p'$ was the over-consolidation ratio OCR where p_c is the mean effective stress that defines the size of the reference surface and p' is the mean effective stress. For normally consolidated clays R_0 reduced to unity and the

equation reduced to the one proposed by Wroth and Houlsby (1985) for the shear modulus of sands.

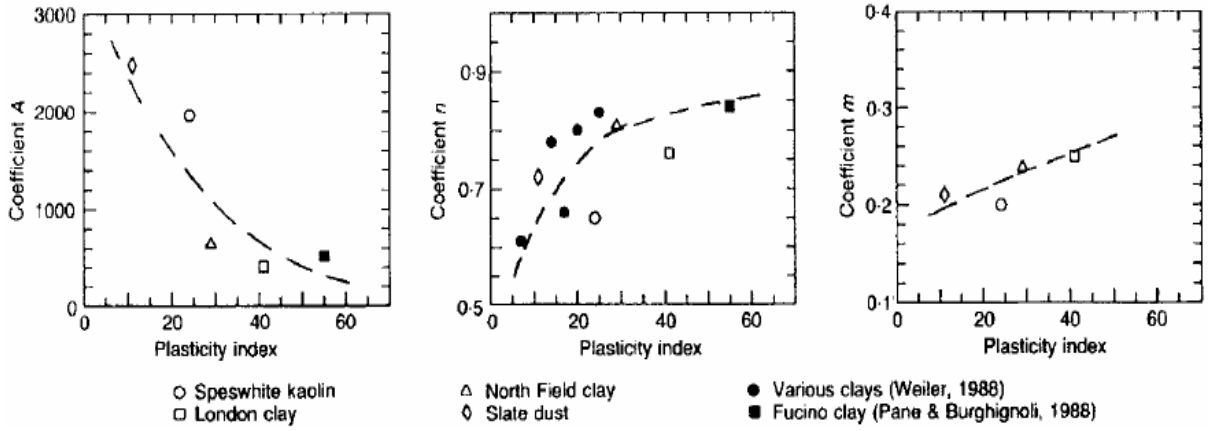

Figure 2.12: Variation of stiffness parameters *A*, *n* and *m* with plasticity index (after Viggiani and Atkinson (1995))

In this formulation, the bulk modulus (***K***) is treated independently of the shear modulus (***G***).Taking into account the relationship between bulk and shear moduli (see below) the possibility that Poisson's ratio could become negative under certain conditions exists. This issue did not occur during the simulations provided in this thesis.

$$G = \frac{3(1-2v)}{2(1+v)}K$$

2.3.3 *Hyperelastic formulation Houlsby et al. 2005*

The notion that the elastic behaviour of granular materials was non-linear has been well documented in literature. This behaviour stemmed from the fact that the small-strain tangent stiffness depended on the stress level. The elastic moduli typically vary as power functions of the mean stress. Houlsby *et al.* (2005), suggested that the simple models that were developed in order to simulate this nonlinearity resulted in behaviour that violated the laws of thermodynamics. They further went to state that it was possible to derive the elastic behaviour from a free energy potential, that lead to the assurance that any elasticity model would be thermodynamically acceptable. Their work was focused on deriving elasticity models that would obey the laws of thermodynamics.

As was shown in the previous sub-section a considerable amount of experimental research was carried out to investigate the mechanical behaviour of soils undergoing very small strains, which lead to semi-empirical formulations for the behaviour of soils in the very small strain region (Hardin and Black, 1969; Hardin, 1978). These models assumed that the stiffness was dependent on other variables, such as the voids ratio and/or the preconsolidation pressure.

Houlsby and his co-workers identified the drawback of these hypoelastic models which implied that for multiple loading cycles, soils could exhibit continuous production of energy. They advocated an alternative way to model the elastic behaviour at very small strains, by adopting the hyperelastic approach, which was based on the existence of an energy potential, from which the reversible response can be derived. This model predicted a conservative elastic response, which assured obedience to the first Law of thermodynamics, and therefore avoided the problems of cyclic loading described above. Their work culminated in the development of the expression for the stiffness matrix for general stress states provided below:

$$d_{ijkl} = p_a \left(\frac{p_0}{p_a}\right)^n \left[n_h K_h \frac{\sigma_{ij}\sigma_{kl}}{p_0^2} + K_h(1-n_h)\delta_{ij}\delta_{kl} + 2G_h(\delta_{ik}\delta_{jl} - \frac{1}{3}\delta_{kl}\delta_{ij}) \right] \quad (2.43)$$

In the above equation, p_0 was a function of stresses as defined in the next equation, p_a was the atmospheric pressure, taken as 100kPa, K_h and G_h were dimensionless bulk and shear stiffness factors respectively and n_h was a dimensionless pressure exponent.

$$p_0^2 = \frac{\sigma'_{mm}\sigma'_{nn}}{9} + \frac{K_h(1-n_h)s_{mm}s_{mn}}{2G_h} \quad (2.44)$$

2.4 Structure in natural soil deposits

In the last two decades significant progress has been made into gaining an in depth understanding of the differing quantitative and/or qualitative characteristics of natural and reconstituted clays. The significance of effects such as structure and structure anisotropy within natural material is a subject which has been discussed extensively with conclusive results.

In this thesis the term '*structure*' will be adopted to describe the combination of 'fabric', which represents the composition of the clay particles, and 'bonding', which describes the forces developed between particles. It should be noted these forces cannot be attributed purely to the frictional characteristics of the soil (Lambe & Whitman, 1969). Fabric encompasses phenomena such as in-homogeneity, fissures developed within the soil mass, dissemination of the soils into layers, as well as particle distribution (Coop et al., 1995). Bonding is the amalgamation of the forces working to keep the sol particles connected.

Burland (1990) conducted a detailed evaluation of the behaviour of numerous high quality samples of clay which had been retrieved with minimum disturbance. The results were then compared to the behaviour of reconstituted samples of the same material. Figure 2.13 plots the comparisons between the intact and reconstituted clay samples, re-enforcing the concept that the strength of the intact samples is higher than the intrinsic strength. The observation was made that natural clays displayed brittle behaviour once peak strength was reached, followed by a prompt reduction to a distinct, post rupture strength. As a result of these studies Burland postulated that most natural clays are not likely to reach the intrinsic critical state when subjected to triaxial shearing.

It was envisaged that among other aspects of soil behaviour, the above observations would indicate a sizeable difference in the preconsolidation pressures. This argument was further corroborated through the results of a series of oedometer tests which illustrated that the natural clay yielded at higher stresses than its remoulded counterpart. When graphs of stress against void ratio were

constructed, the divergent behaviour was still evident even at values of void ratios as low as 0.3.

A point noted is the hypothesis that the strengths of natural soils and their reconstituted counterparts may never converge when subject to laboratory testing. Further discussion as to the varying extent of destructuration will be provided later in this section.

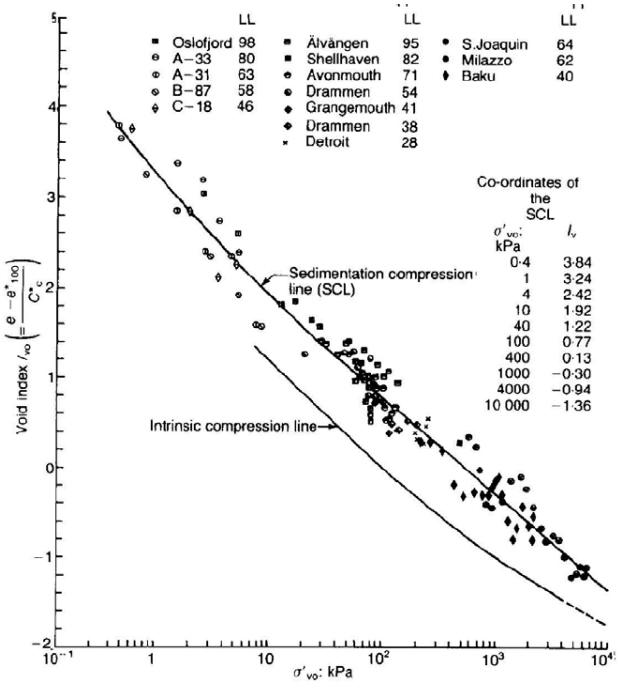

Figure 2.13: Comparison of naturally sedimented clays and one-dimensionally consolidated reconstituted clays

The results of the research work by Cotecchia and Chandler (1997) represent one of the first attempts in specifying the physical differences between structured and reconstituted materials. The authors conducted a series of experiments with the aim to investigate the microstructure of overconsolidated clay in its natural and reconstituted states. The findings indicated that the fabric in natural clay was distinguished as thickly packed and accumulated in several assemblies of parallel particles. These assemblies were observed to be positioned in horizontal layers, pointing towards a uniformly distributed fabric.

Comparatively, the micro examination of the reconstituted sample revealed a moderately open fabric. The authors went on to propose that significantly more intense shearing would be needed to degrade the structure of clay. This supposition presented a topic for further discussion, as it appeared to be debatable whether laboratory testing has the ability to reproduce the mechanisms of complete remoulding.

In addition to the researchers stated previously, the noteworthy role which structure plays within a soil was also highlighted by Leroueil and Vaughan (1990). Triaxial compression tests were carried out on three different clays, each using an intact (structured) sample and in addition what the authors described as de-structured (remoulded) specimens. The results echoed the findings of Burland, with the reconstituted samples reaching lower peak strength and exhibiting far lower stiffness than their structured counterparts. The findings presented by Burland which suggested that a structured soil is more prone to brittle behaviour than its reconstituted equivalent were also evident. The resultant stress-strain graphs indicated that the intact specimens' distinctive yield point occurred at a much smaller strain value, in comparison to the yield point of the remoulded samples.

Leroueil and Vaughan concluded that yielding within structured soils occurs as a gradual process and that structure is only eradicated once the yield strain has been surpassed. Another observation highlighted by the authors was that, whilst a stiff response is noted before yield, this may not always be elastic. This could become a problem within modelling (which will be examined in the following sections) as most simple soil models tend to assume a purely elastic response prior to yield.

2.4.1 Fabric

The work by Sides and Barden (1970) included a classification of primary types of fabric, as encountered in nature. A brief summary of these fabrics is presented in Figure 2.11. The authors distinguish between the following fabrics:

- Flocculated-recognised by the electrical force between the particles which causes them to pull together
- Dispersed- recognised by the close packed particles attributed to the negative force developing during deposition, which prevents particles from pulling together
- Turbostatic-distinguished by the edge to face contacts between paritcles. Furthermore, particles in this fabric are grouped in '*domains*' and '*stacks*' leading to a high degree of particle orientation.

It should be noted that the flocculated fabric is further divided to *'cardhouse'* or *'bookhouse'* fabrics. The former is distinguished by a single particle arrangement, whilst the latter comprises of particles arranged in groups, designated *'domains'*, (figure 2.14). The fabric rsulting from the depositional process is designated as *'primary fabric'*. It is recognised that this fabric may well undergo significant changes, due to activities carried out after the depositional process is completed.

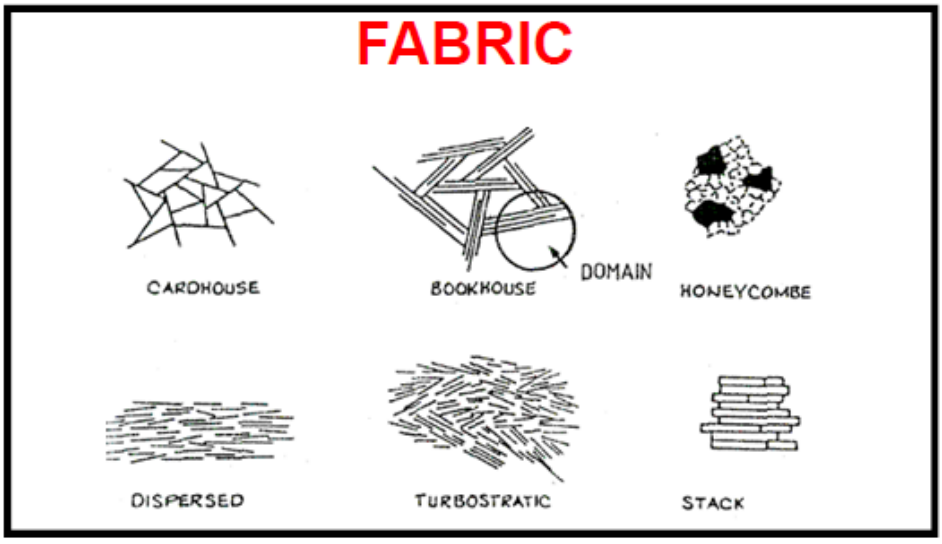

Figure 2.14: Classification of fabric in clays based on geometric arrangement of particles (adapted from Sides and Barden, 1970)

The circumstances under which the soil has been deposited have a substantial influence on the resultant fabric. The two most noteworthy depositional components are thought to be the depositional rate and the degree of water stillness. In particular, it is understood that slow depositional process in relatively still waters is likely to have an outcome of open fabric. Another characteristic identified during sediment deposition in still conditions is the lamination exhibited by soils implying that there was no blend of the particles during deposition. In contrast, during times where precipitous deposition occurs, in conjunction with high currents, it is likely the sediment will exhibit a much more compact, orientated fabric (Burland 1990).

2.4.2 Bonding

Bonding is comprises all the forces acting between particles, which cannot be attributed to the frictional nature of the soil, (figure 2.15). These forces comprise, but are not limited to the following:

- Van der Waal forces
- Electrostatic forces
- Electromagnetic forces

It is generally perceived that bonding comprises of all the elements required to hold the soil particles together.

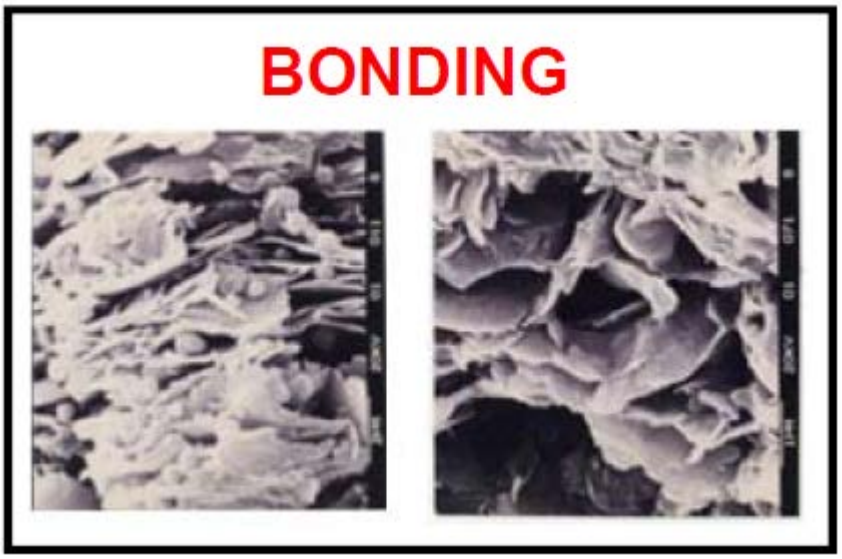

Figure 2.15: Inter-particle bonding in natural clays (adapted from Cottechia and Chandler, 1997)

The descriptions provided above for the composition of *'structure'* in natural soils, point to the fact, that the origin of *'structure'* is an amalgamation of physical and chemical processes occurring at particle level. This feature evolves during the geological life of the soil, resulting from a multitude of factors such as, chemical reactions between soil minerals, inter-particle forces, depositional water conditions, etc. As stated earlier, a soil's *'structure'* is subjected to modifications with time, attributed to external or internal factors. As a result, phenomena during the deposition process of the sediment, as well as developments occurring after deposition, influence the materialisation and the modification of this feature of the soil.

2.4.3 Anisotropy

Anisotropy in natural soils may be *inherent* due to the past stress history of the soil, i.e. developed by the nature of sedimentation, glacial transportation or in situ weathering processes, or *induced* as a result of deformation and loading through the geological history of the soil. Model extensions were developed to account for the effects of inherent anisotropy associated with the material fabric (Sekiguchi & Ohta, 1977). The subsequent evolution of the dimensionless deviatoric fabric tensor was termed rotational hardening as it describes the rotation, with respect to the isotropic axis, of the yield surface in stress space (Hashiguchi *et al.*, 2002; Wheeler *et al.*, 2003).

2.4.4 The process of destructuration

The above sections attempted to provide a comprehensive description of the *'structure'* found in natural soils. The definitions above are in line with the notion of *'intact state'* as described by Leroueil et al. (1984). The authors ascertained that this *'intact state'* is encountered in natural soils. According to Leroueil et al. the phenomenon of *'structure'* encapsulates the general idea of the specific state in which clay soils can be found in nature or even manufactured in the lab.

The authors went further to classify the following categories of structure states:

- intact state of structure

The description of this state is provided above; It refers to the conditions clay soils can be found in nature

- De-structured state

The de-structured state is the resultant condition, which a sample of intact clay arrives at, after being exposed to sufficient loading to instigate large deformations. These deformations lead to the degradation of its initial structure to a lesser magnitude.

- Remoulded state

The remoulded state ensues from the de-structured stage. It is obtained when sufficient loading is transferred to the clay sample which causes the complete destruction of the initial structure, leading to a minimum strength.

- Re-sedimented/reconstituted state.

The re-sedimented or reconstituted state is typically found in laboratory prepared sample. The procedure involves the sedimentation of clay particles of remoulded state through thoroughly mixed slurry. The slurry is consequently consolidated under the weight of an increasing thickness of clay, until the target stress state is reached (Leroueil et al., 1984).

2.5 *S3-SKH model (Baudet and Stallebrass)*

Baudet & Stallebrass (2004) used the 3-SKH model as the basis to further develop a model for structured soil. They proposed a modification of the existing model for reconstituted and reconsolidated soils in order to capture the destructuration process, through the Sensitivity Framework (Cotecchia & Chandler, 2000). The framework was originally established using laboratory prepared, isotropically and consequently the S3-SKH model was not able to predict the structure anisotropy.

The sensitivity, three surface, kinematic hardening, model (S3-SKH) used a fixed relationship between change in sensitivity and plastic stains to model the gradual loss of structure with continuous loading. In this model the degree of structure was entirely interpreted as and related to the sensitivity of a soil specimen. It was assumed that the degree of structure in natural soil deposits that arises from fabric, rather than inter-particle bonding provided a stable component of structure that that did not degrade with strain during loading. Therefore, fabric referred to the stable elements of structure, as originally suggested by Coop et al. (1995). The bounding surface in this model was designated as *sensitivity surface* and its size was controlled by the product of a sensitivity parameter, s and p'_0 (figure 2.16). However, as this eventual value of the sensitivity parameter did not necessarily converge to unity at large strains, the model was able to simulate stable elements of structure such as in Sibari clay (Coop & Cotecchia, 1995). Similar to the preceding 3-SKH model, the sizes of the history and yield surfaces were controlled by the fixed ratios T and S respectively.

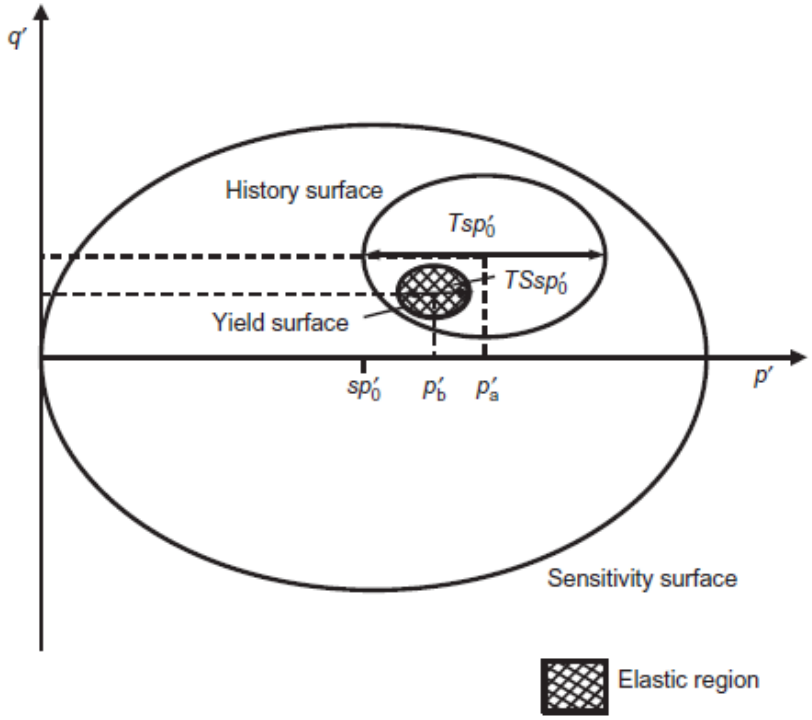

Figure 2.16: Schematic diagram of the sensitivity three surface kinematic hardening model S3-SKH (Baudet and Stallebrass, 2004)

Other constitutive models, contemporary to the S3-SKH, that were developed specifically to model structured soils, simulated the effects of structure in part by an increased size of the bounding surface, which then decreased to that of the reconstituted soil after continuous loading. In those models, the structure-related parameters were depended on a measure strain which resulted in degradation of the natural structure. The models were formulated so that this strain was a dependent on the two components of plastic strain (volumetric and shear). Furthermore those models used different proportions of volumetric and shear strains in the destructuration law, based on parametric studies. In the absence of adequate laboratory test data to investigate the relative importance of volumetric and shear strains in detail, Baudet and Stallebrass assumed that they were of equal importance. The following damage strain expression was proposed, which was equal to the magnitude of the vector of plastic strain increment:

$$\dot{\varepsilon}^d = \sqrt{\dot{\varepsilon}_v^{p\,2} + \dot{\varepsilon}_q^{p\,2}} \tag{2.45}$$

Where $\dot{\varepsilon}_v^{p\,2}$ and $\dot{\varepsilon}_q^{p\,2}$ are the increments of plastic volumetric and shear strain respectively, for a given increment of stress.

The model was used to simulate drained probing tests and undrained triaxial tests on natural specimens of Bothkennar clay. The sensitivity framework was used as the basis for choosing initial and ultimate values of the sensitivity parameter. Both sensitivity and destructuration parameters were derived from standard isotropic compression tests.

2.6 *MSS model Kavvadas and Amorosi (2000)*

As mentioned earlier, models that extended the critical state theory provided the basis for the development of constitutive laws, which attempted to include components that were supported by the knowledge of the behaviour of structured soils at the time. Kavvadas and Amorosi (2000) suggested a two-surface constitutive model for structured soils that combined features, among others, such as stiffness non-linearity in the 'elastic' domain, description of the natural, structured, state of the soil and the consequent damage to it due to loading. The model included two characteristic surfaces (figure 2.17). The plastic yield envelope (PYE) acted in the same manner as the classical yield surface controlling the transition from the elastic to the plastic state. This surface was assigned the designation 'plastic' in order to distinguish between plastic yielding (which may occur at small strains) and the large-scale yielding process which lead to the degradation of the measure of structure in the soil (Jardine *et al*, 1991). The outer bounding surface was termed bond strength envelope (BSE) and represented the material states associated with natural, structured state of the soil. Plastic strains were allowed to develop inside the bounding surface and therefore activate the mechanism that lead to the gradual loss of structure based on the proposed destructuration law.

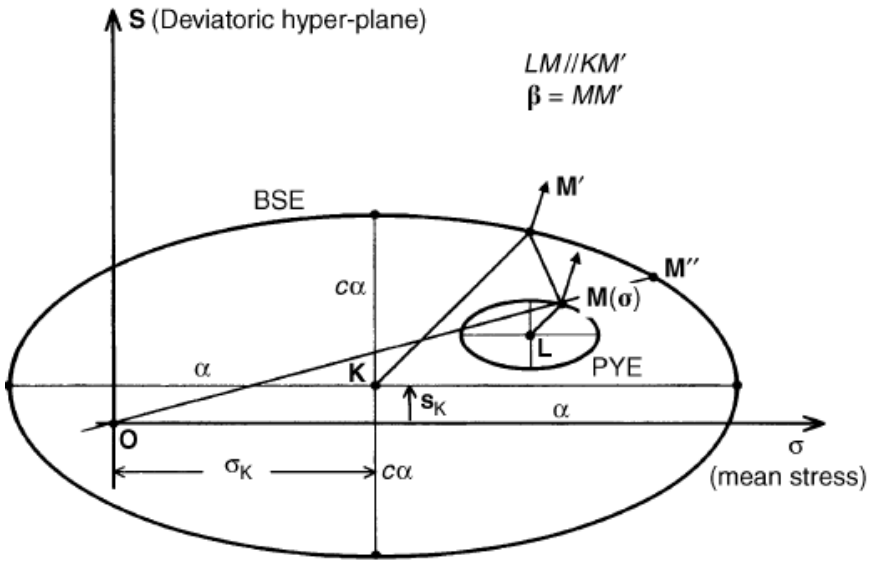

Figure 2.17: Schematic diagram of the model for structured soils MSS (Kavvadas and Amorosi, 2000)

As it is evident in the figure above, the bonding strength envelope was centred off the mean stress axis and therefore the effects of anisotropy could be modelled. This component of the MSS model is fairly important, since anisotropic behaviour is a characteristic of natural soils.

Similarly to the model formulated by Mroz (1967), the ellipsoidal bounding surface allows for some degree of tensile strength, with the surface permitted to exist in negative mean stress space. The mathematical expression for it is provided in the equation below:

$$F = \frac{1}{c^2}(\boldsymbol{s} - \boldsymbol{s_K}) : (\boldsymbol{s} - \boldsymbol{s_K}) + (\sigma - \sigma_K)^2 - a^2 = 0 \qquad (2.46)$$

The ellipsoid was centred at point *K* with coordinates $\boldsymbol{\sigma}_K = \boldsymbol{S}_K + \sigma_K \boldsymbol{I}$ where $\boldsymbol{I}$ was the isotropic unit tensor. α was the half axis of the ellipse in the isotropic axis, whereas the magnitude of the semi-axis in each of the deviatoric axes was factored by parameter *c*.

For numerical simplicity the plastic yield envelope retained the same geometric shape as the bounding surface, but was scaled down by factor ξ. The mathematical expression that described it is given in equation 2.44.

$$f = \frac{1}{c^2}(\boldsymbol{s} - \boldsymbol{s_L}) : (\boldsymbol{s} - \boldsymbol{s_L}) + (\sigma - \sigma_L)^2 - (\xi a)^2 = 0 \tag{2.47}$$

In the MSS model, salient feature is the inclusion of the destructuration law within the isotropic hardening function (eq.2.37). This feature enabled the model to correlate the evolution in size of the bond strength envelope, to the loss of structure brought on by both volumetric and deviatoric accumulated strains. The rate of both volumetric and deviatoric structure degradation was based on an exponential damage type form that was similar to previous propositions by Kavvadas (1995), Lagoia and Nova, (1995) and others.

$$\dot{a} = a\left[\left\{\left(\frac{1+e}{\lambda-\kappa}\right) - \zeta_v exp\left(-\eta_v, \varepsilon_v^p\right)\right\}\dot{\varepsilon}_v^p + \{\theta_q - \zeta_q \exp(-\eta_q, \varepsilon_q^p)\}\dot{\varepsilon}_q^p\right] \tag{2.48}$$

Where parameters (ζ_v, η_v) and (ζ_q, η_q) defined the rate of volumetric and deviatoric structure degradation respectively.

The proposed kinematic hardening law controlled the evolution of the material anisotropy during plastic deformations and was of similar nature to the conventional bubble model (Al-Tabbaa and Wood, 1989). The hardening law, which was again a combination of the isotropic and kinematic components, provided the following expression for the plastic modulus in the general condition when the PYE and BSE surfaces are not in contact.

$$H = H'' + |H''|\{[1 - (\delta/\delta_0)]^{-\gamma} - 1\} \tag{2.49}$$

Where *H*'' refers to the plastic modulus at point *M*'' (figure 2.14), at a point where vector *OM* crosses the BSE; δ refers to the normalized distance of *MM*'' (*M* is the current stress state); δ_0 is the value of δ at the onset of yielding. Thus $\delta/\delta_0 = 1$ referred to initiation of yielding (*i.e.* $H = \infty$) and indicated that the material was located on the bonding strength envelope. The material constant γ (>0) was responsible for the determination of the rate of degradation in plastic modulus *H* between values of ∞ and H''. The formulation of the plastic modulus was such, that in the special case where the surfaces were in contact, *H* = H''.

The difference between the formulation of the MSS hardening function and expression of the hardening law from other models, is that in this model the *H''* is associated with point *M''* which is the intersection of vector OM with the BSE, rather than stress point M', which is the mirror point on the bounding surface that has the same outward normal. The second term of equation 2.48 is related to the first term while in other hardening rule formulations these two terms are independent of each other. Furthermore, δ_0 was associated with the stress state upon onset of yielding and therefore it was dependent on the position of the yield surface at the onset of yielding.. δ_0 took a constant value, up to the point where it was reset when the plastic yield envelope was re-engaged under cyclic loading conditions. This feature departed from previous constitutive laws, such as δ_0 in the model by Mróz's *et al* (1979) or b_{max} in the model by Al Tabbaa & Wood (1989) where those parameters denoted the maximum value corresponding to the current yield surface. The model was calibrated against laboratory tests on the stiff overconsolidated Vallericca clay (isotropic and anisotropic consolidation tests, anisotropically consolidated triaxial shearing at both low and high pressures.). Very small yield surfaces were used.

2.7 Concluding remarks

The development of the Cam clay models marked significant progress in the field of elasto-plastic constitutive models. In recent years a number of researchers proposed more advanced constitutive models that aimed to capture more features of the soil behaviour such the gradual yielding of soils, the smooth transition from elastic to the elasto-plastic phase, gradual accumulation of irrecoverable plastic strains under cyclic loading etc. One recognised framework published in literature is the kinematic hardening concept, which entails the introduction a small kinematically hardening yield surface inside the Cam-clay surface. Recent development of two or three-surface models has been focused in simulating laboratory behaviours of structured soils.

The rate-independent constitutive model (KHSM) for natural clays proposed by Rouainia and Muir Wood (2000) was selected for this work. It is formulated within the framework of kinematic hardening with elements of bounding surface plasticity and was formulated so that it included effects of damage to structure caused by irrecoverable plastic strains due to sampling, laboratory testing, or geotechnical loading. The incentive to adopt these models came from the flexibility in modelling different soil behaviours. Firstly, the model has an anisotropic general formulation, with the yield and plastic potential surfaces not necessarily circular in the deviatoric plane, secondly the model has the ability to model initial anisotropy of the structure surface and lastly contributions to destructuration of structured soil from plastic volumetric strain and distortional strain are not necessarily equal.

Chapter 3: Description of the kinematic hardening model for structured soils (KHSM) and validation

This chapter describes the Kinematic Hardening Rouainia Muir Wood model (KHSM), which was formulated to take into account the temporary existence of structure and its progressive degradation with plastic strains. Some small changes have been included in this version of the model that differentiates it from the original formulation (Rouainia & Muir Wood, 2000). The changes were made in order to improve the model's response in the small strain region. A description of the original model is provided section in 3.1, with a discussion on the motivation for the modifications given in section 3.2. The last section provides the validation of the model against published experimental data through simulation of drained and undrained triaxial tests on Vallericca clay, and a parametric study showing some typical responses of the model.

3.1 Introduction

As covered in the previous chapter, the development of constitutive soil models based on the Critical State theory, marked significant progress in the field of soil modelling. The classical theory of elasto-plasticity however, did not allow for any plastic deformations to take place inside the conventional yield surface. Various techniques have been employed, in order to implement the observed soil response, such as hysteretic behaviour, the existence of natural structure, etc., into numerical models. An example of a strategy that was conceived is the development of the kinematic hardening family of models, firstly proposed by Al-Tabbaa & Muir Wood (1989).

Natural soils exhibited stiffness and strength characteristics that were not accounted for by the classical theory of soil mechanics and resulted from processes such as, cementation, ageing and even overconsolidation (Leroueil & Vaughan, 1990; Burland, 1990; Gens & Nova, 1993; Muir Wood, 1995; Burland et al., 1996). Experimental evidence of the effects of structure were reported in a wide variety of natural soils and weak rocks, including soft clays (Tavenas & Leroueil, 1990; Smith et al., 1992), stiff clays and clay shales (Calabresi & Scarpelli, 1985; Burland et al., 1996; Cotecchia, 1996).

The importance of improving constitutive models to describe the behaviour of natural, structured soils has been the focus of many researchers (Gens and Nova 1993; Liu and Carter 2002, Kavvadas and Amorosi 2000; Baudet and Stallebrass 2004, among others).

3.2 Original formulation of the KHSM model

Rouainia and Muir Wood (2000) proposed additional characteristics to an existing model which was already capable of describing the behaviour of the remoulded material, such as the modified Cam clay model. It further extended the bubble model for reconstituted soil. The following description of the KHSM model is taken from the 2000 Géotechnique paper which forms the basis of this work.

The bubble model (Al Tabbaa & Wood, 1989) was an advancement of the modified Cam-clay model and was developed in line with the kinematic hardening principles analogous to the two-surface model formulated by Mróz et al. (1979), as discussed in Chapter 2. This was achieved by introducing an extra yield surface or bubble, which moved around with the current stress according to a kinematic hardening rule. This model was developed in order to take into account small strain stiffness, stiffness degradation with strain history, and hysteretic response in cyclic loading. The framework for the development of the KHSM model took its inspiration from the early work of Al-Tabbaa & Muir Wood (1989) using the bounding surface plasticity concepts (Dafalias, 1986). It was further extended in order to represent phenomena associated with initial structure, and its progressive loss.

The model was conceived on a kinematic hardening bubble confined within an outer bounding surface. It was assumed that the elastic strain region is quite small for natural clay and can thus be described by a small bubble. The current stress state was always constrained to remain within or on the bubble. Any stress path tending to move beyond the boundary of the bubble caused translational motion of until it eventually was in contact with the structure surface. This was formulated in such a way that the two surfaces never intersected

Three surfaces, namely the reference surface, the bubble surface and the structure surface (see Figure 3.1), were used in this model. They were assumed to have the same elliptical shape as in Modified Cam-Clay model (Roscoe and Burland, 1968). During plastic loading, a destructuration process develops when the structural surface approaches the reference surface until finally these two surfaces coincide

with each other. At this point the soil was assumed to entirely lose its initial structure and was referred to as *fully remoulded*. The model was presented in a form that accounted for the initial anisotropy in soils by presenting a structure surface not passing through the origin and centred off the mean stress axis. It should be noted that the KHSM model was formulated in general stress space, and a dependence on Lode angle was introduced into the yield function. The model could be used for both structured and non-structured soils representing a hierarchical extension of the modified Cam-clay model. The model also hypothesised that the possibility of fabric structure does not exist for remoulded soils.

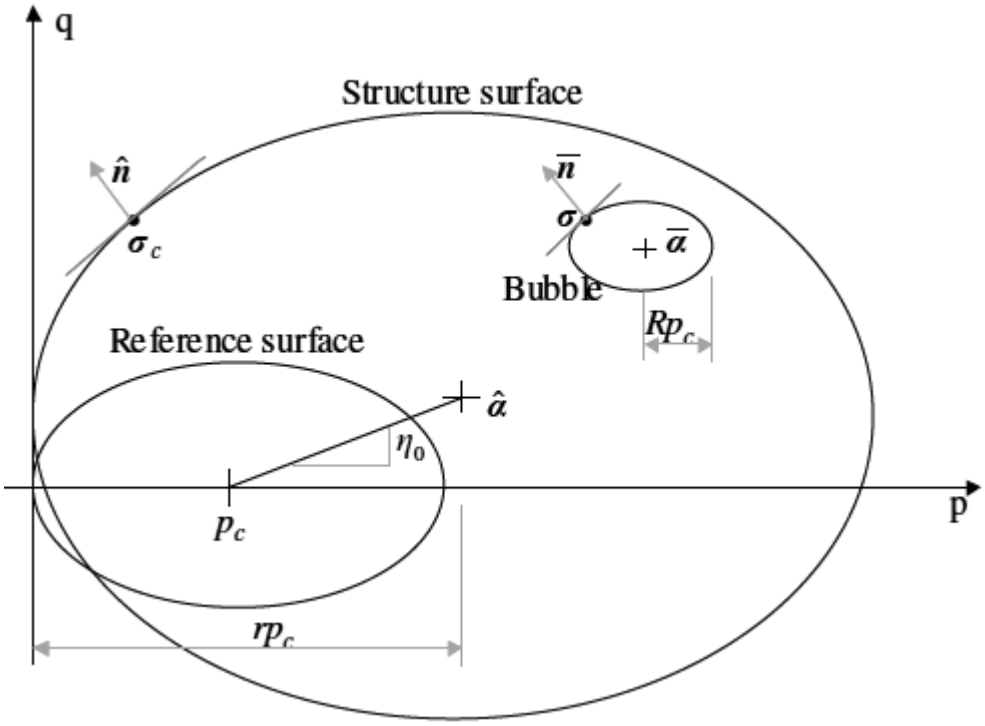

Figure 3.1: The kinematic hardening Rouainia & Muir Wood model (KHSM)

The equations governing the model were expressed in general stress space. All tensor quantities are denoted by bold-faced characters. The model focused on the small strain regime and therefore, the basic elasto-plastic assumption of the strain rate $\dot{\boldsymbol{\varepsilon}}$ comprised of two parts, elastic $\dot{\boldsymbol{\varepsilon}}^{e}$ and plastic, $\dot{\boldsymbol{\varepsilon}}^{p}$, where the superimposed dot denoted time differentiation:

$$\dot{\varepsilon} := \dot{\boldsymbol{\varepsilon}}^{\boldsymbol{e}} + \dot{\boldsymbol{\varepsilon}}^{\boldsymbol{p}} \tag{3.1}$$

3.2.1 Elastic behaviour

The original formulation assumed that when the stress state was situated inside the elastic domain, the response associated of the model was isotropic, with the elastic part portrayed by the bulk and shear moduli, K and G. The elastic properties exhibited a dependency on the pressure *p'* according to the following equations:

$$K = \frac{p'}{\kappa^*} \qquad G = \frac{3\,(1-2v)}{2\,(1+v)}K \tag{3.2}$$

where κ^* was the slope of the swelling line in the ln*v*-ln *p'* space, in contrary to the specific volume-logarithmic mean stress compression plane as described by Butterfield, (1979) and subsequently Hashiguchi. (1985) A constant *value* of Poisson's ratio (*v)*, was also considered.

The incremental relationship during elastic loading was therefore described by the following equation.

$$\dot{\sigma} = D^{\varepsilon} : \dot{\boldsymbol{\varepsilon}}^{\boldsymbol{e}} \tag{3.3}$$

In the D^{ε} denotes the matrix form of the tensor of elastic moduli, expressed as general a function of K and G.

3.2.2 Equations of the surfaces

The KHSM model was formulated in terms of three surfaces of the same elliptical half-section in the *(p', q)* plane shape. The reference surface was considered to be representative of the intrinsic behaviour of the reconstituted soil, in similar fashion to the Cam Clay model.

The mathematical expression to describe it was given by the following equation:

$$f \coloneqq \frac{3}{2M_\theta^2}(\boldsymbol{s}):(\boldsymbol{s}) + (p - p_c)^2 - p_c^2 = 0 \tag{3.4}$$

The hardening scalar variable p_c controlled the size of the reference surface. In the equations, p and $\boldsymbol{s}$ denoted the mean pressure and the deviatoric stress, respectively, given by:

$$p \coloneqq \frac{1}{3}tr[\boldsymbol{\sigma}] \qquad \boldsymbol{s} \coloneqq \boldsymbol{\sigma} - p\boldsymbol{I} \tag{3.5}$$

In equation 3.5 $\boldsymbol{I}$ presents the second-rank identity tensor and tr[·] presents the trace operator of [·]. The slope of the critical state line, M_θ, was expressed as a function of the Lode angle θ, and determined the shape of the failure surface in the deviatoric plane. Accordingly, the functional form adopted for M_θ could be written as:

$$M_\theta = M_{TXC}\left[\frac{2\alpha^4}{1 + \alpha^4 - (1 - \alpha^4)\sin 3\theta}\right]^{\frac{1}{4}} \tag{3.6}$$

By setting the parameter a = (3 -sin φ)/(3 + sin φ) the failure surface coincides with the Mohr-Coulomb hexagon at all vertices in the deviatoric plane (where φ is the friction angle of the soil at critical state), while setting α = 1 recovered the Von

Mises circle (as originally assumed in the Modifield Cam Clay). It should be noted that this surface is differentiable for all stress states and is convex provided, α=0.6. A detailed description of the critical state line in the deviatoric plane using the equations above is presented in Sheng & Sloan (2001).

The bubble, which bounded the elastic region, transferred around within the external surface in line with a kinematic hardening rule. The mathematical equation describing the bubble is as follows:

$$f_b := \frac{3}{2M_\theta^2}(\boldsymbol{s} - \boldsymbol{s_{\bar{a}}}) : (\boldsymbol{s} - \boldsymbol{s_{\bar{a}}}) + (p' - p'_{\bar{a}})^2 - (Rp'_c)^2 = 0 \qquad (3.7)$$

In this equation, $\{p'_{\bar{a}}, \boldsymbol{s_{\bar{a}}}\}^{\mathrm{T}} = \bar{a}$ denoted the location of the centre of the bubble in the stress space, the motion of which is controlled by its kinematic hardening rule. The constant parameter *R* expressed the ratio of the sizes of the elastic bubble and the reference yield surface.

The structure surface, which assumes the role of the bounding surface, governs the development of destructuration, through its interface with the bubble. It is the feature of destructuration which enables the model to capture the characteristics of substantial strain-softening. The mathematical equation of the structure surface was given by:

$$F := \frac{3}{2M_\theta^2}[\boldsymbol{s} - (r-1)\boldsymbol{\eta}_0 p_c] : [\boldsymbol{s} - (r-1)\boldsymbol{\eta}_0 p_c] + (p - rp_c)^2 - (rp_c)^2 = 0 \qquad (3.8)$$

The size of the structure surface was controlled by *r* which was defined as the ratio of the sizes of the structure surface and the reference surface. It may be deduced from equation (3.8) that both the size and the location of the structure surface are affected by the process of destructuration through the variable parameter *r*.

Similar to equation (3.7), the centre of the structure surface was denoted by $\{rp_c\boldsymbol{I}, (r-1)\boldsymbol{\eta}_0 p_c\}^{\mathrm{T}} = \hat{a}$. The centre of the structure surface could be situated off the mean effective stress axis, allowing the KHSM to accommodate the inherent anisotropy, which is a common feature of natural structured clays. The anisotropic features of the model, were captured by the location of the structure surface, governed by parameter $\boldsymbol{\eta}_0$ which was a defined as dimensionless deviatoric tensor, described by the deviatoric component of the centre of the structure surface, $((r-1)\boldsymbol{\eta}_0 p_c)$. It was assumed that the anisotropy parameters degraded to zero and the initial measure of structure reduced eventually to unity upon sufficient plastic deformations. The model assumed the following expression for the anisotropy tensor:

$$\boldsymbol{\eta}_0 = \begin{bmatrix} -\eta_0/3 & 0 & 0 \\ 0 & 2\eta_0/3 & 0 \\ 0 & 0 & -\eta_0/3 \end{bmatrix} \tag{3.9}$$

This type of anisotropy-where two of the principal components are equal- is known as transverse, or cross-anisotropy.

3.2.3 Destructuration process

The degree of structure, *r,* described the relative sizes of the structure and reference surfaces. It was modelled as a diminishing function of the plastic strain, therefore allowing the model to represent the gradual degradation of the material. Accordingly, the following exponential destructuration law was proposed:

$$r = 1 + (r_0 - 1)exp\left[\frac{k\varepsilon_d}{(\lambda^* - \kappa^*)}\right] \tag{3.10}$$

Here, r_0 was set as the initial measure of structure, k was a parameter that expressed the rate of damage to structure with plastic strains, and finally λ* and κ* were the slope of the normal compression line and the slope of the swelling line, respectively (see chapter 2). The incremental form of the above equation is given below:

$$\dot{r} = -\frac{k}{(\lambda^* - \kappa^*)}(r-1)\dot{\varepsilon_d} \tag{3.11}$$

As destructuration is observed in both compression and shearing, and therefore the rate of the damage strain ε_d was assumed to comprise of two components. Both plastic volumetric and deviatoric strains occurring in the clay were taken into account in the expression for the destructuration strain rate $\dot{\varepsilon_d}$ expression. Allowances were made in order to take into account different proportions of volumetric and shear strains in the destructuration law which was assumed to be given by the following expression:

$$\dot{\varepsilon_d} = \left[(1-A)\dot{\varepsilon_v^p}^2 + A\dot{\varepsilon_q^p}^2\right]^{\frac{1}{2}} \tag{3.12}$$

In equation 3.12, A was a non-dimensional scaling parameter, $\dot{\varepsilon_q^p}$ is the equivalent plastic shear strain rate given by:

$$\dot{\varepsilon_q^p} = \left[\frac{2}{3}(\dot{\boldsymbol{\varepsilon}}^p : \dot{\boldsymbol{\varepsilon}}^p)\right]^{\frac{1}{2}} \tag{3.13}$$

and $\dot{\varepsilon_v^p}$ is the plastic volumetric strain rate given by:

$$\dot{\varepsilon}_v^p = \frac{1}{3} tr(\dot{\boldsymbol{\varepsilon}}^p) \tag{3.14}$$

It can also be seen that by setting A=1 the destructuration would be caused entirely by the distortional component of the damage strain, while for A=0 the destructuration was entirely due to the volumetric component. Furthermore, in the absence of adequate laboratory test data to investigate their relative contribution to the destructuration process in detail, a value of A=0.5 could be assumed so that they are of equal importance (Baudet & Stallebrass , 2004).

3.2.4 Hardening functions

In similar fashion to the Cam Clay type models, the assumption that the direction of the plastic strain increment is normal to the bubble yield surface at the current stress state (figure 3.2) was made. Following the same reasoning as used by Al-Tabbaa & Muir Wood (1989), the hardening functions were generated in an identical manner, with the addition of elements that captured the effects of changing structure. Some assumptions made in the early critical state constitutive models were carried through in this model as well.

- Firstly, the fundamental assumption of isotropic hardening was still made, implying that there is a variation in size of all three surfaces starting at the onset of plastic volumetric strain generation.

- Secondly, a simple geometric kinematic hardening rule was adopted to describe this transition of the bubble in stress space provided that a stress increment required movement of the bubble relative to the structure surface.

- Thirdly, a hardening modulus expression was described in order to provide the model with Cam-clay type of behaviour for the special case when the bubble yield surface interacted with the structure surface at the current stress state. It should be noted that the predicted behaviour was only identical to Cam clay when the parameter controlling the size of structure

surface, (r) was set to 1, and the reference and structure surfaces coincided as in the model of Al-Tabbaa & Muir Wood (1989)).

- Finally, the stiffness was made to depend on some geometric measure of the distance between the bubble and the structure surface. In the event plastic strains occurred when the bubble was not in contact with the structure surface at the current stress state, the plastic stiffness was made to be higher and was formulated in a way, so that its magnitude degraded progressively as the two surfaces approached during monotonic loading conditions.

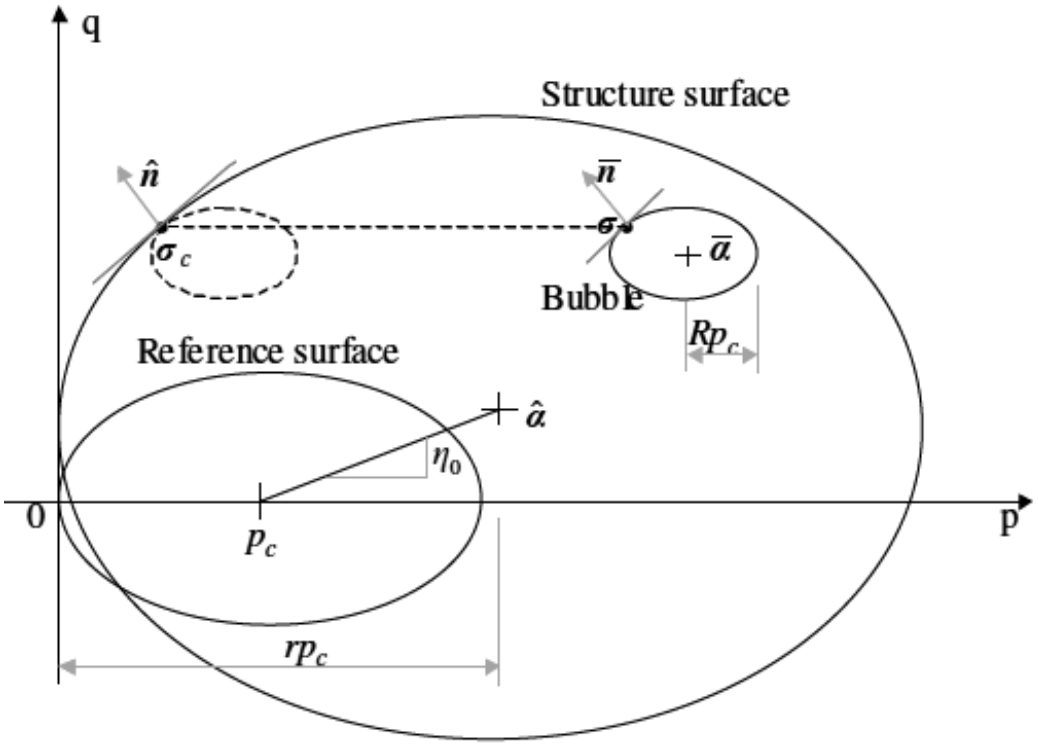

Figure 3.2: Schematic diagram showing the conjugate stress point, the centres and the outward normals of the bubble and structure surfaces.

The isotropic hardening assumption meant that a volumetric hardening law was adopted, meaning that any variation in size of the reference surface, p_c, was governed only by plastic volumetric strain rate, $\dot{\varepsilon}_v^p$ and was given by the following equation:

$$\frac{\dot{p}_c}{p} = \frac{\dot{\varepsilon}_v^p}{(\lambda^* - \kappa^*)} \tag{3.15}$$

An associated flow rule was assumed for the KHSM mode, which implied that the plastic potential was expressed by the same equation as the yield surface of the bubble (see equation 3.7). Therefore, the moment the bubble surface was engaged, (f_b=0), marked the onset of plastic deformation, with the evolution of the plastic strains given by:

$$\dot{\boldsymbol{\varepsilon}}^p = \dot{\gamma}\, \overline{\boldsymbol{n}} \tag{3.16}$$

The plastic multiplier $\dot{\gamma}$ and the yield surface expression f_b had to satisfy the discrete Kuhn-Tucker conditions $\dot{\gamma} \geq 0$, $\dot{\gamma}\ f_b = 0$ and f b ≤ 0, and $\overline{\boldsymbol{n}}$ denoted the normalized stress gradient on the bubble at the current stress state. From simple mathematical manipulation of equation 3.1.6 it can be deduced that for the stress point on the yield surface:

$$\dot{\gamma} = \frac{1}{H}(\overline{\boldsymbol{n}} : \dot{\boldsymbol{\sigma}}) \tag{3.17}$$

and

$$\dot{\gamma} = \frac{1}{H_c}(\overline{\boldsymbol{n}} : \dot{\boldsymbol{\sigma}}_c) \tag{3.18}$$

for the conjugate stress point on the structure surface (see figure 3.2).

The stresses associated with the centres of the bubble and the structure surfaces respectively were described as follows:

$$\bar{\boldsymbol{\sigma}} = \boldsymbol{\sigma} - \bar{a} \tag{3.19}$$

and

$$\hat{\boldsymbol{\sigma}} = \boldsymbol{\sigma} - \hat{a} \tag{3.20}$$

Following common practice when formulating kinematic hardening models, the scalar plastic moduli H and H_c were associated with stress points $\dot{\boldsymbol{\sigma}}$ and $\dot{\boldsymbol{\sigma}}_c$, respectively. The stress tensor on the conjugate point was defined as the stress point on the structure surface which has the same outward normal as the current stress point on the elastic bubble.

The KHSM model utilised elements of bounding surface plasticity theory (Dafalias, 1986) in the formulation of the hardening modulus for the general state where the bubble and structure surface are not in contact. The formulation related the magnitude of H to the hardening modulus at the conjugate stress point, H_c, through a function which had as a feature the degree of approach of the bubble to the structure surface. Bearing in mind the definition of the conjugate stress point, the following relationship was obtained:

$$\frac{\hat{\boldsymbol{\sigma}}_c - \hat{a}}{r} = \frac{\boldsymbol{\sigma} - \bar{a}}{R} \tag{3.21}$$

The formulation of the translation rule of the bubble, followed from the works of Mroz, 1967; Hashiguchi, 1988 among others, and warranted a smooth transition between the bubble and the structure surface, in order to avoid the intersection of the two surfaces. To obtain this, the expression for centre of the bubble was defined so that it translated relative to the centre of the structure surface in a direction parallel to the line that joined the current stress and the conjugate point (line associate with *b* in figure 3.3).

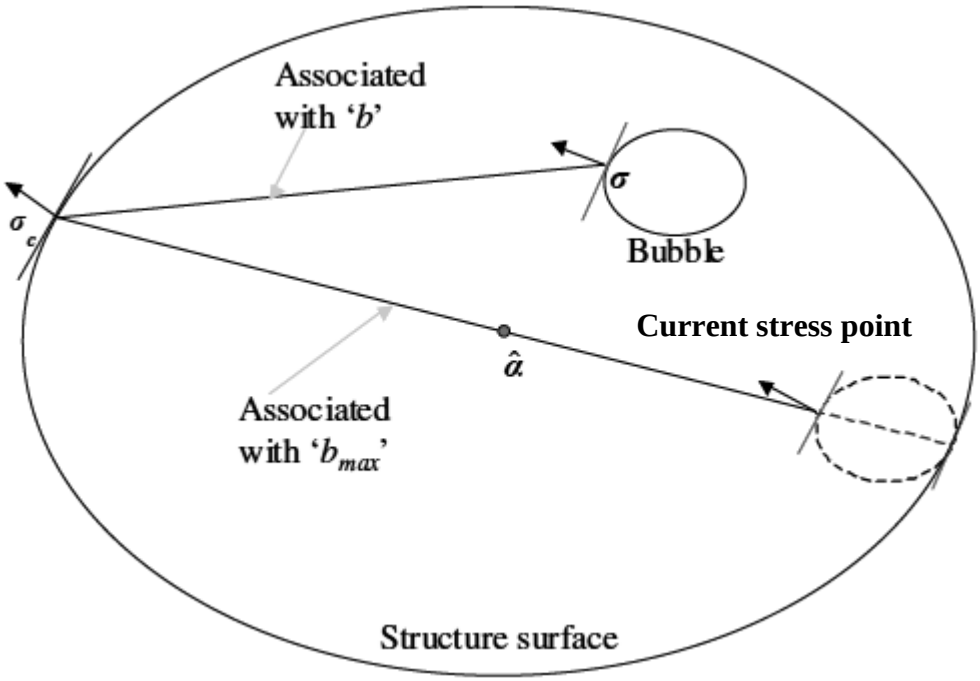

Figure 3.3: Schematic diagram showing the translation rule of the kinematic yield surface along the line connecting the current and conjugate stress points.

The consistency equation of the bubble yield surface f_b (equation 3.7) gave:

$$\overline{\boldsymbol{n}} : \left[\dot{\overline{\boldsymbol{\sigma}}} - \frac{\dot{p_c}}{p_c}\overline{\boldsymbol{\sigma}}\right] = 0 \tag{3.22}$$

The consistency equation, combined with the geometric requirement for non-intersection, resulted in the following expression for the translation rule:

$$\dot{\boldsymbol{\alpha}} = \dot{\hat{\boldsymbol{\alpha}}} + (\bar{\boldsymbol{\alpha}} - \hat{\boldsymbol{\alpha}})\left(\frac{\dot{r}}{r} + \frac{\dot{p_c}}{p_c}\right) + \frac{\bar{\boldsymbol{n}} : \left\{\dot{\hat{\boldsymbol{\sigma}}} - \hat{\boldsymbol{\sigma}}\left[\left(\frac{\dot{r}}{r}\right) + \left(\frac{\dot{p_c}}{p_c}\right)\right] + \bar{\boldsymbol{\sigma}}\left(\frac{\dot{r}}{r}\right)\right\}}{\bar{\boldsymbol{n}} : (\boldsymbol{\sigma_c} - \boldsymbol{\sigma})} \quad (\boldsymbol{\sigma_c} - \boldsymbol{\sigma}) \qquad (3.23)$$

Equation 3.23 comprised of three variable terms that needed to be defined in order to indicate the translation of the centre of the bubble. The first term described the movement of the centre of the structure surface; the second variable term defined the scaling of the space inside the structure surface that followed any changes in the values of r and p_c, respectively; the final term was introduced in order to describe the translation of the elastic bubble along the line joining the current and conjugate stress points (figure 3.3).

As it was mentioned previously, the plastic modulus H for the general case where the structure and bubble surfaces are not in contact was assumed to depend on the Euclidean distance between the current and conjugate stress points. In similar fashion to previous kinematic hardening models, the magnitude of H reduced to the plastic modulus H_c at the conjugate point in the event the bubble and the structure surface were in contact.

When the loading scenario forces the bubble to translate towards the structure surface, the two surfaces will eventually be in contact and the response of the model is controlled by the structure surface (*i.e F=0*) . The consistency condition on the structure yield surface is therefore given by the following expression:

$$\hat{\boldsymbol{n}} : \left[\dot{\hat{\boldsymbol{\sigma}}} - \hat{\boldsymbol{\sigma}}\left(\frac{\dot{r}}{r} + \frac{\dot{p_c}}{p_c}\right)\right] = 0 \qquad (3.24)$$

The combination of equations 3.10, 3.11, 3.14 and 3.15 and by applying the consistency equation above to the equation of the structure surface (equation 3.8), the following expression for the plastic modulus H_c was derived:

$$H_c = \frac{rp_c\left\{T\left[(p-p_{\bar{a}})+\left(\frac{3}{2M_\theta^2}\right)(\boldsymbol{s}-\boldsymbol{s}_{\bar{a}}):\boldsymbol{\eta}_0+Rp_c\right]-(p-p_{\bar{a}})+\left(\frac{3}{2M_\theta^2}\right)(\boldsymbol{s}-\boldsymbol{s}_{\bar{a}}):\left(\frac{\boldsymbol{\eta}_0}{r}\right)\right\}}{(\lambda^*-\kappa^*)\left[(p-p_{\bar{a}})+\left(\frac{3}{2M_\theta^2}\right)(\boldsymbol{s}-\boldsymbol{s}_{\bar{a}}):(\boldsymbol{s}-\boldsymbol{s}_{\bar{a}})\right]} \quad (3.25)$$

Quantity T in the above equation was given by the following equation:

$$T = (p-p_{\bar{a}}) - k\left(\frac{r-1}{r}\right) x \left[(1-A)(p-p_{\bar{a}})^2+\left(\frac{3A}{2M_\theta^4}\right)(\boldsymbol{s}-\boldsymbol{s}_{\bar{a}}):(\boldsymbol{s}-\boldsymbol{s}_{\bar{a}})\right]^{\frac{1}{2}} \quad (3.26)$$

The proposed form of the hardening modulus enabled the KHSM to reduce to the kinematic hardening bubble extension of Cam clay for reconstituted soils as formulated by Al-Tabbaa & Muir Wood, (1989), provided that the parameters r_0 and η_0 were set to 1 and 0, respectively. In the case of a natural soil where the initial measure of structure r_0, and therefore, consequent values of r, might have been larger than 1, equation 3.26 took into account that the destructuration process of the material comprised of both plastic volumetric and plastic deviatoric components, according to the value of A ($0 < A < 1$).

In line with the requirements for a smooth variation of stiffness as the bubble approached the structure surface and the non-intersection rule, the expression which prescribed the distance between the two surfaces needed to be described.

$$b = \bar{\boldsymbol{n}} : (\boldsymbol{\sigma}_c - \boldsymbol{\sigma}) \quad (3.27)$$

It was evident from the above equation that in the case where the two surfaces are in contact, the conjugate and current stress points are the same and therefore the value of distance *b* reduced to zero. With the expression for distance *b* in mind, its maximum value was calculated with a simple extrapolation. The maximum distance b_{max} was obtained in the event when the bubble was in contact with the external surface at a stress point which was diametrically opposite to the conjugate point $\boldsymbol{\sigma}_c$. It should be noted that in that case, the current stress was situated on the bubble diametrically opposite this point of tangency (figure 3.3).

$$b_{max} = 2\left(\frac{r}{R} - 1\right)\bar{\boldsymbol{n}} : \bar{\boldsymbol{\sigma}} \tag{3.28}$$

In equation 3.28 the hardening modulus in the case when the stress point is either situated on the structure surface (*i.e.* b=0) or when the bubble and structure surface are not in contact was defined. The general form of the hardening modulus was the last component of the model to be defined. It should be noted that it is possible to prescribe a multitude of types of equations, depending on the material under consideration. The KHSM model adopted the following expression:

$$H = H_c + \frac{1}{\|\bar{\boldsymbol{n}}\|^2}\frac{Bp_c^3}{(\lambda^* - \kappa^*)R}\left(\frac{b}{b_{max}}\right)^{\psi} \tag{3.29}$$

It should be noted, that the form adopted for the interpolation function was found to influence the response of soils, as it was shown in section 3.3 of this chapter. However, any other form which is able to provide a good calibration to the available information could potentially be adopted with minimal effects on the fundamental principles of the model. Additionally, the above equation for the plastic modulus *H* allowed for plastic deformation to occur for stress states within the structure surface, depending on the distance b. This was important for simulations of non-monotonic loading, and finally, when *b* was equal to b_{max}, the plastic modulus became significantly large, which resulted in the material

corresponding to the elastic response within the bubble. A discussion of some alternative stiffness variation schemes is provided in Chapter 7 of this thesis, with some indicative results.

Note: The above literature review of the KHSM model is largely based on information from the Geotechnique paper in 2000 which describes the model

3.3 Numerical implementation in commercial finite element software

The KHSM model was implemented by Dr. M. Rouainia, in the commercial finite element package Plaxis. The software has the facility that allowed users to implement a wide range of models, by providing information about the current stresses and state variables. The software then provided information about the previous values of stresses and state variables as well as information about strain increments. The model was implemented using an explicit stress integration scheme with automatic error control (Zhao *et al.,* 2005).

In order to define a material model in the calculation part of the software some issues needed to be addressed. Firstly the initialisation of the state variables or hardening parameters as they are also called needed to be done. These are used in 'hardening models' to indicate the current position of the yield locus. Since the update of these state variables was considered in the calculation of the constitutive stresses of the model, based on the previous state of the stress variables, it is necessary to know their initial value prior to the beginning of the calculation step. It should be noted that the resulting values of the state variables from one step are automatically transferred to the next one and consequently used as the initial values for that step. The second issue is the calculation of the constitutive stresses, which forms the main part of the user defined model. Here, the stress integration and correction are performed in accordance with the constitutive relations of the soil model. A discussion of the stress integration scheme adopted for this model is provided in the following section. The next step is the formation of the effective material stiffness matrix, where full elasto-plastic behaviour is stored.

In the course of elastic-plastic finite element simulations, it is required to solve the ordinary differential equations presented below:

$$d\boldsymbol{\sigma}' = D^{ep} d\boldsymbol{\varepsilon} \tag{3.33}$$

$$d\boldsymbol{\chi} = d\lambda \boldsymbol{B} \tag{3.34}$$

In equation 3.33, d$\boldsymbol{\sigma'}$ denotes the increment of effective stress and d$\boldsymbol{\varepsilon}$ is the respective strain increment. D^{ep} is defined as the elasto-plastic matrix.

Equation 3.34 comprises of the plastic multiplier $d\lambda$, the vector which stores the increments of the hardening parameters from the model $d\boldsymbol{\chi}$ and the operational vector **B** which is utilised in the finite element formulation.

The constitutive model in this thesis contains eight hardening parameters, namely the six components of the stress vector (as described in the previous chapter), at the bubble centre, and p_c and r. Consequently, the vector storing the hardening parameters can be expressed as follows:

$$\boldsymbol{\chi} = \{p'_c, r, \bar{\alpha}^T\}^T \tag{3.35}$$

The components of the operational vector **B**, require equations (3.12), (3.16) and (3.23) in order to be evaluated. In matrix form they are given by:

$$\boldsymbol{B}_{(8x1)} = \begin{bmatrix} \frac{\partial p_c}{\partial d\lambda} \\ \frac{\partial r}{\partial d\lambda} \\ \frac{\partial \bar{\boldsymbol{\alpha}}}{\partial d\lambda} \end{bmatrix} = \begin{bmatrix} \frac{p_c}{\lambda^* - \kappa^*}\left(\frac{\partial f_B}{\partial p'}\right) \\ -\frac{k}{(\lambda^* - \kappa^*)}(r-1)\sqrt{(1-A)\left(\frac{\partial f_B}{\partial p'}\right)^2 + A\left(\frac{\partial f_B}{\partial \boldsymbol{s}}\right)^2} \\ \bar{\boldsymbol{\alpha}}\left(\frac{B_1}{P_c} + \frac{B_2}{r}\right) + \frac{H - \boldsymbol{n}:\left[\frac{B_1}{P_c}\boldsymbol{\sigma'} + \frac{B_2}{r}\bar{\boldsymbol{\alpha}}\right]}{\boldsymbol{n}:(\boldsymbol{\sigma} - \boldsymbol{\sigma_c})}(\boldsymbol{\sigma} - \boldsymbol{\sigma_c}) \end{bmatrix} \tag{3.36}$$

The remaining components of equations 3.33 and 3.34 that need to be defined is the elasto-plastic matrix and the plastic multiplier, which are given by equations 3.37 and 3.38 respectively:

$$\boldsymbol{D}^{ep} = \boldsymbol{D} - \frac{\boldsymbol{D}\boldsymbol{m}\boldsymbol{n}^T\boldsymbol{D}}{H + \boldsymbol{n}^T\boldsymbol{D}\boldsymbol{m}} \tag{3.37}$$

$$d\lambda = \frac{\boldsymbol{n}^T\boldsymbol{D}d\boldsymbol{\varepsilon}}{H + \boldsymbol{n}^T\boldsymbol{D}\boldsymbol{m}} \tag{3.38}$$

Terms **n** and **m** are equal and define the stress gradient on the bubble at the current state $\frac{\partial f_b}{\partial \boldsymbol{\sigma'}}$**.** Term $\boldsymbol{D}$ denotes the elastic stress-strain matrix and H is the hardening modulus.

Given that the equation of the bubble surface (eq. 3.7) maybe be written as:

$$f_b \coloneqq \frac{3}{2M_\theta^2} Q + (p - p_{\bar{a}})^2 - (RP_c)^2 \tag{3.39}$$

With

$$Q = (\boldsymbol{s} - \boldsymbol{s_{\bar{a}}}) : (\boldsymbol{s} - \boldsymbol{s_{\bar{a}}}) \tag{3.40}$$

Consequently the stress gradient on the bubble may be determine by the first derivative of equation 3.39 with respect to the stress $\left(\frac{\partial f_b}{\partial \boldsymbol{\sigma'}}\right)$ as follows:

$$\boldsymbol{n} = \frac{\partial f_b}{\partial \boldsymbol{\sigma}'} = \frac{\partial f_b}{\partial p'}\frac{\partial p'}{\partial \boldsymbol{\sigma}'} + \frac{\partial f_b}{\partial Q'}\frac{\partial Q}{\partial \boldsymbol{s}}\frac{\partial s}{\partial \boldsymbol{\sigma}'} + \frac{\partial f_b}{\partial M_{\boldsymbol{\theta}}}\frac{\partial M_{\boldsymbol{\theta}_b}}{\partial \theta}\frac{\partial \theta}{\partial \boldsymbol{s}'}\frac{\partial \boldsymbol{s}}{\partial \boldsymbol{\sigma}'} \tag{3.41}$$

Derivatives of equations (3.31) and (3.40) are provided in Appendix A.

3.3.1 Stress integration algorithm

The stress integration scheme used in this work has its origin on the explicit Euler method with automatic sub-stepping and error control (Zhao *et al.* 2005). This scheme employed the classical elasto-plastic stiffness matrix and was used here to assimilate the rate form of the stress–strain relations for the KHSM model. The general procedure as described in the 2005 paper comprised of the following steps. Firstly, the identification of the location of the yield surface intersection with the elastic trial stress path, followed by the integration process of the stress–strain relations using the modified Euler scheme with sub-stepping and error control, and finally the correction of any drift of the yield surface that may have occurred during the numerical computations.

The first step was to assume an elastic trial stress increment upon an imposed strain increments. The obtained elastic trial stress increment was then be used to check if plastic yielding occurred. Once the portion of the given strain increment that caused plastic yielding was quantified, a set of stress increments and the corresponding set of hardening parameters increments were computed using the forward Euler method. It should be noted that all stress dependent quantities were estimated at the current stress state.

With the aid of the updated stress state and the updated hardening parameters to estimate elastic stiffness and gradients of the yield surface and plastic potential, another set of stress increments and hardening parameter increments, was obtained and therefore the modified Euler solution was used. The difference between the two sets of solutions was then used to evaluate the error measure. The strain increment was consequently subdivided, provided that the error was larger than the prescribed tolerance. In the case that the error was within the limits of the prescribed tolerance, the stress state and hardening parameters were updated according to the modified Euler method. The relative error in the stress solution followed the procedure described in Sloan *et al.* (2001). The difference of this scheme was the evaluation of the relative error of the hardening parameters which was given by the following expression:

$$Error = \sqrt{\frac{\Delta p_{c2} - \Delta p_{c1}}{p_c^2} + \frac{\Delta r_2 - \Delta r_1}{r^2} + \frac{(\Delta \bar{\boldsymbol{a}}_2 - \Delta \bar{\boldsymbol{a}}_1) : (\Delta \bar{\boldsymbol{a}}_2 - \Delta \bar{\boldsymbol{a}}_1)}{\bar{\boldsymbol{a}} : \bar{\boldsymbol{a}}}} \tag{3.42}$$

In the above expression, subscript 2 denoted the second-order accurate solution obtained by the modified Euler method, whereas subscript 1 denoted the first-order accurate solution obtained by the forward Euler method. All the denominators used the second-order accurate solution. It is noteworthy that in above equation, the error in each hardening parameter was taken into account, even though some parameters-such as the parameter controlling the structure size- did not explicitly appear in the current yield surface.

The formulation of the translation law in the KHSM model, should have theoretically guaranteed that the bubble was always inside the structure surface. In numerical computations, however, this was not always possible and in the event the bubble drifted slightly outside the structure surface, a correction procedure was applied as described by Potts & Gens (1985).

3.3.2 Model parameters required for the numerical simulations

The model was extended from implementations of the traditional Cam clay and thus required two parameters to describe its elastic response: κ^*, the elastic volume change characteristics for change in mean stress and ν, Poisson's ratio (if the traditional elasticity law was used). Furthermore, the KHSM model also required three plastic/elasto-plastic parameters, namely, λ^*, the total volume change characteristics for isotropic compression; M, the slope of critical state line which controlled geometry of yield and other surfaces in the (p', q) plane.

The inclusion of the elastic bubble, introduced another three parameters. The ratio of sizes of bubble and reference surface R; The stiffness interpolation parameter, B; and finally the stiffness interpolation exponent, ψ. It should be noted that the bubble was centred on the initial stress state. The addition of the destructuration process required the definition of two further parameters: The rate of loss of

structure with damage strain, *k* and *A*, the relative contribution of distortional and volumetric plastic strains in the destructuration process.

In order to complete the model, the initial conditions of the soil required initiation. These were: p_{co}, which defined the size of the surfaces (as for Cam clay); $\bar{\boldsymbol{\alpha}}$, the centre of the bubble yield surface in similar fashion to the bubble model; and r_0 and η_0, which, described the initial degree and anisotropy of structure of the soil, respectively. The formulation of the volumetric response of the soil using parameters λ^* and κ^*, which were defined in (*ln v: ln p'*) compression plane is advantageous in the sense that for the calculation of stress-strain response, which is the primary application of constitutive models, no reference value of specific volume was required, unlike some classical implementations of Cam clay (Roscoe & Burland, 1968; Britto & Gunn, 1987). Tables 3.1-3.5 present the input parameters required in the finite element software.

	Symbol	**Description**
General elastic and plastic parameters common with modified Cam clay type of models	λ^*	Slope of normal compression line in (*ln v: ln p'*) compression plane
	κ^*	Slope of swelling line in (*ln v: ln p'*) compression plane
	M	Critical state stress ratio
	Φ	Angle of friction at critical state
	V	Poisson's ratio

Table 3.1: General parameters for KHSM model

	Symbol	Description
Parameters introduced by the Bubble model	R	Ratio of sizes of Bubble and reference surfaces
	B	Stiffness interpolation parameter
	Ψ	Stiffness interpolation exponent

Table 3.2: Parameters required for the inclusion of the elastic bubble.

	Symbol	Description
Parameters introduced by the Structure surface	A	Contribution of volumetric and distortional strains to damage to structure
	K	Parameter controlling the rate of damage to structure
	η_0	Scalar controlling the initial anisotropy of structure
	R	Initial degree of structure-ratio of sizes of structure and reference surfaces

Table 3.3: Parameters required for the inclusion of initial structure and the consequent destructuration process.

	Symbol	Description
Elasticity law	*1*	Traditional Cam clay
	2	Viggiani's semi-empirical law
	3	Hyperelastic law by Houlsby *et al.*
Input parameters for Viggiani's model (2)	*Pref*	Reference pressure (taken as 1Kpa)
	A_g	Dimensionless parameter defined by the plasticity index of the soil
	n_g	Dimensionless parameter defined by the plasticity index of the soil
	m_g	Dimensionless parameter defined by the plasticity index of the soil
Input parameters for Houlsby's hyperlastic model (3)	n_h	Dimensionless pressure exponent
	K_h	Dimensionless Bulk stiffness factor
	G_h	Dimensionless Shear stiffness factor

Table 3.4: Parameters for the selection of elasticity law and required parameters for the Viggiani and Hyperelastic models respectively.

	Symbol	Description
Parameters defining the initial state of soil	*OCR*	Isotropic overconsolidation ratio of soil under consideration
	K_{0NC}	Coefficent of earth pressure at rent in normally consolidated conditions

Table 3.5: Parameters required for the definition of initial state of the soil.

3.4 Initialisation procedure of the KHSM in Plaxis

The process of initialisation of User Defined Models in Plaxis is provided in the subsequent Section. The software requires information to initialise the state variables which are used to specify the initial position of the yield surface. The stresses are initialised using the normal Plaxis procedure. In normally consolidated conditions, the initial position of the yield surface is calculated based on the following expressions:

$\sigma_1 = \sigma'^{0}_{yy}$ and $\sigma_2 = \sigma_3 = \sigma_1 \times K0^{NC}$

where:

σ'^{0}_{yy} is the effective vertical stress from Plaxis

and

$K0^{NC}$ is the K0 value related to normally consolidated conditions, and is an input parameter for the KHSM model. The information is then used to compute the size and position of the reference surface for Normally Consolidated (NC) conditions as it can be seen in Figure 3.4.

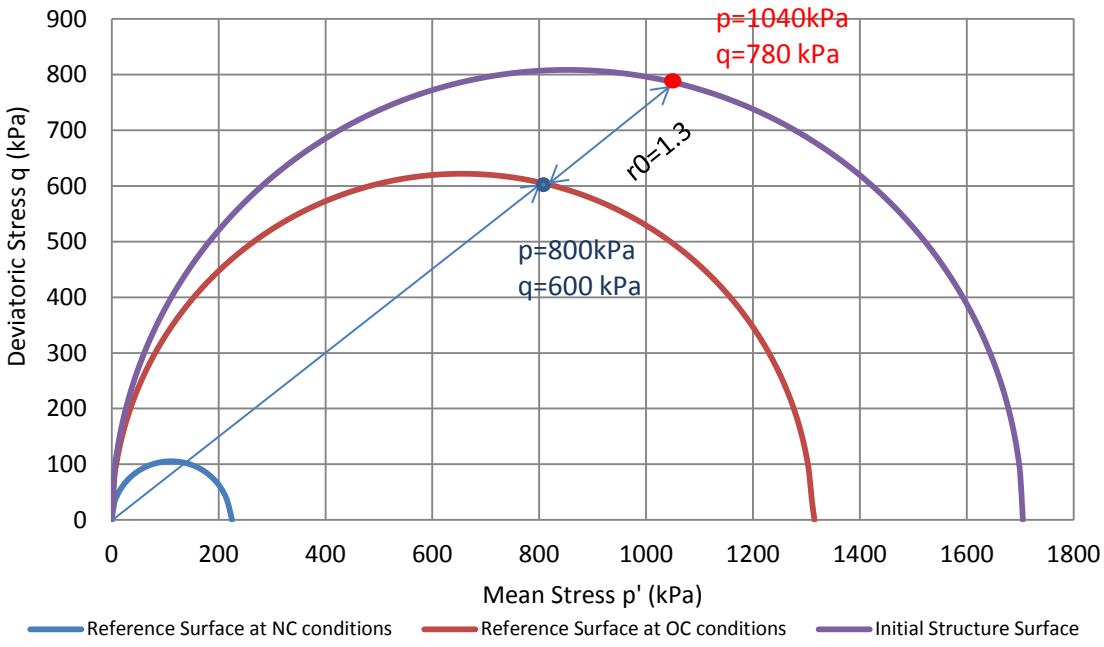

Figure 3.4: Yield surfaces based on the Initialisation process for the KHSM in Plaxis

In the cases where a material is overconsolidated, the computed vertical stress (σ'^{0}_{yy}) is multiplied by the input value of OCR from the KHSM model, resulting in the maximum vertical effective stress (σ'_{p}), previously experienced by the soil. A diagram of the principle of overconsolidation is provided in Figure 3.5.

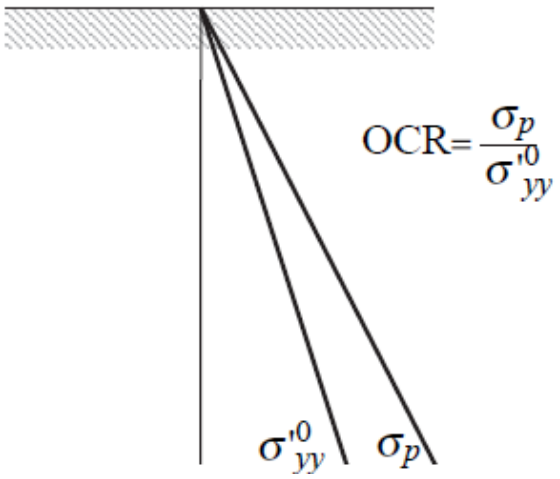

Figure 3.5: Principle of Vertical Preconsolidation Stress (after Plaxis 2D manual)

The initial size and position of the yield surface is then calculated taking into consideration the following expressions:

$\sigma_1 = \sigma'_p$ and $\sigma_2 = \sigma_3 = \sigma_1 \times K0^{NC}$

where:

σ'_p is the maximum effective vertical stress (preconsolidation stress)

The information is then used to compute the size and position of the reference surface for Normally Consolidated (OC) conditions as it can be seen in Figure 3.5. The initial ellipse passes through the point on the NC line characterised by a vertical stress that is OCR x σ'^{0}_{yy}.

For example, assuming a triaxial specimen under isotropic conditions with $\sigma'_{yy} = \sigma'_{xx} = 200$kPa and $K0^{NC} = 0.5$, and OCR=6 the initial ellipse passes through (p',q)=(800,600) (see Figure 3.5).

In the cases where a structured soil is modelled and therefore r0 is great than 1, the computed value of p'_0 is multiplied by the input parameter of r0. In the example described above, assuming a value of r0=1.3, the ellipse is size of the ellipse along the NC line is multiplied by 1.3. Consequently the ellipse for the structure surface passes through (p',q)=(1040,780). This initialisation process has been followed thoughought the work reported in this thesis.

3.5 Validation of the KHSM model-undrained capacity of footing

In order to assess the performance of the KHSM model in simulating the behaviour of clay soils, a validation process was carried out by analysing a geotechnical problem which has a known theoretical solution. The benchmark analysis that was chosen for this exercise was the undrained bearing capacity of a strip footing founded on clay soil with constant shear strength. The results from the Finite Element simulations results were corroborated against the well-known analytical results presented by Terzaghi (1943). During his work, Terzaghi proposed a semi-empirical method for evaluating the bearing capacity of strip foundations, by considering the cohesion, friction and initial weight of the soil. The Rouainia Muir Wood constitutive model (KHSM) employed in this thesis is able to collapse to Cam clay by making the size of the bubble, equal to that of the outer surface, which has the same function as the Cam-clay yield surface. The parameters used for this validation exercise were chosen to simulate the modified Cam clay ellipse. The bubble size, controlled by parameter R and was set to 1 so that it is equal to that of the outer surface. The degree of initial structure r_0 was also set to 1 so that the KHSM model simulates the behaviour of un-bonded soils. The remaining parameters was chosen based on the Rouainia and Muir Wood paper (2000) and are provided in Table 3.6 below.

λ^*	κ^*	M	R	r_0	φ	N
0.252	0.0297	1.35	1	1	33.5	0.22

Table 3.6: Soil parameters adopted in the validation simulations. (Rouainia and Muir Wood, 2000)

The theoretical triaxial undrained shear strength of the clay soil, correlates to the constitutive model material properties through the following equations:

$$S_u = \frac{Mp_0'}{2}\left(\frac{OCR}{2}\right)^{\Lambda} \qquad \Lambda = 1 - \frac{\kappa^*}{\lambda^*}$$

A value of K0=1 was assumed for the simulations, leading to an isotropic initial stress state. Initial vertical stress of $\sigma'_1 = \sigma'3 = 28.7$ kPa, with OCR=1 so that the theoretical undraned shear strength is calculated to be 10kPa. The water table was placed at the bottom of the geometry so that pore pressures were assumed to be zero. The geometry of the finite element model is provided in Figure 3.6. The strip footing was defined as a surface displacement. The width of the footing was assumed to be 6m with the out of plane dimensions assumed to be 10m.

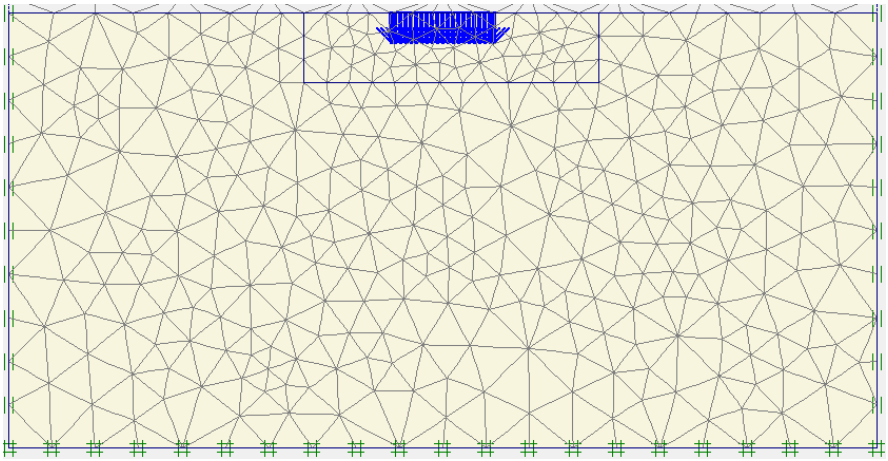

Figure 3.6: Finite Element geometry for undrained capacity of strip footing

Figure 3.7 shows the incremental displacement shadings at failure. It is evident that the model successfully predicts the shear wedge failure under the footing termed the Rankine zone, as well as the development of the passive zones of failure radiating outwards.

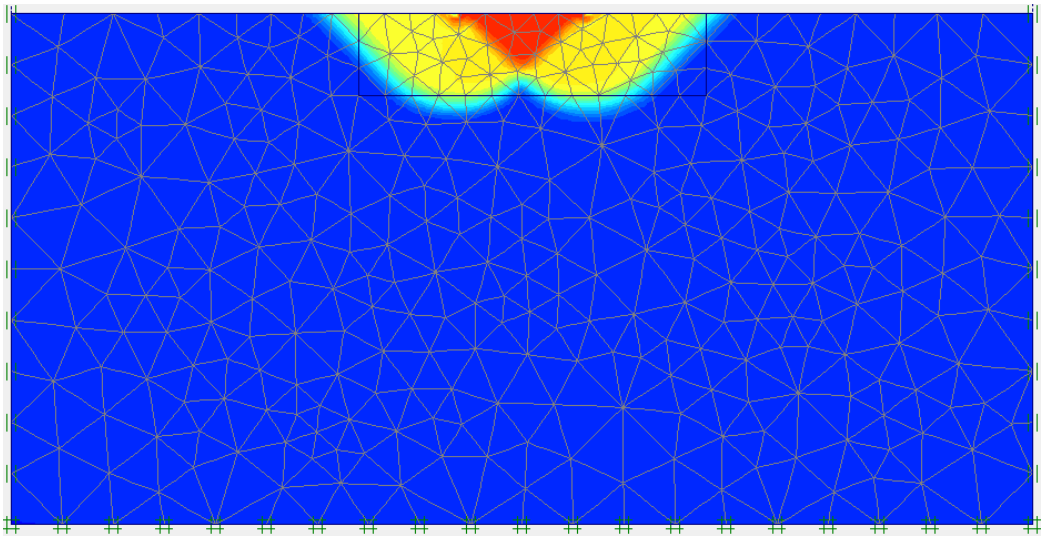

Figure 3.7: Incremental displacement shadings for undrained capacity of strip footing

The finite element simulation results in a failure load of approximately 355kN/m giving an ultimate capacity of 3550kN. The theoretical solution yields a bearing capacity of 3700kN. The error in the Plaxis model is of the order of 4%, which is deemed acceptable.

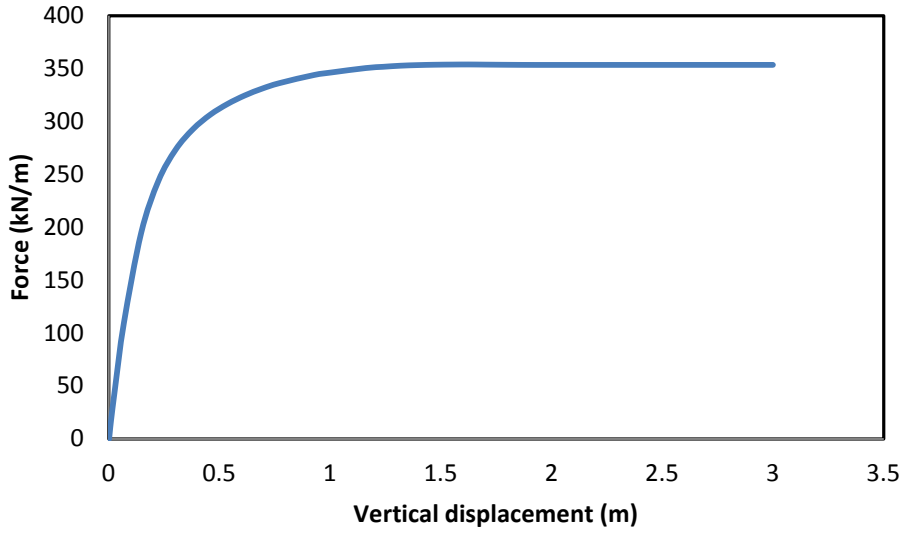

Figure 3.8: Load vs displacement curve for undained capacity of strip footing

3.6 Validation of the KHSM model with Vallericca clay triaxial tests

In this part of the chapter, the kinematic hardening model described in the previous section was used to reproduce the yielding and stress– strain behaviour of the structured soft clay found in the Vallericca region, near the valley of river Tiber. To minimise the effects of sampling disturbance, large block samples were extracted from vertical faces of deep cuts. The blocks samples were taken in different years from two adjacent brick pits a few kilometres north of Rome. A series of undrained triaxial tests uder anisotropic consolidation modes were performed on undisturbed samples of Vallericca clay to study the yielding characteristics and the permanent differences between reconstituted samples and fully destructured natural samples. It was described in detail in Amorosi & Rampello (2007) and summarised here.

Vallericca clay is a stiff overconsolidated clay deposit of Plio-Pleistocene age that was deposited in a marine environment in the depression that currently coincides with the valley of river Tiber. The soil is a medium plasticity and activity clay with a calcium carbonate content of about 30%.

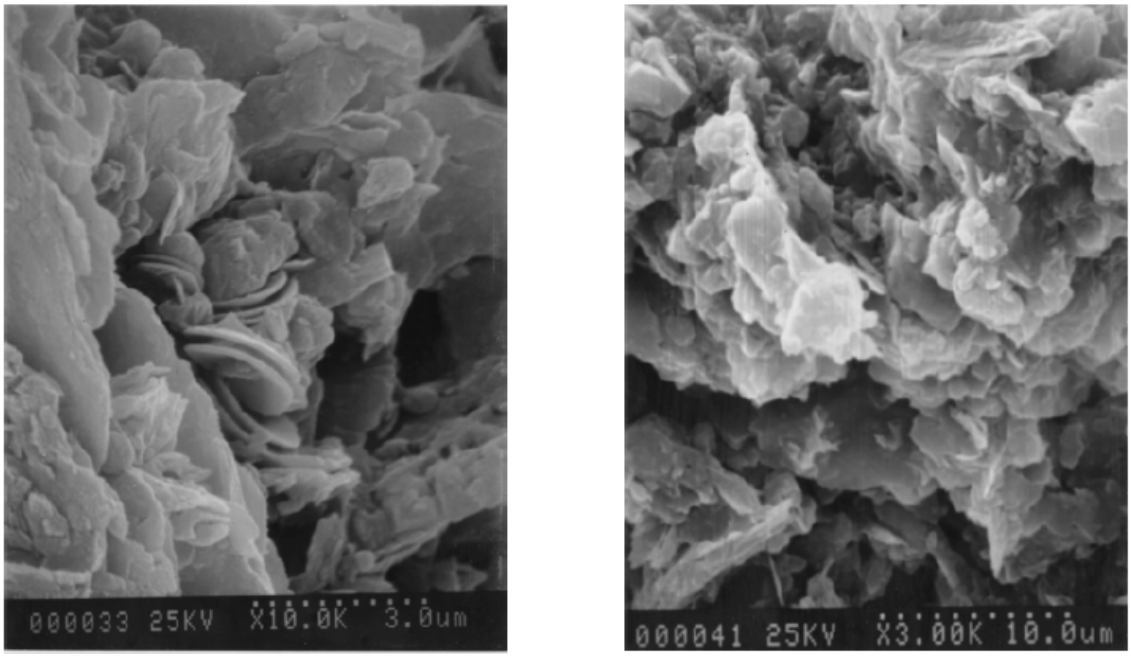

(a) (b)

Figure 3.9: Photographs of Vallericca clay : vertical sections for (a) natural and (b) reconstituted samples (Sciotti, 1992)

Table 3.7 illustrates the average index properties and natural water content of the blocks from the two batches retrieved from two separate trial pits. Attention is paid in the Plasticity Index, which provided the values for the small strain elastic model by Viggiani, adopted in this study.

Batch No	**Specific gravity G_s**	**Clay fraction CF (%)**	**Liquid limit W_L (%)**	**Plasticity index I_P (%)**	**Natural water content W_0 (%)**	**Liquidity index I_L (%)**
1	2.78	42	59.2	31.6	28.6	0.03
2	2.75	47	53.9	29.2	29.2	0.06

Table 3.7: Index properties of Vallericca clay (after Amorosi & Rampello, 2007)

The deposits of Vallericca clay had been the focus of extensive studies since the 1990s (Rampello *et al.,* 1993), with a substantial amount of research work carried out in order to investigate in depth, the role of natural structure and its influence on the mechanical behaviour of the soil. Burland *et al.* (1996) identified the influence of micro-structural effects on the compressibility and shear strength of Vallericca clay, by carrying out comparison of results from oedometer and triaxial tests on natural and reconstituted samples. Further experimental research on Vallericca clay, recently carried out by Amorosi (1996), confirmed that the mechanical behaviour of the soil is significantly affected by its natural structured state. It was also established that the direction of the stress path influenced the destructuration process, as it was observed that it occurred during both the consolidation and the shear stages of the tests. This observation was believed to be related to the accumulation of volumetric and deviatoric plastic strains. The KHSM model has the facility of describing these features explicitly and therefore a direct comparison between the two could be made.

3.6.1 Summary of experimental programme

A number of laboratory experiments in the form of oedometer and triaxial compression tests were conducted to evaluate the engineering parameters of the clay. The oedometer tests carried out on natural samples included cells with a smaller diameter (35.7mm) with the logic of obtaining vertical stresses ranging up to 12.8 MPa.

Figure 3.10 illiustrates the resultant oedometer curves, within the void index-vertical stress space (I_v –logσ_v), with the derived compression parameters provided in table 3.8. As it can be seen, the compression corresponding to the natural samples overlap the intrinsic compression line (ICL) and then move down, a point which marked the onset of significant destructuration. Following yielding, the structured samples fall back to the normal compression line.

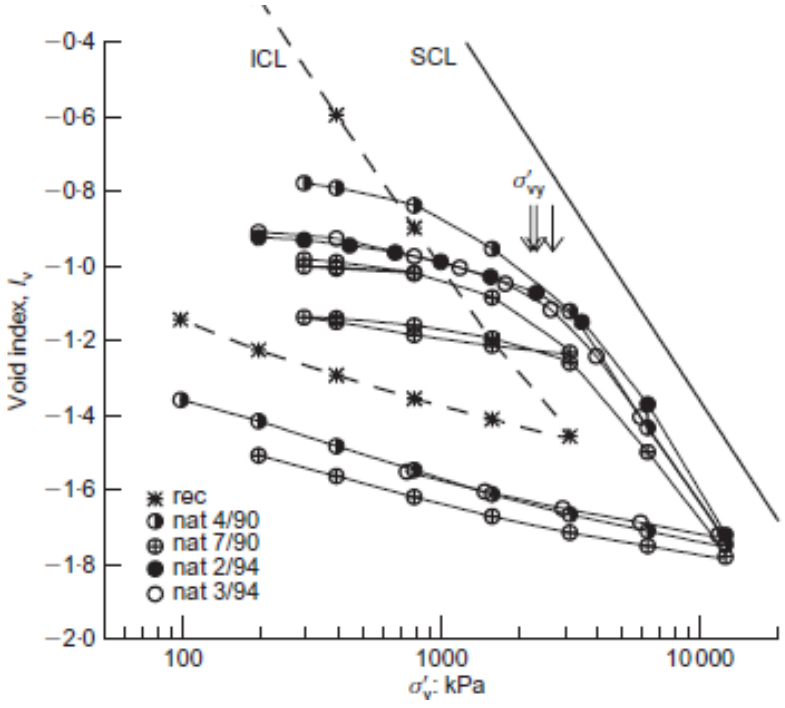

Figure 3.10: Compressibility of Vallericca clay under (a) oedometric conditions

Batch No.	Sample	e_0	C_c	C_s	σ'_{vy} (MPa)	σ^*_{ve} (MPa)	$\sigma'_{vy}/\sigma_{ve}^*$	C_c/C_c^*
1	4/90	0.775	0.40	0.08	2.15	0.89	2.42	0.99
1	7/90	0.712	0.37	0.07	2.33	1.15	2.03	0.90
2	2/94	0.735	0.44	-	2.70	1.03	2.62	1.09
2	3/94	0.743	0.42	0.06	2.70	1.13	2.39	1.03

Table 3.8: Compression characteristics in oedometer tests (Amorosi & Rampello, 2007)

The ability of the natural samples to exist in stress states that are higher than their intrinsic counterpart, for the same void ratio-or in this case the void index-, is attributed to the in-situ structure which is a feature of most natural soils (Burland, 1990; Burland *et al* 1996). The ratio of $\sigma'_{vy/}\ \sigma_{ve}^*$ provided an indication of that measure of initial structure and was used in order to estimate the value of the parameter, which controlled the size of the structured surface (r_0). An average value of 2.4 was adopted for the simulations, which is in accordance with the reported value.

The triaxial apparatus consisted of a computer-controlled stress path cell, with a cell pressure capacity of 3.2 MPa. The system was equipped with mid-height pore water pressure probe, internal and external axial load cells as well as a couple of miniaturised submersible linear variable differential transducers which evaluated the axial displacement over the central length of the sample. This apparatus was thought to enable the recognition of the development of slip surfaces through the samples, as described in detail in Amorosi & Rampello (2007). For each test adopted in the validation of the model, the data were limited to those observed prior to the development of the slip surfaces and therefore in a technically homogeneous state.

For the triaxial tests that were used in the validation of the model, intact specimens of 38 mm in diameter and 76 mm high, obtained from the block samples were positioned in the apparatus and consequently subjected to compression under anisotropic conditions. Triaxial compression tests were then carried out, at the end of the compression stage, in order to obtain an over-consolidation ratio of 1. All samples were compressed from an initial isotropic effective stress state of $p_{initial}$=400 kPa to a final state with mean effective stress p_{max} =1770 kPa and deviatoric stress q_{max} =1210 kPa, resulting in a stress ratio of K_{0NC} = 0.53. The stress ratios adopted for the anisotropic swelling were in accordance with the following equation:

$$K_0 = K_0^{OC} = (1 - \sin\varphi)OCR^{\sin\varphi} \tag{3.43}$$

For triaxial tests in lightly to moderately overconsolidated states, the specimens were anisotropically unloaded to obtain values of OCR equal to those imposed (1.7, 2.4 and 4) before the shearing stage. This was achieved by applying distinct increments of axial and radial stresses followed by consolidation. The stress history imposed in the laboratory was considered to minimise structure alteration prior to shearing, in terms of both fabric and bonding. Undrained shearing was carried out at a constant rate of axial strain equal to 4.5% per day.

A constant-volume angle of shearing resistance $\varphi = 28^0$ was assumed in this study. The vertical effective stress at the final state (σ'_{vmax} of 2570 kPa) was marginally lower than the vertical stress of σ'_{vy} .=2600 kPa which was associated with the onset of appreciable rates of structure degradation. The radial strain observed during the re-compression and swelling stages were minimal and therefore ensured the K_0 conditions were maintained for all tests.

A summary of the triaxial test that were used to validate the model is provided in table 3.9 comprising of the values of the maximum applied effective stresses (p'_{max}, q_{max}), the values of void ratio (e_0), and the effective stress (p_0', q_0) and over-consolidation ratio (OCR) attained prior to shearing.

Test No.	Test conditions	p'_{max} (kPa)	q_{max} (kPa)	p'_0 (kPa)	q_0 (kPa)	e_0	OCR
VrL4	CAU	1777.0	1208.0	1777.0	1208.0	0.710	1
Vr11	CAU	1773.8	1227.0	1221.9	523.7	0.718	1.7
Vr14	CAU	1763.0	1205.7	942.0	234.6	0.719	2.4
Vr17	CAU	1796.0	1224.0	695.8	8.8	0.728	4.0

Table 3.9: Anisotropic compression triaxial tests used for the validation of the KHSM model (adapted from Amorosi & Rampello, 2007)

Figure 3.11 illustrates the compression and swelling behaviour of the Vallericca clay intact specimens under triaxial conditions plotted in log*p'-(1+e)* scale. As it can be seen, the compression curves of the structured samples are more or less parallel to the isotropic intrinsic compression line for both isotropically and anisotropically compressed samples. As reported by Amorosi & Rampello (2007), (see table 3.9) the samples in their entirety were characterised by a single value the slope of normal compression line λ, as well as a single value of the slope of the swelling line κ. However, the formulation of the model under consideration requires the values of the normal compression and swelling slopes in ln*p'*-ln*(1+e)* scale. These values were obtained based on the following equations:

$$\lambda^* = \frac{\lambda}{1+e_0} \qquad and \qquad \kappa^* = \frac{\kappa}{1+e_0} \tag{3.35}$$

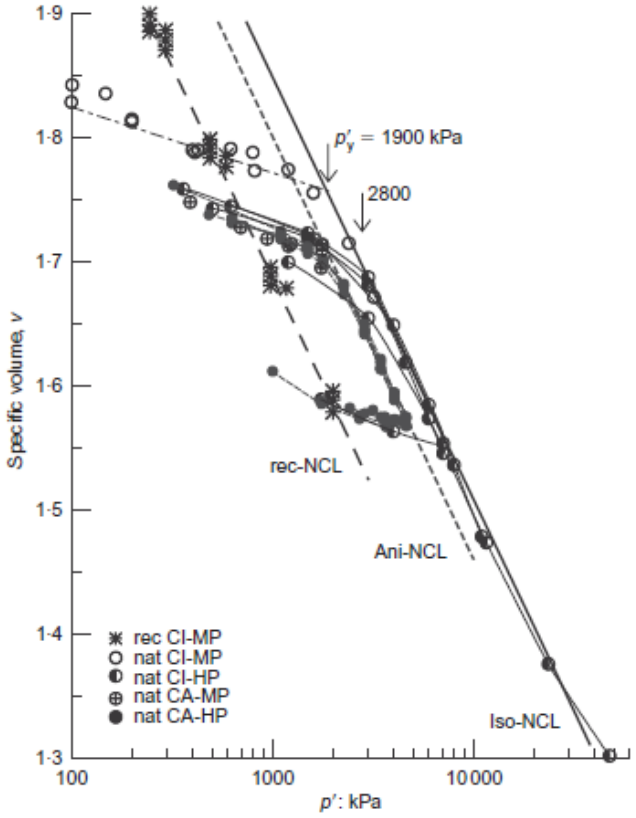

Figure 3.11: Compressibility of Vallericca clay under isotropic and anisotropic triaxial stress conditions (Amorosi & Rampello, 2007)

Sample type	**State**	**Specific volume at 1kPa (*N*)**	**Slope of normal compression line (λ)**	**Slope of swelling line (κ)**	**p'_y (MPa)**
CI-MP	Natural*	2.87	0.148	0.023	1.9
CI-HP	Natural	2.87	0.148	0.023	2.8
CA-MP/HP	Natural+	2.82	0.148	0.023	1.9

*Rampello *et al.* (1993)
+ Amorosi & Rampello (1998)

Table 3.10: Compression characteristics in triaxial tests (adapted from Amorosi & Rampello, 2007)

3.6.2 Model parameter evaluation

The compression and swelling parameters for the model were based on equation 3.35. An average value of e_0 of 0.7185 was calculated from table 3.8. Combining this value and the values provided in table 3.9, the required input parameters for the model were estimated to have values of $\boldsymbol{\lambda^*}$***=0.087*** and $\boldsymbol{\kappa^*}$ ***=0.013***, which are in good agreement with values used by Kavvadas and Amorosi (2004). The value of the critical state ratio ***M*** was set to 1.11 based on the value of angle of shearing resistance ($\varphi = 28^0$). Based on observation from Amorosi and Rampello, (2007), parameter ***A*** was assumed to have a value of 0.75 in order to account for the large amount of destructuration that occurred due to the deviatoric component of the plastic strains. The nonlinear elastic behaviour was assumed to be described by the equation proposed by Viggiani and Atkinson (1995) (see equation 2.42), with the required parameters evaluated from figure 3.5, based on an average value of plasticity index ($\boldsymbol{I_P}$) of 30%. Based on data from table 3.6 values of parameters $\boldsymbol{A_G}$, ***n***, and ***m*** for the elastic model were estimated as 1250, 0.78 and 0.26 respectively. The remaining parameters of the model were estimated by a trial and error procedure and the calibrated values of the KHSM model are provided in table 3.11.

Calibrated model parameter	**Value**
Slope of swelling line, $\boldsymbol{\kappa^*}$	0.013
Slope of normal compression line, $\boldsymbol{\lambda^*}$	0.087
Critical state stress ratio, ***M***	1.11
Ratio of size of bubble and reference surface, ***R***	0.15
Stiffness interpolation parameter, ***B***	0.85
Stiffness interpolation parameter,$\boldsymbol{\psi}$	1.9
Destructuration parameter, ***k***	2.3
Destructuration strain parameter, A	0.75
Initial degree of structure, $\boldsymbol{r_0}$	2.4
Anisotropy of initial structure, $\boldsymbol{\eta_0}$	0.15
Viggiani elastic model $\boldsymbol{A_G}$, ***m,n***	1250,0.78,0.26

Table 3.11: Calibrated KHSM parameters for Vallericca clay

3.6.3 Comparison of experiment and finite element simulations

Figures 3.11-3.15 show the comparison of the experimental and the simulated curves of the deviatoric stress ($\boldsymbol{q}$) and the axial strain ($\boldsymbol{\varepsilon_a}$) for the four anisotropic, undrained triaxial compression tests that were selected for the validation of the model. The corresponding effective stress paths are plotted in Figure 3.17. The dotted lines with points denote the experimental results for the Vallericca anisotropic tests, whereas the solid lines represent the model predictions with the calibrated values from Table 3.11.

It can be observed that that the general trend is well captured by the proposed model in terms of deviatoric stress as well as stress path and versus strain response. Figure3.12 illustrates the capability of the model to capture the brittle stress-strain behaviour as well as the post-peak strain softening a feature that was observed in normally consolidated undrained tests. The peak of the stress-strain curves was obtained at approximately 2% of axial deformation, for the simulation of the normally consolidated specimen (VrL4). The simulations of the overconsolidated specimens, Vr11, Vr14 and Vr17 can be seen in figures 3.13-3.15. The specimens exhibit a post peak softening behaviour that decreased as the OCR value increased. This again is in excellent agreement with the observations from Amorosi & Rampello (2007). Strain hardening behaviour is prevalent for the stress states that place the effective stress paths inside the structure surface. When the paths place the bubble in contact with the structure surface, the rate of de-structuring becomes appreciable and the material starts to strain soften. This was also attributed to the dependence of the shear modulus on the mean effective stress (through the non-linear Viggiani expression), which controlled the initial stiffness, and combined with the variation in plastic incremental stiffness as the bubble approached the structure surface, allowed the non-linearities of these curves to be well reproduced.

The smooth undrained stress paths indicated that plastic deformation and hardening occurred as soon as the bubble starts to move inside the structure surface. Furthermore, the predicted effective stress paths were found to converge towards the ultimate undrained strengths on the critical state line.

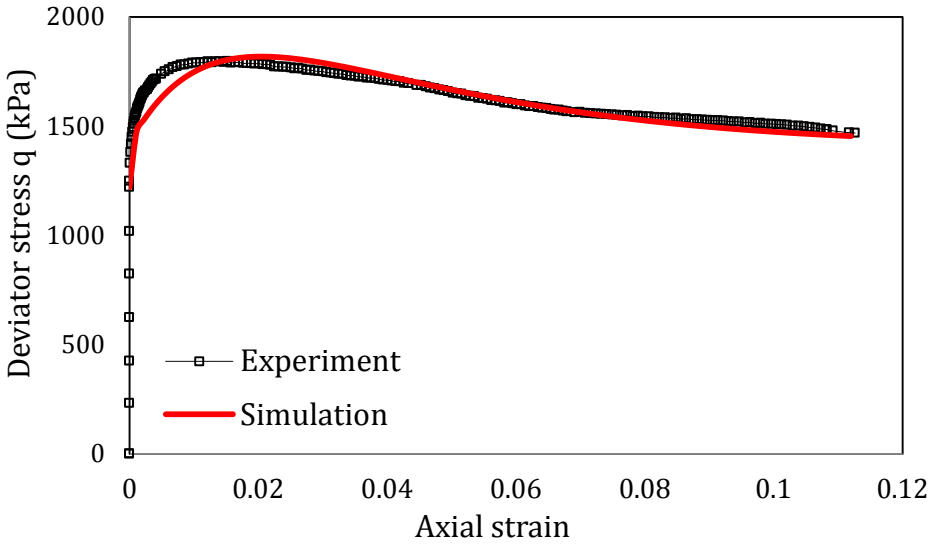

Figure 3.12: Undrained triaxial compression test (VrL4) on anisotropically consolidated Vallericca clay, OCR=1.0. Comparison of deviatoric stress versus axial strain between model simulation and experimental data.

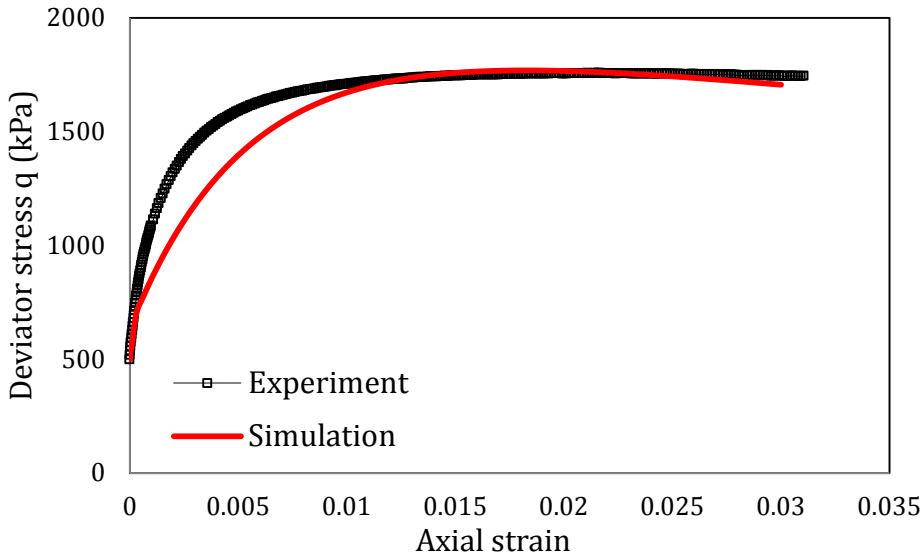

Figure 3.13: Undrained triaxial compression test (Vr11) on anisotropically consolidated Vallericca clay, OCR=1.7. Comparison of deviatoric stress and axial strain between model simulation and experimental data.

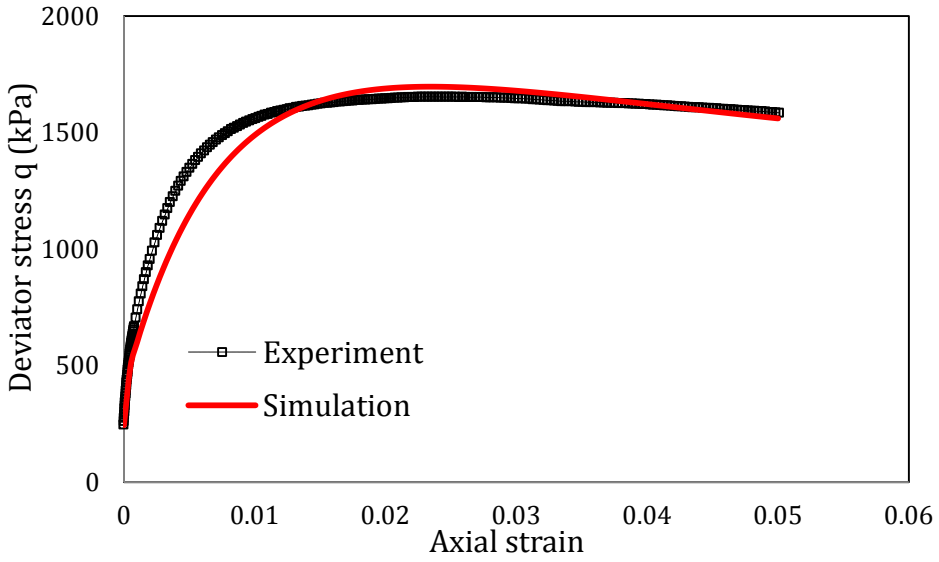

Figure 3.14: Undrained triaxial compression test (Vr14) on anisotropically consolidated Vallericca clay, OCR=2.4. Comparison of deviatoric stress versus axial strain between model simulation and experimental data.

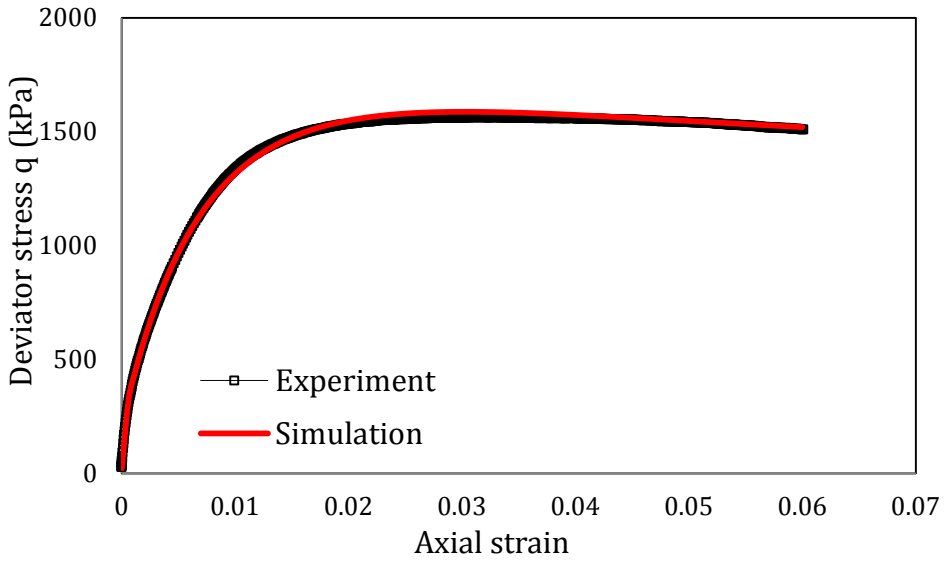

Figure 3.15: Undrained triaxial compression test (Vr17) on anisotropically consolidated Vallericca clay, OCR=4.0. Comparison of deviatoric stress versus axial strain between model simulation and experimental data.

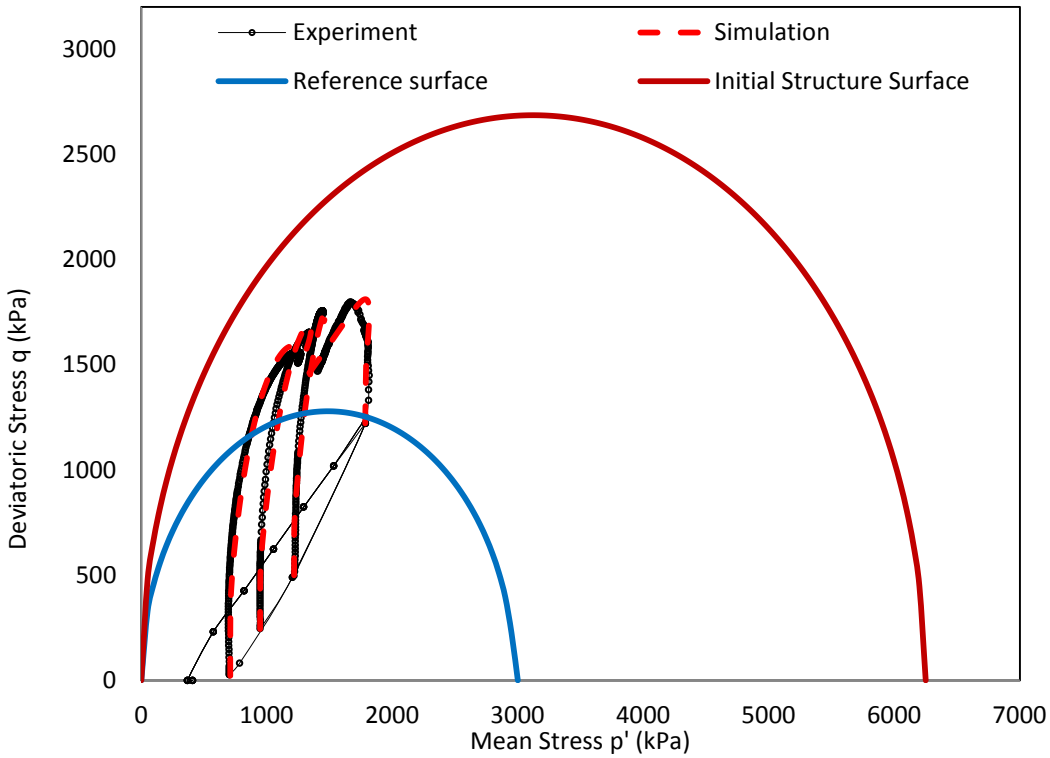

Figure 3.16: Comparison of Effective stress paths in *p'-q* plane between model predictions and experimental data for all four triaxial compression tests on anisotropically consolidated Vallericca clay.

3.7 Parametric analyses

The use of advanced constitutive models, such as the one presented here, requires the calibration of a relatively large number of input parameters. Some parameters cannot be directly determined from simple experiments and therefore a parametric analysis is able to give an insight on the sensitivity of the model to these.

The undrained triaxial test Vr17 was chosen for this parametric study. The work for this section adopts the calibrated values of the input parameters from table 3.11, and consequently varying one parameter while assuming other parameters unchanged. Table 3.12 provides the range of values for the parameters that have been explored for the purpose of this section.

Parameter	Values adopted for the sensitivity analysis
r_0	1,4, 8
K	0,5,10
A	0.0,0.5,1.0
η_0	0.0,0.5,1.0
Ψ	1.5,2.5,3.5
B	0.5,3.0,5.0
R	0.05,0.1,0.2
A_g,m_g,n_g,	(400,800);(0.6,0.8); (0.2,0.4)

Table 3.12: Exploratory parameters for the parametric analyses

3.7.1 Structure related parameters

As it can be seen in figure 3.17a, by increasing the value of the initial degree of structure r_0, results in higher and sharper peak in the stress-strain relationship. The structure surface always decreases in size upon occurrence of plastic deformation and collapses towards the reference surface no matter the plastic deformation is contractive or dilative. When the initial structure is totally removed, *i.e.* r is reduced from r_0 to 1.0 the two surfaces are in contact. Under undrained condition the destructuration is mainly controlled by distortional plastic strain.

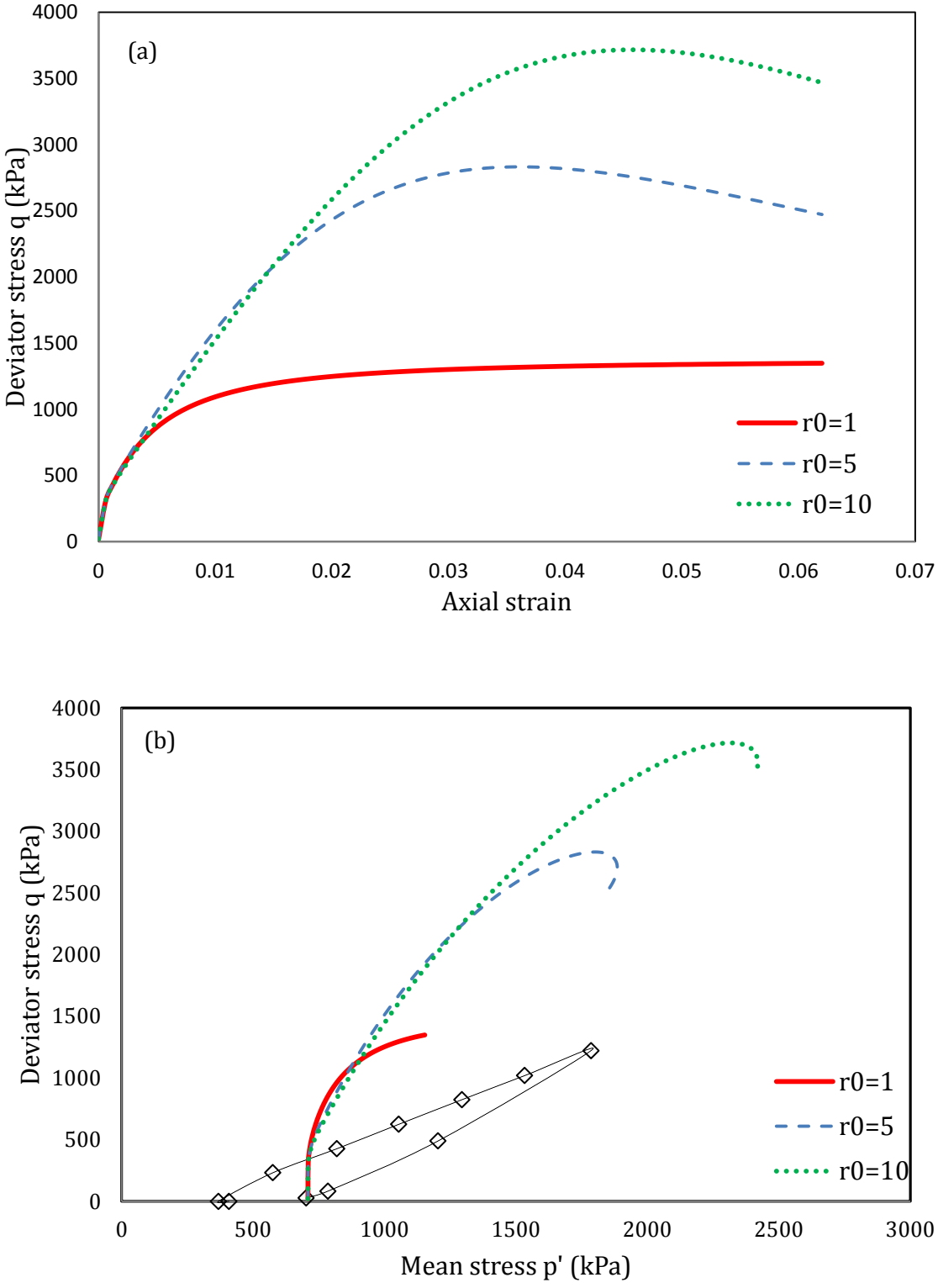

Figure 3.17: Influence of initial structure. (a) deviatoric stress versus axial strain and (b) effective stress paths in *p'-q* plane.

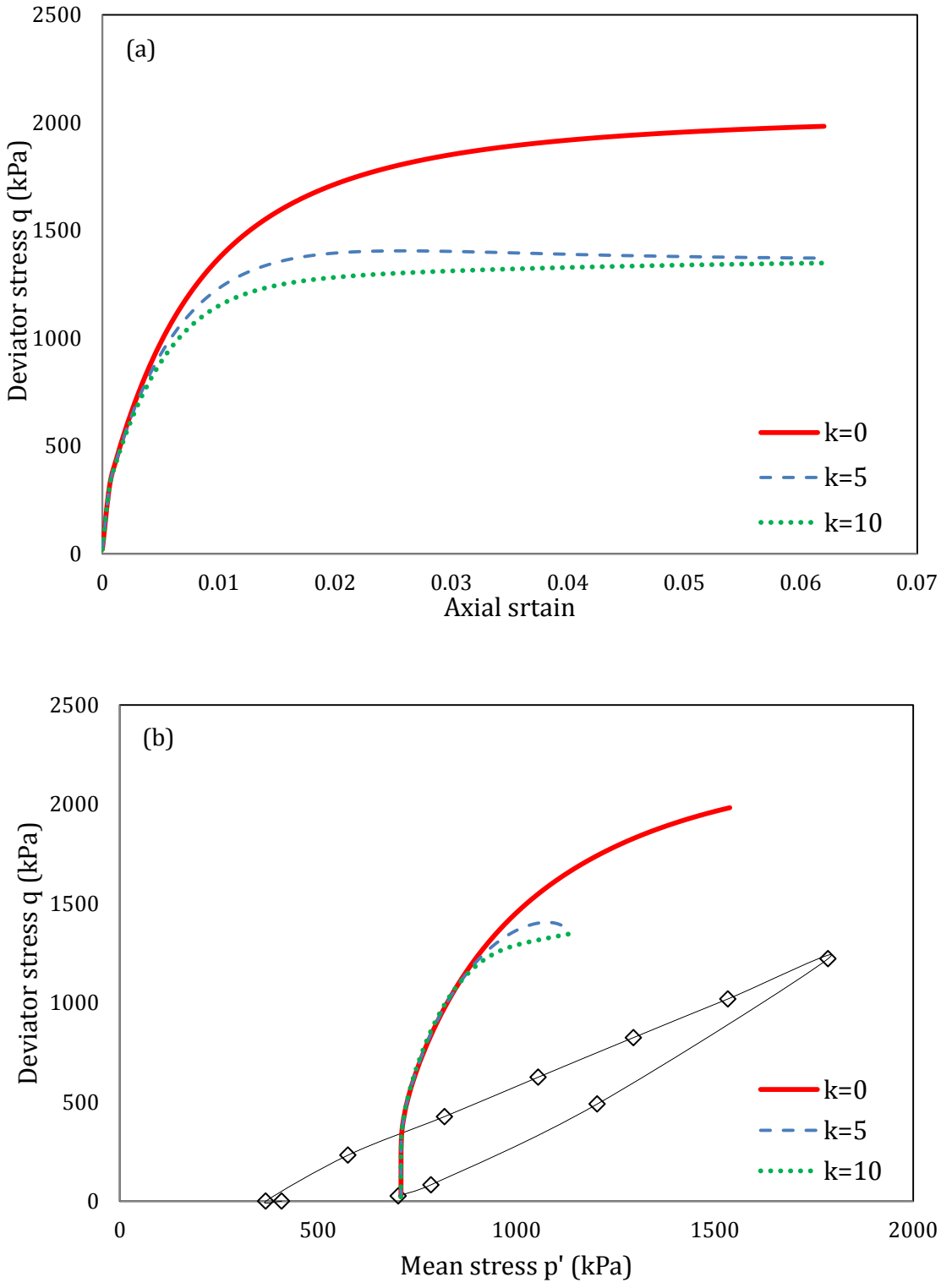

Figure 3.18: Influence of destructuration parameter *k*. (a) deviatoric stress versus axial strain and (b) effective stress paths in *p'-q* plane.

As can be seen in figure 3.18, a reduction of the value controlling the destructuration rate, *k* results in increased values of both stiffness and strength. This is attributed to the rate at which structure is lost with continuing strain and

hence smooth the peak somewhat, but also raises the peak because destructuration takes place more slowly.

Figures 319a and 3.19b illustrate the results from the sensitivity analysis on the scaling parameters in the destructuration law, *A.* Increasing A to 1, so that the destructuration is produced solely by distortional strain, slightly speeds the loss of structure because the undrained test is predominantly a distortional deformation. By setting the value of A equal to 0, the assumption that the destructuration process is completely governed by the volumetric component of the plastic strains is evoked. As it can be seen this assumption leads to higher values of peak and residual strengths, and the soil hardens rather that exhibiting any softening behaviour .

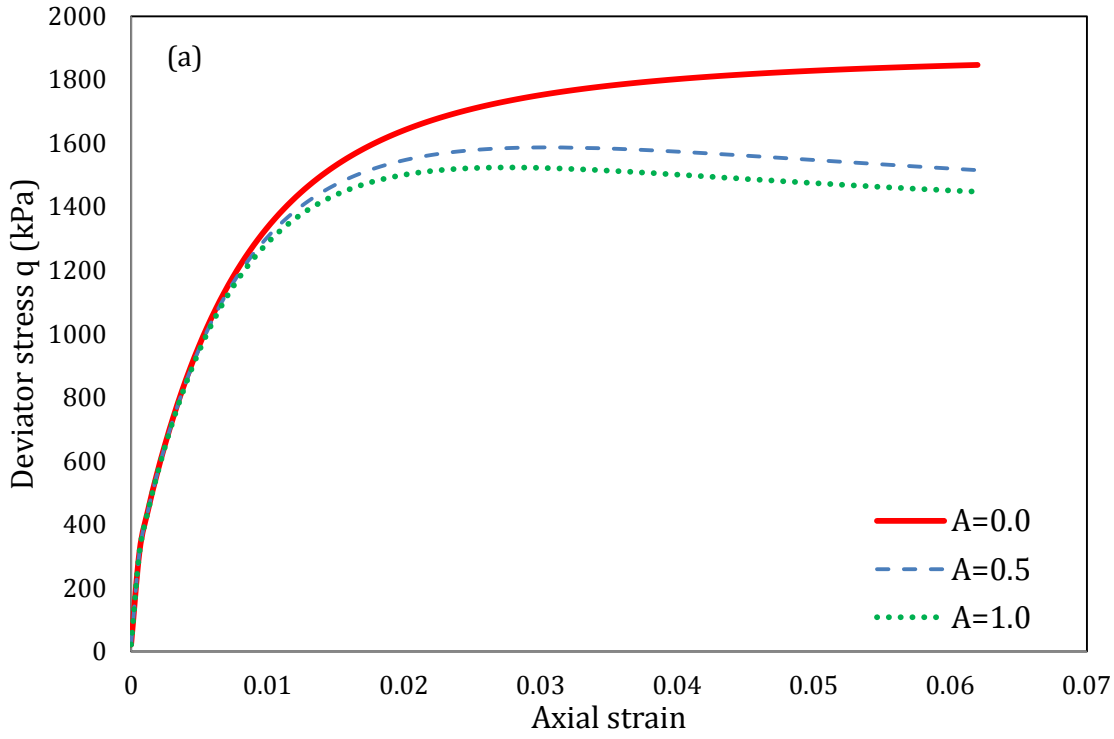

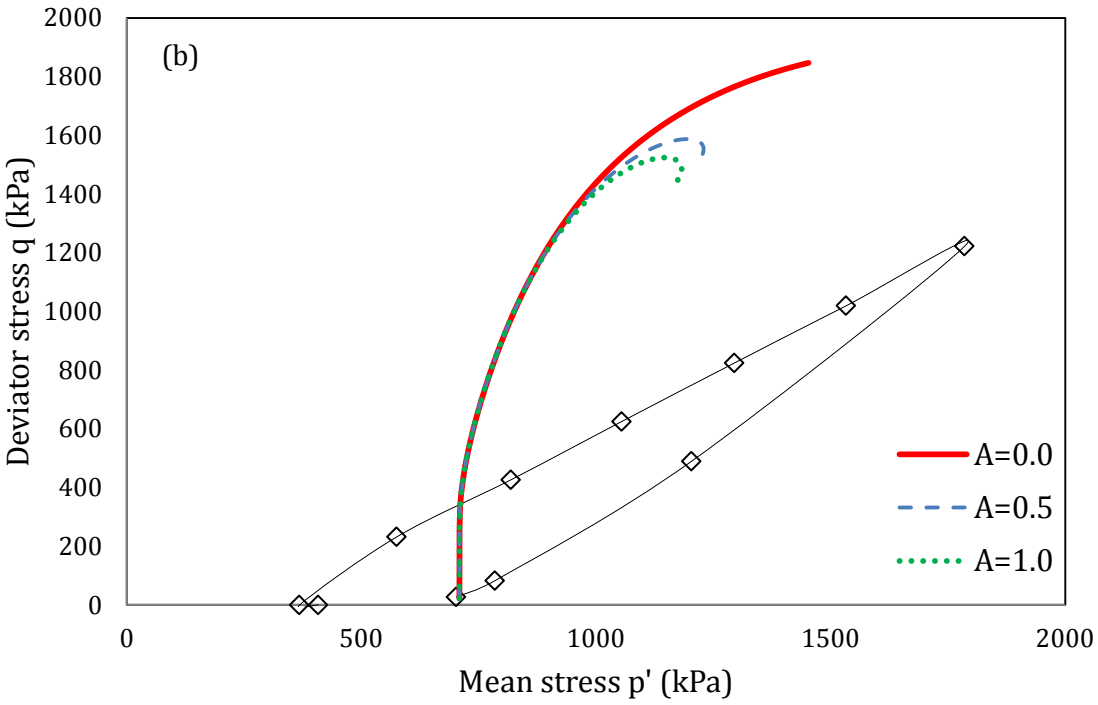

Figure 3.19: Influence of scaling parameter *A*. (a) deviatoric stress versus axial strain and (b) fffective stress paths in *p'-q* plane.

Parameter $\boldsymbol{\eta_0}$ controls the anisotropy of the structure surface. As it can be seen from figure 3.20, if the structure surface is assumed to be anisotropic i.e $\boldsymbol{\eta_0}$ >0 there is an increase in stiffness at small strains and strength (large strains). However with continuous mechanical loading the structure surface will collapse towards to remoulded surface and the same residual strength will be reached irrespectively of the initial value of $\boldsymbol{\eta_0}$.

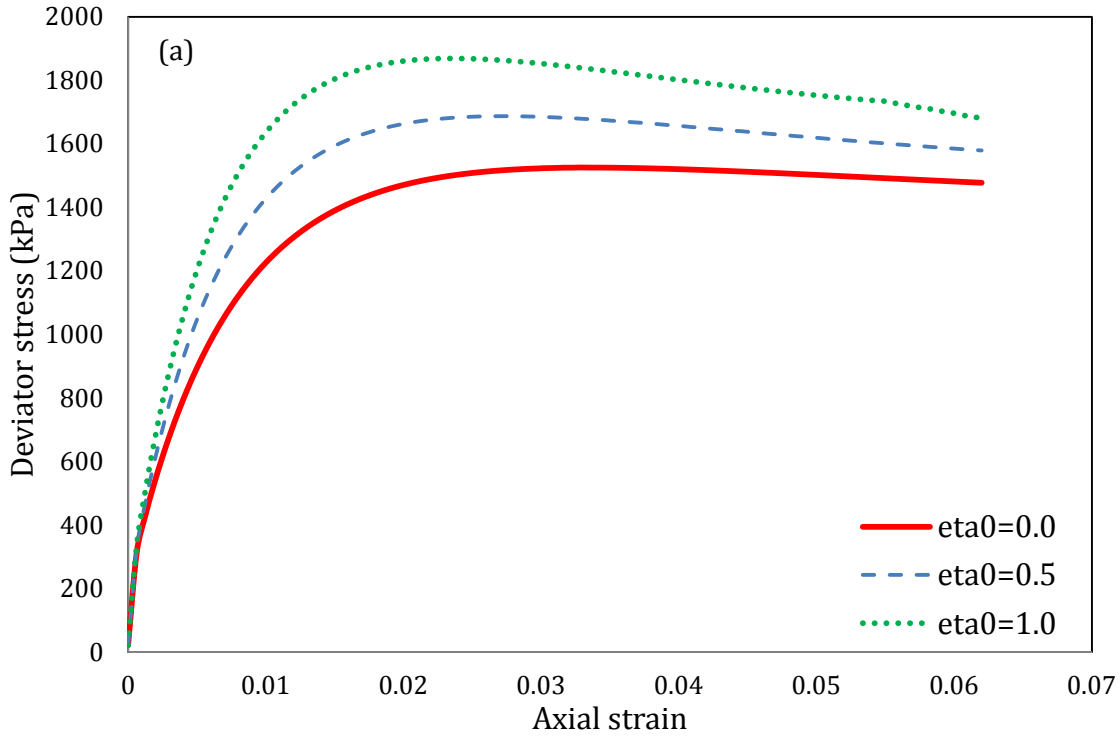

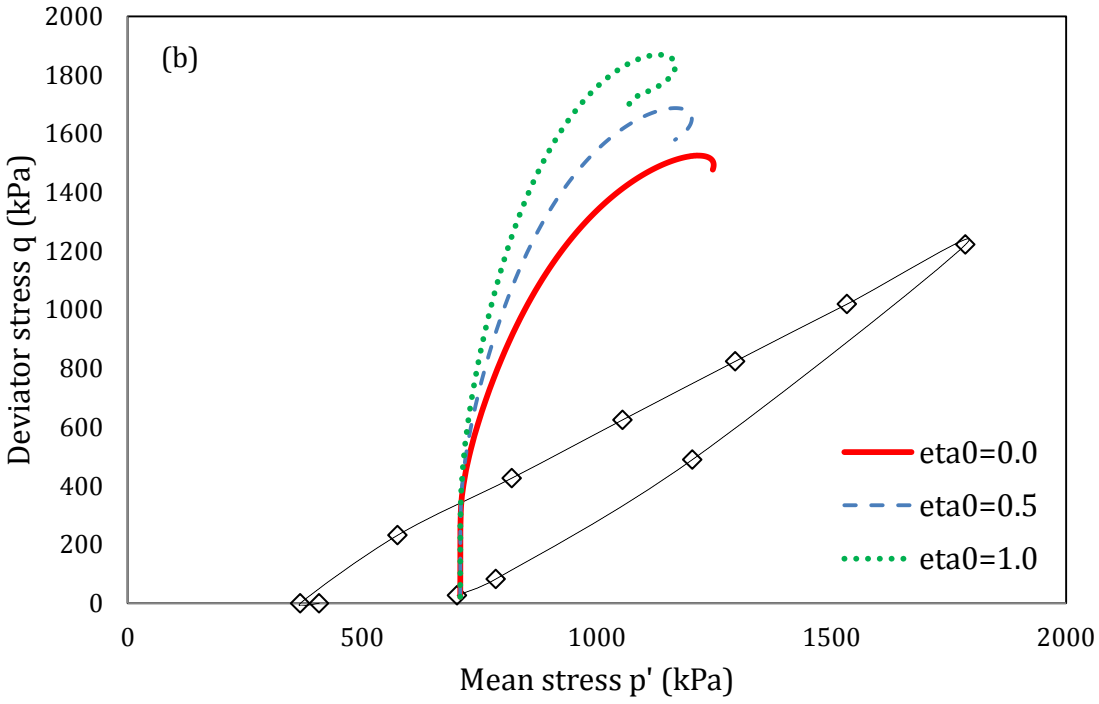

Figure 3.20: Influence of structure aisotropy $\boldsymbol{\eta_0}$. (a) deviatoric stress versus axial strain and (b) fffective stress paths in *p'-q* plane.

3.7.2 Kinematic hardening parameters

The results from the parametric analyses on the plastic modulus parameter *B* are shown in figure 3.21. The increase of parameter *B*, results in a higher peak in the stress-strain plot. It is observed that lower values of parameter *B*, (figure 3.22a and b) give rise to a softer response, although with continuous loading the three tests are expected to eventually attain the same residual strength.

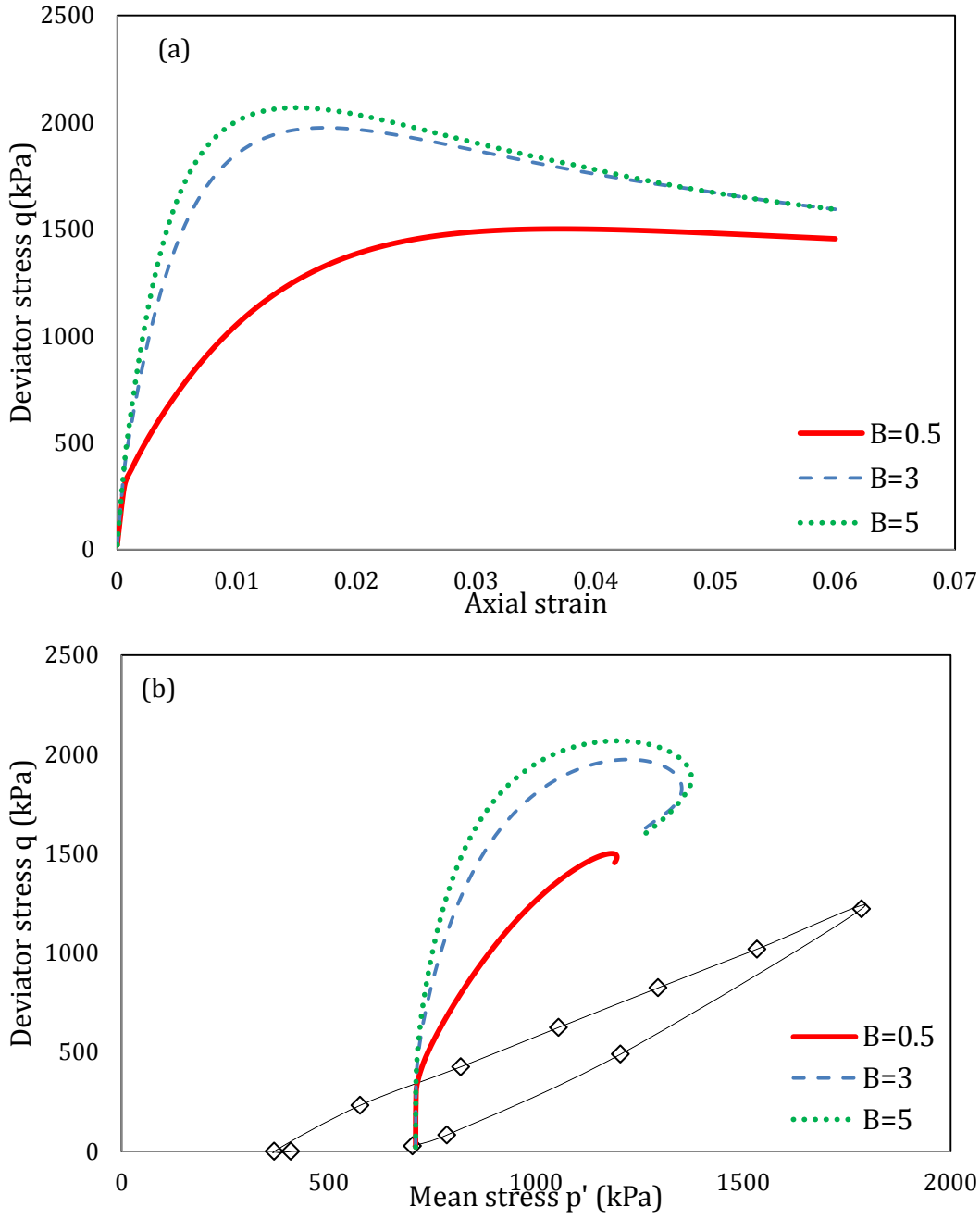

Figure 3.21: Influence of plastic modulus parameter *B*. (a) deviatoric stress versus axial strain and (b) fffective stress paths in *p'-q* plane.

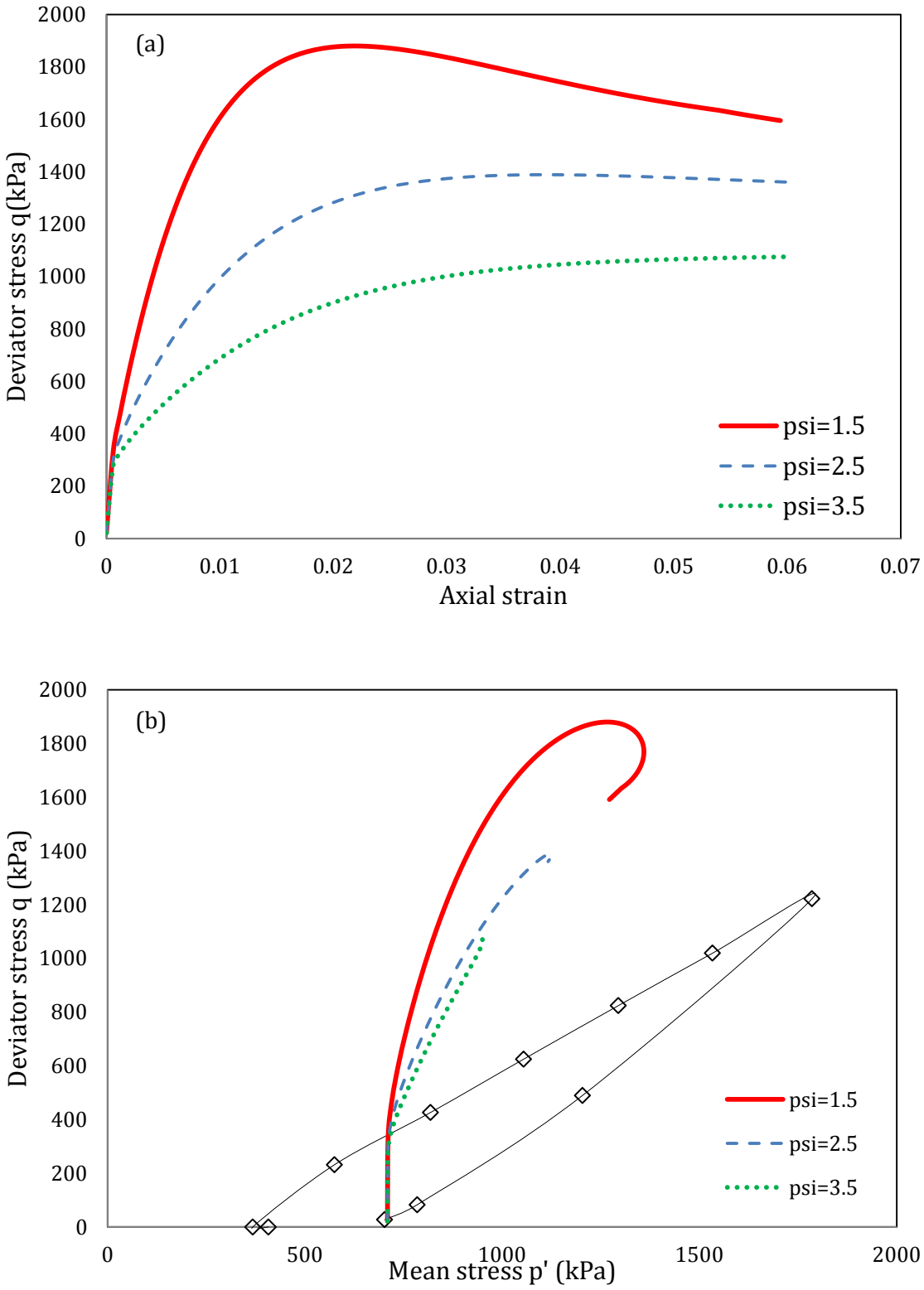

Figure 3.22: Influence of plastic modulus parameter ψ. (a) deviatoric stress versus axial strain and (b) fffective stress paths in *p'-q* plane.

The effect of the plastic modulus exponent ψ is shown in figure 3.22. It is observed that the plastic modulus and hence the behaviour under a triaxial test is considerably more sensitive to the variation of ψ, rather than parameter *B*. This is

attributed to the formulation of the plastic modulus (eq. 3.29), where the magnitude is controlled by the power function for ψ, compared to a linear relationship with B. Consequently, a higher value of ψ results in a softer behaviour, at both small and large strain regions, with a large variation on the residual strength. It should be noted that the stiffness interpolation exponent (ψ), is dependent on the distance of the current stress, to the conjugate point (*b in eq. 3.* 27), so as the bubble approaches the structure surface, a more rapid reduction is stiffness is obtained.

3.7.3 Influence of bubble size

Figures 3.23a and b illustrate the influence of the bubble size on the results from the triaxial tests. It is evident that the behaviour of the model is fairly sensitive to the variation of this parameter. Smaller values of the bubble size result in a more stiff behaviour in the small strain region, with higher peak and residual values of strength. This can be explained again by the formulation of the plastic modulus (eq. 3.29). The stiffness degradation is inversely proportionate to the size of the bubble, and although a smaller value of R indicates plastic strain develops sooner, the magnitude of the plastic modulus is higher.

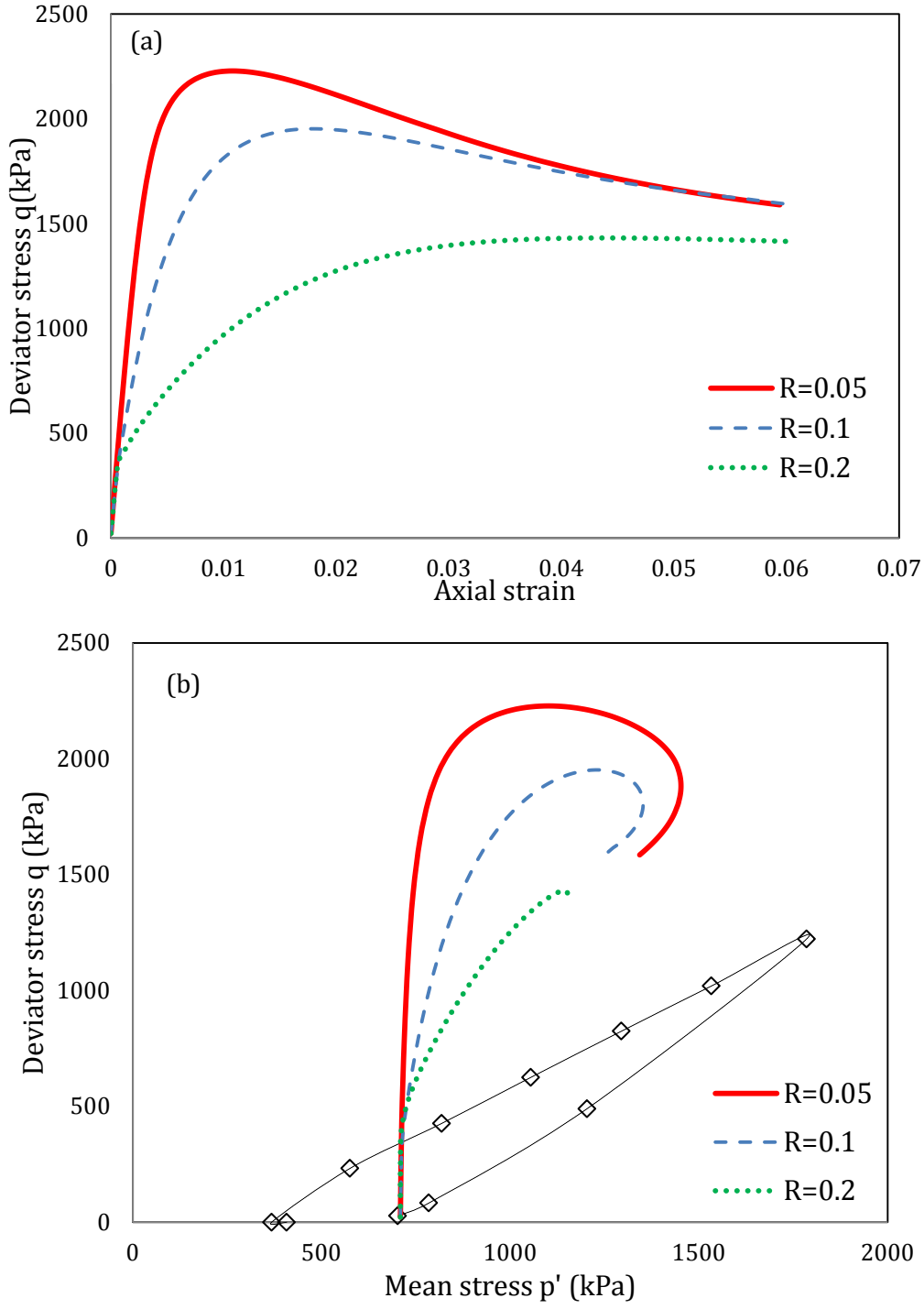

Figure 3.23: Influence of Bubble size *R*. (a) deviatoric stress versus axial strain and (b) fffective stress paths in *p'-q* plane.

3.7.4 Influence of elasticity model

The final section of the parametric analyses examined the influence of the elasticity law adopted in the simulations. The response of the proposed model, using Viggiani's formulation for elasticity has been explored. Comparisons are made between conventional elasticity, which is typically employed in Cam clay type models and varying parameters of the new elastic model. A constant Poisson's ratio of 0.2 was assumed for traditional elasticity. Figure 3.24a-c present the results from this sensitivity analysis. It is evident that the response is highly affected by the elasticity model. The introduction of Viggiani's formulation for elasticity produces an increase in the stiffness of the soil in the small strain region. Parameters A_g and n_g, are seen to have large bearing on the model's response at region small strain, with the ultimate strength remaining largely unaffected by the choice of the elastic model and the associated parameters. The response from variation of parameter m_g is almost negligible. It can be seen that the conventional elasticity law results in fairly low stiffness at small strains as it is shown in the shape of the stress-strain curves and only at strains <1% would show comparable stiffness values to the alternative elasticity formulation.

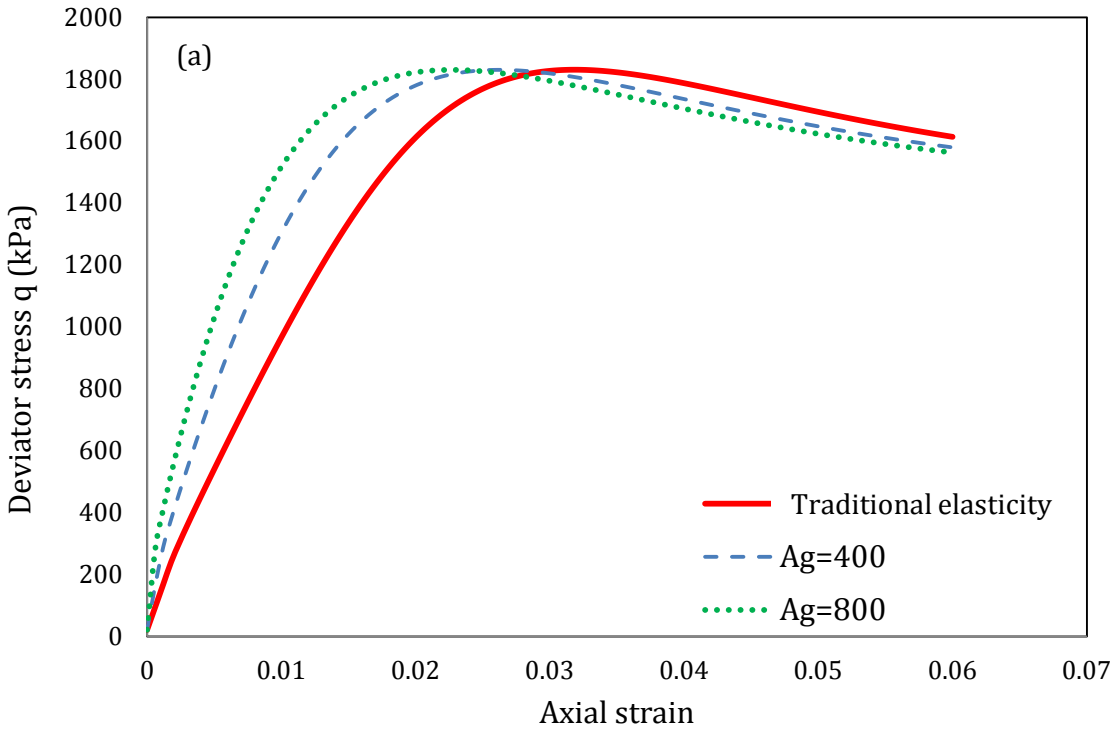

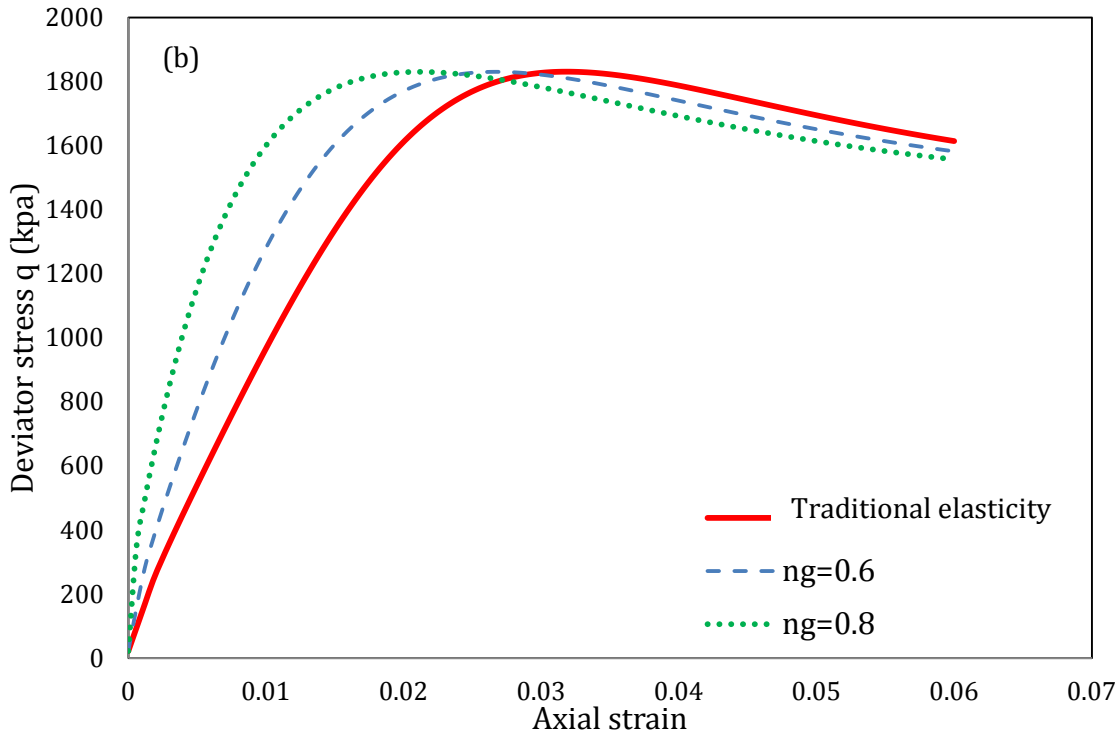

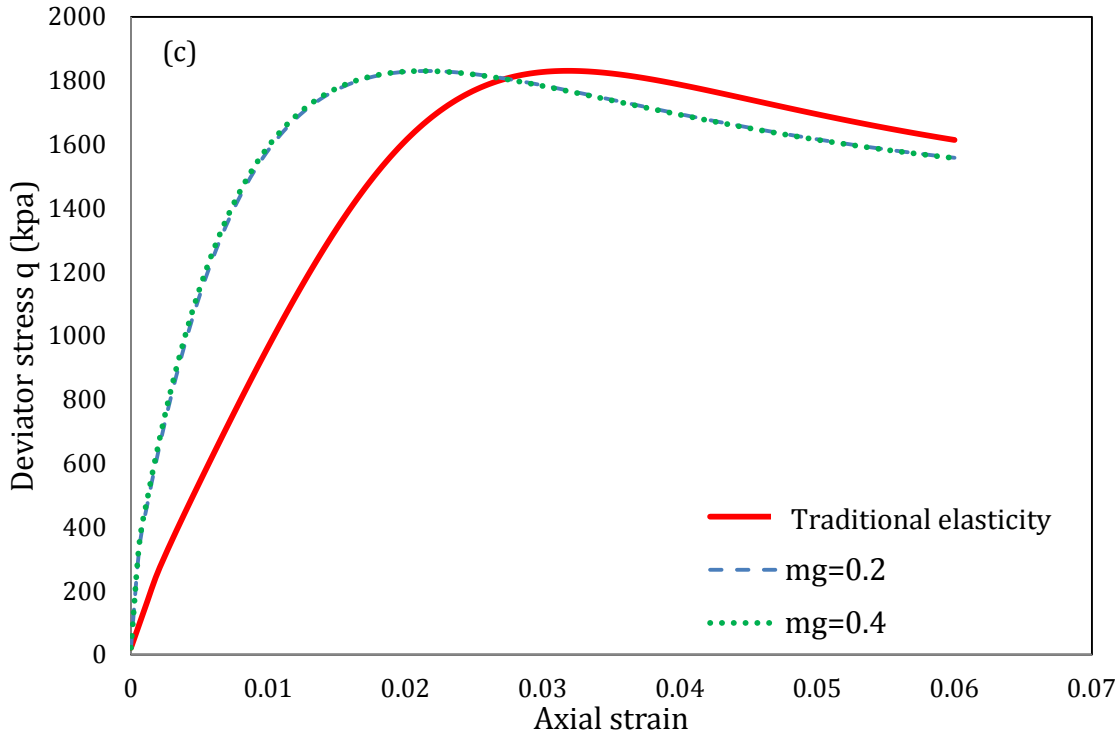

Figure 3.24: Influence of elasticity parameters for Viggiani's model: (a)A_g, (b)n_g and (c)m_g

3.8 Concluding remarks

The development and implementation of the KHSM (Rouainia & Muir Wood, 2000) model explores the hypothesis that the effects of structure in natural soils can be modelled through a simple, logical extension of an existing model for reconstituted, un-structured soil. The proposed model therefore converts the concept of natural and intrinsic behaviour as described by Burland (1990) into a full constitutive model. The existing model that has been used is Cam clay, but in a form already extended within the framework of kinematic hardening and bounding surface plasticity.

The model that was implemented for this study incorporates some modifications from the original formulation that were adopted in order to improve predictions of stiffness in the small strain region, by implementing two new elastic models in the formulation. The first one is based on the empirical relationship proposed by Viggiani & Atkinson (1995) which was based on results from bender element tests on reconstituted samples of a number of clays. The authors suggested that the small strain shear modulus, was depended on two variable terms, the mean effective stress, p', and the isotropic over-consolidation ratio R_o. The second elastic model that was implemented originated from the suggestion by Houlsby *et al,* (2005), that the simple models that were developed in order to simulate this nonlinearity violated the laws of thermodynamics. They were able to derive the elastic behaviour from a free energy potential, which consequently lead to a thermodynamically acceptable elasticity model.

The constitutive model was formulated in general stress space in order to make the implementation into the code possible. The implementations procedure for the commercial package Plaxis was explained in the second part of the chapter. The anisotropic formulation of the KHSM model allowed for different shapes for the yield and plastic potential surfaces to be assumed in the deviatoric plane.

Validation of the proposed model was conducted in the final section of this chapter. The predicted response of the model has been demonstrated through simulations on a single element finite element analysis of a number of different undrained triaxial compression tests on stiff clay from the outskirts of Rome.
It was shown that the model can successfully capture the general trend in terms of stress path and peak strength observed in laboratory experiments.

A general indication of the influences of the key soil parameters of the model, on the response in the conventional undrained triaxial compression test from which the reference parameters were deduced was conducted in the parametric analysis section. Such a study provides assistance in the search for the optimum set of parameters to match any given set of experimental observations.

Chapter 4: Finite element analysis of self-boring pressuremeter tests in structured clay

The geotechnical engineering community has always had strong interest in the continuous improvement of in situ testing methods in order to obtain more accurate results. This was in recognition of the fact that, for many soils, obtaining an undisturbed sample for conventional laboratory testing is very difficult at best. The self-boring pressuremeter (SBPM) is especially valuable for the determination of soil properties for sensitive and/or soft cohesive soils due to its significantly reduced soil disturbance. This chapter presents the simulation of self-boring pressuremeter (SBPM) tests in London clay. The reported initial conditions on site were validated through modelling of the geological history of the London Clay deposit. The hypothesis of disturbance of the mechanical state of the surrounding soil during the installation process was investigated in order to understand the mechanism of the disturbance effects and their influence on the subsequent pressuremeter test results.

4.1 Introduction

The purpose of geotechnical site investigations is to establish the definitive estimates of engineering soil properties, which are imperative for use in engineering design. This is achieved by amalgamating the results from the laboratory and *in-situ* tests carried out as part of the site investigation programme.

Geotechnical tests in the laboratory may take several forms, extending from the simplest index tests, which are typically carried out on disturbed samples, to state-of-the-art experiments on undisturbed samples. The high quality samples are typically obtained using advanced sampling techniques. The drawback of using cutting-edge apparatus and the techniques associated with them is that they are typically laborious, time consuming and command a hefty price.

The achievement of a pristinely undisturbed soil specimen is usually very challenging, therefore the influence of sampling disturbance almost inevitably leads to erroneous assessments of the engineering soil parameters. In addition, the laboratory testing methods are constrained in utilising specimens which do not accurately reflect the overall mechanical behaviour at large scale. Large scale elements which are missed contain the influence of macrostructure, which is frequently challenging to specify. The above inadequacies of laboratory testing methods added to the ever-increasing need of composing ideas for in-situ testing. This type of tests may prove beneficial due to the following:

- They permit the assessment of engineering properties at locations where the sampling process is, at best, challenging

- The influence of sampling disturbance is addressed to a large extent, since engineering properties are derived from the soil's natural state

- They address the issue of scale, given that the tests reflect the magnitude of applied stresses within an appropriate the soil volume

Natural soils are well known to exhibit anisotropy as a result of the geological processed involved during their sedimentation as well as consolidation, driven by gravity. This initial measure of structure is a product of the electro-chemical processes occurring with time. It is well established that it has significant consequences on the resultant mechanical behaviour of natural soils. Experimental observations have indicated that as a specimen of natural clay is subjected to deformations, the initial structure is progressively degraded and eventually the soil is transformed into a fully remoulded material. A typical example of the effects induced by initial structure is the extreme sensitivity of Scandinavian quick clays. In contrast, reconstituted clays that are prepared in the laboratory do not usually exhibit any effects induced by cementation or inter-particle bonding, however they may potentially show attributes of anisotropy, ensuing from an anisotropic consolidation process.

Soft clays are an extreme example as the loading process beyond yield may cause breakdown of the insitu measure of structure (Mitchell, 1976; Callisto & Calabresi, 1998; Smith et al., 1992). Mitchell (1976) coined the term 'structure' as an amalgamation of the effect of the soil fabric (the arrangement of the particles), and the bonding between these particles. Compelling evidence of the presence of initial structure can be found in the results of oedometer tests conducted on natural and reconstituted, sometimes referred to as *'sedimented'* samples, by Leroueil & Vaughan (1990). Structure is not limited to clay soils, but has similar effects on other natural materials. The influences on clay shales and weak mudstone are similar to those present in overconsolidated clay samples. Ohtsuki et al. (1981) carried out work on weak Japanese volcanic mudstone subjected to triaxial and isotropic compression. His findings indicated that the volcanic mudstone exhibited comparable behaviour to that of the soft clay studied by Tavenas and Leroueil (1990).

A prime example of the development of in-situ testing methods is the Self Boring Pressuremeter Test (SBPM). This test was designed to measure engineering properties of the ground *in situ*. The relatively small amount of disturbance created (zero disturbance theoretically following perfect installation) through the use of the SBPM allowed for the reliable determination of *in situ* horizontal stress, shear strength, stress-strain behaviour, and, in some cases, coefficient of consolidation with minimum disturbance of the surrounding soil. The tool was developed to address the disturbance involved in sample retrieval methods, such as push samplers and corers which influenced the characteristics of the material being sampled as covered previously.

The following section aims to provide s description of the self-boring process:

A rotating cutter is positioned within the tapered shoe, which is attached at the tip of the instrument. As the instrument is forced steadily against the soil at the end of the borehole, a core of the soil is moves into the taper, similar to an open ended pile. The top of this extracted core is sheared by the cutter in order to equate the pressure required to push the soil up the instrument tube to the insitu vertical stress. The remaining soil spoils are transported from instrument tube by means of a flushing liquid, which typically water fed from the ground surface. The flushing fluid does not typically influence the properties of the surrounding soil, since it circulates in a close circuit.

An important feature of pressuremeter testing that has proven advantageous from a geotechnical design perspective is the fact that the test can capture the entire ground response curve. This is a significant feature, since it portrays the non-linear nature of the soil's stiffness. It should be noted that few other tests can produce this non-linear stiffness profiles (downhole plate tests and consolidated triaxial tests in which local strains are measured). The importance of being able to measure non-linear stiffness is increasing with improvements and availability of numerical methods and advancements in soil constitutive models.

4.2 The history of self-boring pressuremeters

The first patented pressuremeter was used in Chicago by Louis Menard and known as the Menard Pressuremeter (Menard, 1957), a form of pre-bored pressuremeter (PBP), as the testing area was pre-drilled prior to the insertion of the instrument. The installation process for PBP systems was causing concern to Menard, as disturbance originating from the drilling process was found to influence the insitu soil conditions and therefore measurement taken could not be interpreted by means of the conventional cavity expansion theory. Following Menards' hypothesis that soil disturbance adversely affected readings taken from the ground using PBP systems, the notion of the self-boring pressuremeter (SBPM) was firstly proposed by Jézéquel *et al.* (1968). The comparatively small amount of disturbance resulting from the use of the SBPM permitted the consistent evaluation of *in situ* horizontal stress in the ground for the first time. Wroth and Hughes (1973) validated these beliefs when they stated that the true *insitu* stresses were key to understanding soil behaviour.

Developed simultaneously in France (Baguelin et al. 1972) and in the UK (Wroth & Hughes, 1973), the SBPM comprises of a thin wall at the lead tip with the aim of minimising soil disturbance as it is advanced through the soil. As the SBPM is progresses through the soil, spoils are guided into the shoe by the chamfered angle of the lead edge and consequently trimed by the cutting head, and extracted up within the probe by the drilling fluid, which can then be recycled, a method standardised by Wroth & Hughes (1973), as shown in Figure 4.1.

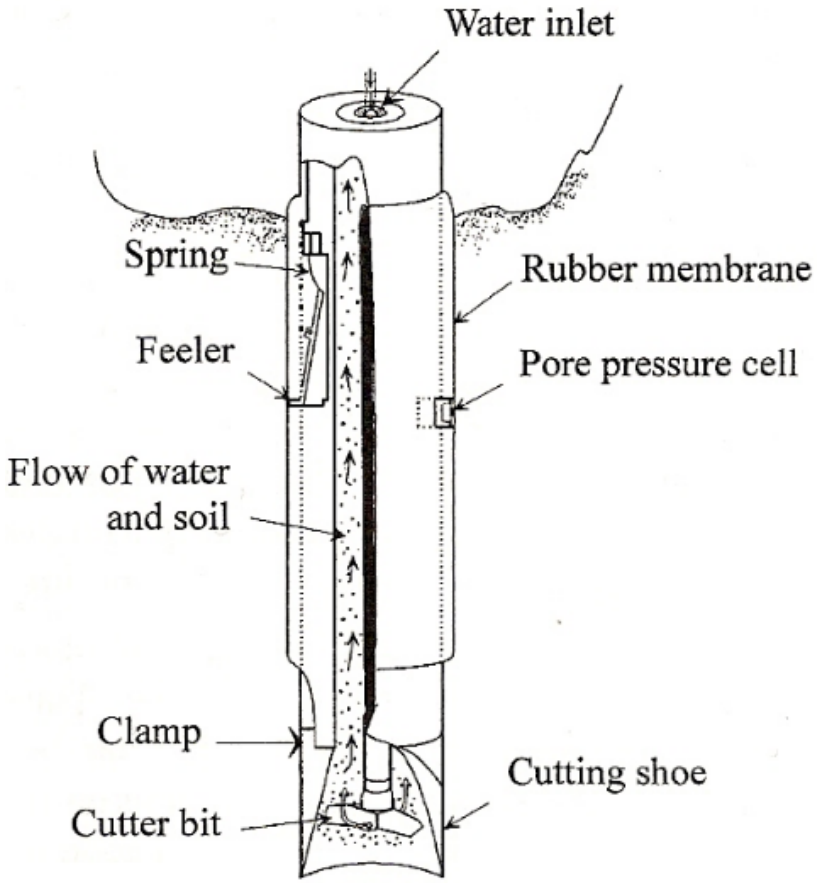

Figure 4.1: The features of the self boring pressuremeter.

Figure 4.2: The SBPM, showing the cutting shoe (A), the inflatable membrane (B), crossover (C) and umbilical (D). Source: Adapted courtesy of *CAM-INSITU.*

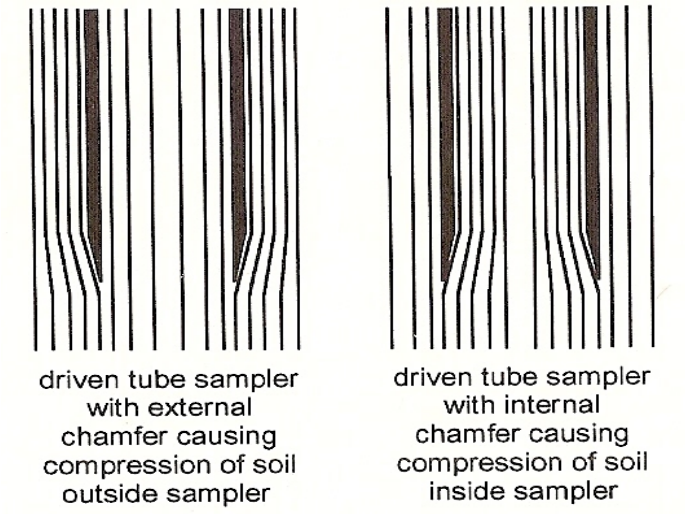

Figure 4.3: Sample edges similar to the leading edge of the SBPM. From Clarke (1995)

Figure 4.3 depicts a sampler with similar edges to that of the SBPM. Rather than using a chamfer on the outside of the probe which could result in significant disturbance to the soil on the outside, (figure on the left) , the chamfer is located internally, minimising the disturbance to the surrounding soil, thus, improving results.

Practically, careful consideration of these elements is required, otherwise the result might be that soil is either forcibly displaced by the thrust of the system or alternatively washed away due to excess flow. In addition common observations of blockages resulting from incorrect installation procedure have also been reported. Analytical analysis of the installation procedure was conducted by Whittle and Aubeny (1993).

4.2.1 The Pressuremeter Curve

As the membrane is inflated, the pressure to perform the inflation is measured, and the displacement, the distance from the original origin of the membrane and the new distance is measured. It is then standard procedure to convert this measured displacement into cavity strain. As the pressure, p, is increased in the cavity to p_{max}, the maximum displacement of a_{max} is reached, before unloading. Here, σ_h, the *insitu* horizontal stress is given as the starting point of cavity expansion, as the ideal conditions have been assumed.

Wroth (1982) noted that the main use of the SBPM was to calculate soil stiffness. During the test, a series of unload/reload loops are performed. At these points, clearly visible in Figure 5, a reading of shear modulus can be taken from the gradient of the loops. Two unload-reload loops are achieved in this example, highlighting hysteresis within the soil. The loops are created twice for continuity, and conducted away from the starting point of inflation, so not to be affected by any disturbance that may have occurred during installation.

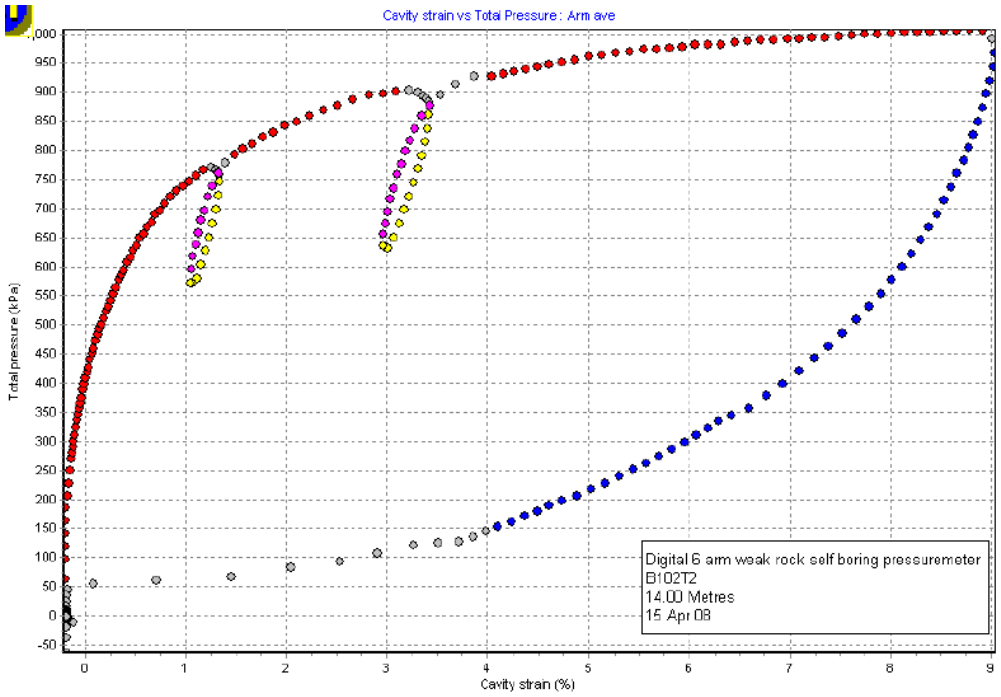

Figure 4.4: A SBPM curve generated from tests in London Clay, showing Cavity Strain (%) on the *x* axis and Total Pressure (kPa) on the *y* axis

4.2.2 Other types of Pressuremeter

Other types of pressuremeter have different installation methods. The pre-bored pressuremeter (PBP) which is mainly used in rock requires the creation of a test pocket via core drilling and disturbance to the surrounding material is expectedly high. The push in pressuremeter (PIP), most commonly attached behind a geotechnical cone probe, is forcibly pushed into the material, normally sands and soft clays, by hydraulic rams with a large counter reaction. Once the pressuremeter is in the required position in the ground, the cylindrical membrane is inflated with nitrogen gas or sometimes deionised water. During this time, radial feeler arms measure the displacement of the membrane. The test, inflation of the membrane and recorded displacement, should by conducted immediately following the creation of the test pocket. The key parameters determined from the test are: shear strength, shear modulus, consolidation characteristics and *insitu* horizontal stress.

It should be noted that the application of the SBPM as a well established site investigation tool, is not only limited to clays and sands (Yu, 2004). Tests have also been conducted in glacial ice (Puswewala et al, 1992) and weak rock (Clarke and Smith, 1992). Other types of pressuremeters are available for different materials and applications.

The cone pressuremeter, a device which if forcibly pushed into the ground via hydraulic rams, known as a push-in pressuremeter (PIP), was analysed by Houlsby & Withers (1988) shortly after its conception and adopted use. Problems arose due to the cavity creation technique used and the subsequent methods for calculation and determining parameters. Complex logarithms were required for the determination of horizontal stress, which needed to be adapted for differing ground conditions, making the system awkward and specialised. Similar problems were encountered with the pre-bored pressuremeters (PBPM) used in rock.

The *insitu* total horizontal stress, $\sigma_{h,}$ is challenging to define in the PIP test since during installation and the subsequent densification of the surrounding material, additional stresses acts upon the membrane, which are greater that the lateral stresses present in the ground. The initial pressure applied is therefore significantly greater than the true horizontal stress, and this means that a reference point is often not available for the generation of true values.

With the PBP, the pressure is increased until first it equals the drilling mud pressure, then again to compensate for membrane stiffness, until it reaches the test pocket wall, denoted by p_0. This cannot be said to be equal to $\sigma_{h,}$ since the drilling process has unloaded the rock; a reduction in horizontal stress. In both the PIP and the PBP, the identification of σ_h is difficult as neither test gives suitable datum points from which to obtain reliable results.

The SBPM test's distinctive feature is that test borehole is of the equal diameter to the inflatable membrane itself, and therefore as the tool is penetrated into the soil; it prohibits any unloading from occurring. However, a number of researchers have indicated that a comparison between measurements from pressuremeter tests and insitu and laboratory results exhibit a certain amount of discrepancies. Baguelin *et al.* (1972) presented results which indicate a 55 increase in soil strength determined by the pressuremeter when compared to measurement of in-situ vane strength of Saint-Andre-de-Cubzak clay.

These discrepancies are believed to be a result of a number of factors. Inaccurate reconsolidation of soil specimens and therefore incorrect initial stress state is thought to be the main reason for laboratory tests. Moreover other in-situ testing methods result in significantly increased soil disturbance. In addition to the above, the engineering community has tried to rationalise the discrepancies from the opposite side of the SBPM. A significant amount of research has been conducted, with the aim of exploring on the following topics:

- Effects of soil disturbance during installation
- Influence of unclear drainage conditions
- Effect strain rate during SBPM testing
- Dimensional investigation of SBPM probe
- Effect of various shearing modes encountered during an SBPM test

It is widely accepted that pressuremeter testing in clay soils takes place under undrained conditions; however a certain degree of consolidation is likely to occur and therefore the soil behaviour is unmistakeably time-dependent. This particular topic was investigated by Anderson *et al* (1987) who assessed the effect of time by means of experimental work and numerical investigation on the resulting parameters.. The research work of Fahey and Randolph (1984) comprised of a number of self-boring pressuremeter tests in sand employing various cutting shoe and cutter geometries to examine the resulting parameters. Their work led to them to the conclusion that resultant friction and dilation angles were significantly influenced by soil disturbance. The authors went on to recommence correction factors to take account of the disturbance. Another topic that was investigated by Aubeny *et al* (2000) was the influence of various extraction ratios bore on the resulting SBPM parameters

Silvestri (2004) investigated the disturbance effects due to drilling errors employing the conventional cavity expansion theory. In particular he examined the consequences of two distinct cases:

- Disturbance due to under-drilling: Results indicated that in this incident the derived undrained shear resistance was underestimated, however the extent of this error was not easily quantified

- Disturbance due to over-drilling: In this case the swelling of soil was exhibited. On resumption of loading the stress-strain line returned to the intact pressuremeter test curve. A comparison between the reloading portion of the loading curve and the virgin intact curve, indicated up to 100% overestimation of the undrained shear strength

A numerical investigation founded on based on the premise that there is a remoulded annulus was carried out by Prapaharan *et al* (1990). This study extended the work of Baguelin *et al* (1978), who ascertained that, a reduced modulus and strength is is existence around the SBP probe. In addition, Prapaharan *et al.*, considered that the swelling of the surrounding soil occurs during equipment installation, something that was first proposed by Eden and Law (1980). The 1990 study concluded that the alleged remoulded annulus alluded to an erroneous increase of undrained shear strength in the order of 15% and conversely a decrease of the shear modulus by as much as 40%.

4.3 Numerical model

The fundamental assumption that the pressuremeter problem can be simulated as the expansion of an infinitely long, cylindrical cavity, has been employed (Collins and Yu, 1996). This essentially reduces the problem to one dimension since any movement of the membrane will occur in the radial plane. Conditions of plane strain have been adopted in the vertical direction. In order to avoid the influence of the external boundaries, the geometry was extended 30 times the initial cavity (Zentar et al. 1998). All boundaries were deemed to be impermeable, with the fully saturated soil having an isotropic permeability of 10^{-9} m/s. This procedure was successfully used by Gonzalez et al. (2009) during a numerical study on pressuremeter tests in clay.

The axisymmetric model adopted in the software package Plaxis, to model the idealised geometry of the self-boring pressuremeter, was constructed with approximately 110, 15-noded triangular elements, in order to avoid mesh-dependent results (Sloan and Randolph, 1982). The mesh adopted for this study can be seen in Figure 4.5. The initial horizontal stress and pore-water pressure at each depth were read from the SBPM curve at lift-off. The vertical stress was computed from the corresponding depth and the unit weight of London clay.

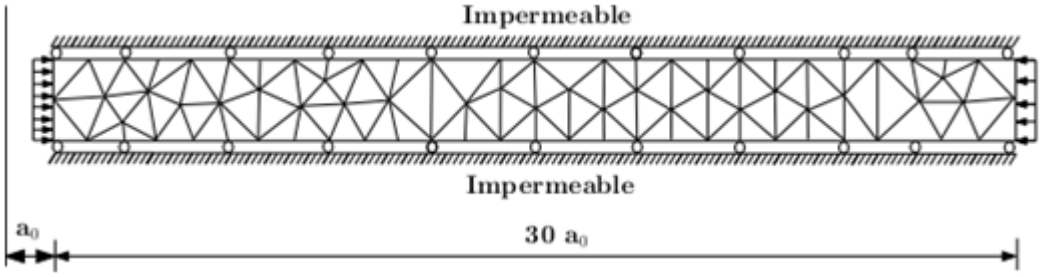

Figure 4.5: Finite element geometry

4.3.1 Validation of numerical model

In order to ensure that the methodology employed in this study would yield the correct response, the numerical model results were corroborated against the well known analytical results presented by Collins and Yu (1996) and Yu and Collins (1998). In those studies the authors presented their findings for critical state unstructured soils. The Rouainia Muir Wood constitutive model (KHSM) employed in this paper is able to collapse to Cam clay by making the size of the bubble, which is the kinematically hardening yield surface for the material, equal to that of the outer surface, which has the same function as the Cam-clay yield surface. The present model is deliberately designed in such a way that it can be made to degenerate to the bubble model (Al Tabbaa and Muir Wood, 1989) and thence to Cam clay (Roscoe and Burland, 1968) by the appropriate selection of soil parameters.

The parameters used for this validation exercise were chosen to simulate the modified Cam clay ellipse. The bubble which represents the elastic behaviour domain of the soil is controlled by parameter R and was set to 1 so that it is equal to that of the outer surface. The degree of initial structure r_0 was also set to 1 so that the KHSM model simulates the behaviour of un-bonded soils.

λ^*	κ^*	M	R	r_0	φ	ν
0.0805	0.031	0.888	1	1	22.75	0.3

Table 4.1: Soil parameters adopted in the validation simulations. (Collins and Yu, 1996)

An isotropic initial stress state was adopted with $\sigma'_r = \sigma'_\theta = \sigma'_z = 170.8$ kPa, with the pore pressures assumed to be zero, so that the effective and total pressures coincide at the start of the test. Four tests were simulated with varying degrees of isotropic overconsolidation (OCR=1, 4, 15, 30, 50). The self-boring pressuremeter membrane was expanded to double the size of the initial cavity ($a/a_0=2$) and the values of the excess pore pressures were documented at that point. The values of the excess pore pressures were normalised by the theoretical triaxial undrained shear strength of the soils, which correlates to the soils properties through the following equations:

$$S_u = \frac{Mp'_0}{2}\left(\frac{OCR}{2}\right)^{\Lambda} \qquad \Lambda = 1 - \frac{\kappa^*}{\lambda^*}$$

As it can be seen in Figure 4.6, the magnitude of the predicted excess pore pressures is in agreement with the analytical results, predicting similar magnitudes of limit pore pressures as the modified cam clay, with the normalised pore pressure becoming negative for an OCR value higher than 30. Similar observations were reported by Collins and Yu (1996).

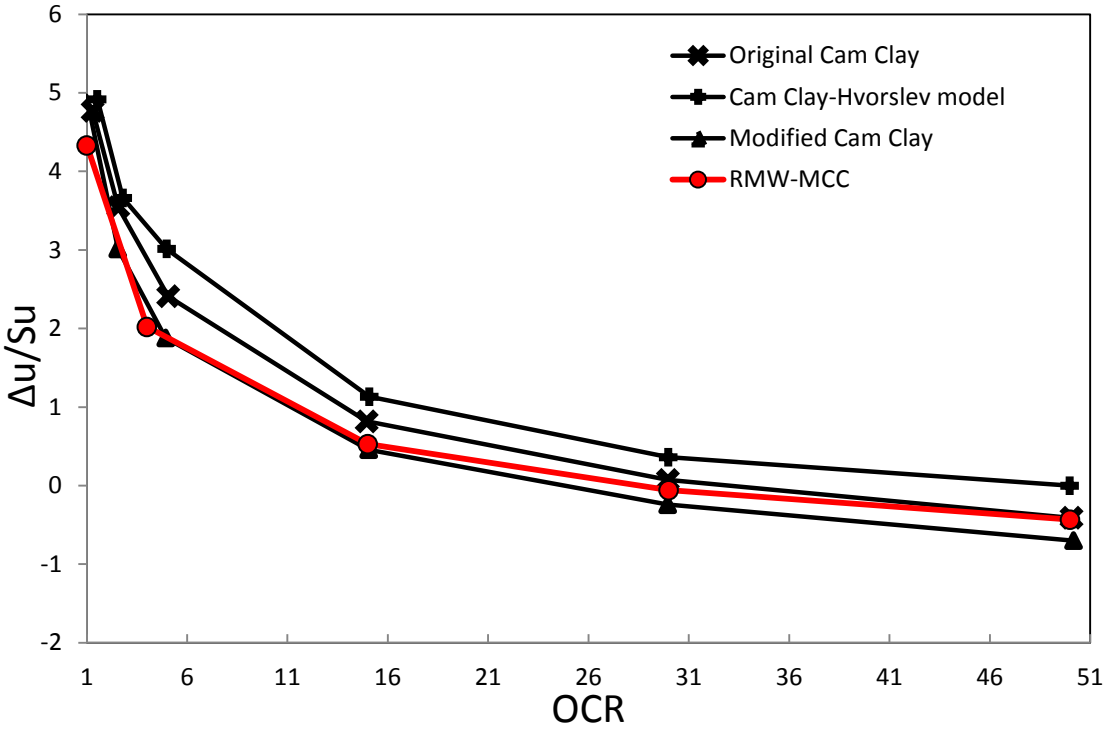

Figure 4.6: Comparison of normalised excess pore pressures for various OCR values between numerical simulations of the collapsed KHSM model and analytical results from Collins and Yu (1996)

4.4 Structure evidence in London clay

London clay is typically described as very stiff and heavily consolidated, fissured clay. It is believed to have been formed within a marine depositional environment approximately 30 million years ago within the Eocene era. London Clay contains an array of marine silty clays, layered with clayey and sandy silts, as well as subordinate sands (Standing & Burland, 2006). King, (1981) ascertained that the London Clay formation may be classified in five principal units, termed A to E with E being at the top. He arrived at this conclusion based on a review of biostratigraphy and lithological variation of the deposit. It is widely believed that in the best part of the greater London area, the lower part of this lithological arrangement is prevalent (units C to A)

Gasparre et al. (2007) tested natural samples of London Clay together with reconstituted samples taken during the construction of Heathrow Airport Terminal 5. They concluded that the state boundary line, when plotted was significantly higher for natural clays than reconstituted samples. This was seen to be a confirmation of structure existence, following the deposition and burial of the London clay formation. Furthermore it was recognized that the nature and structure of the London clay formation have a considerable influence on the compression behaviour of the soil.

The reconstituted state of T5 samples meant that all parameters derived as a result of testing would demonstrate the intrinsic properties of London clay. Another observation that was highlighted in this study was that although the intrinsic compression lines differed from lithological unit to unit, the slopes corresponding to normal compression and swelling were virtually undistinguishable. The authors went even further to state that all the geological units had a comparable distance between the ICL and critical state lines. This observation was valid for both one dimensional and triaxial testing.

The comparison of the results from oedometer tests on natural and reconstituted samples revealed the general trend of the natural compression curves surpassing the intrinsic compression lines and higher stress yield points. This observation

was a clear indication of the effect of the initial structure of London clay. It was noted that the measure of initial structure was more or less consistent throughout all the samples regardless of depth. A further point for discussion was the fact that the virgin compression lines did not degrade towards intrinsic values even when experiencing very large strains associated with high stress.

During their work, Gasparre and Coop (2008) established three distinct classes of structure evaluated based on results from oedometer tests, which are summarised below:

- **Class I-Stress Sensitivity**: This is characterised as the ratio of the yield stress of the natural material to the vertical stress on the Intrinsic Compression Line at the same void ratio (see Figure 4.7).
- **Class II-Yield Stress Ratio (YSR):** According to Burland (1990) this feature denotes the magnitude of stress beyond which large volumetric deformations can be seen
- **Class III-Swell Sensitivity:** This can be described as the ratio between the intrinsic and intact swelling indices.

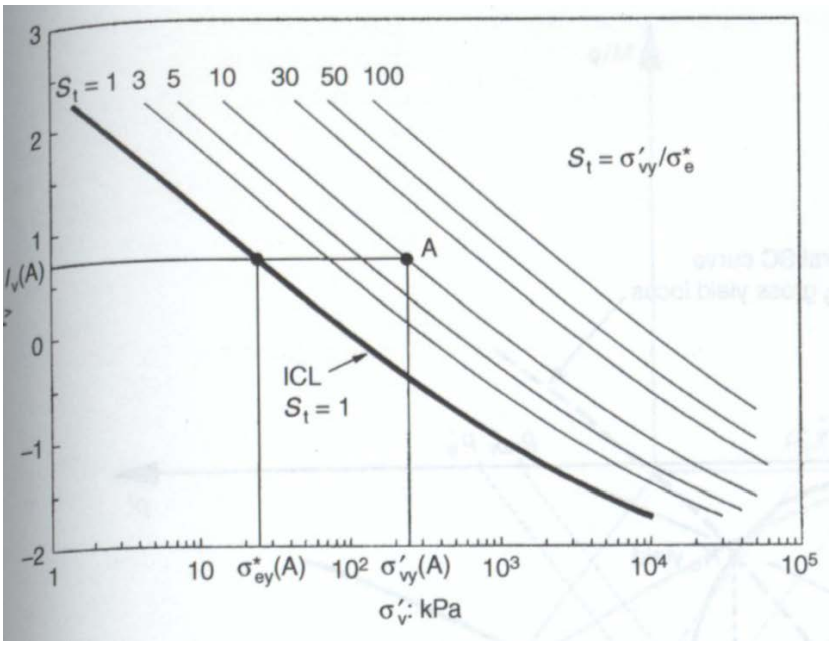

Figure 4.7: Definition of Yield Stress Ratio (Cottechia and Chandler, 2000)

The author's effort to quantify a definitive yield stress range was unsuccessful since the *YSR* values were quite varied and therefore were not deemed to be reliable. This was in contrast to the estimated stress sensitivity values, since these fell in a much narrower band and were less sensitive to disparity with depth and thus providing a more reliable estimation of the initial structure. However some reservations existed about the quantification of initial structure through this method, since the curvature of the ICL, as reported by Burland (1990), could potentially adversely influence the results. The values of the swelling sensitivity were assumed to present a more truthful portrayal of the degree of structure for London clay, given that the results from oedometers carried out corresponded to stresses that were very close to the insitu stress state. A summary of the sensitivity profiles with depth are shown in figure 4.8, for the average stress sensitivity and the swell sensitivity at insitu and high stress states.

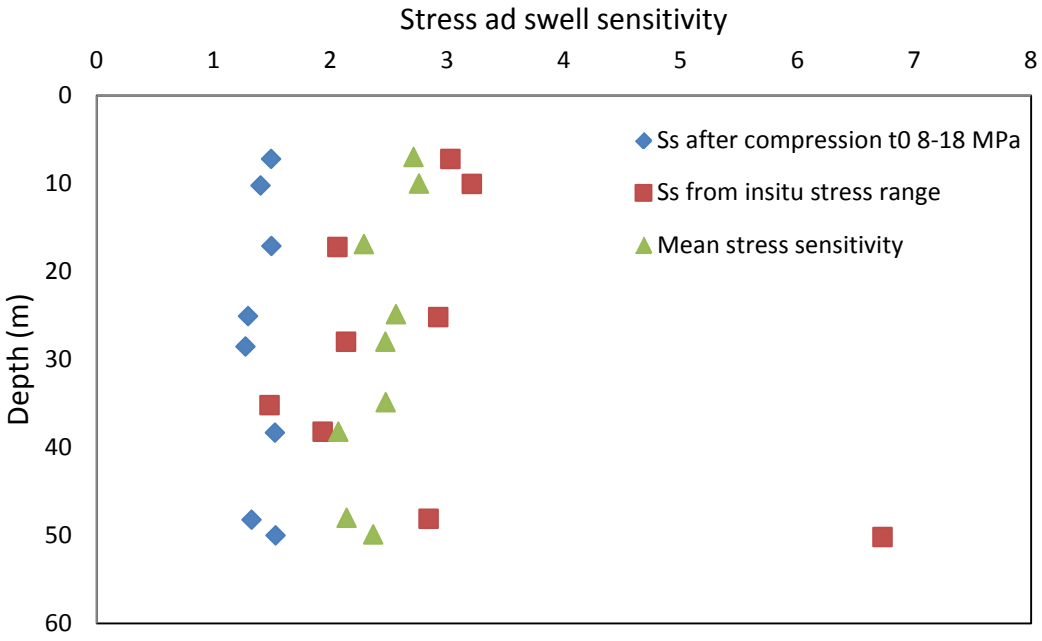

Figure 4.8: Profiles of stress and swell sensitivity at Heathrow T5 (Gasparre and Coop, 2008)

4.5 Site conditions and clay properties

The site under consideration falls within the National Grid reference of TQ298812, situated in Camden. It is located at a south-eastern direction from Charring Cross

Road and Andrew Broade Street junction, and in an eastern direction from the Charing Cross Station. The publically available geological information suggested that the site overlaid the Quaternary River Terrace Deposits which was underlain by the London clay formation. The London clay formation in turn was underlain by the Lambeth. The current landscape and previous development of the site indicated that a layer of made ground was likely to be anticipated on the site. The geotechnical testing in the form of exploratory boreholes re-affirmed the stratigraphic profile suggested by the published geological records. The typical stratigraphic profile is provided in figure 4.9 below.

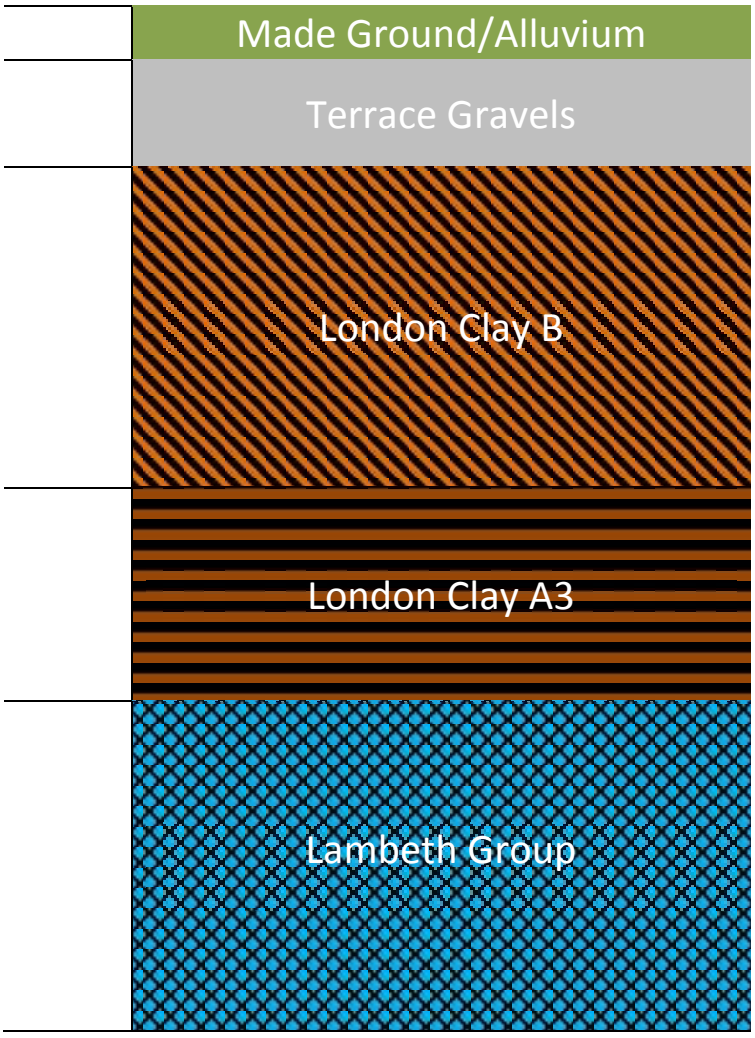

Figure 4.9: Geotechnical profile at Denmark Place

The profiles at the site under consideration and T5 can be seen plotted together in Figure 4.10. To facilitate the comparison they have been matched at the lower boundary of unit B.

Ground conditions (Table 4.2) at the site were fairly uniform, with the groundwater table locaed at a depth of 5.6m below ground level. The bulk unit weight was calculated as 20kN/m^3. *In-situ* testing of comprised self-boring pressuremeter tests. The site investigation concluded to average values for the Liquid Limit of 67%, Plastic Limit of 27% and Plasticity Index of 40%. The Denmark Place site is in close proximity to two other areas, the St James's Park and the Royal Opera House, for which detailed profiles have been presented by Hight *et al.* (2003) and Grammatikopoulou *et al.* (2008) among others. Figure 4.10 plots the comparison of the London clay profile at the site under consideration, the St Jame's site and Heathrow T5. At the Terminal 5 site a layer of sandy gravel of approximate thickness of 4.5m lies directly on a layer of London Clay of about 52m thickness which consists of lithological units A2,A3, B and C. At Denmark Place and St James's Park sites, unit C of London clay is absent, with unit B having a smaller thickness than at T5.

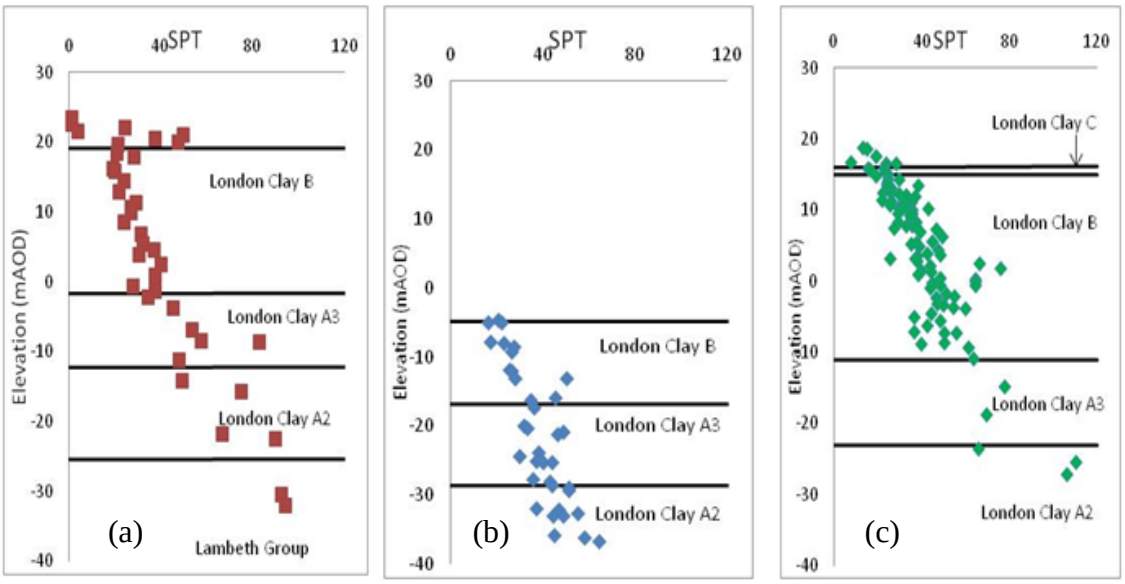

Figure 4.10: Soil profile and identification of lithological units in London clay for (a) Denmark place site and (b) St James site and (c) Heathrow T5 (Hight et al, 2003).

4.6 In situ stresses and K_0

The geological processes involved in the formation of London clay meant that the high degree of overconsolidation alluded towards high horizontal effective stresses and therefore dictated K_0 >1. Extensive research work concluded that within the upper 10m of the London Clay K_0 ranged between 2 and 2.5, decreasing with depth to a value of 1.5 at about 30m below surface. Figure 4.11, presents the K_0 profile from Bishop et al. (1965) and Hight et al. (2003) for Ashford Common and T5.

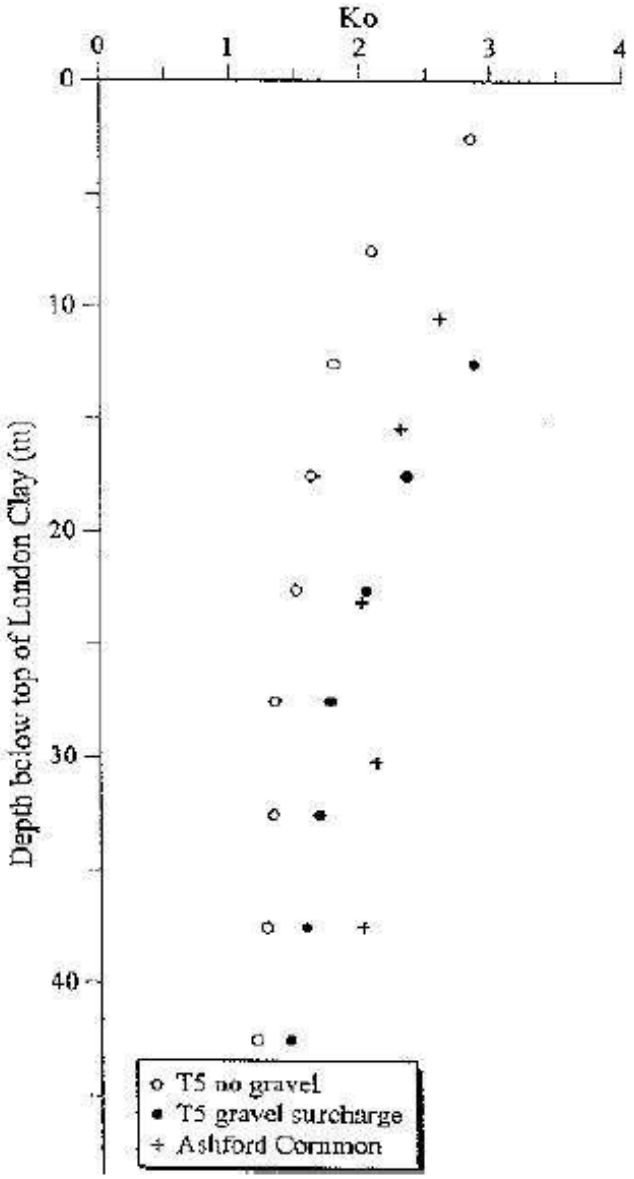

Figure 4.11: K_0 profiles for the London Clay at T5 and Ashford Common (Hight et al., 2003)

Description of ground	Depth to top of stratum (m BGL)	Thickness (m)
Made Ground	G.L	3.50 to 4.40
River Terrace Deposits	3.50 to 4.40	1.60 to 2.50
London Clay Formation	6.00	24.25
Lambeth Group	30.25	18.55
Thanet Sand	48.8	4
White Chalk	52.80	10.70

Table 4.2: Ground conditions at the site.

4.7 Calibration procedure for the model

In order to apply the KHSM model, in boundary value problems four field variables need to be specified. In particular, the first two are the stress tensors controlling the initial state of the soil, and the initial location of the bubble centre. The remaining two are of scalar form, with the first one setting the intrinsic preconsolidation pressure of the soil ($2p_c$), whereas the final field variable is related to the initial degree of structure (r_0).

These variables are inherently related to the stress history of the soil, resulting from the geological processes such as deposition and erosion. As reported by King (1981) some locations in the London area, have retained the original thickness of the formation with thicknesses varying between 150 m in Essex and the Isle of Sheppey, and 90 m at Reading. In most parts of the London Basin, substantial erosion has taken place, consequently removing the shallower portions of London Clay according to Pantelidou & Simpson (2007). The degree at which clay has been eroded exhibits significant variations spanning through the London and Hampshire regions. De Freitas & Mannion (2007) suggested that in addition to the erosion thickness the subsequent degree off geological loading differs at different locations.

The proximity of the Denmark Place site to the St James site which has been previously analysed in using similar models (Grammatikopoulou et al. 2008, Gonzalez *et al*. 2012) lead to the assumption that the erosion of the site under consideration was of the same order of about 180 m. The geological history of the site was possible to be modelled, give that a certain erosion thickness was considered. This process assisted in the corroboration if the initial conditions as encountered at the Denmark Place site. It should be noted that the geological history modelling was carried out employing the "degenerated" KHSM model that did not contain the initial structure. This was necessitated by the fact that any measure of initial structure would be damaged in conjunction with loading or unloading processed. The course of structure development and evolution is a multifaceted electro-chemical process, as described in Chapter 2. This geological features does not form part of the KHSM model, since according to the formulation, the structure size is allowed to increase. As a result, the initial measure of structure for the London clay formation was defined from the onset, since its roots and evolution could not be captured.

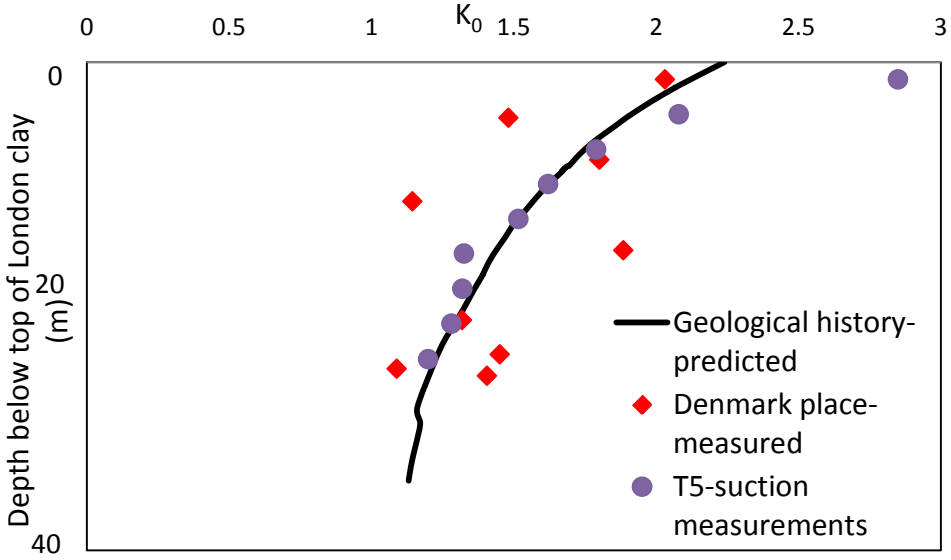

Figure 4.12: K_0 profiles at Denmark Place from measurement and numerical simulations and measurement from T5 (Hight et al., 2003).

Figure 4.12 shows the comparison of the predicted K_0 profile from the stress history simulation and the measurements from the Denmark Place site. The figure also includes values of K_0 at T5, derived from suction measurements on thin-wall samples using a suction probe on site soon after sampling (Hight, 2003). The direct comparison between measurements at T5 and Denmark place is feasible, since the elevation of the top of the London clay for both sites is very similar (see figure 4.8).

For the purposes of numerical simulations, the decision to set the initial position of the bubble centre to coincide with the current stress state was made. This decision was based on results from experimental work by Clayton & Heymann (2001) who proved that the development of creep neutralises the influence of stress history relating to mechanical loading. It should be noted however, that it is indeed feasible to specify this variable by means of a stress history simulation.

State-of –the-art constitutive models are widely criticised that they require a relatively large number of input parameters before they can be employed in numerical simulations. Moreover, these parameters are frequently riddled with ambiguity. One way of addressing these concerns is the adoption of a sequential nature of the model calibration procedure to minimise the risk associated with any doubts relating to the model parameters.

Some fundamental soil properties are more reliably derived than others. In the absence of test data from the Denmark Place site, the material parameters of London clay that describe the intrinsic properties of the soil such as λ^*,κ^* and M were set to 0.097, 0.003 and 0.87 on the basis of a series of laboratory tests on reconstituted overconsolidated London Clay from the Canons Park site, London (Jardine, 1985; Hight et al., 2003). These parameters were derived for a similar kinematic hardening model (M3-SKH) by Grammatikopoulou (2004). A secondary set of parameters is relating to the intrinsic properties of a soil, are the following kinematic hardening parameters: bubble size R and the plastic modulus parameters B and ψ. These were assumed respectively as R=0.016, B=4.0 and ψ=*6.0* based on the calibration process described previously.

The remaining parameters to be definer related to the size of the structure surface and the consequent degradation process. As mentioned previously, published information from Gasparre (2008) provide an indication of the range of values of the measure of structure present in the London Clay formation. The lack of information about intact and reconstituted properties of London clay in the Denmark Place site, lead to the assumption that the structure developed during the geological stress history is of similar magnitude for both sites. A value of A=0.75 was adopted implying that the contribution of the plastic deviatoric strains in the destructuration process is 3 times higher than the contribution of the plastic volumetric strains was chosen. Table 4.3 provides the reference KHSM model parameters adopted in this work.

Material Constants	**Value**
Slope of normal compression line λ^*	0.097
Slope of swelling line κ^*	0.003
Critical state stress ratio M	0.875
Elastic bubble size R	0.025
Stiffness interpolation parameter B	1.0
Stiffness interpolation exponent ψ	1.5
Destructuration parameter k for:	
SBPM102T2 (14m) SBPM102T3 (20m) SBPM102T4 (26m)	5.0 3.0 3.0
Destructuration strain parameter A	0.75
Initial degree of structure r_0 for:	
SBPM102T2 SBPM102T3 SBPM102T4	2.0 2.1 3.0
Anisotropy of initial structure η_0	0.1

Table 4.3: Soil parameters for London clay for all tests

4.8 Results and discussion

In this section the results from the three simulated SBPM tests assuming fully undrained conditions are presented. Plotted along with the experimental data are the results from the numerical simulations that adopted the material parameters detailed in the previous section. Cavity pressure-cavity strain curves and pore-water pressure-cavity strain curves were matched using a trial and error procedure. The fitted profile of the initial size of the structure surface (r_0) with depth is provided in figure 4.13. The figure also includes the range of values estimated from oedometer tests at the T5 site (Gasparre, 2007), as well as fitted values from simulation of triaxial tests on natural samples from the T5 site that were carried out by Gonzalez *et al.* (2012) using the KHSM model. As it can be seen the fitted values from the SBPM tests are in good agreement with the experimental and numerical results.

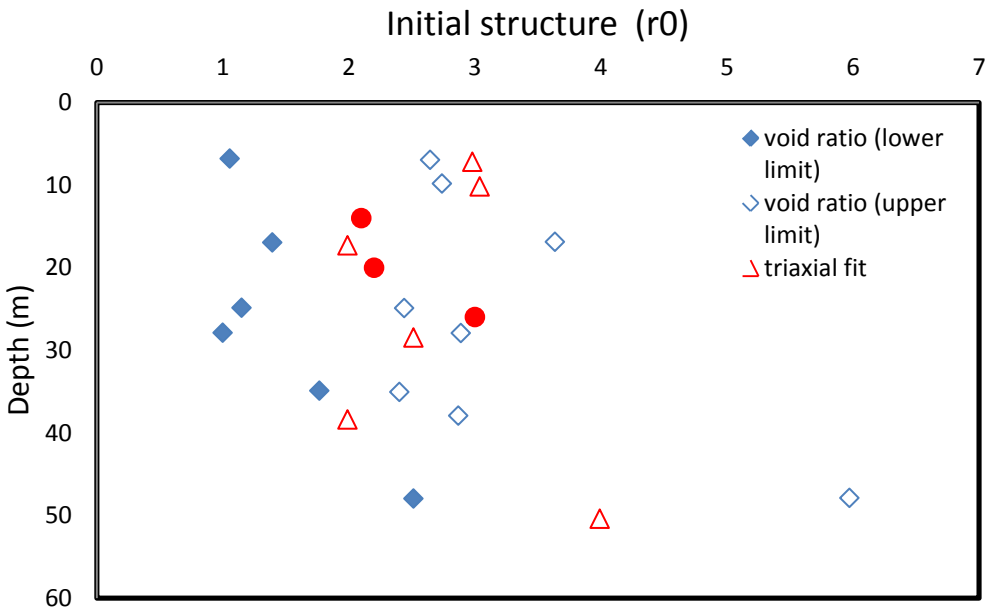

Figure 4.13: Profile of variation of the measure of initial structure at T5 and Denmark place

Parameter k which controls the rate of degradation of the structure surface was calibrated at values of 5 for SBPM 102T2 (14m Below Ground Level), and 3 for SBPM 102T3 and 102T4 (20m and 26m BGL) respectively.

Figure 4.14 shows the distribution of the destructuration zones at the end of the analysis corresponding to test SBPM 102T2. As can be observed from the simulation the complete destructuration, with r=1.0, takes place in the soil elements adjacent to the cavity face. The destructuration zone then gradually decreases, as it moves away from the cavity wall, until a zone where no break-up of the inter-particle bonding occurs, corresponding to r=2.0.

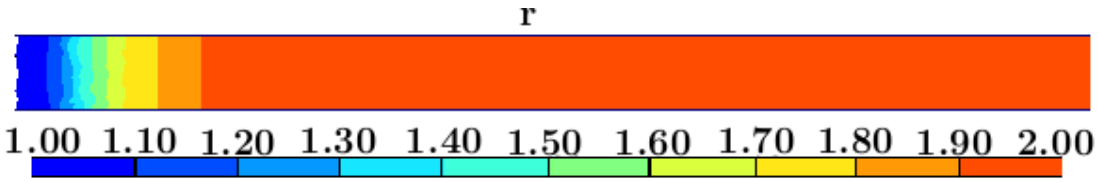

Figure 4.14: Distribution of structure at the end of one simulation

4.8.1 Self boring pressuremeter test 102T2

The first finite element test was conducted at a depth of 14m below ground level. The comparison of the experimental results with the numerical predictions for the cavity pressure is shown in figure 4.15a. It can be seen that the response from the KHSM during the expansion and contraction stages of the test is in excellent agreement with the observed measurements. The reasonable predictions of the KHSM are reaffirmed in the comparison of the predicted and experimental cavity pore-water pressure plots (see figure 4.15b). There is a slight over-estimation of the simulated pore-water pressures during the latter stages of the expansion curve; however the overall behaviour of the model is satisfactory

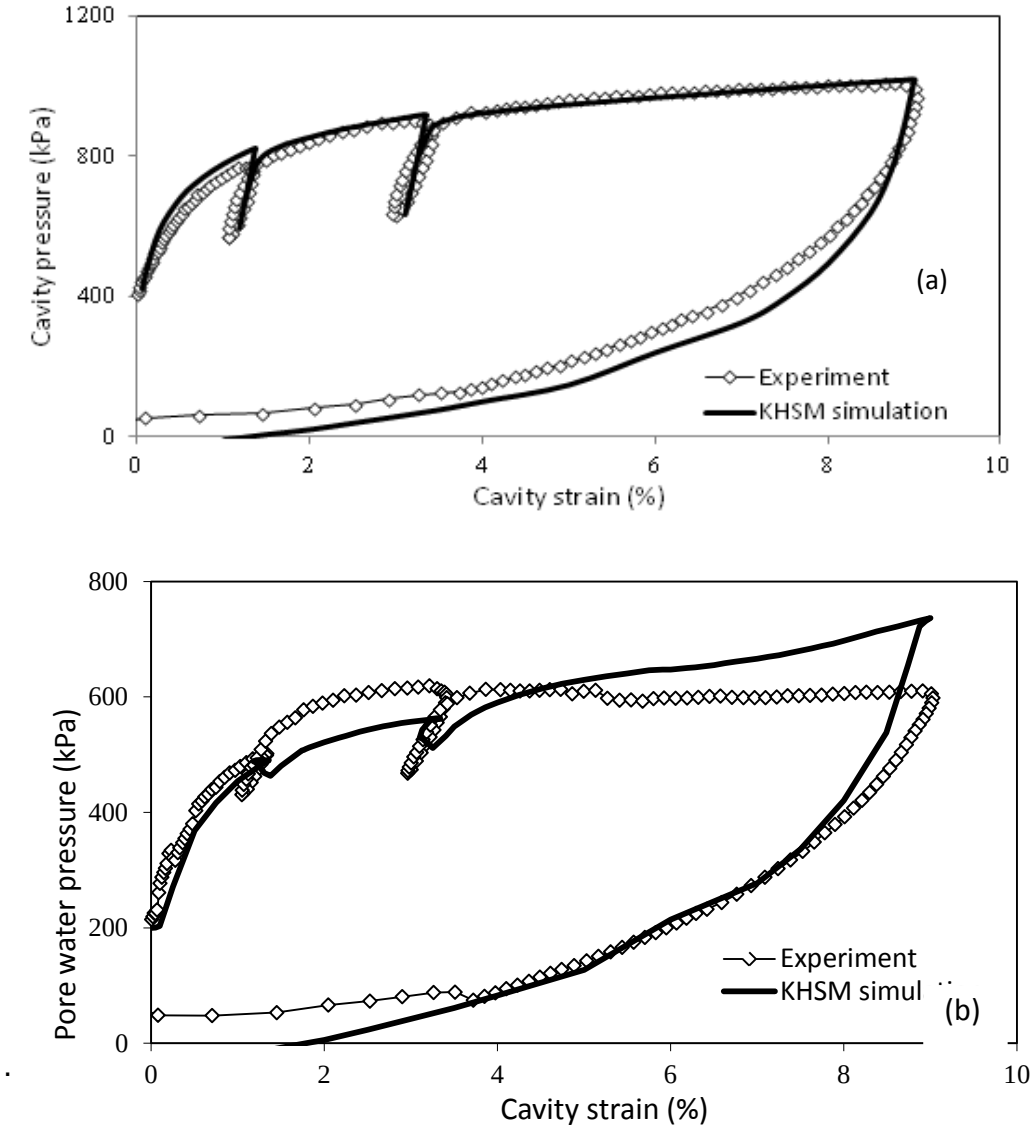

Figure 4.15: Comparison of numerical and experimental results at depth of 14m : (a) cavity pressure v cavity strain and (b) cavity pressure v pore pressure

Figure 4.16 shows the stress path followed during the course of the self-boring pressuremeter test.. It can be seen that the stress path follows the normal compression line to reach the insitu stress state. At that time the initial expansion of the cavity begins and due to the fact that the size of the elastic bubble is quite small, generation of plastic strains commences at an early stage in the test. Plotted also in the figure are the positions of the reference surface, the initial structure surface, as well as the position of the structure surface when softening behaviour begins, i.e. when the stress path comes into contact with the collapsing structure surface. It was found that a significant proportion of the structure was degraded by

the time the first unload-reload cycle was conducted since the structure surface at the point of contact with the stress path was found to have a magnitude of r=1.5.

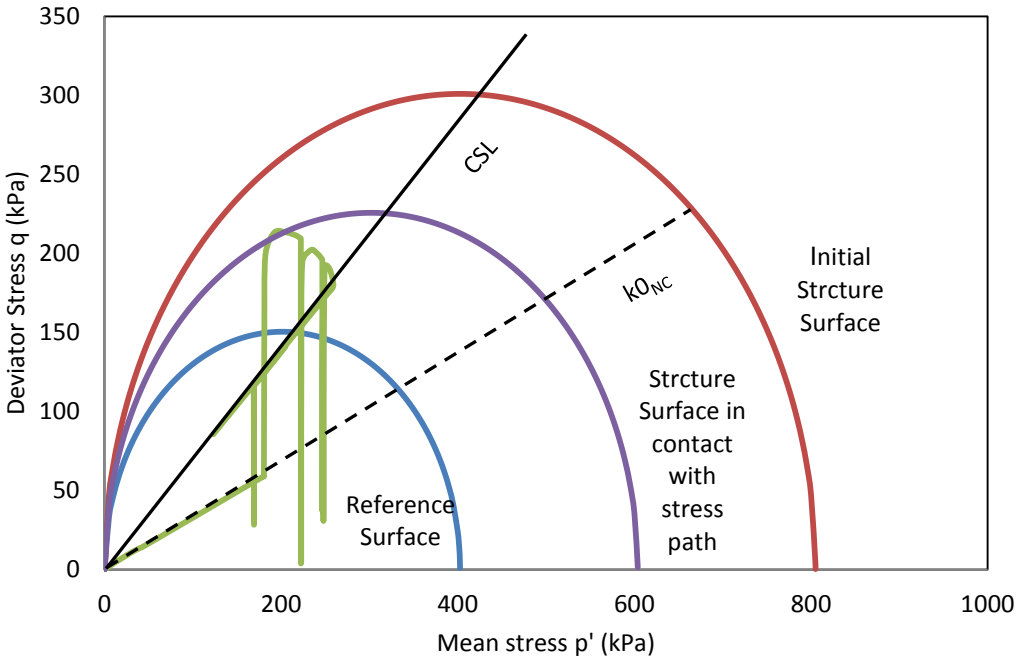

Figure 4.16: Illustration of stress path during SBP2012T2 test

4.8.2 Self boring pressuremeter test 102T3

In the absence of any laboratory data several of the material parameters have been kept the same for all simulations. The assumption that samples from the same depth have the same initial conditions (stresses, size and location of the bubble and outer surface) at their in-situ stress state was made. Therefore, for different depths the parameters that control the size and the process of destructuration have been altered in order to improve the correspondence between observation and simulation.

Figure 4.17a illustrates the comparison between the numerical and experimental results of the cavity pressure: cavity volume change curve. It can be observed that the KHSM exhibits a somewhat stiffer behaviour in the initial stages of the expansion and contraction parts of the test, but then quickly converges toward the values of the experimental data. The comparison of the numerical and observed pore pressures shows that the magnitudes for the initial stages of the expansion portion of the curve are different (see figure 4.14b). However, the magnitude of the

generated pore pressures at the end of the loading and the behaviour of the model during the contraction phase are well captured.

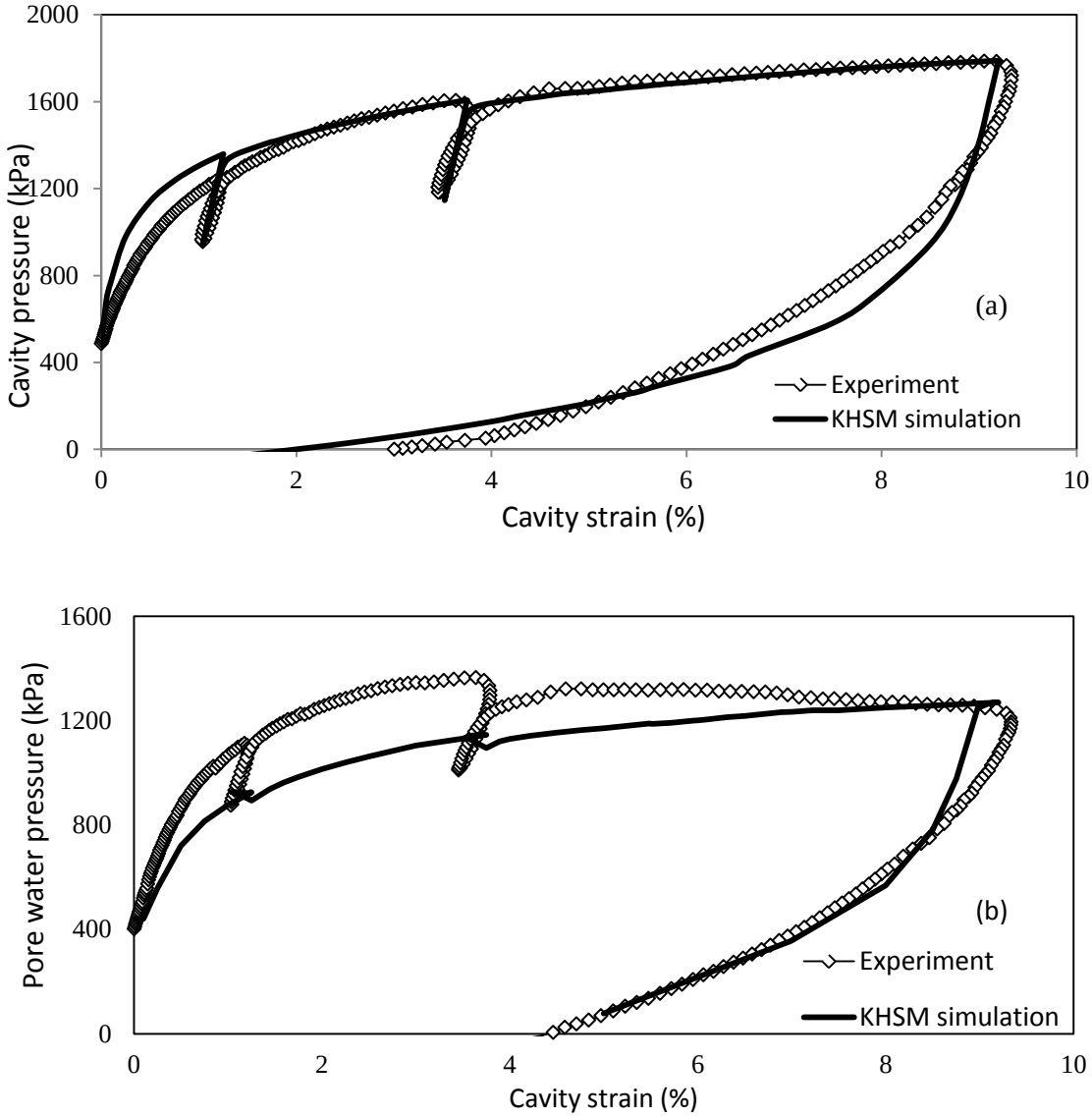

Figure 4.17: Comparison of numerical and experimental results at depth of 20m : (a) cavity pressure v cavity strain and (b) cavity pressure v pore pressure

Figure 4.18 shows the stress path followed by SBP102T3. The behaviour is similar with what was observed in SBP102T2 with the softening occurring just before the first ulnoad-rleoad cycle was performed. On completion of the second loading cucle, the stress parth reaches the Cristical State Line and follows a path with reducing deviaoric stress, until the test is complete.

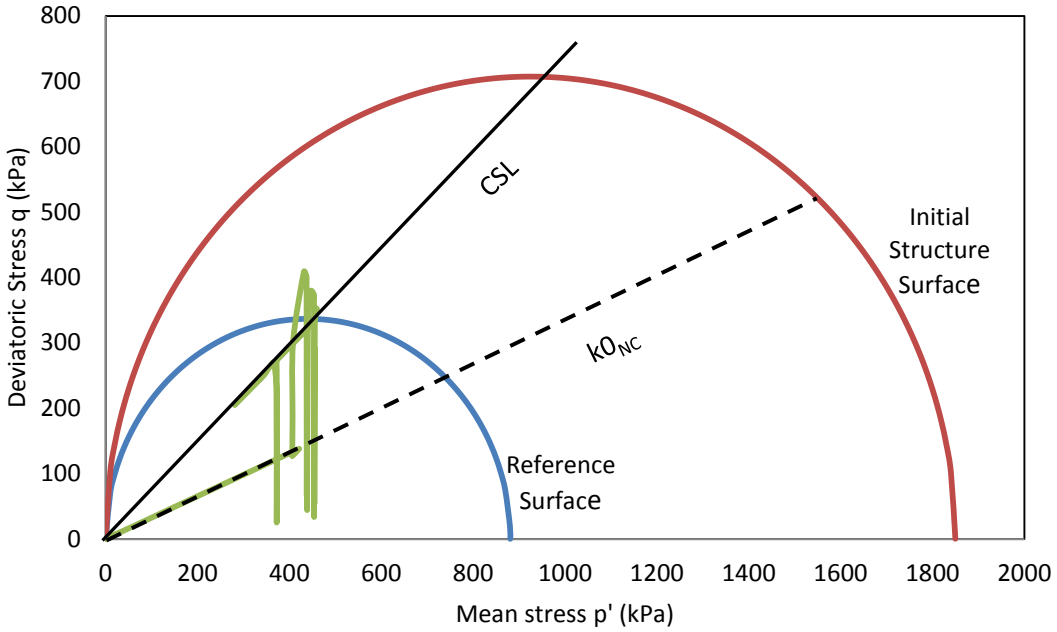

Figure 4.18: Illustration of stress path during SBP2012T3 test

4.8.3 Self boring pressuremeter test 102T4

Figures 4.19a and 4.19b show the simulation results for test 102T4. The overall behaviour during the test is reasonably captured by the KHSM. Similarly to the previous test, the initial values of the structure and the destructuration rate have been changed slightly to correspond with the experimental observations. The trend of the proposed model to predict marginally stiffer behaviour during the onset of loading and unloading is evident in this simulation as well. This discrepancy may be attributed to the determination of the material parameters for the elastic part of the model.

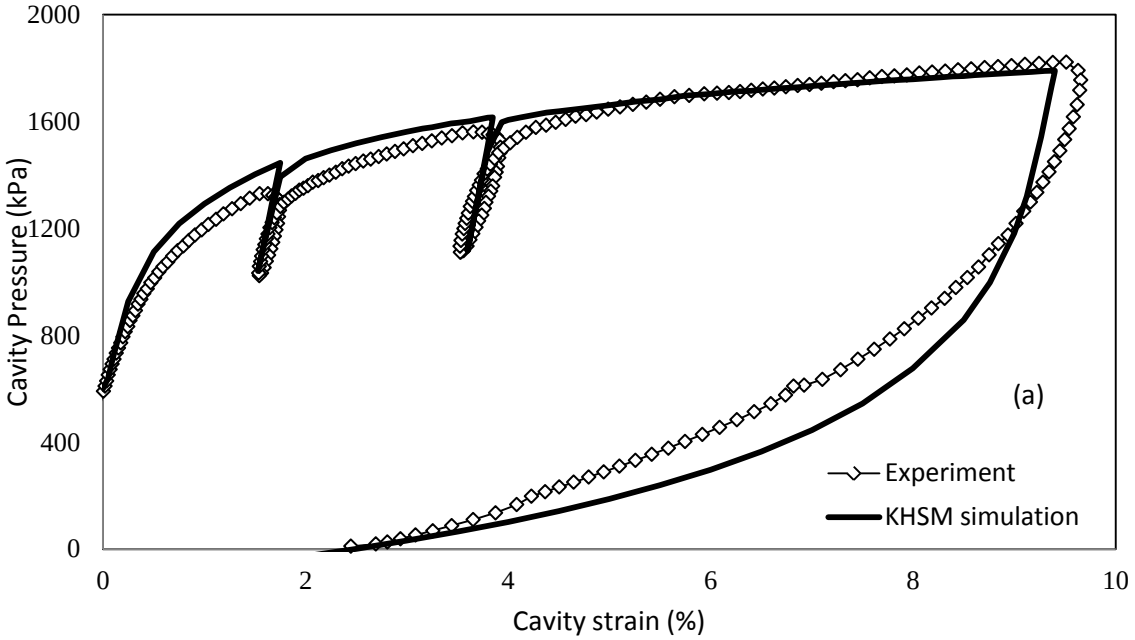

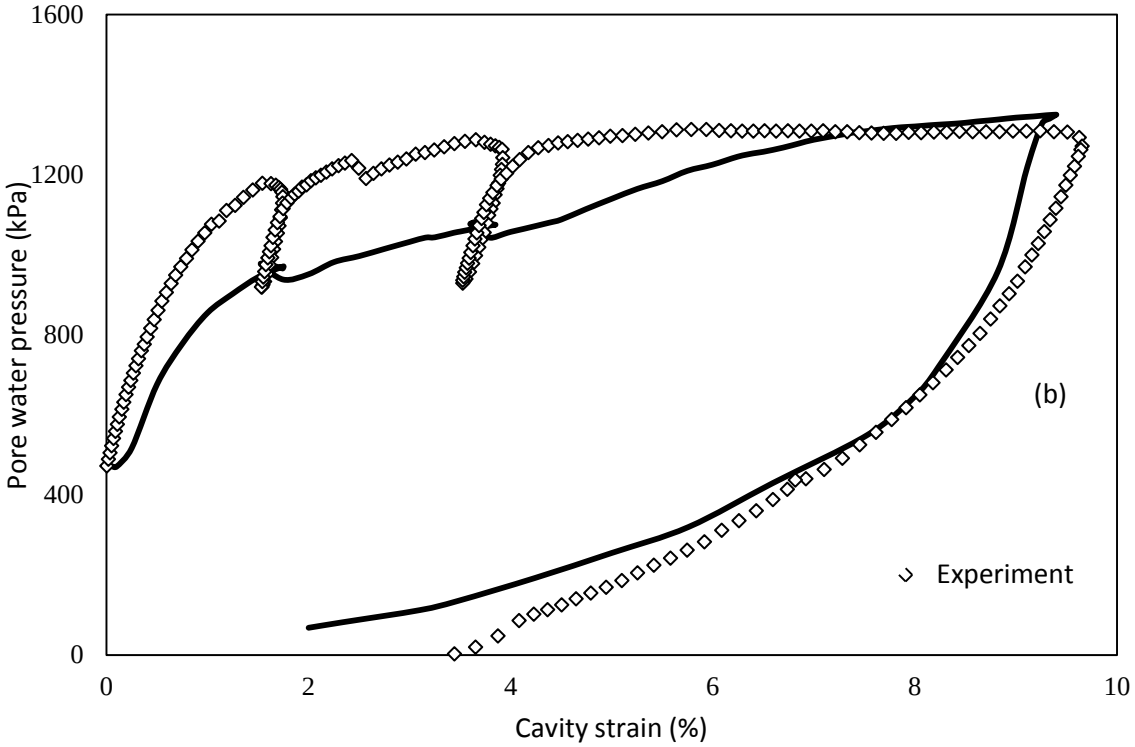

Figure 4.19: Comparison of numerical and experimental results at depth of 26m: (a) cavity pressure v cavity strain and (b) cavity pressure v pore pressure.

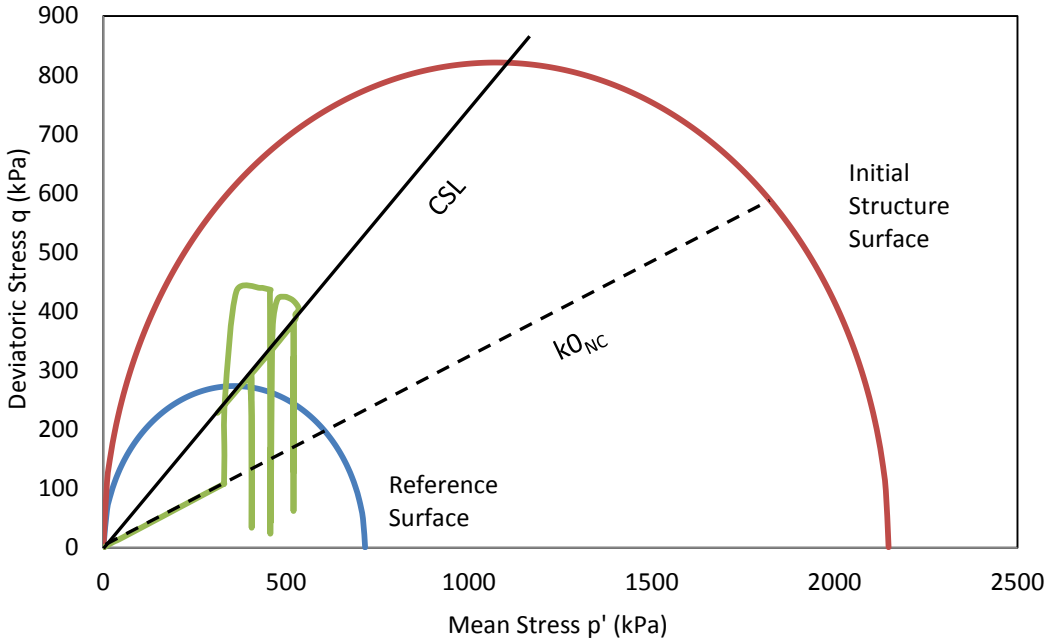

Figure 4.20: Illustration of stresspoath during SBP2012T4 test

As it can be seen in Figure 4.20, the stress path for SBP102T4 engages the collapsing structure surface at an earlier stage in the test. As a result contact with the Critical State Line is seen to occur between the two ulnoad-reload cycles with the stress state following a path of reduced deviatoric and mean stresses until the completion of the test.

4.9 Parametric Analyses

The aim of this sensitivity study was to investigate the impact the parameters that control the initial measure of structure, r_0, and the destructuration rate parameter, k, have on the model's response during the SBPM test. In order to provide an insight into this, the calibrated values of these material parameters for test SBP102T4 were varied in the following manner. Simulations designated as $2r_0$ and $2k$ were carried out with the magnitude of r_0 and k doubled from the calibrated KHSM values and the simulations designated as $0.5r_0$ and $0.5k$ were run with the calibrated values halved

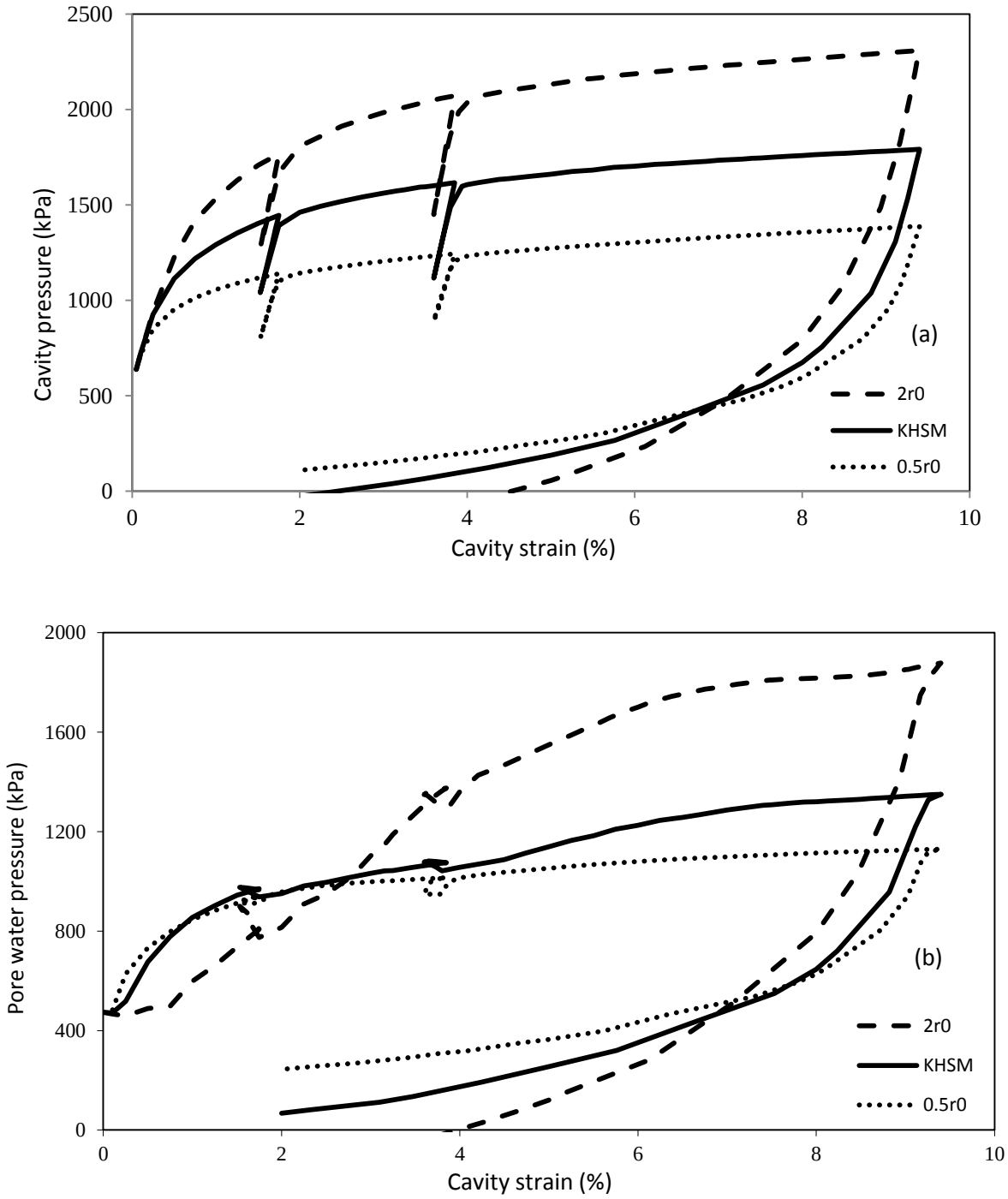

Figure 4.21: Numerical analysis curves from sensitivity analysis on structure size (a) cavity strain and (b) pore pressure

4.9.1 Initial degree of structure r_0

Parameter r_0 controls the amount of structure within the model. When r_0=1, the KHSM converges on the bubble model (Al-Tabbaa and Wood, 1989). As it can be seen from Figures 4.21a and 4.21b, the degree of initial structure has a significant influence both on the cavity pressure and pore-water pressure curves. The increase of r_0 leads to a stiffer response from the KHSM, leading to an overestimation of the cavity pressure

of 30% at a strain of 9%. The opposite behaviour is observed when the initial degree of structure is halved. The cavity and pore-water pressure responses are reduced by 25% and 16% respectively.

4.9.2 Destructuration parameter k

Parameter *k* controls the rate of destructuration with strain. The higher the value of *k* the faster structure will be lost with the increase in strain. In relation to the reference value, it can be seen that there is a stiffer response when *k* is low than when it is higher (Figure 4.22a). This is due to the effect of the structure being lost quickly when *k* is high. The variation of *k* does not appear to have a notable influence on the loading part of the pore pressure curve (Figure 12b) but does have a significant influence on the response during the unloading portion.

Figure 4.23 depicts the distribution of the measure of structure at the end of the test for the three cases analysed above. As it can be seen, when parameter k is doubled from the calibrated value of 3.0, the breakdown of the interparticle bonding penetrates deeper in the cavity wall. This is more notable in the transition zone between the values of 2 and 2.4, where the results using the calibrated value of k illustrate an extended zone of r_0=2.2. This intermediate zone is absent from the 2k analysis. At the other end of the scale, when the destructuration parameter is halved, the destructuration process is incomplete and as a result the breakage of the particle bonds is not as severe as in the previous simulation. Whereas in the previous two simulations, complete loss of structured occurred at the cavity face, it is evident from figure 4.23 that a magnitude of 2 of the degree of structure is maintained at the cavity wall at the end of test, with the initial value of 3 recovered at a much shallower distance from the wall. A very thin zone of material with r_0=2 can be seen adjacent to the cavity wall, with the transition zone between the values of 2 and 2.4 occurring at approximately half the distance when compared with the results from the calibrated value of k.

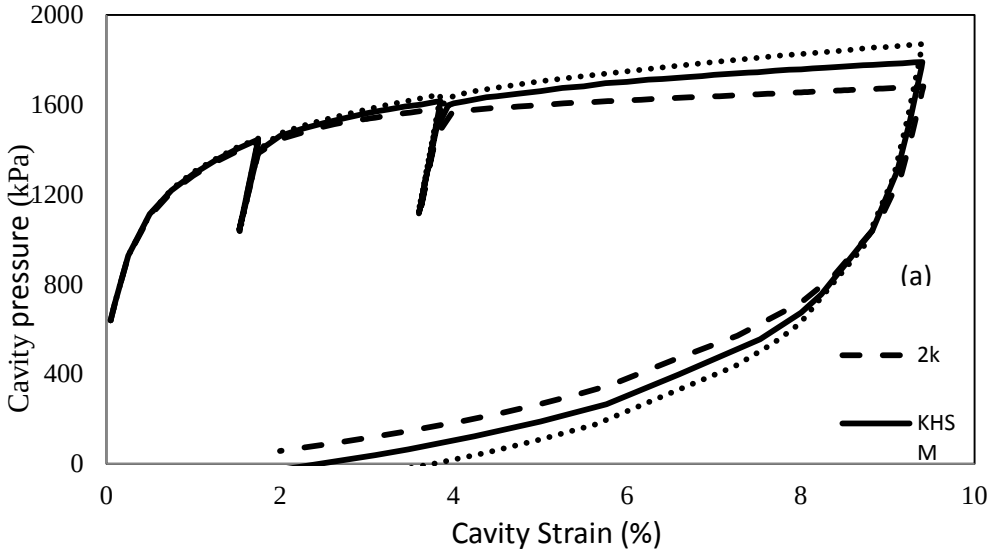

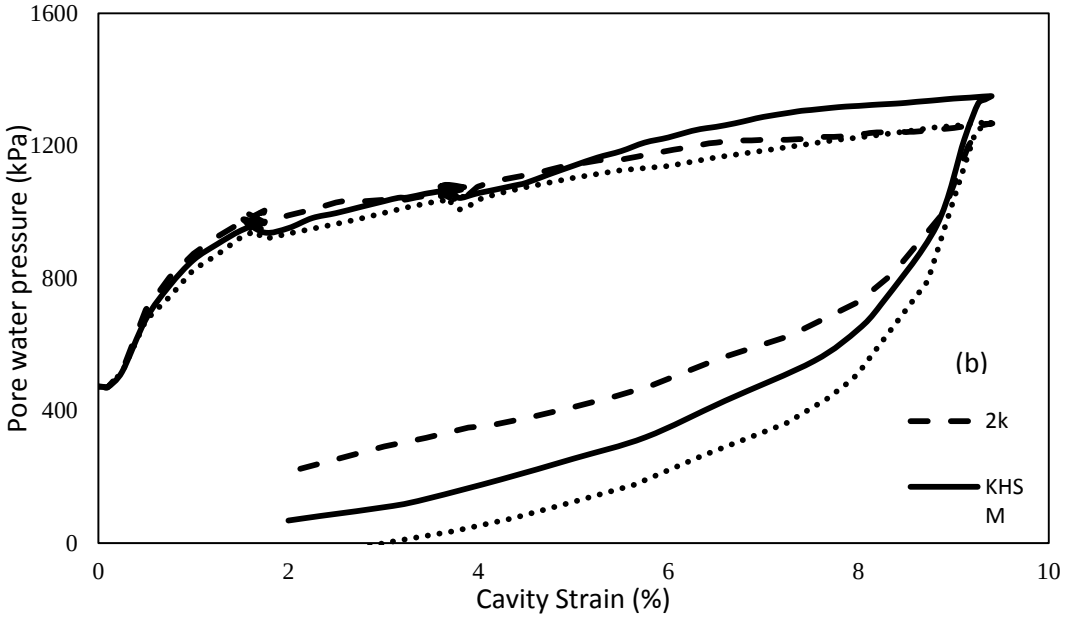

Figure 4.22: Numerical analysis curves from sensitivity analysis on destructuration parameter (a) cavity strain and (b) pore pressure

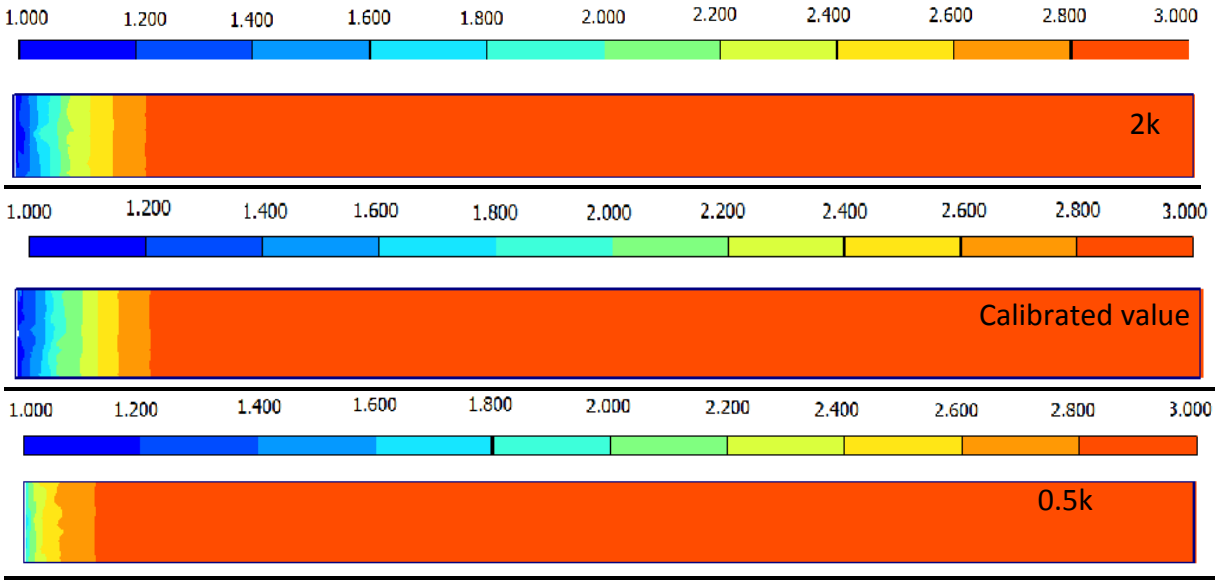

Figure 4.23: Numerical analysis curves from sensitivity analysis on destructuration parameter k. Plots of the distribution of structure at the end of the test.

4.10 Geometry effects and permeability study

4.10.1 Finite membrane length study

The traditional methods of interpreting pressuremeter tests effectively reduce the problem to one dimensional. Consequently, the effects of the finite length of the pressuremeter membrane are not considered. In this part of the paper, an investigation in the effects of modelling the two dimensional geometry of the SBPM was carried out.

Numerous numerical studies have been performed in the past in order to assess the consequences of ignoring the finite length of the pressuremeter membrane, (Yu, 1990, Yeung and Carter, 1990, Yu and Collins, 1998 and Yu et al. 2005). The general conclusion from these investigations is that by omitting the two-dimensionality of the problem, the predictions are lead to an overestimation of the undrained shear strength and also a stiffer loading response which in turn will influence the prediction of the friction angle.

Yu et al. (2005) propose that in the case where a pressuremeter with a large length to diameter ratio is used, the test will occur under conditions which are analogous to the assumptions adopted in the interpretation procedure of Gibson and Anderson (1961); axial symmetry and plane strain conditions in the vertical direction. . Many self-boring pressuremeters that are used commercially have small length to diameter ratios and therefore the geometry effects may be significant in the evaluation of the undrained shear strength.

The finite membrane length study was performed for a test with typical length to diameter ratio of 6. In order to avoid the influence of the external boundaries, the geometry was extended 50 times the initial cavity in the radial direction. The centre of the membrane was placed in the centre of the mesh, with the boundaries in the vertical direction extending to 25 times the initial cavity radius in both directions. All boundaries were deemed to be impermeable. The axisymmetric model used in Plaxis to model the two dimensional geometry of the self-boring pressuremeter, was constructed with approximately 3100, 15-noded triangular elements, in order to avoid mesh-dependent results. Figure 4.24 shows a schematic diagram of the two dimensional mesh. As it can be seen the region adjacent to the pressuremeter membrane was refined in order to achieve more accurate results. The radius was taken as 0.0416m, which is typical for a pressuremeter with L/D=6.

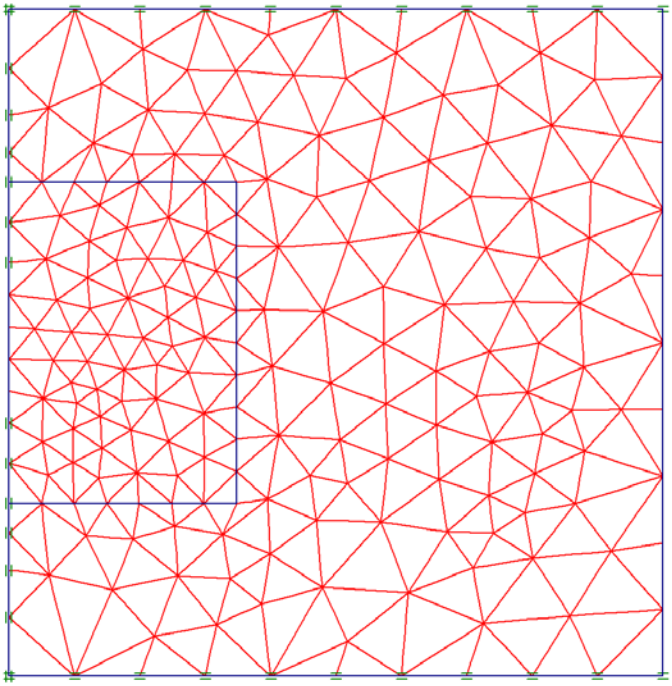

Figure 4.24: Two-dimensional finite element geometry adopted in this study

In the following figure (figure 4.25) we present the comparison of the results from the simulation of the SBP 102T2 test using the two different mesh geometries and the same material parameters, calibrated with the infinite cavity analogue. As it was anticipated, the cavity pressure curve for the finite membrane length (L/D=6) demonstrates a stiffer response during the loading phase of the test. This characteristic is less prominent during the unloading portion, with the two mesh geometries following approximately the same trajectory back to zero cavity pressure. As suggested by Houlsby and Carter (1993) the two-dimensional geometry appears to have minimal effects on the loading-unloading cycles and consequently small difference in the measurement of stiffness.

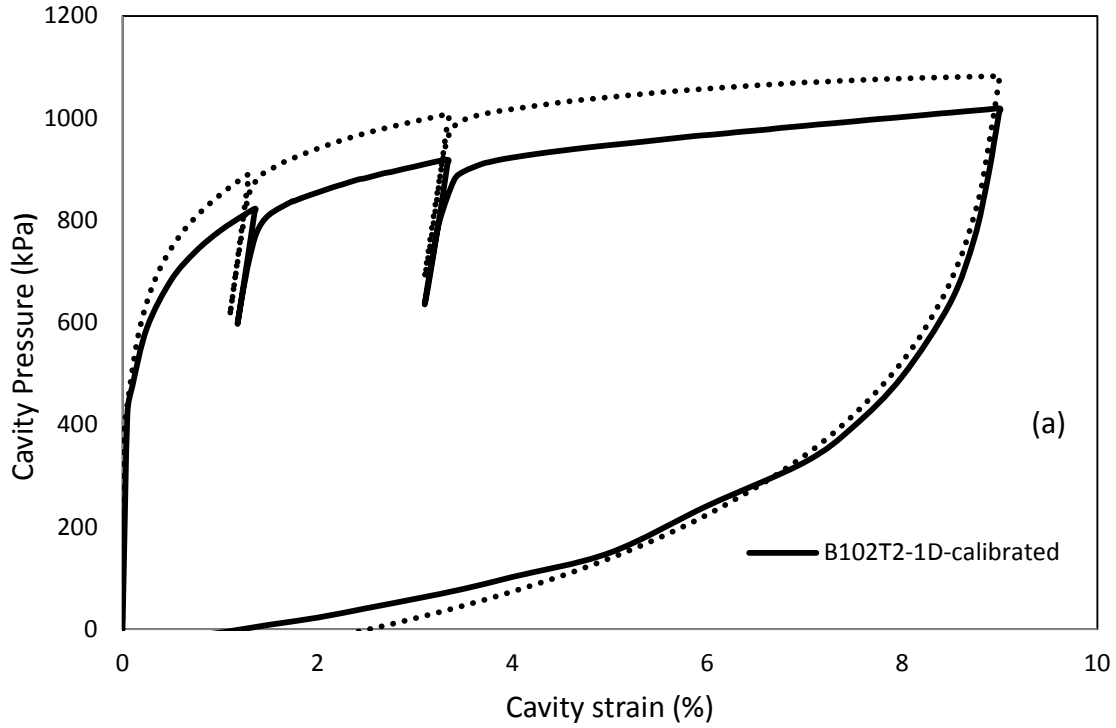

Figure 4.25b shows the comparison between the predicted pore water pressures for the two geometries. The stiffer response of the pressuremeter curve is echoed in the pore water pressure predictions. As it can be seen the geometry effects are very small up to the first load-unload cycle, corresponding to a cavity strain of ~1%. From that point, the two -dimensional mesh geometry predicts consistently higher values of the pore pressure, resulting to a difference of 90 kPa at the end of the loading phase. During the unloading part, the upward shift of the predicted curve from the finite membrane length simulation is still evident, with the magnitude of the pore water pressure still higher than the simulation using the infinite length analogue. Similar behaviour was observed by Gonzalez et al (2009), when they applied an elasto-plastic model that accounts for inter-particle bonding to simulate pressuremeter tests in natural clays.

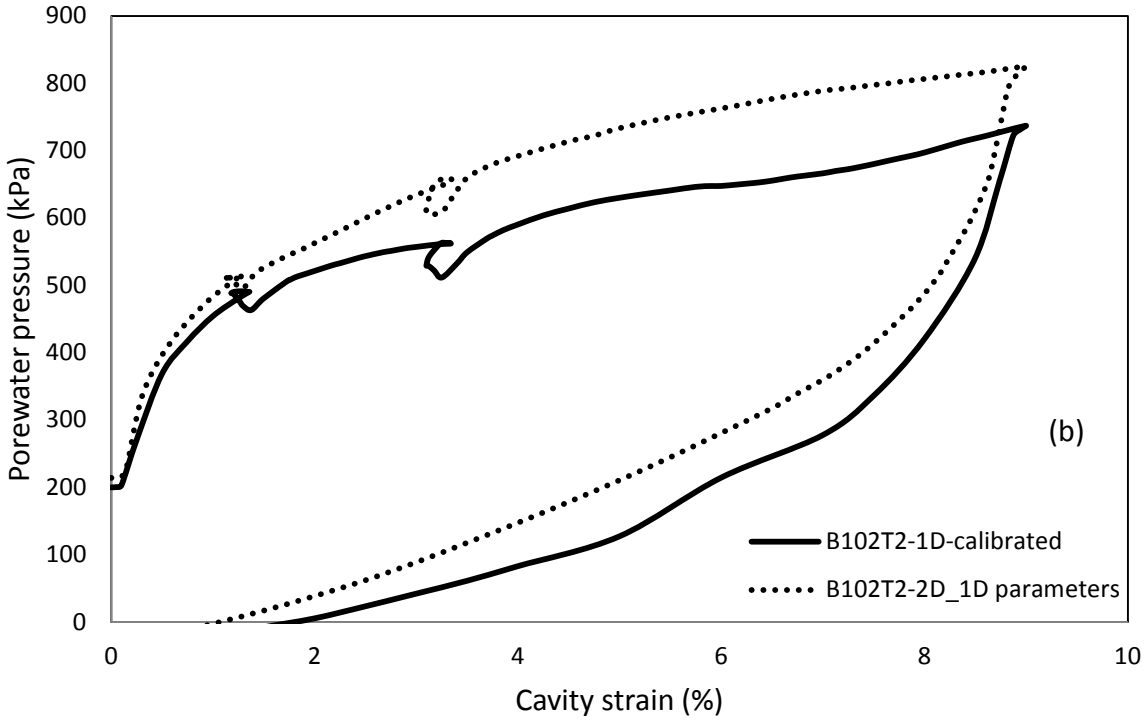

Figure 4.25: Numerical analysis curves from comparing the two finite element geometries for SBP102T2, (a) cavity strain and (b) pore pressure

The figure (figure 4.26a) below depicts the distribution of structure at the end of loading for test SBP102T2. The destructuration process follows the same pattern as the one observed in the one dimensional geometry simulations. The expansion of the pressuremeter membrane causes a breakup of the interparticle bonding on the face of the cavity wall. As a result at the end of the inflation of the membrane to approximately 9% cavity strain, there is complete loss of structure on the face of the cavity, with the destructuration process progressively slowing down as it moves deeper in the soil where it finally recovers the initial value of r_0=2. With the help of figure 4.26b which shows the incremental total displacement shadings at the end of the loading phase, we can identify the extent of the failing soil mass and therefore validate the depth of the destructuration zone in the soil.

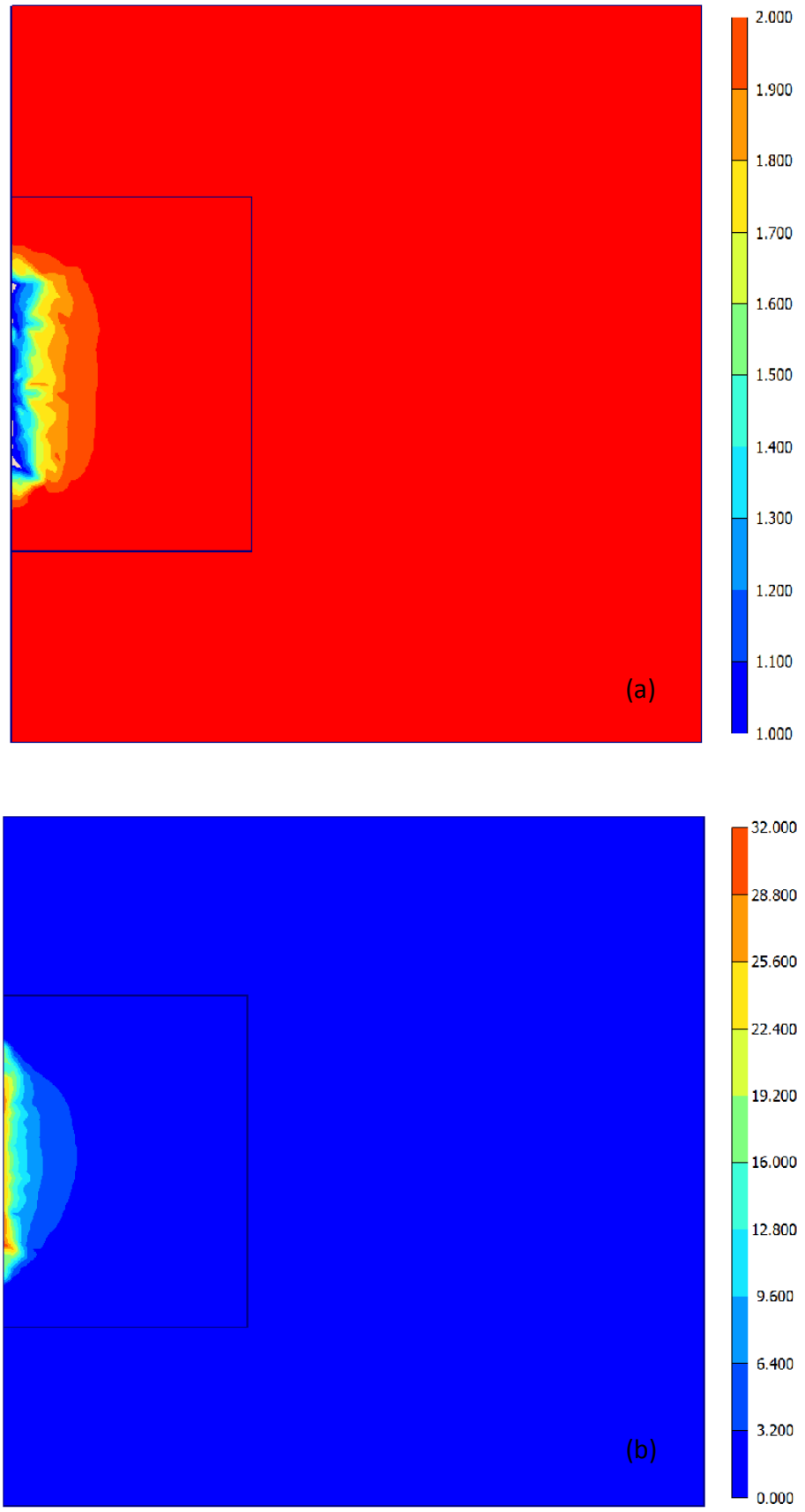

Figure 4.26: Identification of soil failure zone at the end of loading in SBP102T2; (a) Distribution of structure and (b)shading of incremental displacement

4.9.2 Permeability study

The pioneering work from Gibson and Anderson (1961), which forms the basis for the analysis of self-boring pressuremeter tests that are widely used in the geotechnical engineering field, was developed based on some fundamental simplifications. The assumption about the pressuremeter geometry was investigated in the preceding section of the chapter. One other aspect which distinguishes pressuremeter tests carried out on site from the undrained cavity analogue is the water drainage conditions during the course of the test. As suggested by many researchers who studied the effect of partial drainage during pressuremeter tests (Fiovarante et al, 1994; Rangeard et al, 2003 etc) the anisotropic stress state that is created around the pressuremeter apparatus during a test, may well lead to partial drainage of the soil and therefore influence the mechanical characteristics of the soil (Rangeard et al. 2003).

In this section of the chapter we will investigate the effects of varying the isotropic permeability coefficient on the prediction of the cavity and porewater pressures. The study was conducted based on the cylindrical cavity geometry model for test SBP102T2, with the rate of loading was assumed as 1% / min which is typical for the self-boring pressuremeter test.

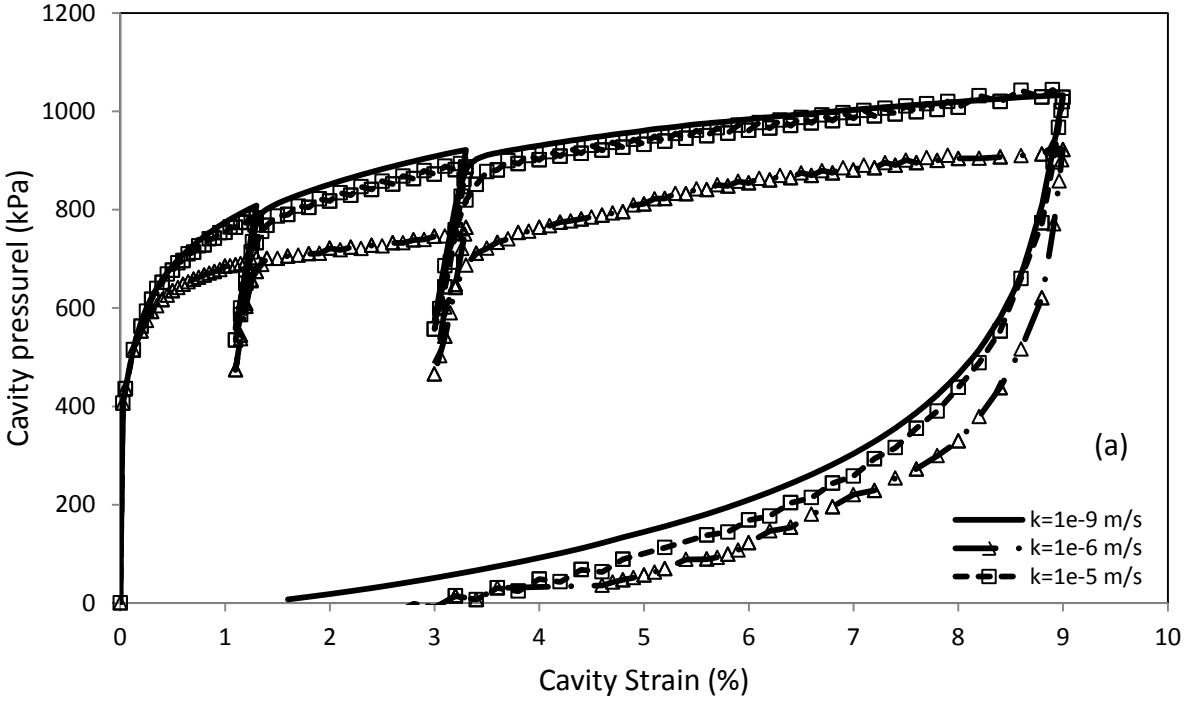

As expected a reduction of the predicted cavity pressure magnitude is observed when the partial drainage condition is applied in the simulations. This reduction is caused from the dissipation of the excess pore water pressure during the cavity expansion (see figure 4.27b).

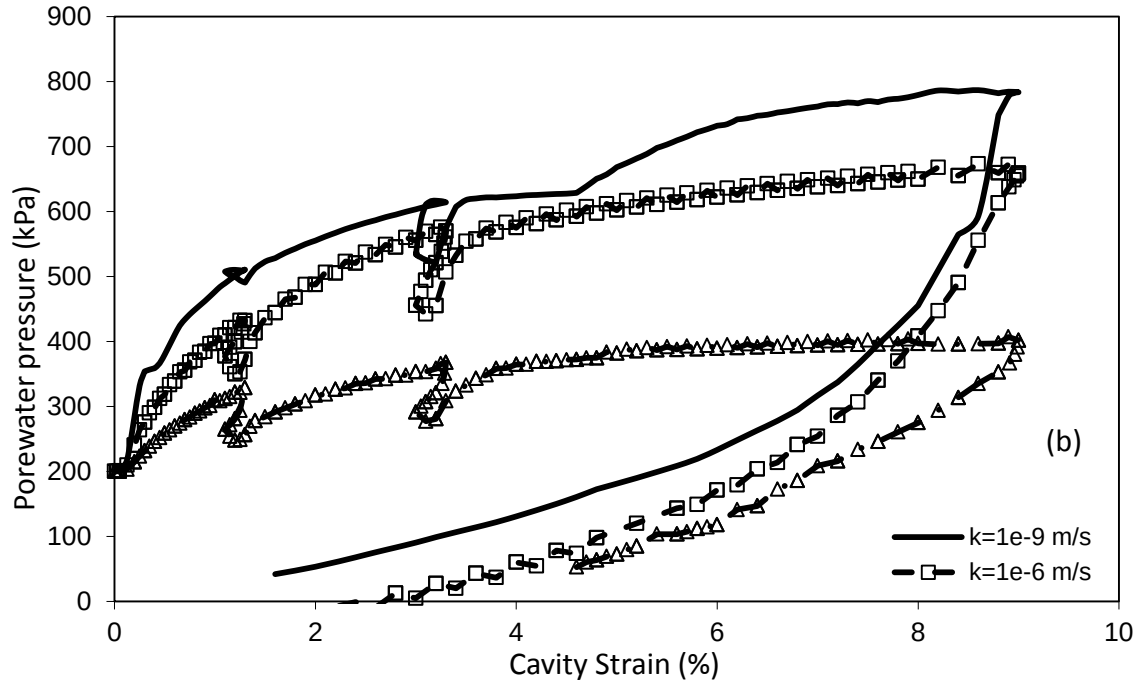

Figure 4.27: Numerical analysis curves from sensitivity analysis on permeability coefficient (a) cavity pressure v cavity strain and (b) cavity pressure v pore pressure

Figure 4.28 shows the distribution of structure at the end of the loading phase for the parametric analyses on the isotropic permeability coefficient. It is clear that the dissipation of the excess pore water pressure and the resultant void reduction causes the immediate collapse of the inter-particle bonding on the face of the cavity wall. As the permeability coefficient reduces, the measure of structure is maintained at values close to the initial magnitude in regions that are in proximity with the cavity wall, as the load imposed by the membrane inflation is taken by the water rather than the soil skeleton.

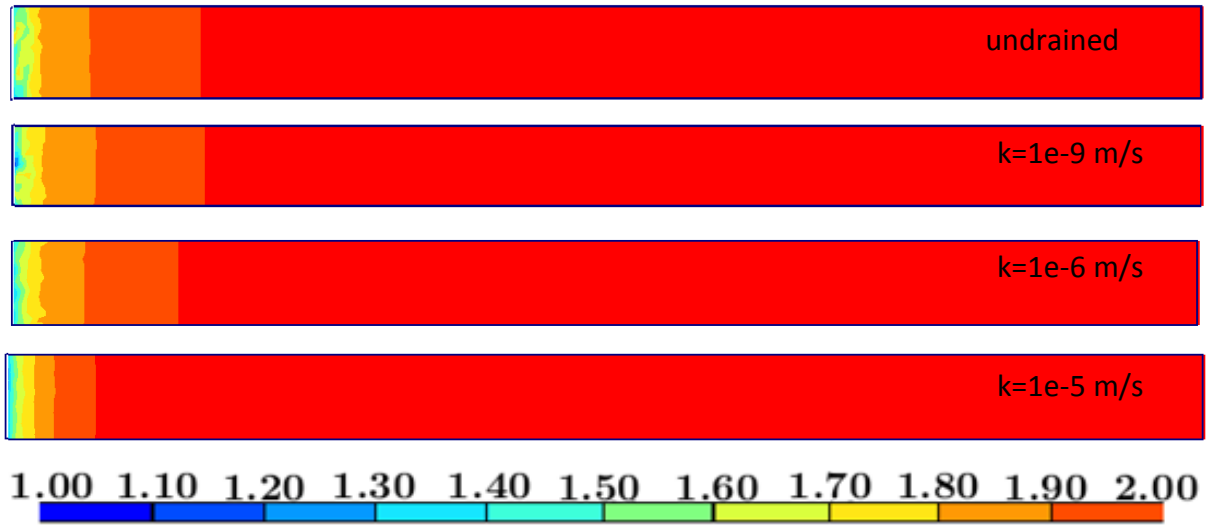

Figure 4.28: Distribution of structure at the end of loading from sensitivity analysis on permeability coefficient

4.10 Disturbance effects

The finite element simulations of SBPM test that was carried in the previous sections revealed a variation between simulations and measurements, which predominantly indicated a different shape of pore pressure generation, which is faster in the measurements than in the simulation. One hypothesis whose influence on the results might provide an explanation is that the SBPM is installed without damage. It should be noted that the installation process will damage the initial structure, but not uniformly. Structure will but be somewhat smaller close to the cavity and retain its intact value at some distance from it.

The Self-Boring Pressuremeter was developed based on the theory that the soil entering the cutting shoe by means of the circulating fluid at a volume which is matched by the penetration of the instrument and therefore surrounding soil is not affected by the volume of soil, replaced by the instrument. Most of the available interpretation methods assume that the pressure-displacement curve produced by the Self-Boring Pressuremeter test is an undisturbed response from loaded material. However, the nonlinear nature of most soils implies that even a small amount of disturbance would have consequences on the initial stress state.

When the self-boring pressuremeter drills its way into the ground, the drilling procedure should in theory retain the surrounding soil at the initial in-situ state. However this is not always possible even for experienced operators. This theoretical minimum-disturbance condition is ideally achieved by addressing two issues. Firstly, the soil extruded into the cutting shoe has to be removed efficiently. Failure to do so will results in blockage of water circulation path-this scenario is called underdrilling- and the insertion process would be similar to pushing a closed-end pile into the ground (see figure4.29b). The second issue, as shown in figure 4.29a occurs if the cutter is installed too far ahead; this will result in stress unloading of the soil below the pressuremeter-called overdrilling. It should be noted, that even if the cutting device is installed in the proper position (see figure 4.29c), the friction between the surface of the instrument and surrounding soil causes unavoidable disturbance.

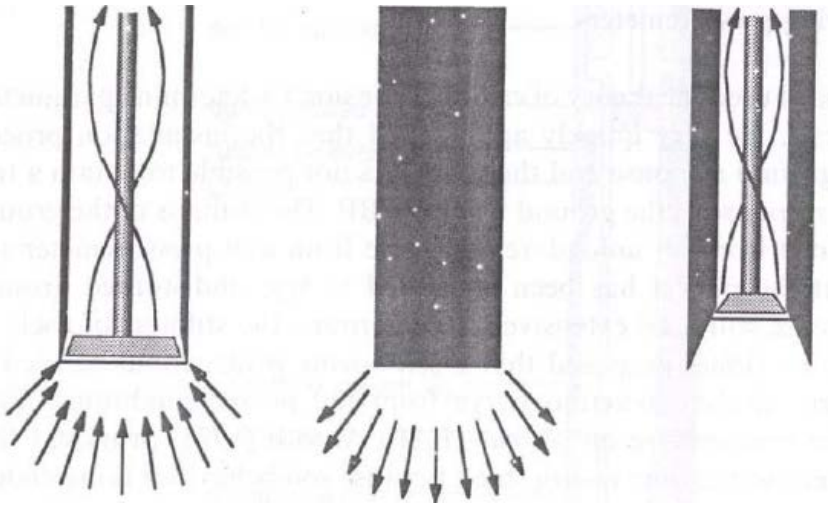

Figure 4.29: the principle of Self-Boring Pressuremeter (Clarke, 1995)

In order to investigate the effects of installation disturbance to the prediction of the self-boring pressuremeter tests a detailed investigation on the effects the various installation disturbance scenarios would have on the strains applied to the cavity wall. The study utilised the strain path method in order to simulate the soil deformation during the installation of the self-boring pressuremeter probe. The author concluded that underdrilling, overdrilling and smearing disturbance scenarios generate a range of radial strains on the cavity wall extending up to a distance of $0.1a_0$ in the soil, where a_0 denotes the radius of the cavity. The range of observed radial strains extended from -4% (relaxation) to 7% strain. It should be noted that even in the event where perfect drilling was assumed, streamline at a/a_0=1.1, the stress state of the soil was found to be altered due to the geometry effect of the cutting show. Furthermore, it was established that the stress states almost return to the undisturbed state distances from a/a_0=1.3 and 1.7.

In conjunction with the above observations, data for London clay, from results by Gasparre (2007) and Hight et al. (2003) on undrained triaxial compression and extension tests for the different lighological units at T5, were used to assume a reasonable profile of the shape of a $r_0(a)$ due to damage. Consequently the structure field was initiated based on the assumed distribution and the results were compared with the predictions from the simulation assuming intact structure before testing.

The experimental results from T5 indicated that the intact shear strength was mobilised at axial strains between 2% and 4% and therefore two linear interpolations of the structure size as a function of the cavity radius were adopted for this study. Figure 4.30 illustrates the assumed profiles that were adopted for test SBP102T4. The first distribution that was assumed consisted of a reduced size of r_0=1.4 extending to a zone of a/a_0=1.1 into the soil and reaching the intact calibrated value of r_0=3.0 at a distance of a/a_0=1.5. The distance at which the intact initial structure was recovered was based on the average of a/a_0=1.3 and 1.7. The second profile that was adopted for this study assumed that the disturbance of the installation process had a smaller effect on the structure size, with r_0=2.0 initialised at the face of the cavity and once again extending to a zone of a/a_0=1.1 into the soil. Similarly to the previous distribution, the structure increased linearly, reaching the intact calibrated value of r_0=3.0 at a distance of a/a_0=1.5.

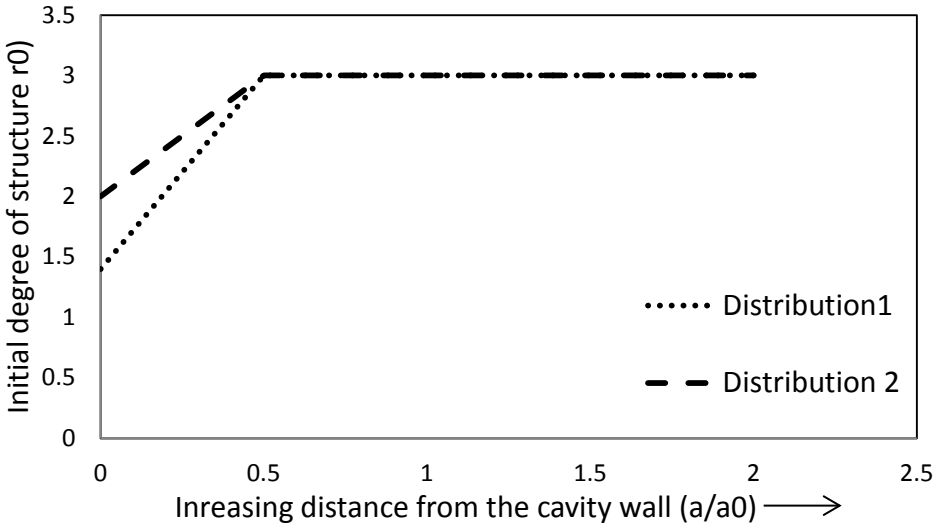

Figure 4.30: Assumed profile of initial structure varying with distance in the soil for the parametric analysis on disturbance.

Figure 4.30 shows the comparison of the results from the parametric analysis on SBP102T4, when the structure field was initiated based on the assumed distributions with the results of the predictions from the simulation assuming intact structure before testing. For comparison, the figure also plots in the experimental observation from the test. As it can be seen, the cavity pressure: cavity strain response is not greatly affected by the variation of the structure size at the face of the cavity. All three simulations agree reasonably with the experimental data.

However, the plots of porewater pressure v cavity strain reveal a dramatic effect of the installation disturbance on the numerical predictions. When a variation of structure field of distribution 1 in Figure 4.30 was adopted, the predicted porewater pressure is in excellent agreement with the observed behaviour in the initial part of the curve, however from 2% cavity strain and until at the end of the test, distribution 1 consistently overpredicts the porewater pressures, with the maximum difference reaching an increase of 21% at the end of cavity loading. The results from distribution 2 provide a considerable improvement from both the intact and distribution 1 predictions. The stress strain curve is reasonably well matched, with the prediction of porewater pressures providing a very good agreement with the experimental results.

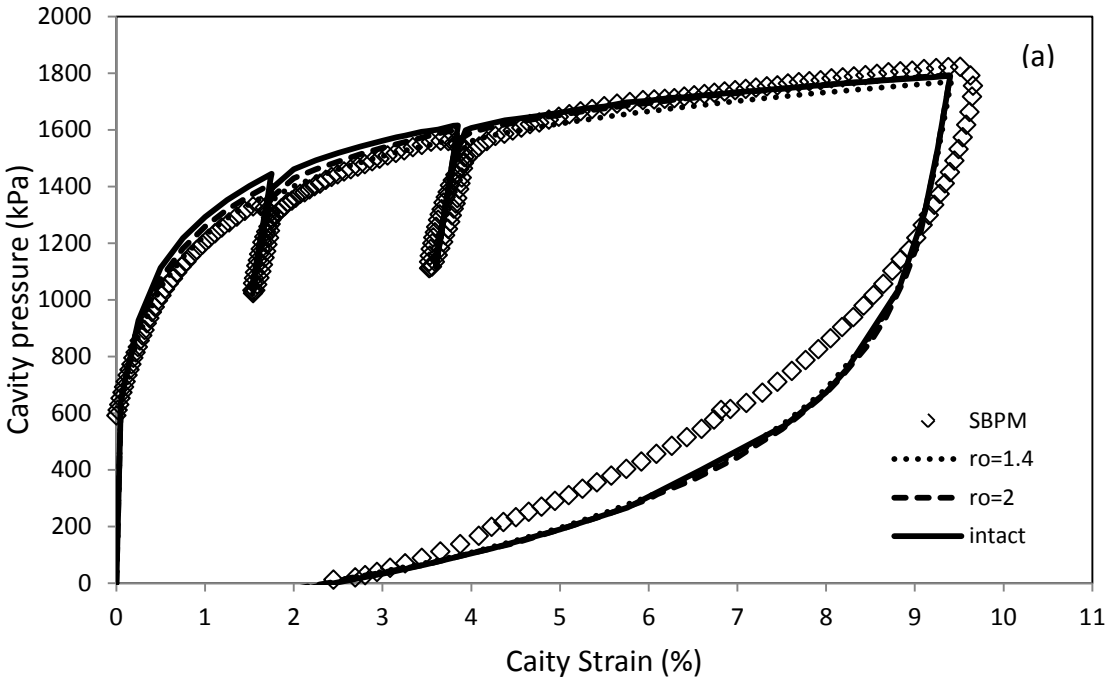

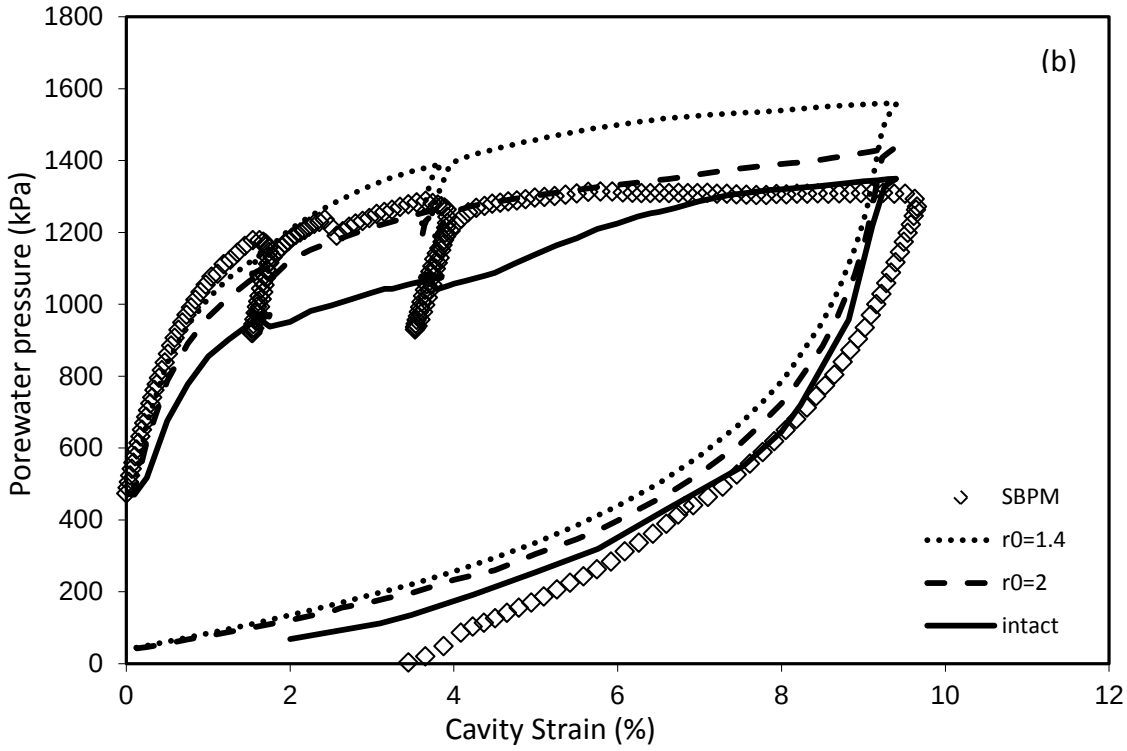

Figure 4.31: Comparison of numerical and experimental results for the sensitivity analysis on the disturbance effects : (a) cavity strain and (b) pore pressure

4.11 Summary and conclusions

The aim of this study was to analyse the performance of the KHSM in the context of the SBPM test and to characterise the degree of initial structure of London clay deposits for a site in central London, based on comparisons with experimental data. A set of material parameters have been produced that can be used as a benchmark for subsequent numerical models in London clay at similar depths. Overall, it can be stated that the KHSM, which incorporates structure and its degradation, produced cavity pressure-cavity strain and pore pressure-cavity strain predictions that are in good agreement with the observed behaviour. Since there is an abundance of information about soil properties related to the reconstituted state of the London clay, this study was able to outline some indicative values for the bond related properties of this soil. The premise that the SBPM is installed without damage was also investigated. Numerical analyses were performed to investigate the effect of drilling disturbance of the Self Boring Pressuremeter results. Overdrilling, underdrilling and smearing are considered as the main causes of disturbance for the test in clay The drilling process normally changes the pore pressure profile significantly. The findings indicate that the installation process caused some damage the initial structure. The degree of initial structure will but be somewhat smaller close to the cavity and retain its intact value at some distance from it.

Chapter 5: The influence of degradation of structure on the behaviour of a full scale embankment

This chapter investigated the behaviour of a full scale embankment, constructed at Saint Alban, Quebec. The soft clay foundation was modelled with the kinematic hardening model for structured soils (KHSM) described in Chapter 3. The chapter is divided into two parts. The first part deals with the pre-failure behaviour of the embankment in a two-dimensional analysis. It presents a comparison of the deformational behaviour predicted by the three-surface model (KHSM) and the standard two-surface bubble model (KHM) when the same undrained strength is assigned to both models. The numerical predictions of pore-water pressures and settlements are also compared with field measurements. The second part of the chapter studies the three dimensional effects on the pre-failure response of the embankment. Comparisons between the two and three dimensional analyses are made with emphasis paid on the aspects that could not be modelled correctly with the two dimensional plane stain models in the past.

5.1 Introduction

Design and construction of engineered structures on soft soils is becoming more commonplace because of the lack of better land available for construction in both developed and developing regions of the world. The design challenges involve the identification of appropriate constitutive modelling of the behaviour of the soils, including fundamental features, such as historical and induced anisotropy, presence of and damage to soil fabric or structure, and variation of stiffness with strain. Whilst it would be possible to consider the influence of soil structure in a number of situations, for the purpose of this research the effects upon a man made earth embankment were investigated. Earth embankments are one of the most common geotechnical structures and have uses within a number of industries including transport, flood defence and the investigation of new geotechnical technologies. Due to their function they are very often built upon soft clay deposits in river estuaries which almost always exhibit anisotropic behaviour (Zdravković *et al.*, 2002). This behaviour is present within the Champlain clay deposits of Quebec, Eastern Canada, on which a test embankment was constructed by Laval University in 1972. A wide range of literature is available covering both the geotechnical behaviour of Champlain clay and the Laval University embankment indicating that there is a large scope for comparison and discussion. This research was aimed to further investigate the pre-failure response on the previous findings by trying to offer a more accurate simulation of the field observations whilst concurrently providing an original approach to soil structure modelling.

Settlement and stability are the two basic geotechnical design challenges for embankments on soft clays. Traditional soil mechanics estimates the settlements of structures on saturated clays using one-dimensional compression data from oedometer tests, while stability is estimated using limit equilibrium methods. Although such classical approaches provide useful information to guide engineering design and are still widely used in practice, their accuracy has largely been limited by the shortcomings in the assumed models of soil behaviour and the uncertainties in estimating the material parameters (Lambe and Whitman 1979). With a more realistic model for soil behaviour numerical simulations provide the

possibility of following the progressive yielding of the foundation soil so that settlement and stability can be studied together. A practical difficulty associated with numerical analysis using advanced models, however, is that a larger number of material parameters and greater computational effort are required. Nevertheless, in combination with relevant experimental data, numerical methods have proved to be a popular tool for geotechnical analyses.

Advanced geotechnical design for soft clays has often made use of finite element analyses using soil models, such as Cam clay, constructed within the framework of elasto-plasticity (Roscoe and Burland 1968; Muir Wood 1990), as described in detailed in chapter 2. Traditional approaches to soil modelling have rested upon constitutive laws which consider the physical and mechanical characteristics of what can be termed a reconstituted material. However, many natural types of clay exhibit some degree of initial structure or fabric (Burland 1990; Leroueil and Vaughan 1990) and exhibit distinctly anisotropic behaviour, both in strength and stiffness because of their depositional origin and subsequent consolidations under self-loading (Tavenas and Leroueil 1977). Through robust processes of sampling at site and remoulding within the laboratory any structure which the soil possessed is thus destroyed and therefore, it is understood that the soil parameters derived from tests on reconstituted materials do not provide an accurate indication of true soil behaviour. The natural structure in existence within a soil can be classified into two distinct components; the soil fabric which represents the geometry of the particles, and the bonding which represents the interparticle forces. A soil material can thus be referred to in one of two ways; either natural/structured or reconstituted. A natural soil will exhibit a defined structure which is often anisotropic and the mechanical properties of the soil are often reliant upon this feature.

In choosing constitutive models for the finite element analysis, however, different soils may require different models to account for their individual properties. This is particularly true for natural clays, as they are generally described by state, stress history and structure. During the loading process beyond yield, natural soils progressively lose their in situ structure and sensitivity and are transformed into

remoulded materials with mechanical behaviour controlled by the intrinsic properties of the soils (Cotecchia and Chandler 1997).

Soft clays are a group of materials that display such characteristics, as the loading process may cause a breakdown to the initial interparticle bonding and thus a loss of structure (Smith *et al*. 1992; Callisto and, Calabresi 1998). The response of natural soils upon loading depends in many cases on the inherent anisotropy which stems from the soil's geological history and in frequent cases is dictated by the mode of deposition of the geological material as well as the consolidation pressures which the soil has experienced in the past (Yildiz *et al.*, 2009). Leroueil and Vaughan (1990) stressed the importance of considering structure, stating its importance to be as great as those of porosity and stress history. If this notion is to be adhered to, then it is clear that the traditional approaches that have been used to model soils will be deficient within realistic geotechnical applications. The drawback of the Modified Cam-Clay that does not account for the temporary existence of structure in soft clays dictates the use of an alternative constitutive model that is capable of including the initial structure and its progressive degradation. Therefore, it is essential when modelling geotechnical problems on soft structured clays to use a constitutive model that accounts for the effects of loss of structure and anisotropy (Karstunen et al. 2005; Yildiz et al. 2009).

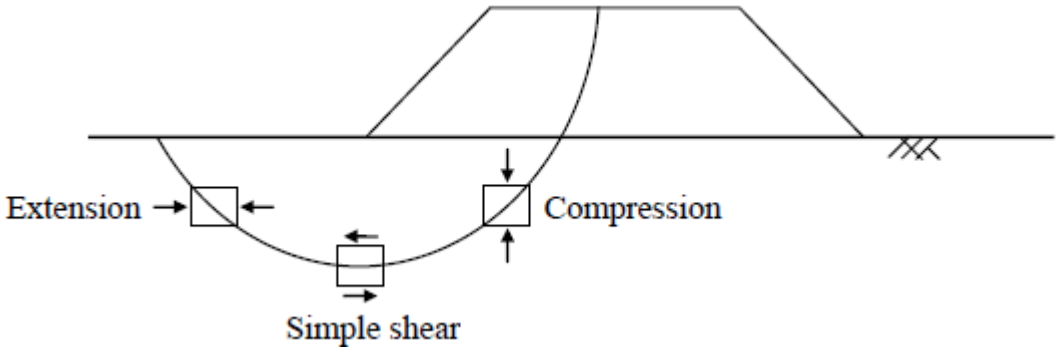

Figure 5.1: Idealised embankment cross-section

The significance of the above statements can be displayed by considering the common failure mode in figure 5.1. As an embankment fails in this manner a shear surface is produced. Along this surface a number of mechanisms take place, including; extension, pure shear and compression of the soil mass, factors which the simpler modelling techniques are deficient in their representation of. The occurrence of these mechanisms within a structured soil can result in the

aforementioned effect of destructuration. The extents to which this processes occur, and the mechanisms controlling this phenomenon, are some of the aspects which will also be studied.

Currently there is an abundance of models which can be used to run finite element analyses of an embankment type problem. In the majority of examples however constitutive models for reconstituted clays are used to simulate the behaviour of natural clays, neglecting effects such as anisotropy and degradation of structure (destructuration). To this end, there have been considerable advances in constitutive modelling of natural soils which explicitly account for structure and damage to structure, within a single yield locus elastic-plastic framework (Gens and Nova 1993; Liu and Carter 2002; Asaoka et al. 2000). Other proposals for modelling such clays use a framework of kinematic hardening and bounding surface plasticity (Kavvadas and Amorosi 2000; Baudet and Stallebrass 2004).

The available experimental data for the Saint Alban embankment provided a useful opportunity to verify a finite element code for elasto-plastic analysis, which in turn was used to analyse the performance of the several embankments at St Alban under varying design scenarios. Embankment A at the St Alban site has been a subject of various studies in the past. Constitutive models that have been used to predict the failure height and deformation behaviour of this embankment include the MIT-E3 model (Whittle and Kavvadas, 1994) and Modified Cam-Clay as used by Zdravkovic et al. (2002). More recently, the embankment was modelled by Grammatikopoulou et al. (2007, 2008) using the 2-SKH and 2-SKH-S models, the latter accounting for natural structure and its progressive loss.

5.2 Site conditions at St Alban

Four fully instrumented trial embankments were constructed by the geotechnical group at Laval University on sensitive Champlain clay foundations at a site, St Alban, situated approximately 80 km to the east of Quebec City. The first of the four embankments (embankment A), which is the focus of this study, was built to fail. The other three were constructed for long term monitoring of settlement behaviour. Details of these are given in Tavenas et al. (1974, 1983). The conditions

at the site would seem to be ideal for further study of the influence of structure in soils. The area is underlain by Champlain clay deposits to which numerous publications have provided a vast array of test results describing the material's physical and mechanical characteristics.

The extent to which the strength of this particular soil varies when considering anisotropy was highlighted in the works of Lo and Morin (1972). The authors adopted a method of triaxially testing samples of Champlain clay which had been cut at a series of angles between 0 and 90 degrees to the vertical. It was evident within the findings that the plane on which the principal stress is applied performs an important role. The results obtained displayed that strength across the stratification of the material was approximately 3 times of that along the plane. The importance of this finding becomes evident when considering the slip surface highlighted in figure 5.1 where it is evident that the direction of principal stresses would be acting at numerous angles along the failure plane. Thus if the above findings are to be taken into account an extensive variation in mobilised strength would occur.

Along with strength variance, within the original report discussion is also provided regarding the brittle behaviour which structured clays are shown to exhibit, a factor that can be attributed to the degradation of cementation bonds (Lo and Morin, 1972). Destructuration and thus reduction to residual strengths will therefore occur at relatively small strains. Evidence of this was presented by Lefebvre and La Rochelle (1974) where tests on Champlain deposits displayed peak strength that was achieved at approximately 1% strain. This was consequently accompanied by a rapid decrease in strength.

The underlying drift geology comprises of soft of sensitive Champlain clay, a marine clay formed during the period 12000 to 50000 years ago as the retreat of glaciers and the Champlain sea from North America took place. A rapid sedimentation of around 1600 cm/1000 yrs (Leroueil et al. 1990), coupled with the high salinity environment in which the clay was formed has created a formation of open structures in the clay. This has contributed to a very high

natural water content and high sensitivity, low shear strength and high compressibility under foundations

The financial repercussion of constructing embankments on foundations of sensitive Champlain clay deposits become quite evident when one considered the distribution of these deposits on the territory of eastern Canada; they cover the major part of the lowlands on both sides of the rivers Saint-Laurent, Ottawa, and Saguenay and also the region of the Lake Saint-Jean (figure 5.2). For that reason, a detailed site investigation was undertaken at St Alban prior to the construction of the four trial embankments.

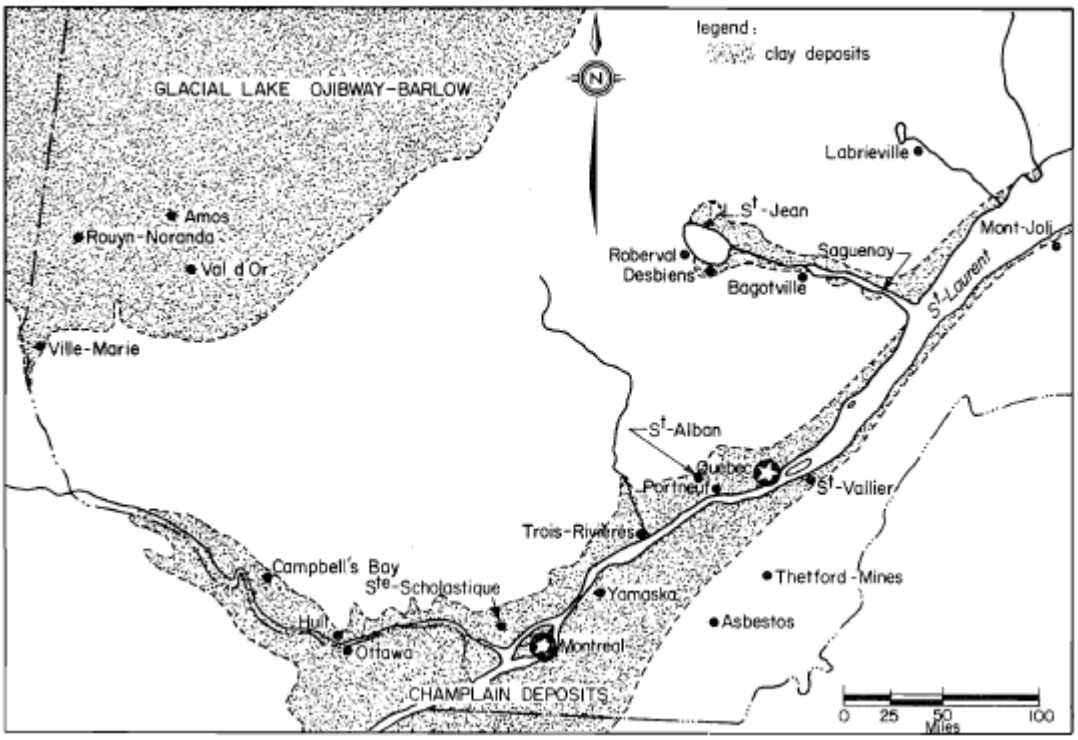

Figure 5.2: Geographical distribution of the sensitive clays in part of eastern Canada. (LaRochelle et al. (1974))

Ground conditions at the site were fairly uniform and comprised a weathered clay crust 2m below the ground level. Underlying the clay crust, extending to a depth of 13.7m below ground level, was soft, silty, marine clay. Beneath this soft clay, a dense fine to medium sand was found extending to more than 24m below ground level. The soil profile at the Saint Alban site can be seen in figure 5.3 below.

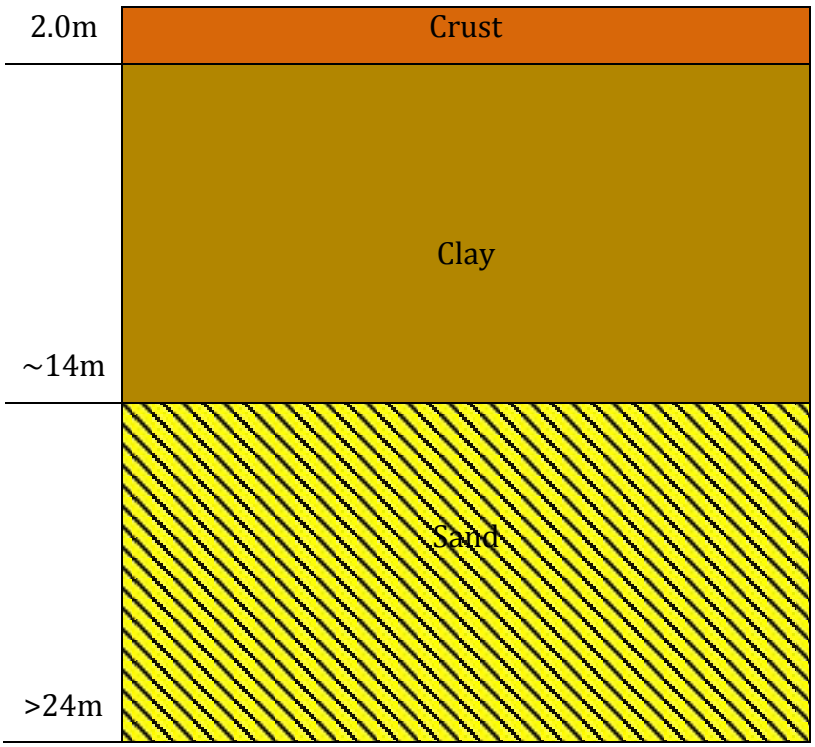

Figure 5.3: Typical Soil Profile at St Alban site. (LaRochelle et al. (1974))

The groundwater table was encountered close to the surface at 0.7m below ground level. The bulk unit weights above and below the water table were calculated as 19 kN/m^3 and 16 kN/m^3 respectively (La Rochelle et al. 1974). A number of *in-situ* and laboratory tests were performed during the detailed investigation. *In-situ* testing comprised vane tests, with samples retrieved (as intact as possible) for isotropically consolidated undrained (CIU) and unconsolidated undrained (UU) triaxial tests. Tavenas *et al.* (1983) showed that the permeability of the Champlain clay is around 10^{-10} to 10^{-9} m/s.

As can be seen in figure 5.4 the vane tests produced a wide range of undrained shear strength throughout the soil profile, particularly in the crust and at a depth of 7-8 m. It was initially thought that the in-situ vane test yielded higher strength values than the standard laboratory triaxial tests, but laboratory tests on block samples of the Champlain clay produced higher values of undrained shear strength than measured with the vane. La Rochelle et al. (1974) suggested that the disturbance resulting from the intrusion of the vane into the soil mass was partly responsible, since structure of the clay was partly damaged prior to the

commencement of the test, therefore resulting in underestimate of the *in-situ* peak strength.

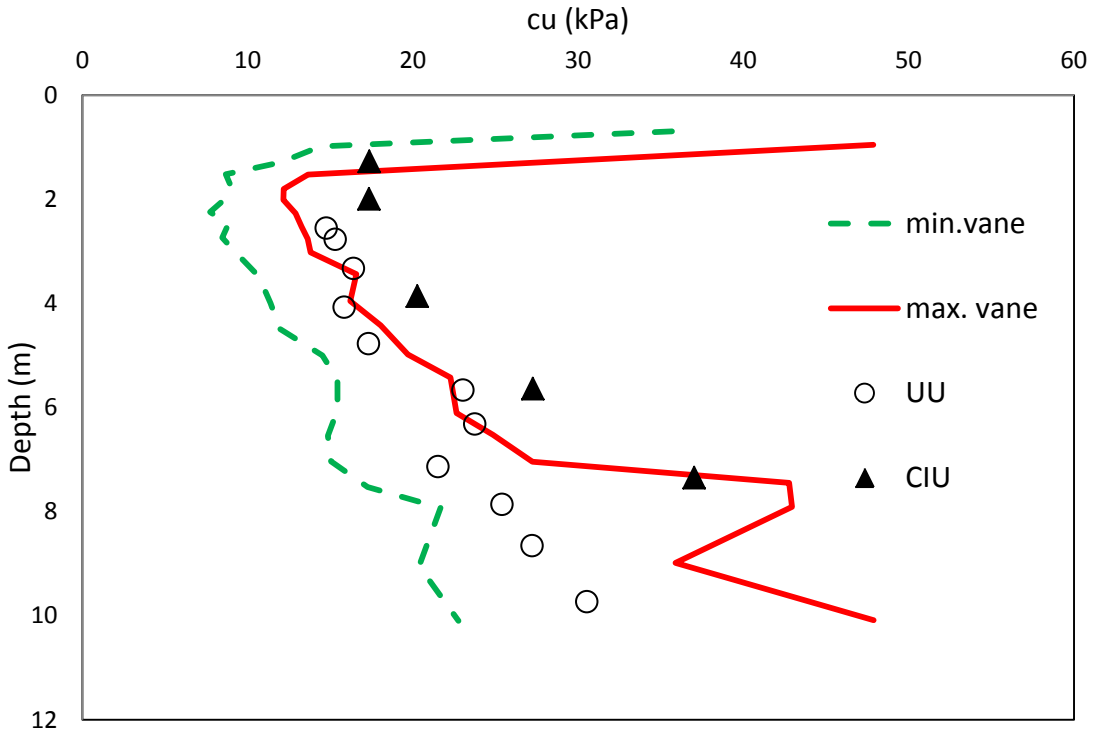

Figure 5.4: Undrained strength profiles for the clay at Saint-Alban (data after La Rochelle et al. (1974))

5.3 Embankment geometry and construction sequence

Figure 5.5a depicts the cross-section of the embankment adopted in the simulations. Three sides of Test embankment A had a 2:1 slope and were supported by placing a 1.5m high berm. Conventional stability analysis indicated that Test embankment A could be constructed to a height of 4.6m. At that height, the crest length would be 30.5m, with a width of 7.6m. The fourth face of the embankment had a steeper slope of 1.5:1 in order to encourage failure to occur in this direction. The construction of the embankment is described by La Rochelle et al. (1974). First, 0.6m of sand fill was placed and compacted by two passes of a vibrating roller. Then each day a further 0.3m was placed twice a day until failure occurred. To ensure uniform density, each layer of fill was compacted with the same energy as the initial 0.6m. The slope faces were trimmed by hand to ensure dimensional accuracy.

Additionally, vane tests and cone penetration tests were carried out to confirm the location of the failure surface. Settlement plates were installed beyond the toe of the embankment (R1 to R15) and within the embankment (R16 to R27). The latter plates were only installed after the first 0.6m of fill had been placed. The vertical and horizontal movements were measured using precise levelling and other surveying methods.

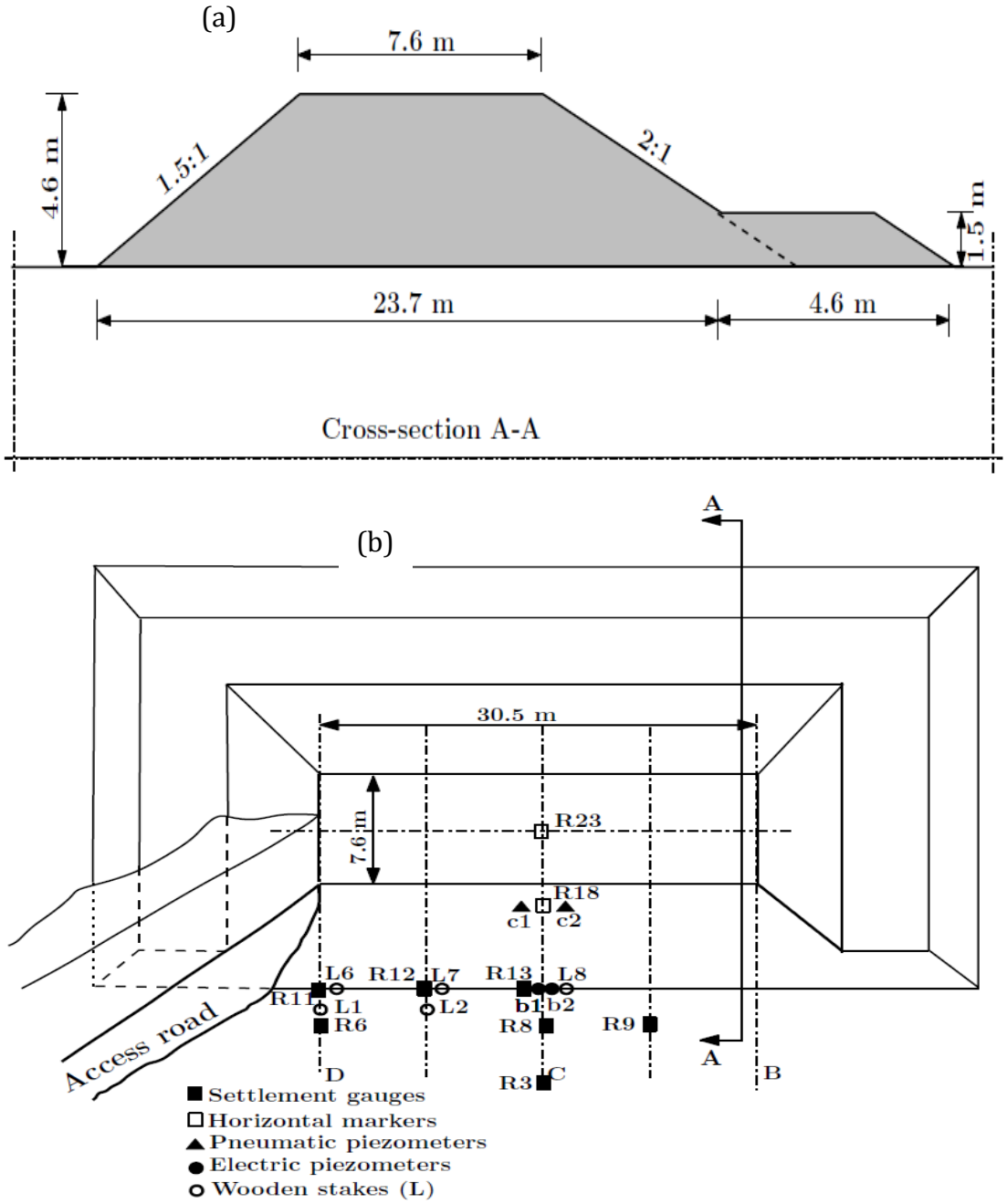

Figure 5.5: St Alban test embankment: (a) plan view and (b) cross section A-A of the embankment.

Instrumentation was located within and beyond the unsupported side of the embankment, in order to record details of the pore water pressures and settlements. The location of the failure surface was determined by placing ten, 5.5m long, fragile wooden stakes L1 to L10 (Figure 5.5b) into the ground at and beyond the toe of the embankment. Following failure, the wooden stakes were dug out and the position of the circular failure arc was estimated from the fractures in these stakes.

5.4 Previous finite element analyses

Zdravkovic *et al*. (2002) performed a number of plane strain finite element analyses of the test embankment A, investigating the effect of strength anisotropy on the behaviour of the embankment. The study used the test embankment built by Laval University in 1974. A comparison was carried out between the MIT-E3 (Massachusetts Institute of Technology) Constitutive Model for Overconsolidated Clays and the modified Cam-clay. Details of the MIT model were provided by Whittle and Kavvadas (1994).

From in-situ and laboratory tests it was discovered that foundation clay to be analysed had significant strength anisotropy. The anisotropic MIT-E3 model predicted a failure height of 3.9m which was the actual height observed. It also provided a good agreement between observed and predicted horizontal and vertical displacements. However whilst failures were in good agreement, there was a large discrepancy within the position of the failure surface. The authors attributed this as a limitation prescribed by the plane strain analysis, whereas using three dimensional software packages, may have yielded more accurate behaviour. No failure plane was predicted for the modified Cam-clay analysis; however the inaccuracies of the model were highlighted with a predicted failure height of 4.9m.

The extent to which advanced soil models can influence the results attained from simulations, in comparison to more rudimentary counterparts were further investigated by Grammatikopoulou *et al.* (2008). Simulations of the same embankment were executed; one in which a model incorporating a parameter to

model destructuration of the foundation material was implemented, and one in which a version of the Muir Wood, Al-Tabbaa bubble model was to be utilised. The model bore similarities to that presented by Baudet and Stallebras (2004), this however only utilised two surfaces; a Natural Bounding Surface and an Inner Kinematic Yield Surface.

The results from running the comparative analyses were measured against the test embankment constructed in St Alban, Quebec (1974) and again highlighted the importance of the accurate simulation of destructuration. For small embankment heights (up to 2.5m) little difference could be observed when considering displacement with respect to height. However above this value the model which accounted for destructuration displayed a more brittle response and thus failed at a lower height. The paper thus demonstrates the dangers of neglecting destructuration, the most prominent being an overestimation of embankment height.

5.5 *Derivation of the KHSM model parameters*

5.5.1 *Slopes of normal compression and swelling lines λ^* and κ^**

These material parameters were derived from an oedometer test from a depth of 6.5 m (data from Leroueil (1977)) as reported by Grammatikopoulou (2004). Figures 5.6 (a) and (b) plot the oedometer data in ln$v$-lnp' space, with the estimations for the material parameters values.

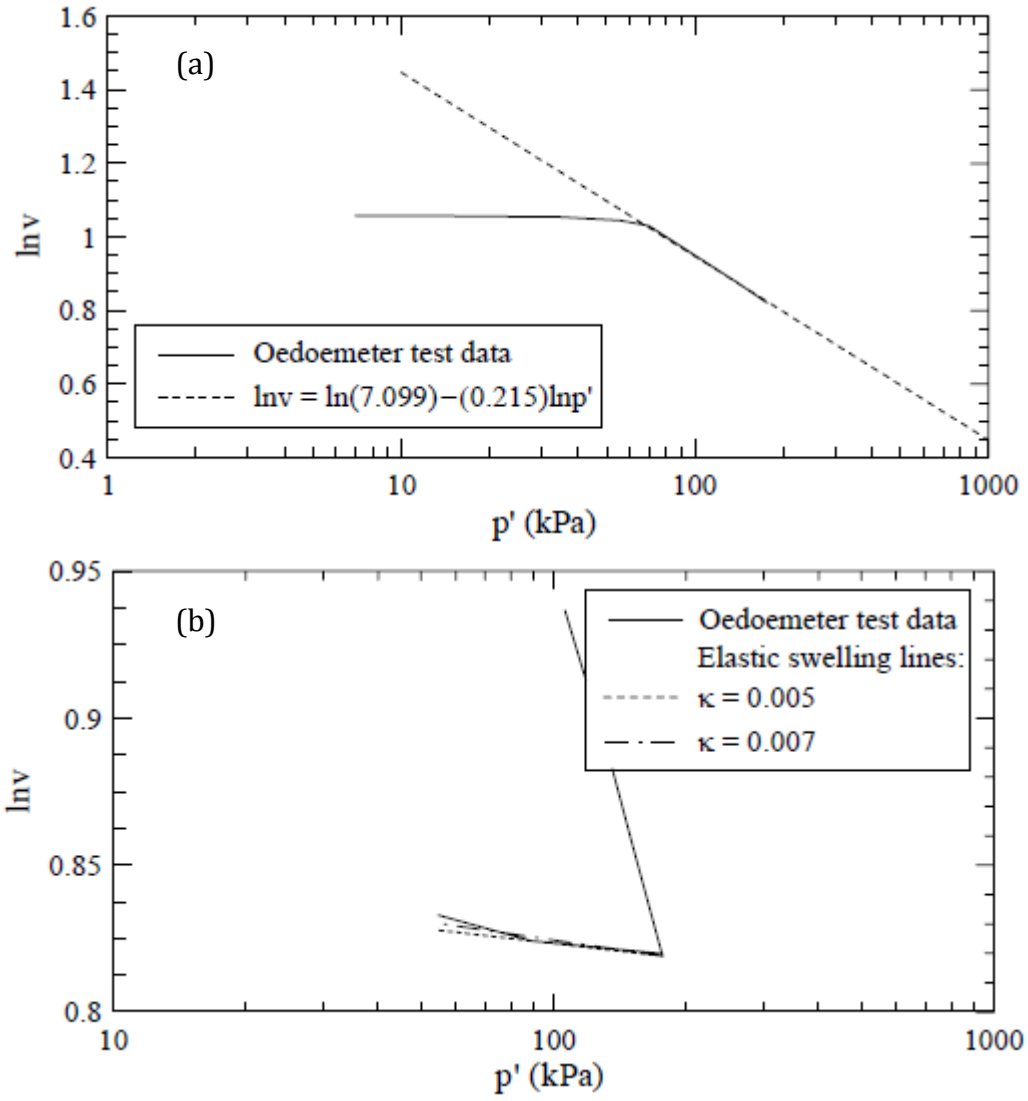

Figure 5.6: Determination of material parameters (a) compression parameter λ^* and (b) swelling parameter κ^* (Grammatikopoulou, 2004-data from Leroueil (1977))

5.5.2 *Elastic properties*

The elastic behaviour described within the bubble surface, was assumed to be nonlinear elastic (see Chapter 3) and was described by the following equation proposed by Viggiani and Atkinson (1995):

$$\frac{G}{p_r} = A_G \left(\frac{p'}{p_r}\right)^n R_0^m \tag{5.1}$$

where A_G, n and m are dimensionless parameters which were estimated using the plasticity index of Champlain clay, p_r is a reference pressure which is usually taken equal to 1 KPa and $R_0 = p_c/p'$ is the overconsolidation ratio. The overconsolidation ration value was varied in order to achieve the required undrained shear strength (see Section 5.7). For a plasticity index of 22% reported by Tavenas et al. (1974), the following parameters were estimated: A_G = 1400, n = 0.76 and m = 0.22.

5.5.3 *Friction angle and critical state ratio*

The value of φ' at the critical state was taken equal to 27°, based on the work of Leroueil (1977). This in turn gave a critical state ratio M of 1.07clalculated from the following equation:

$$M = \frac{6 \sin \varphi'}{3 - \sin \varphi'} \tag{5.2}$$

5.5.4 *Bubble size R and kinematic hardening parameters B and ψ and structure related parameters r_0, k and A*

Calibration of the remaining KHSM model parameters was carried out by simulating three undrained triaxial compression tests on isotropically compressed samples (Tavenas and Leroueil 1977), taken from a depth of 3m. In view of the lack of available test data with measurements of strains in the very small and small strain region, a value of R equal to 0.11 was adopted for the calibration process.

It has been well established that the form adopted for the interpolation function will influence the response of soils. The calibration process for the determination of the additional material parameters ψ and B, which control the rate of decay of stiffness with strain and the magnitude of the contribution of the interpolation term, respectively, yielded values equal to 1.6 for the stiffness exponent and a value of 1 for parameter B. These values provided an excellent fit to the experimental data under consideration.

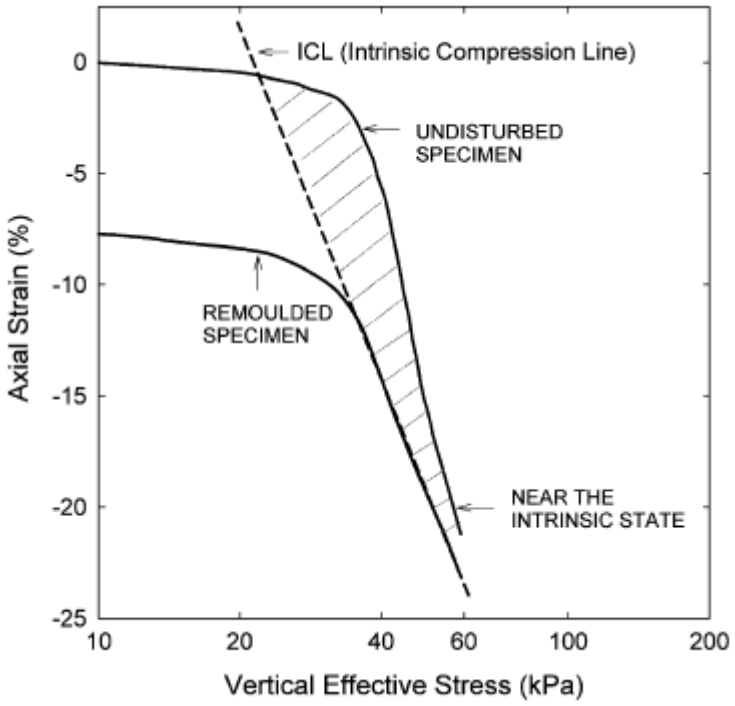

Figure 5.7: The influence of structure on the yielding of St. Alban clay: Structured and intrinsic oedometer compression curves (Leroueil *et al*, 1979).

Review of published literature provided an indication of the range of values for the measure of the initial degree of structure, which was assumed for the foundation soils. Figure 5.7 shows the difference between the oedometric behaviour of structured and reconstituted St Alban clays. It is evident that there is a clear yield point for the natural, undisturbed specimen at vertical stress of 45 kPa. Gasparre and Coop (2008), defined the stress sensitivity of London clay as the ratio of the yield stress of the natural material to the vertical stress on the intrinsic compression line (ICL) at the same void ratio. Following that definition, if the vertical stress of the remoulded specimen is assumed to be in the region of 22kPa for the same axial strain (figure 5.7), the stress sensitivity of clay for the site under consideration may be extrapolated from the above results to have an estimated value of 2.1. This value for the stress sensitivity was assumed to correspond to the initial structure parameter in the KHSM model and therefore r_0=2.1 was adopted for the finite element analyses. It should be noted that this value was found to be in good agreement with the measured sensitivity value of 2.4 at a depth of 3m as reported by Silvestri (1995). The fact that this type of sensitive clay had been modelled previously using similar models for structured clays was very helpful in

speeding the calibration process. The destructuration strain parameter A was taken as 0.75, which implies that the contribution of the plastic shear strain to the destructuration process is 3 times larger than that of the plastic volumetric strain. Parameter k which controls the destructuration process was calibrated to a value of 5.7. The anisotropy of the initial structure surface was found to be best captured if a value of η_0=0.3 was adopted.

The calibration process described above yielded the material parameters provided in Table 5.1.

Material constants	Value
Slope of swelling line κ^*	0.005
Slope of normal compression line λ^*	0.215
Critical state stress ratio M	1.07
Ratio of size of bubble and reference surface R	0.10
Stiffness interpolation parameter B	1.0
Stiffness interpolation parameter ψ	1.6
Destructuration parameter k	5.7
Destructuration strain parameter A	0.75
Initial degree of structure r_0	2.1
Aniotropy of initial structure η_0	0.3

Table 5.1: Calibrated KHSM Parameters

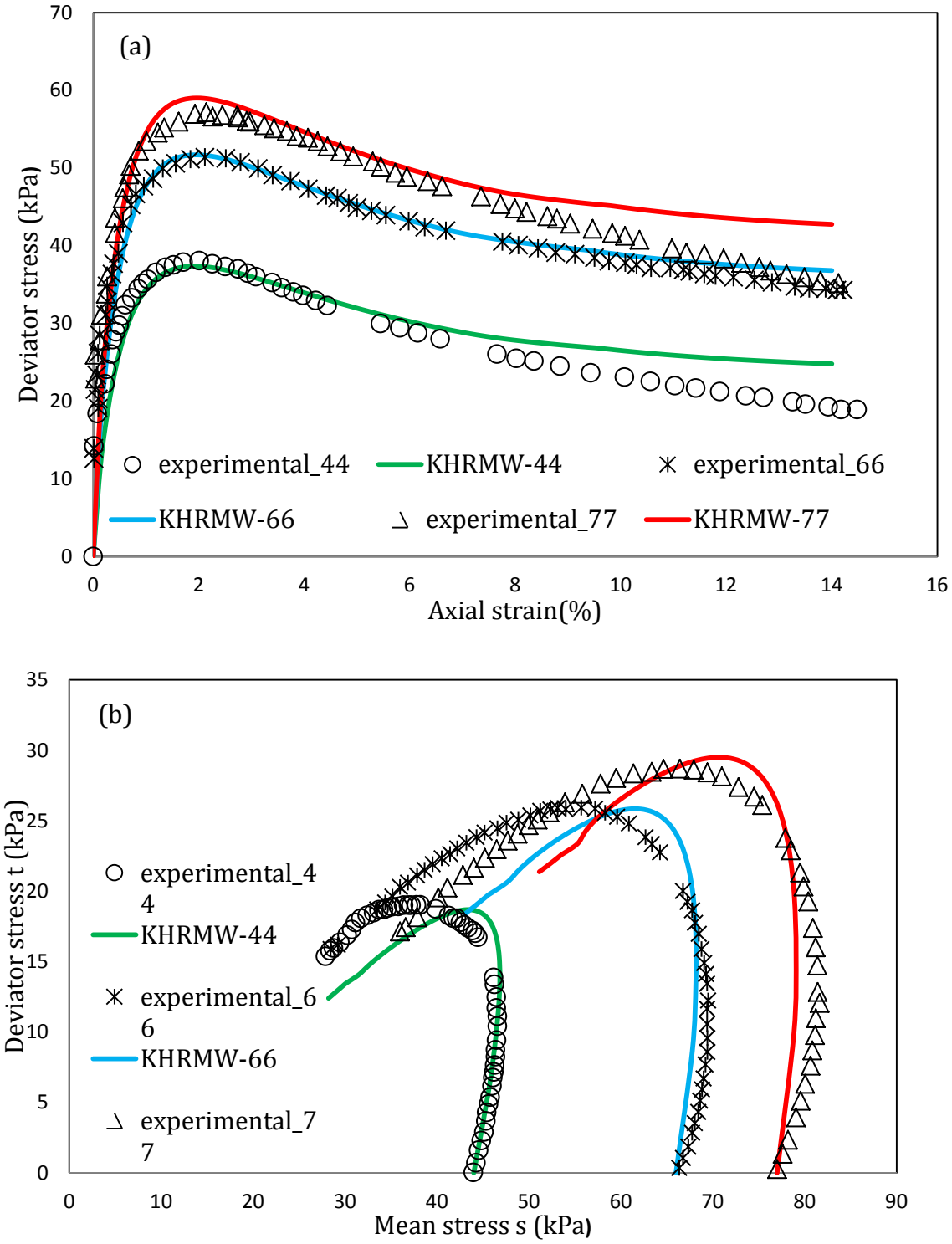

Figure 5.8: (a) Stress-strain curves and (b) stress paths for CIU normally consolidated tests taken at a depth of 3m

Figure 5.8 presents the simulations for the three different isotropic consolidation pressures of 44, 66 and 77 KPa. It can be seen that the simulations with the optimized parameters provide excellent agreement with the experimental results.

The overall behaviour is very well captured in terms of peak strength (figure 5.8a) and stress path (figure 5.8b)

5.5.5 *Model validation with KHM-bubble model*

The importance of the contribution of the cementation bonds to the shear strength of the Champlain clay was better understood, after elaborate laboratory testing programs were carried out back in the 1970's by a number of researchers. The bonds were found to be responsible not only for the relatively high peak strength but also for the remarkable brittleness of the clay structure. Furthermore it was found that the cementation bonds was significantly strain sensitive and brittle, as the residual strength was reached at fairly low strains.

Taking into account the strain softening characteristics of this clay and the possibility of progressive failure of the trial embankment, an investigation on the effects of structure degradation was carried out as a part of this work. In order to investigate the influence of the strain softening response on the behaviour of test embankment A, the KHSM model was reduced to the bubble model (KHM) by setting parameter r_0 equal to 1 and therefore not considering any initial measure of structure. A re-calibration procedure for the now reduced KHM-bubble model was carried out so that the predicted ultimate strength was very close to the peak strength predicted by the KHSM model (figure 5.9a and b).

As it can be seen from figure 5.9a and b, the reduced model predicts almost identical behaviour with the full structured model in terms of ultimate strength and effective stress paths. The predicted behaviour of the conventional bubble model bears many similarities with the non-linear elastic-plastic models that are widely used in industry. The inclusion of structure in the KHSM model gives rise to the salient difference between the models, which was the prediction of significant softening with loss of structure as plastic strains occur.

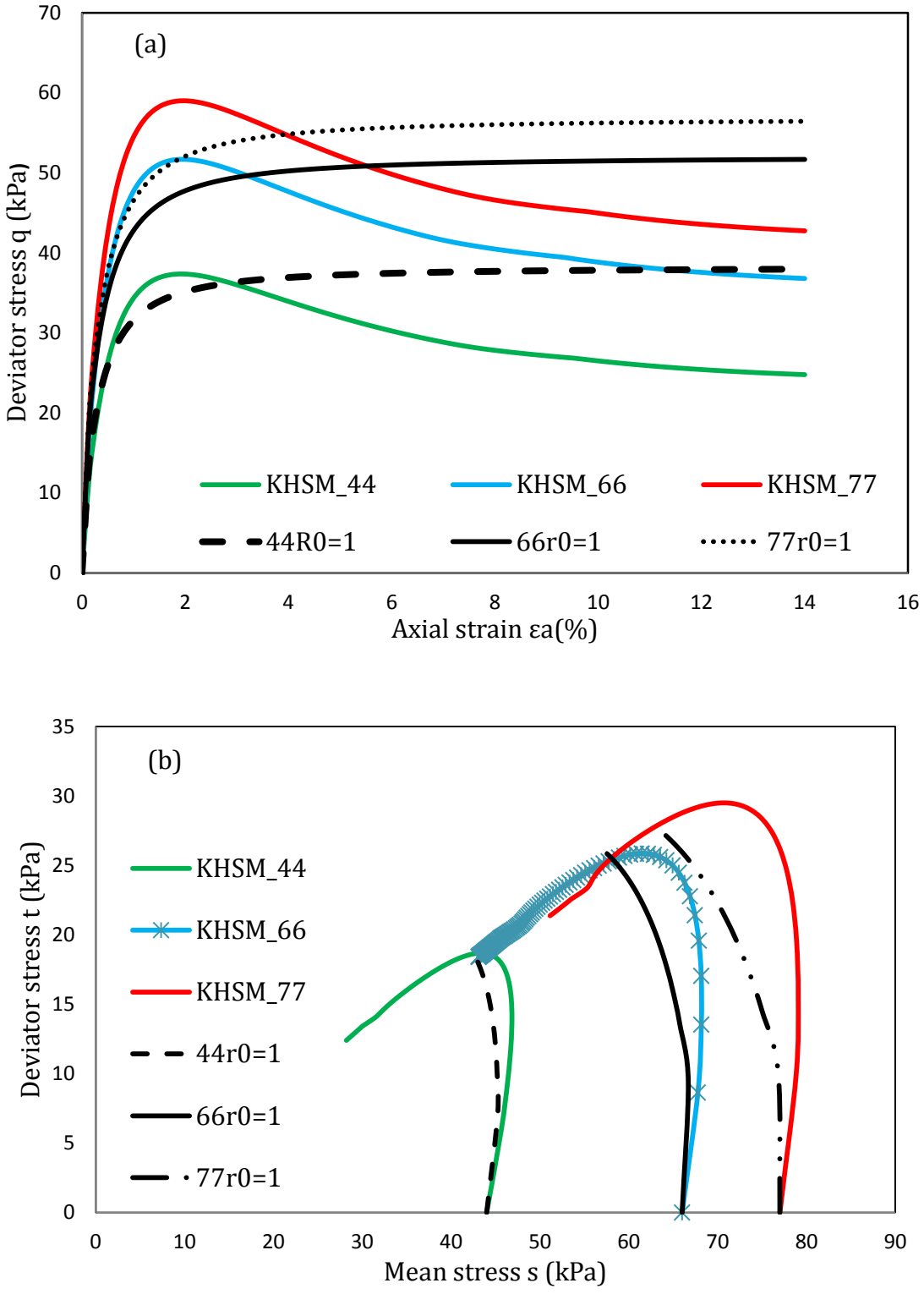

Figure 5.9: Comparison of KHSM and KHM-bubble model simulations results for undrained triaxial compression tests on isotropically consolidated clay: (a) stress: strain response; (b) effective stress paths.

5.5.6 *Embankment fill material*

The embankment was constructed using a uniform medium to coarse sand, with approximately 10% fine sand and 10% gravel and, was modelled using a non-associated Mohr-Coulomb model, which has proven to be satisfactory in previous studies. Triaxial tests performed on the sand, with densities similar to those in the field, gave an angle of shearing resistance $\phi' = 44^0$ (La Rochelle et al. 1974). A Young's modulus, E, of 10000 kPa and a Poisson's ratio, v', of 0.3 were assumed. The cohesion was assumed to be zero, and the angle of dilation $\psi = 22^o$.

5.6 Soil properties and undrained shear strength profile

The deposition process of Champlain clays has given rise to a very high natural water content, low shear strength and high compressibility. As with most soft clays, the surface desiccation linked with the fluctuating water table has encouraged the formation of a weathered clay crust with an undrained strength higher than would be expected for lightly overconsolidated clays. This characteristic can have a substantial role in the stability and deformation of any engineering structure, so that the determination of the distribution of the undrained shear strength in the crust is a matter of great importance. If the assumed strength is too high, the crust can dominate the analysis of the embankment behaviour. In order to prevent this, the undrained shear strength for the crust is usually taken to be lower than that measured *in situ*, and this is justified by the existence of fissures and other reasons (La Rochelle et al. 1974; Lefebvre and La Rochelle 1974). Lo (1970) showed that the undrained shear strength for overconsolidated fissured clays on site may be only 25- 40% of the strength measured on small laboratory samples. At Saint Alban, the undrained shear strength in the upper half of the crust was taken as 32 kPa, (La Rochelle et al. 1974). This value was adopted as the undrained shear strength of the crust at the surface for the present finite element analyses.

The undrained shear strength is not a soil property but was calculated using KHSM by running undrained triaxial compression tests starting from the *in-situ* stress conditions at several points through the depth of the crust layer with varying OCR values. The profile of peak shear strength predicted by the model is plotted in figure 5.10. It can be seen that the numerical simulations are in good agreement with the CIU laboratory results. The undrained strength profile predicted using the KHM-bubble model (i.e. $r0 = 1$) in triaxial compression is also depicted on figure 5.10. A high surface strength for the crust implies a high over-consolidation ratio, decreasing with depth to a minimum value of 2, at the bottom of the weathered crust, below which it remains constant (figure 5.11) This figure shows also the OCR profile obtained by matching the observed initial strength profile with the simulated response using the bubble model (KHM with $r0 = 1.0$). The only difference between the models is the prediction of significant softening with loss of structure as plastic strains occur.

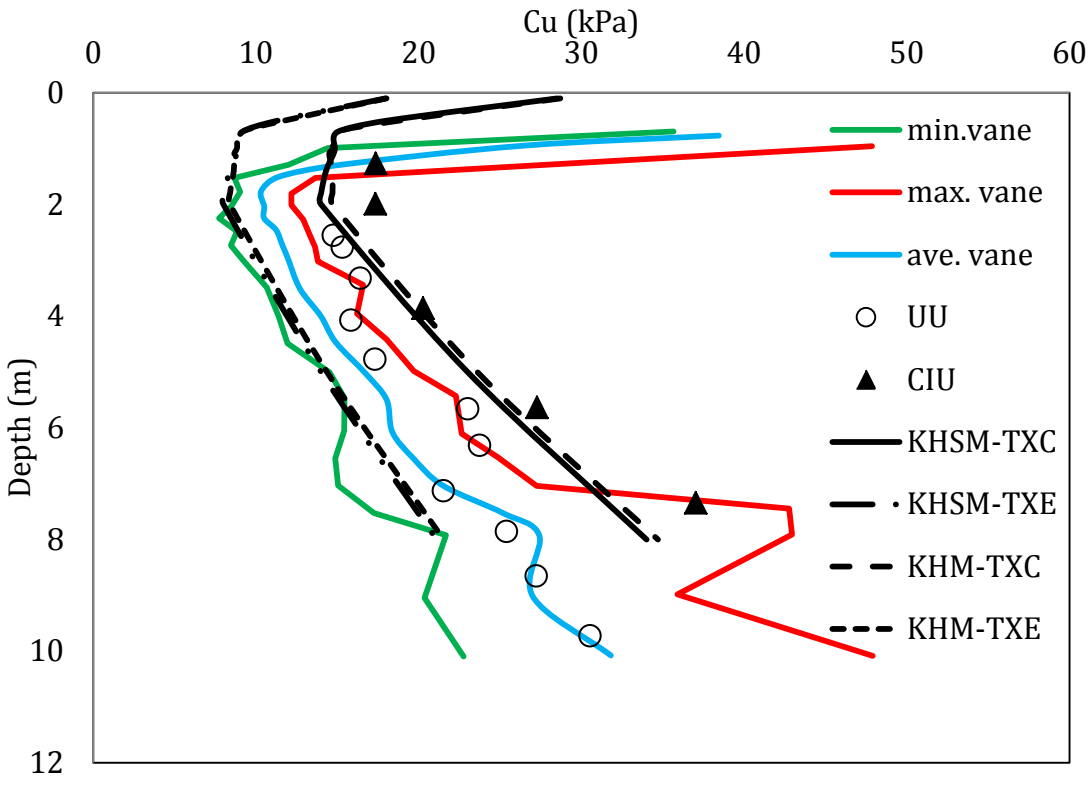

Figure 5.10: Undrained shear strength profile simulated and measured using various tests.

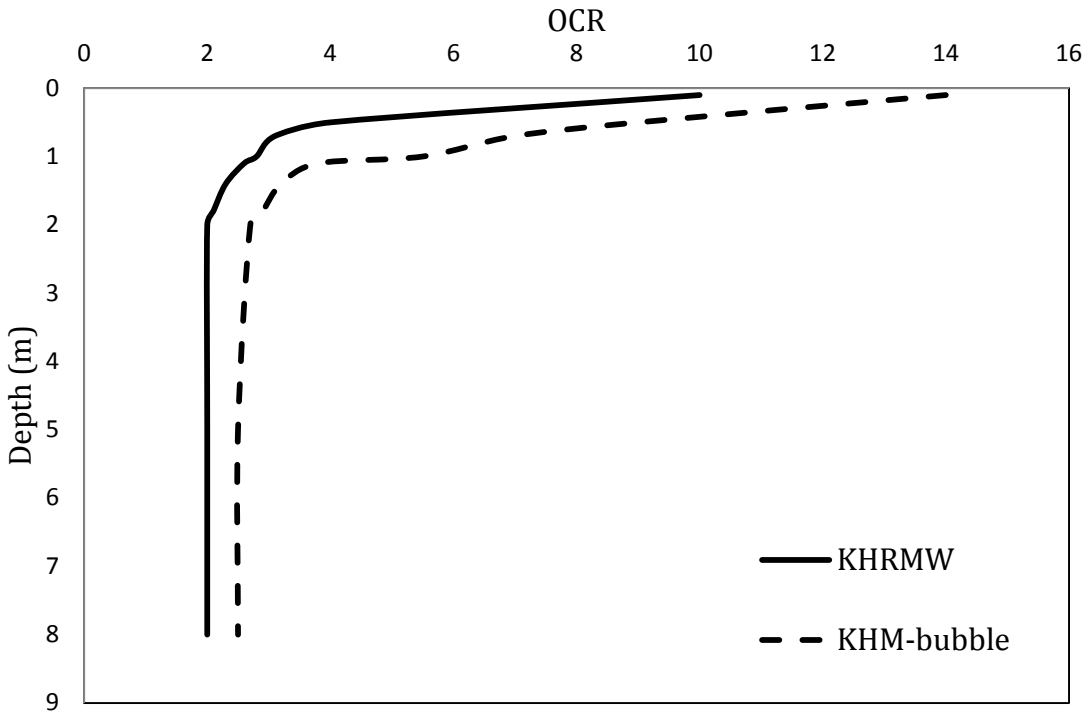

Figure 5.11: OCR profile of the clay deposit used in the numerical simulations

5.7 Finite element model

The software package Plaxis 2D was used to run the simulations in this study. The finite element mesh for the plane strain analysis of the cross-section C (La Rochelle *et al.* 1974) which is provided in figure 5.21, consisted of ~2100, 15 node triangular elements. The boundary conditions applied to the models, utilised the standard fixities option in the software, which dictates that the vertical geometry lines for which the x-coordinate is equal to the lowest or highest x-coordinate in the model obtain a horizontal fixity ($u_x=0$). Furthermore, the horizontal geometry lines for which the y-coordinate is equal to the lowest y-coordinate in the model obtain a full fixity ($u_x=u_y=0$).

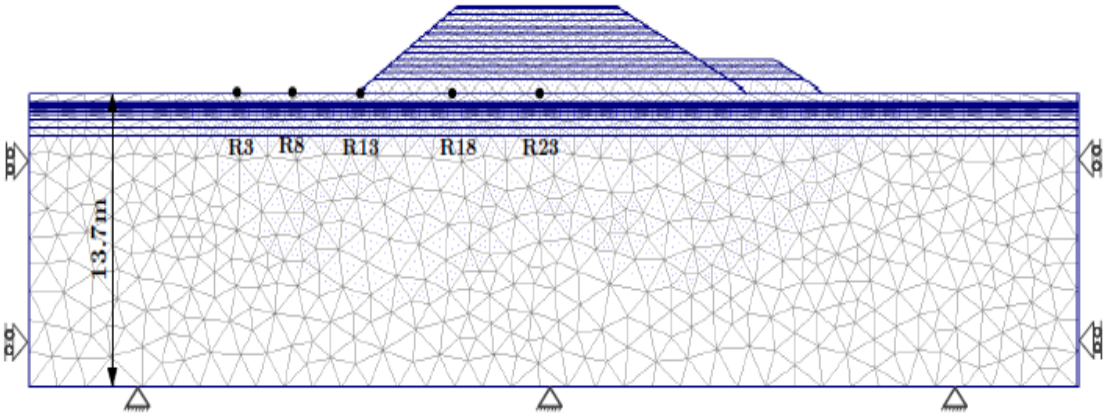

Figure 5.12: Finite element mesh for the geometry of Saint-Alban embankment

During the staged construction in 1972, the successive building of layers was followed by a very short period of consolidation, lasting less than a day. The Saint Alban test embankment A, which is the focus of this study was constructed with an initial 0.6m fill on the first day, followed by 0.3m each day until a height of 1.5m was achieved. After this height, two 0.3m layers per day were added until failure occurred. The construction sequence followed in the finite element simulations can be seen in figure 5.13. It should be noted that the two different types of calculation, plastic and consolidation, which are available in the software package were employed in order to replicate the exact construction sequence. The embankment model was designed to a height of 4.6m, which is the failure height calculated from conventional stability analysis.

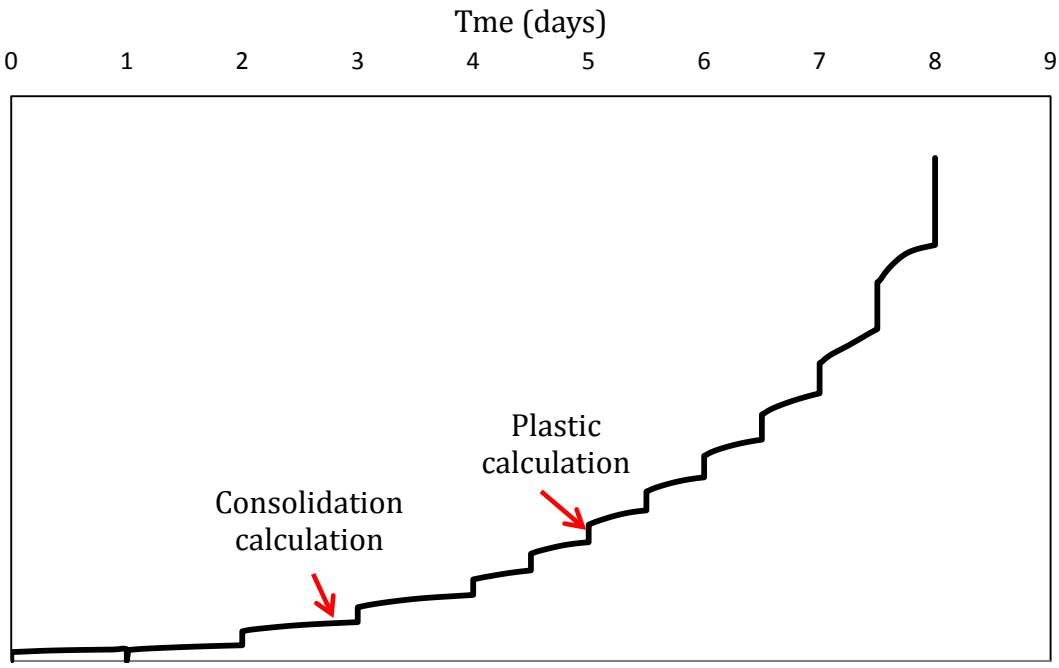

Figure 5.13: Modelling stages of the construction sequence for St Alban test embankment A

5.8 Finite element results and discussion

5.8.1 *Embankment Deformations*

Figure 5.14 shows a comparison of the observed vertical displacements on site and the calculated settlements from the finite element analysis, at settlement plate R23. It can be seen that the numerical response agrees very well with the observed settlements at both locations. The plots confirm the observations of Tavenas et al. (1974) and also reported results from other finite element studies on the embankment (Zdravkovic et al. 2002) concerning the critical height of 2.4 m, which marks the onset of more rapid deformations as the embankment height is increased and local yielding within the clay starts to have a significant effect on the overall foundation stiffness. A failure height of 3.93 m was calculated which agrees well with the actual failure height for embankment A. It can be seen that when the failure height is approached the KHSM model calculates a total displacement very close to the observed total settlement at failure. The numerical simulation, predicts a softer response of the soil between heights of 1.8 and 2.4m. The tendency of the

model to overpredict settlements is reversed between embankment heights of 3.3 and 3.6m, where the simulation under predicts the settlements by ~6.2%. When the failure height is approached the KHSM model predicts a total displacement of 0.14m, which is very close to the observed total settlement at failure of 0.15m. What can be deduced, is that the numerical simulations describe the pre-failure deformation behaviour of the soils very well around the centreline of the embankment. The figure also shows the predicted vertical settlement at R23 obtained without destructuration and by matching the observed initial shear strength profile. It can be seen that the bubble model without destructuration (KHM) predicts smaller settlement than the structure model up to an embankment height of approximately 3.3 m. Thereafter the response becomes stiffer, leading to an embankment failure height of 4.35 m. The difference is due to significant softening attributed to loss of structure which was accounted for in the predictions by the KHM.

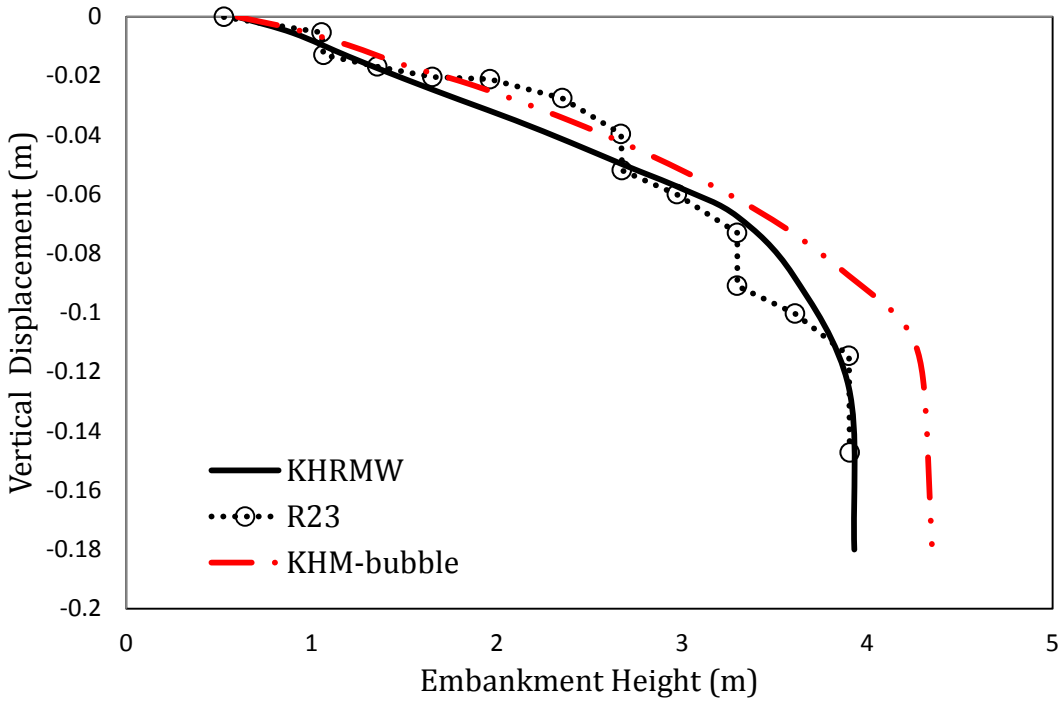

Figure 5.14: St Alban test embankment: measured and predicted vertical displacement at settlement plate R23

The comparison between the simulated and observed settlements at R18, at the surface of the clay below the crest of the embankment also shows a good agreement (figure 5.15). From an embankment height of 2.4 m onwards, more rapid deformations were observed with the numerical prediction using the KHSM converging to the settlements that occurred on site. However, for the bubble model (KHM) it can be seen that a stiffer behaviour is predicted after an embankment height of approximately 3.35 m, which resulted in overestimating the embankment failure height by 0.42 m. This is again due to the significant influence of destructuration.

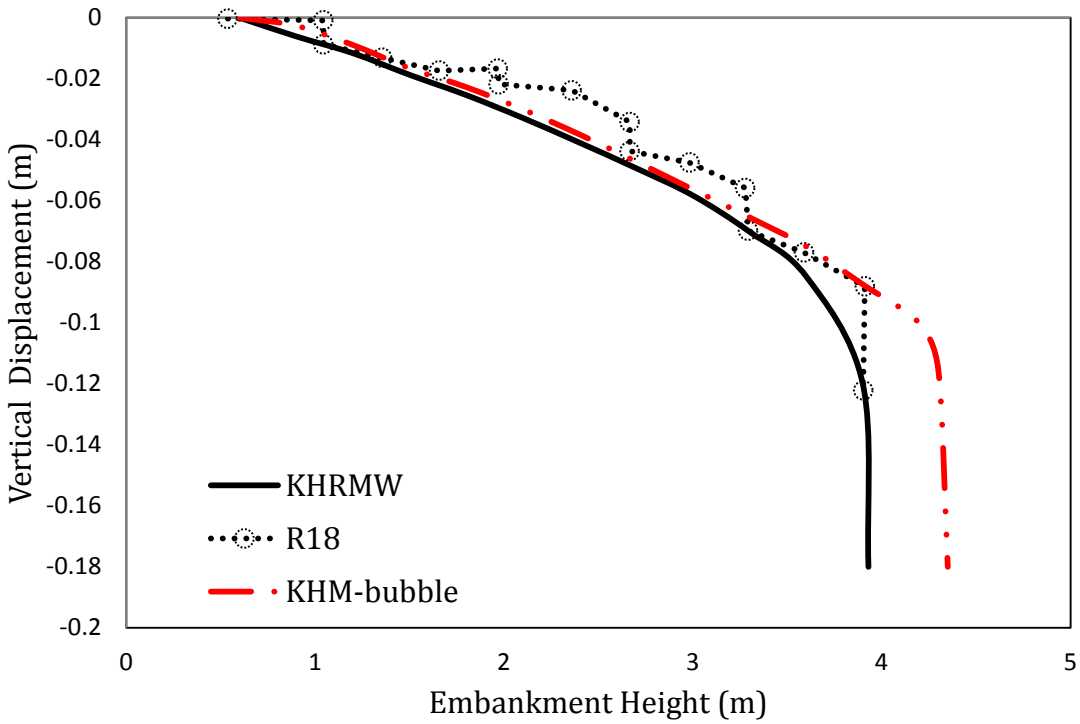

Figure 5.15: Comparison of obsereved and predicted vertical settlement at the centre of the embankment

Available data from La Rochelle et al. (1974) permit a comparison between the KHSM predictions and the observed settlements on the clay surface at different points beneath section A-A. Information was available for the vertical deformation of four points which correspond to settlement plates R23-R3 (figure 5.12). The data were collected during the application of the last 1.5 m of fill. Profiles of the observed and simulated vertical movements of the soil surface in section A-A are plotted in figure 5.16. Overall, the numerical results predict a very similar

distribution of vertical movements. The heave observed at the toe of the embankment was also successfully modelled. There is a tendency of the constitutive model to overpredict the heave at the toe (R13) and at the points corresponding to R8 and R3 for fill thicknesses of 2.4 m up to 3.3 m. The magnitude of the heave at the toe, for the failure height, is correctly estimated. As can be seen in the figure below, at a height of 3.9m the R8 plate exhibited a larger vertical displacement than the toe, which contradicts the experimental data from all lower fill heights. This *irregularity* may be explained by the description of the failure provided by La Rochelle et al. (1974), where it is stated that the toe heaved, forming a roll up to 1.2m high. In contrast, the finite element analysis maintains the trend predicting a smaller magnitude for the heave at that point (R8) for all embankment heights. For the node corresponding to settlement plate R23, the KHSM model suggests a softer behaviour when compared with the observed data at an embankment height of 2.4 m. The observed data for fill thicknesses of 3.3 m has a slightly higher magnitude than the simulated results. A final vertical movement of 0.140 is estimated by the KHSM as the embankment failure height of 3.93 m is approached.

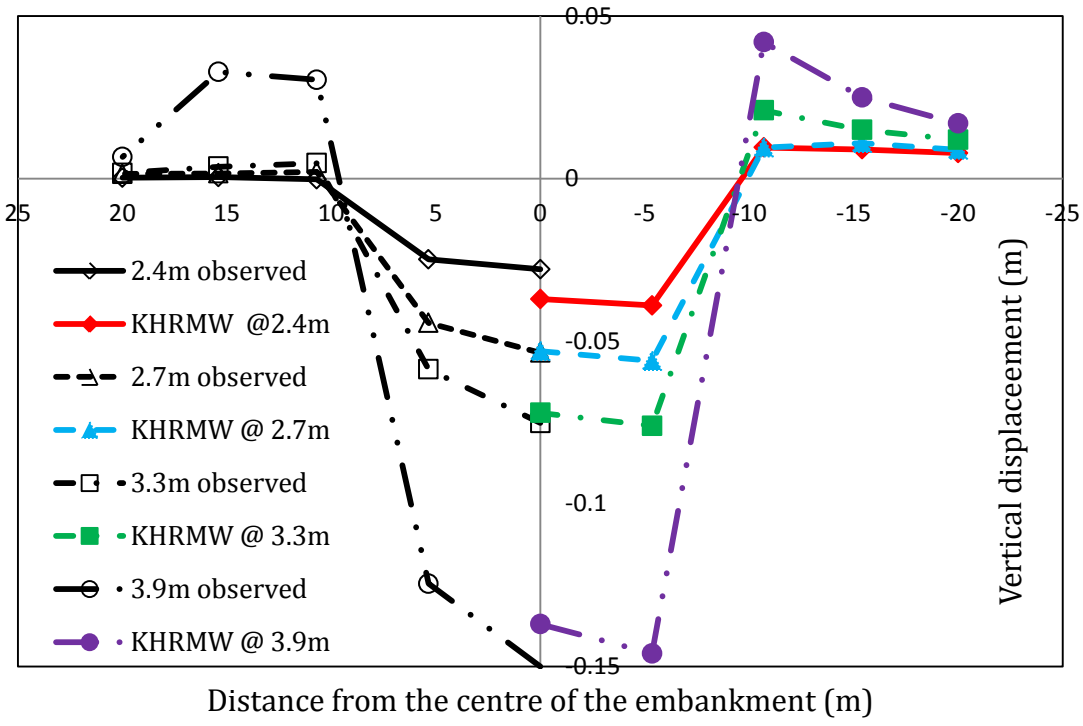

Figure 5.16: St. Alban test embankment: measured and predicted vertical displacements profile at different embankment heights

No field data were available for the horizontal displacements in the clay beneath the toe of the embankment, and hence no validation of the calculations was possible. The only available data for horizontal displacements were for settlement plates R6 and R9 (La Rochelle et al. 1974), which lay outside the failure mass and were therefore not useful for this study. It should be noted that the assessment of the three dimensional behaviour of test embankment A was carried out in the second part of this chapter and a comparison of field measurements and predicted results is given for all available settlement plates.

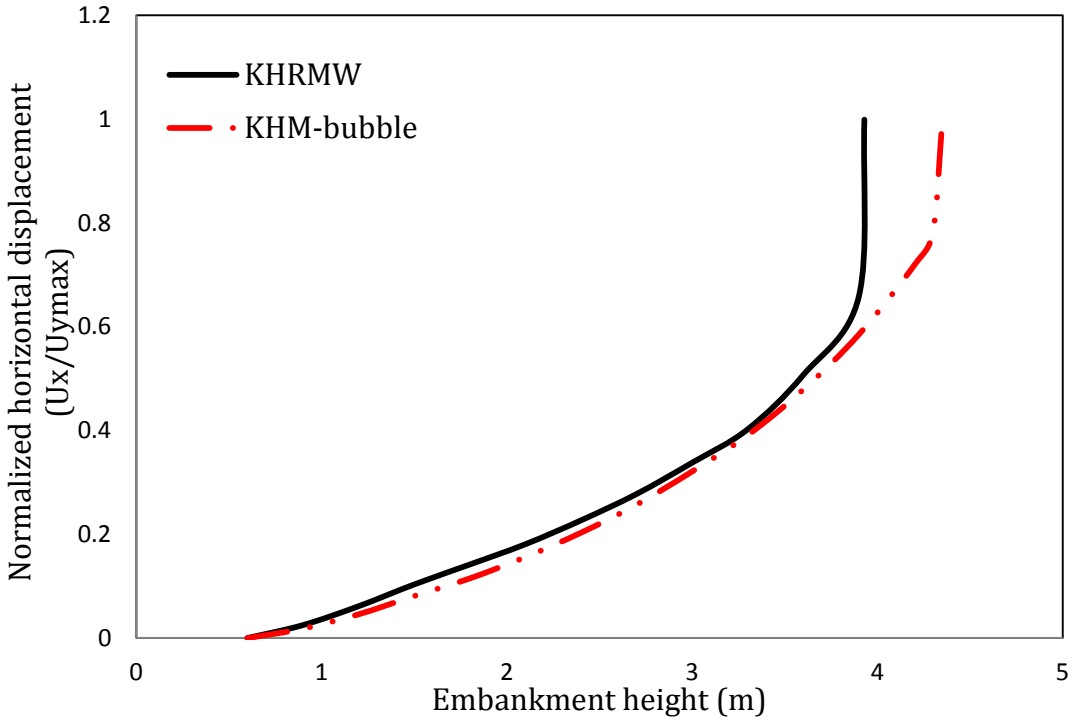

Figure 5.17: St Alban test embankment: comparison of normalised horizontal displacements at the embankment toe using the KHSM and KHM-bubble models.

The above diagram (figure 5.17) plots the predicted ratio of lateral displacements beneath the toe (u_x) and the maximum settlement u_{ymax} against the embankment height for analyses with the KHSM and the bubble model (KHM). As expected, the lateral displacements remain small in the early stages of embankment loading with the ratio u_x/u_{ymax} varying approximately between 0.02 and 0.33 for both models up to an embankment height of 3 m. This is in agreement with the range of experimental data reported by Tavenas et al. (1979). In the presence of destructuration the calculations indicate an acceleration of horizontal movement

above an embankment height of 3 m with the ratio u_x/u_{ymax} gradually increasing from 0.4 to 0.68 as the embankment failure height is approached. The bubble model, in which the destructuration is ignored, exhibits a similar response up to an embankment height of 3.35 m, beyond which the predicted response is stiffer.

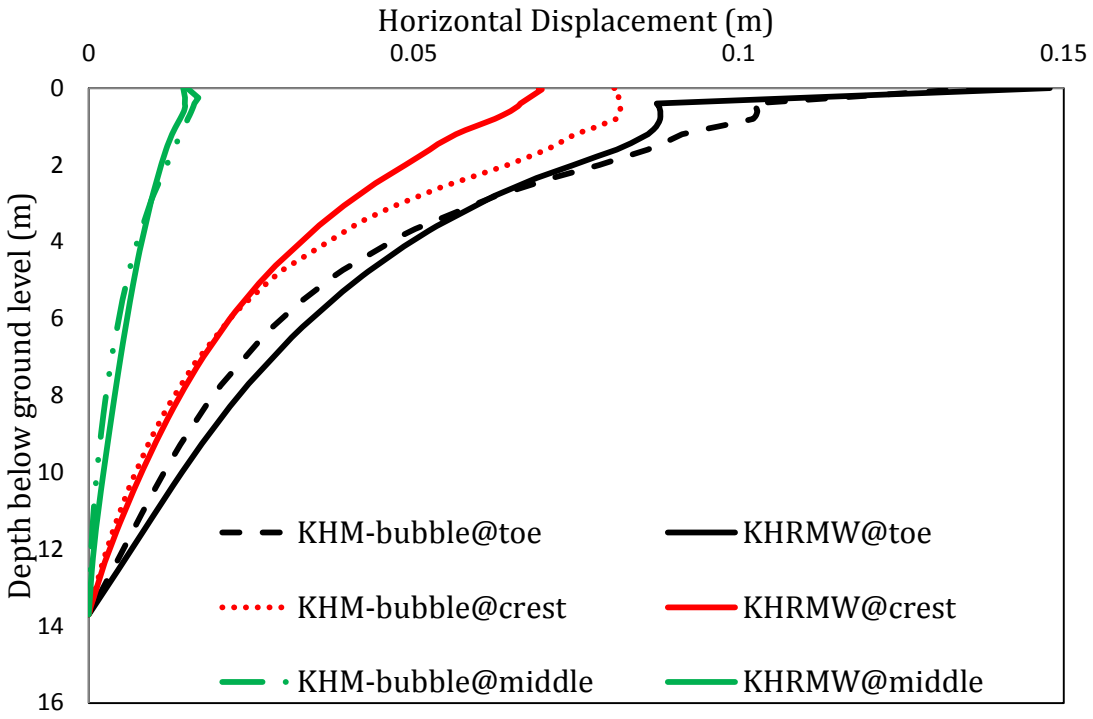

Figure 5.18: St Alban test embankment: comparison of predicted horizontal displacements with depth at the centreline, toe, and crest of the embankment for the KHSM and KHM-bubble models.

Figure 5.18 presents a comparison at failure of the horizontal displacements with depth at the centreline, toe, and crest of the embankment for the KHSM and KHM. It can be seen that the two models predict virtually identical horizontal movements at the centreline. The responses at the toe and crest show that the KHM predicts greater horizontal movements than the KHSM up to a height of approximately 3 m and 6 m, respectively. This is due to the additional 0.42 m of fill which has been placed on the clay foundation to reach failure using the KHM.

A small parametric analysis was carried out on the effect the initial measure of structure has on the profile of vertical movements along the soil surface. The results are given in a subsequent section of this study.

5.8.2 Extent of failure surface and destructuration zone

As mentioned previously at the bottom of the failing mass the soil elements experience loads that approximate conditions during a direct shear test and therefore, the depth of the failure surfaces for the analyses with the KHSM and KHM-bubble were located by inspecting the contours of shear strain in the clay foundation when the failure height was reached. These can be seen in figures 5.18a and b respectively. The analysis using the KHSM produced a failure mechanism extending to an approximate depth of 2.9 m, initiating approximately at the centre of the embankment crest. From the field data provided by La Rochelle et al. (1974), the failure surface was found at a depth of 3.8 m below the ground surface, originating also at the midpoint of the embankment crest. The discrepancy between the predicted failure surface of the KHSM and that observed in the field data may be attributed to the assumed plane strain condition which cannot fully describe the three dimensional deformation characteristics of the foundation soil. Supporting evidence is provided by Grammatikopoulou et al. (2007) who also assumed plane strain conditions. The three dimensional response of the embankment is covered in the next section if this chapter. In addition, the location of the access road to the North West may have accentuated the movement of the trial embankment, as reported by La Rochelle et al. (1974). In contrast, when no destructuration is taken into account in the bubble model there is an increase in the depth of the failure surface of approximately 1.6 m, resulting in a failure depth of 4.5 m below the ground surface (figure 5.19b). The failing soil mass now extends over the whole of the top surface and beyond: the failure surface intersects the ground surface on the rearward facing slope. Furthermore, plots of the incremental displacements for the two cases are provided in figure 5.20.

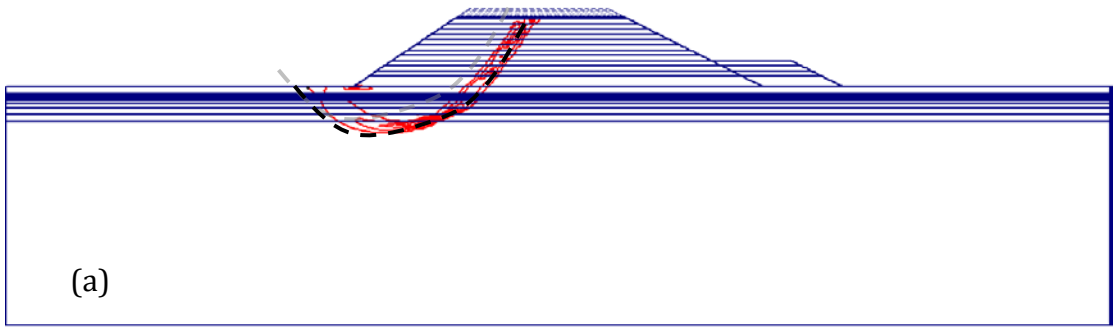

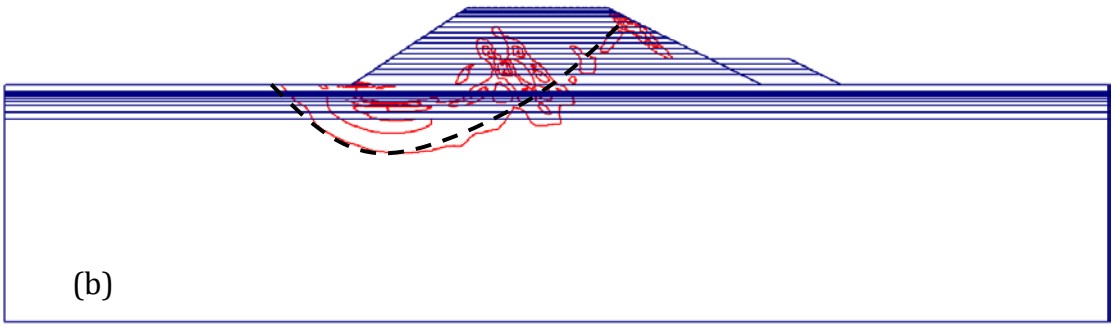

Figure 5.19: St Alban test embankment: Shear strain increments at failure: with the KHSM and (b) with the bubble model KHM.

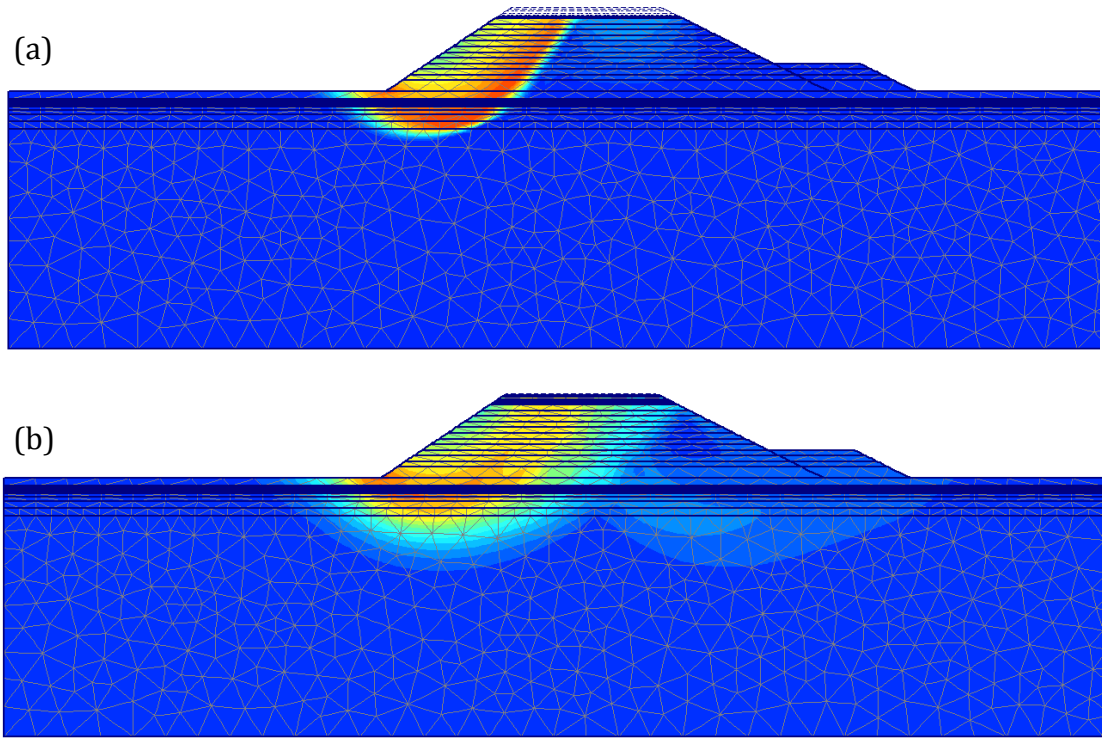

Figure 5.20: St Alban test embankment: incremental displacement shadings at failure: (a) with the KHSM and (b) with the bubble model KHM

The shadings of total displacement are helpful in the sense that they provide an indication of localization of movements within the soil mass as plastic deformations occur. Furthermore the incremental displacements are able to identify the directions of movement of the failing soil mass for the last stable increment of the analysis. It is their relative magnitudes that define the failure mechanism. Hence their absolute values are not important. Also evident in the

above figure is the outline of the failure surfaces that were identified by the incremental shear strains.

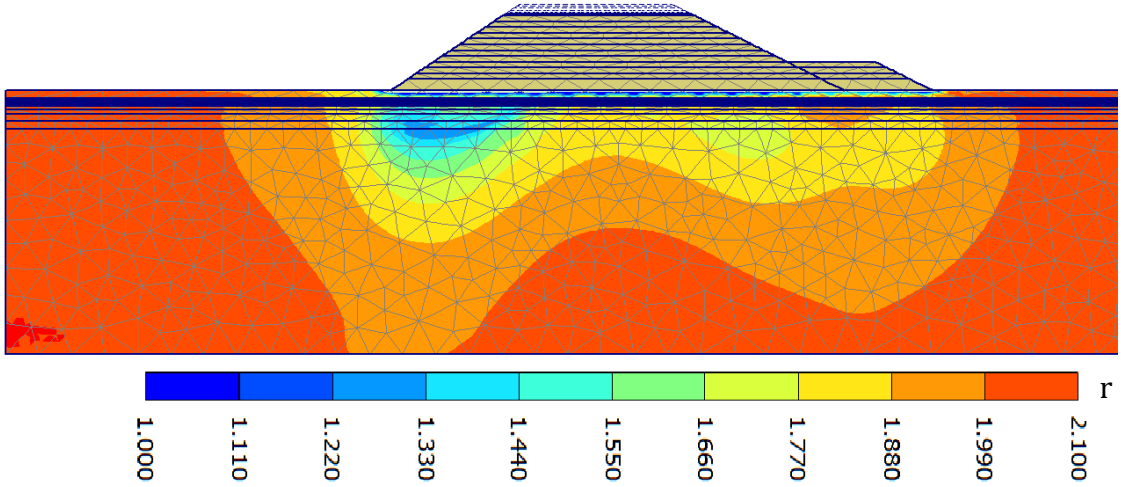

Figure 5.21: St Alban test embankment: spatial distributions of degree of structure contour at failure using the KHSM.

Figure 5.21 shows the destructuration zones in the foundation soil at failure. It can be noticed that the initial structure has virtually been destroyed under the toe of the embankment indicating the development of potential failure. It is also evident that the destructuration propagation follows the same outline as the eventual failure surface, since the combination of stiffness degradation as the elastic domain approached the structure surface and the gradual collapse of the structure surface towards the reference surface as structure is destroyed lead to the development of localised phenomena, where the failure surface initiated at regions of intense deformation. The figure also shows that the destructuration has propagated into a large zone below the located failure surface extending to an approximate depth of 7.5 m.

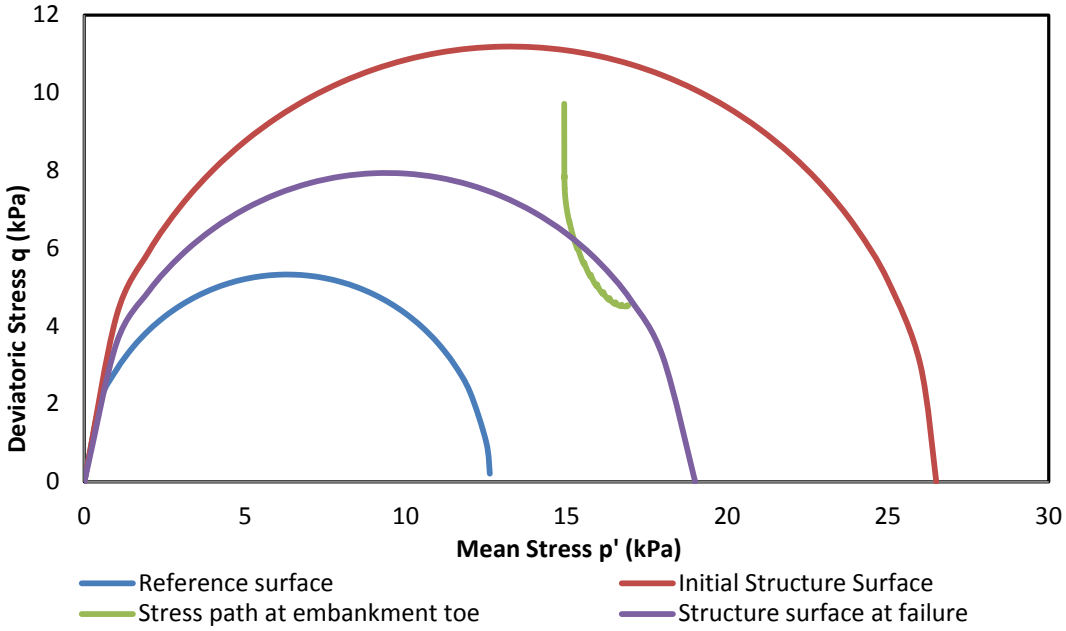

Figure 5.22: Stress path followed during the construction of the embankment at a point near the toe

Figure 5.22 shows the stress path followed by a soil element near the toe of the embankment during the construction process. Due to the element distribution, no stress point was situated exactly on the crust surface at the tow of the embankment. It can be seen that the stress path follows a reduction of the deviatoric stress with increasing mean stress. This observation confirms the expected response of the soil since the soil element under consideration is in extension while the loading from the embankment occurs. At failure the structure surface has not completely collapsed, but retains a magnitude of approximately 1.55, which is also verified by Figure 5.21.

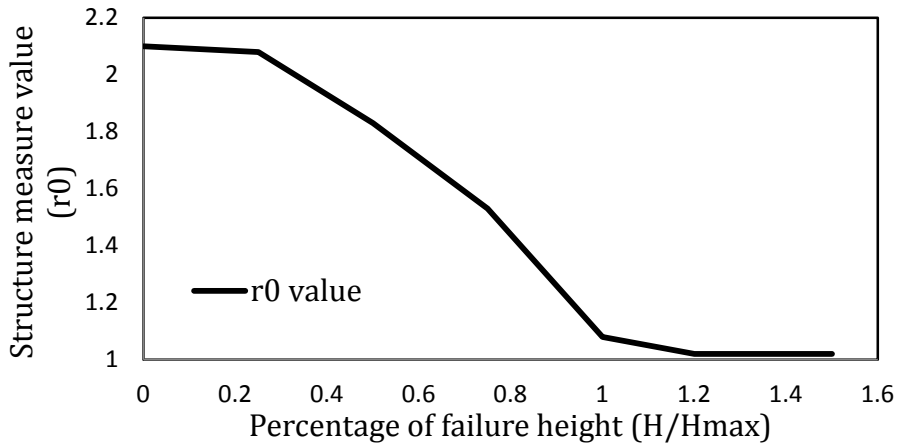

Figure 5.23: Degradation curve of the measure of structure during loading of the St Alban embankment

Figure 5.23 illustrates the gradual decrease of the initial measure of structure r_0 for a selected point that lies in the vicinity of the failure surface. What can be seen is that, for the initial stages of the embankment erection, there is little if any destructuration, since no significant plastic strains had developed. Afgter the embankment has reached a height of 0.2m, significant degradation of structure measure is observed. Beyond the 0.6m mark, when presumably intense plastic deformation occurred, r_0, decreases rapidly, to a value of 1.05 at the failure height, where essentially the complete destructuration of the particle bonds has taken place.

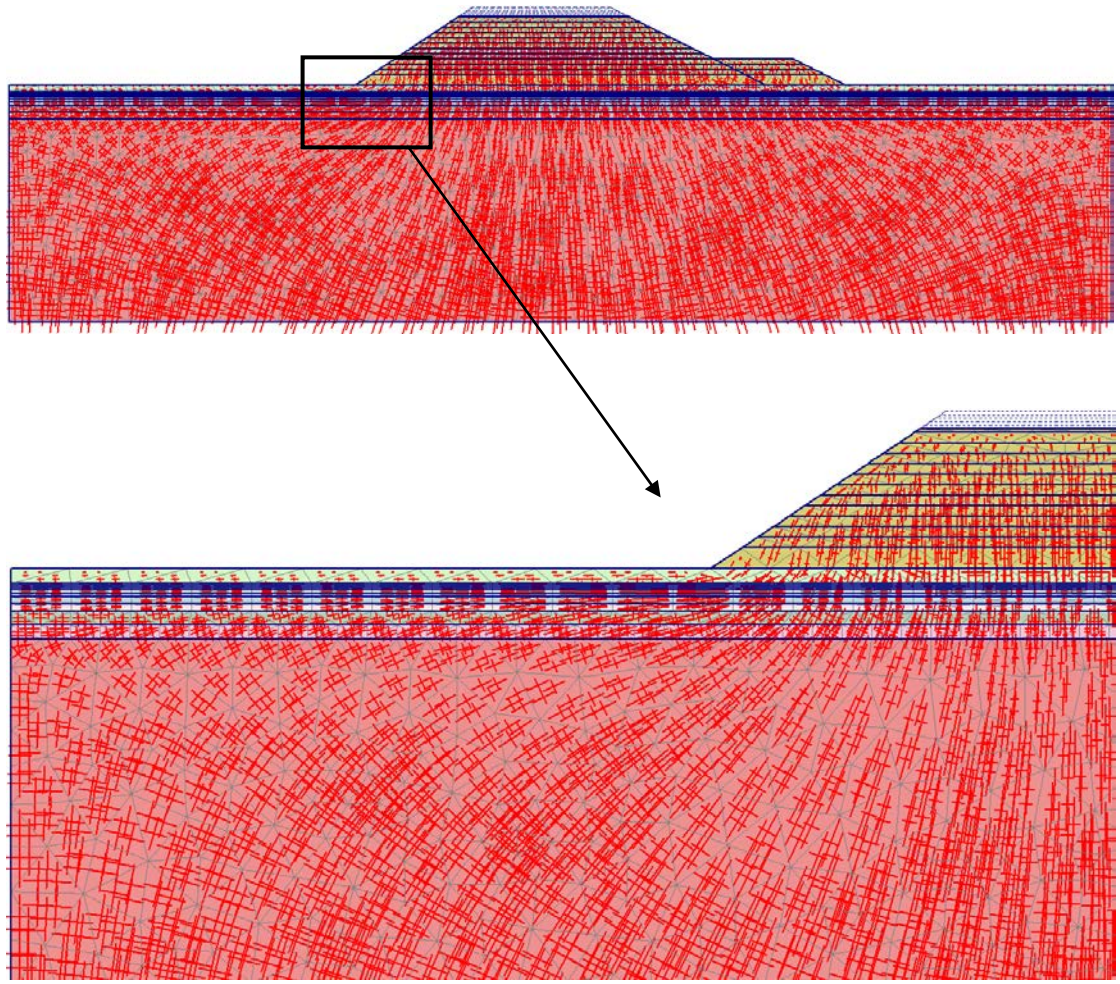

Figure 5.24: St Alban embankment. Inclinations of major principal to the vertical at failure

Figure 5.24 plots the orientation of the principal stresses at failure of test embankment A. This plot provides further confirmation to the statement that constitutive models that assume an isotropic behaviour of the soil are not suitable for simulating soil deposits that are well known to be anisotropic in strength and stiffness. It is clear that a significant change in the inclination of this stress is happening along the failure surface and hence a soil constitutive model which allows for anisotropy will be far more accurate in simulating the failure height and consequent failure mechanism that will develop at failure.

5.8.3 *Excess pore water pressure*

Two types of quick-response piezometer were installed in the clay foundation beneath the section under consideration in this study. At point c1 a pneumatic piezometer was placed at a depth of 3m below the ground level. The location of piezometer c1 in relation to the centreline of the embankment places it beneath loading plate R18. An electric vibrating wire piezometer b1 was situated at a depth of 3.45 m below the clay surface, at a location below settlement plate R13. The values of the calculated and measured excess pore pressures at the nodes corresponding to piezometers b1 and c1 are presented in figure 5.25.

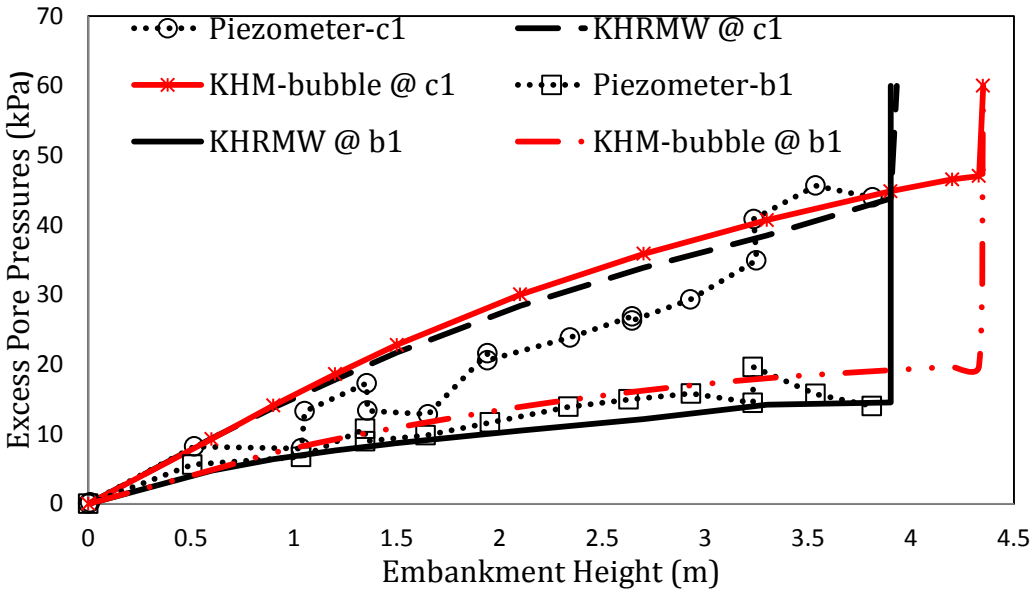

Figure 5.25: St Alban test embankment: measured and calculated excess pore water pressure at piezometers b1 and c1 at a depth of 3.45m and 3m, respectively.

The excess pore pressures increase during the construction period of the embankment up to the point where failure occurs. As can be seen, the KHSM model is remarkably successful in matching the general magnitude and rate of dissipation of the excess pore pressures induced in the soil during the construction of the embankment. These results are made even more significant, by the proximity of the piezometers to the observed failure surface. Results for the KHM show that the predicted excess pore water pressures are slightly higher than those of the KHSM up to the failure height of 3.93 m after which the two simulations diverge. Figure 5.26 shows the shadings for development of excess pore pressures at failure for the two different simulations. It can be seen that when destructuration is accounted for, the zones with equal excess pore water pressures (see figure 5.25a) are shallower and more localised than those predicted using the KHM (see figure 5.25b).

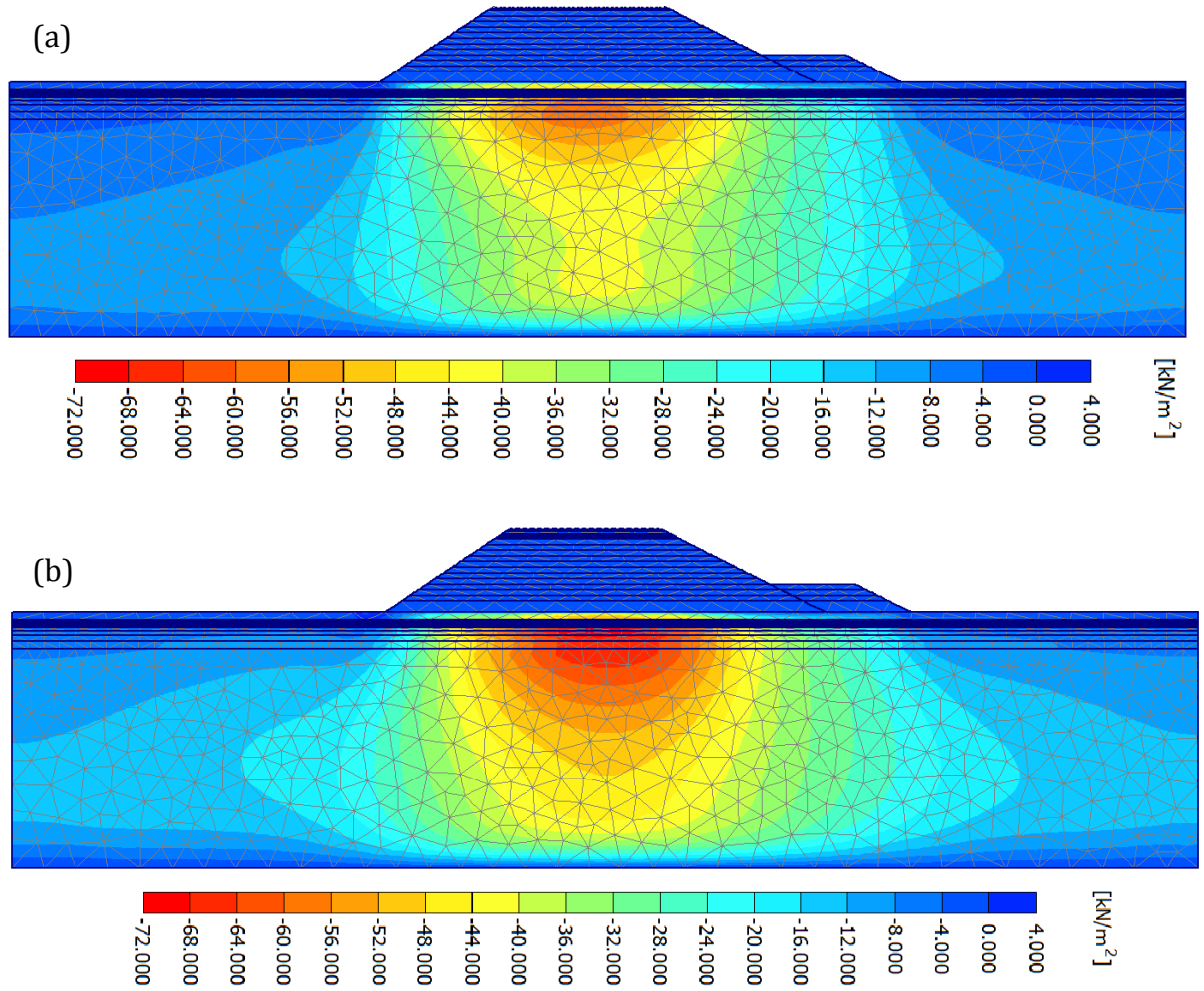

Figure 5.26: St Alban test embankment: excess pore water pressure distribution at failure: (a) with the KHSM and (b) with the bubble model KHM.

5.9 Parametric study

In this section, the effects induced by changing the initial degree of structure, r_0, the rate of destructuration, k, and the non-dimensional damage shearing parameter, A, on the embankment failure height are presented. Simulations are made with one parameter at a time changed from its reference value given in section 5.6.4. The results can be summarised as follows. The initial degree of structure represents the size of the structure surface relative to the reference surface. This parameter is difficult to quantify in reality and a parametric study provides a good indication of the influence of the initial degree of structure on the simulated behaviour. As r_0 increases from 2.0 to 2.5 there is an overestimation of the failure height of embankment by 10% compared with the observed value, as shown on figure 5.26, reaching a height of 4.32 m. Decreasing the value of the initial structure r_0 from 2.0 to 1.5, the calculated failure height of 3.55m is 9% less than the observed value. A simulation was run with the parameter controlling the size of the structure surface set to $r_0 = 1$. This reduces the model to the intrinsic mechanical properties of the soil, taking away the added strength provided by the cementation of the soil fabric. The analysis shows that the effect of complete elimination of the initial structure is dramatic, as the estimated failure height falls to 3.15 m, an under-estimate of 19%, as can be seen in figure 5.27.

The parametric study included also a comparison of the calculated profiles of vertical movement at the soil surface at the cross-section A-A. As the embankment failed at a height of 3.15 m in the analysis using remoulded clay without initial structure ($r_0 = 1$), the comparison was made for one embankment height of 2.7 m, as shown in figure 5.28. From the figure, it can be observed that the simulations performed without initial structure predict higher values of vertical deformations for the points corresponding to settlement plates R18-R8, whether the movement is upwards or downwards. For the point corresponding to plate R23 and R3, the difference in the magnitudes of heaving is less, with the analyses performed with and without initial structure indicating similar movements at the ground surface

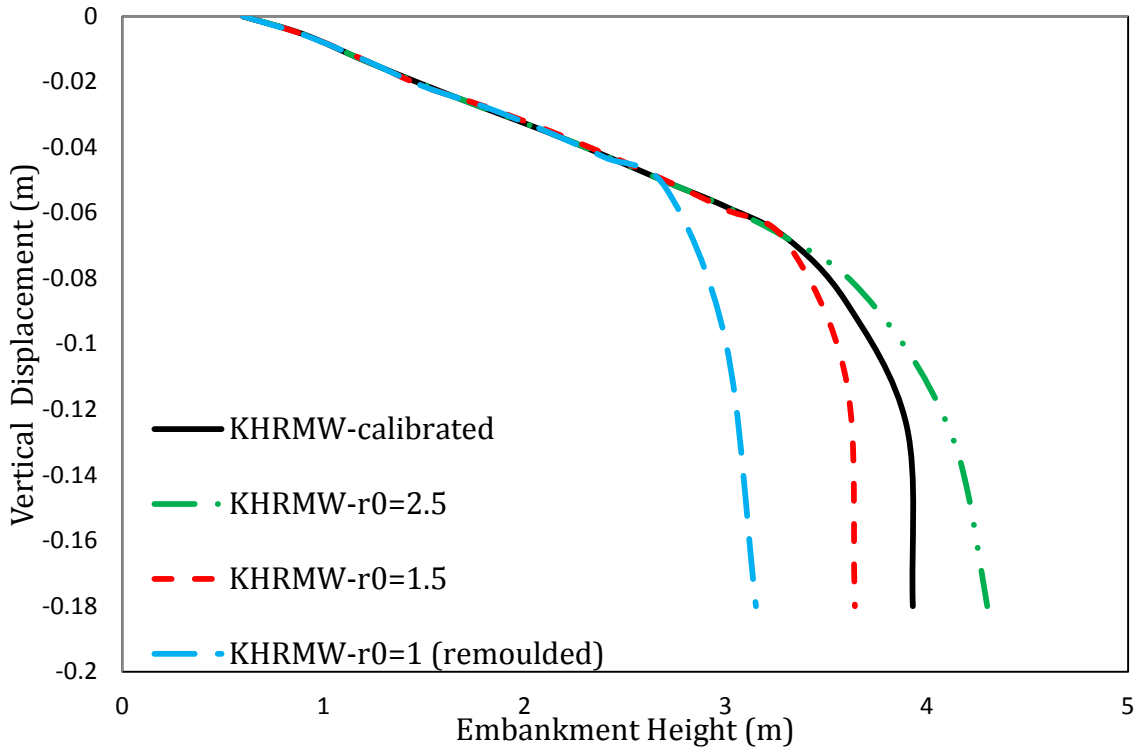

Figure 5.27: St Alban test embankment: parametric study of the effect of different values of initial structure r_0 on the vertical displacement at the embankment centreline.

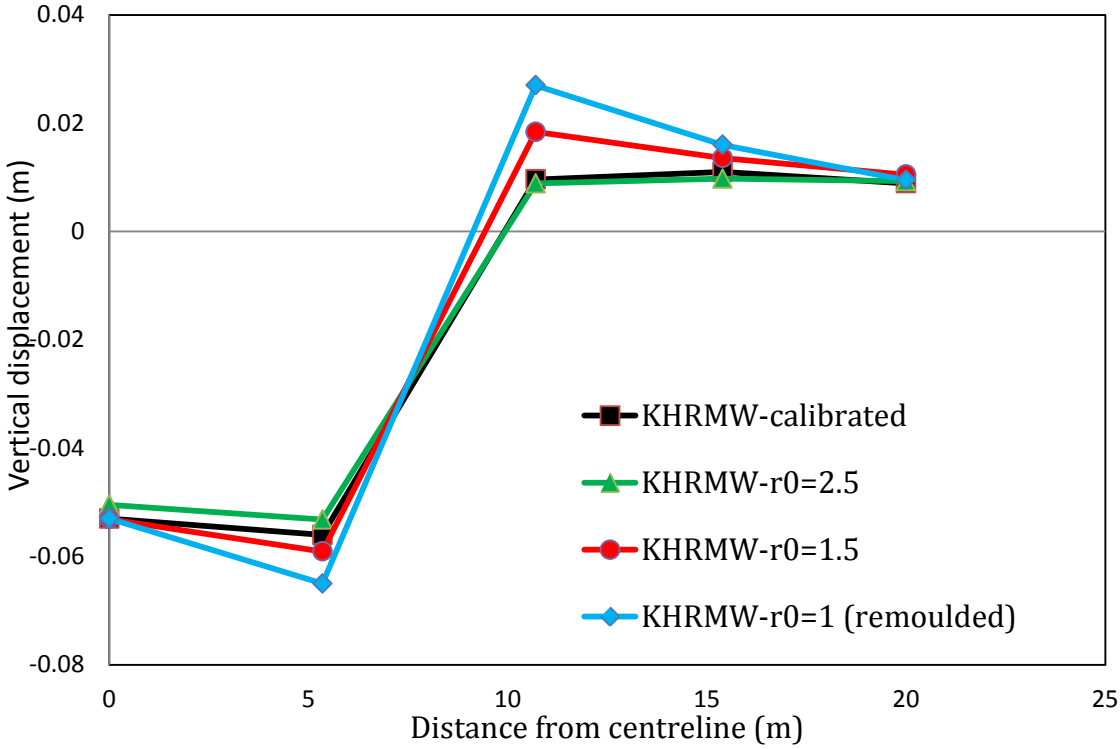

Figure 5.28: St Alban test embankment: parametric study of the effect of different values of initial structure *r*0 on the vertical displacement at different depths.

Figure 5.29 shows the effects induced by changing the rate of destructuration, *k*, on the embankment failure height. It can be observed that increasing *k* leads to a softer response of the foundation soil as the loss of structure becomes more rapid. If *k* is not sufficiently high then the embankment failure height is over predicted at 4.6 m, as can be seen for a value of *k*=3.

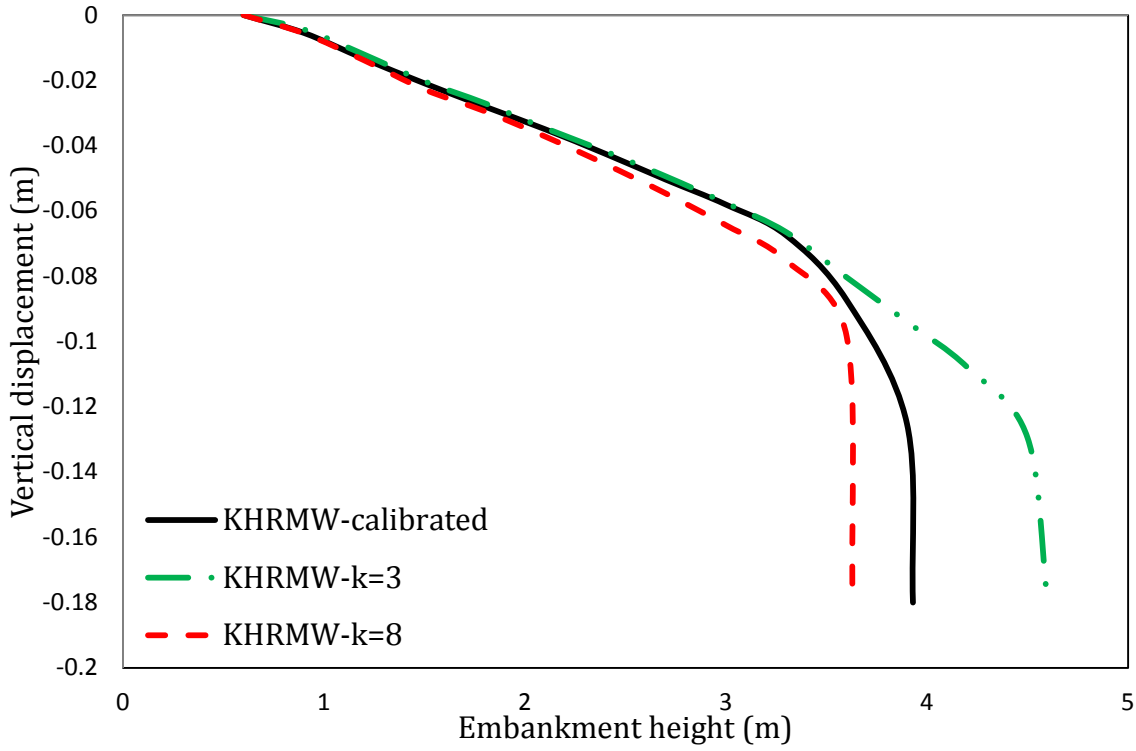

Figure 5.29: St Alban test embankment: parametric study of the effect of different values of destructuration coefficient *k* on the vertical displacement at the embankment centreline.

A depiction of the spatial distribution of the measure of structure at failure is provided in figures 5.30a and b, for the parametric analyses on the destructuration parameter *k*.

In the first instance (figure 5.30), the results from the simulation with a lower value of *k* is presented. As it was seen in figure 5.29, this result to a higher failure height, (4.6m) which can be attributed to the far more gradual loss the natural bond of the clay with plastic strains. This is supported by the distribution of r_0. It is also evident that the development of a de-structured zone is at the initial stages,

since the degree of structure is somewhat retained at a value of 1.55 around the slipping soil mass.

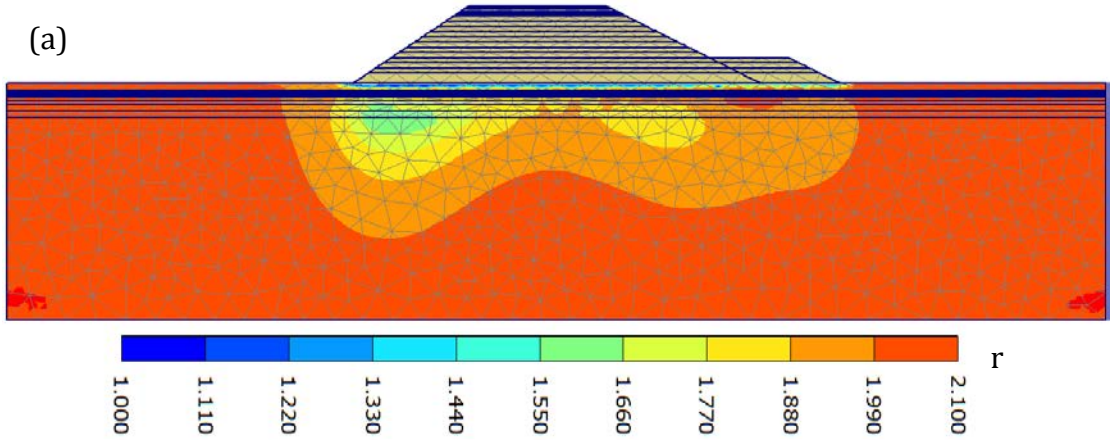

As a direct comparison on the effect of the destructuration parameter, figure 5.30b plots the spatial distribution with the increased value of k=8. A clearly defined de-structured zone is evident, which causes localisation of the slip surface that eventually leads to the under-estimation of the failure height.

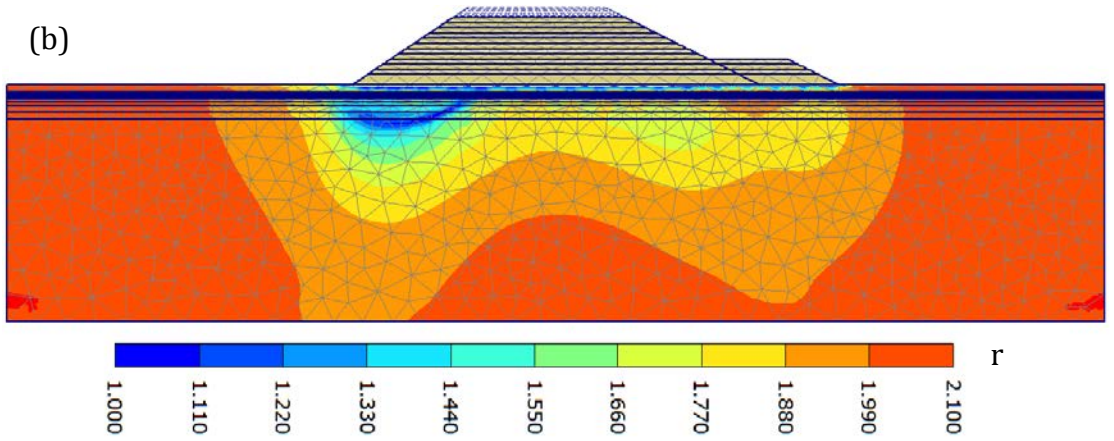

Figure 5.30: St Alban test embankment: spatial distributions of degree of structure contour at failure using the KHSM (a) *k*=3 and (b) *k*=8.

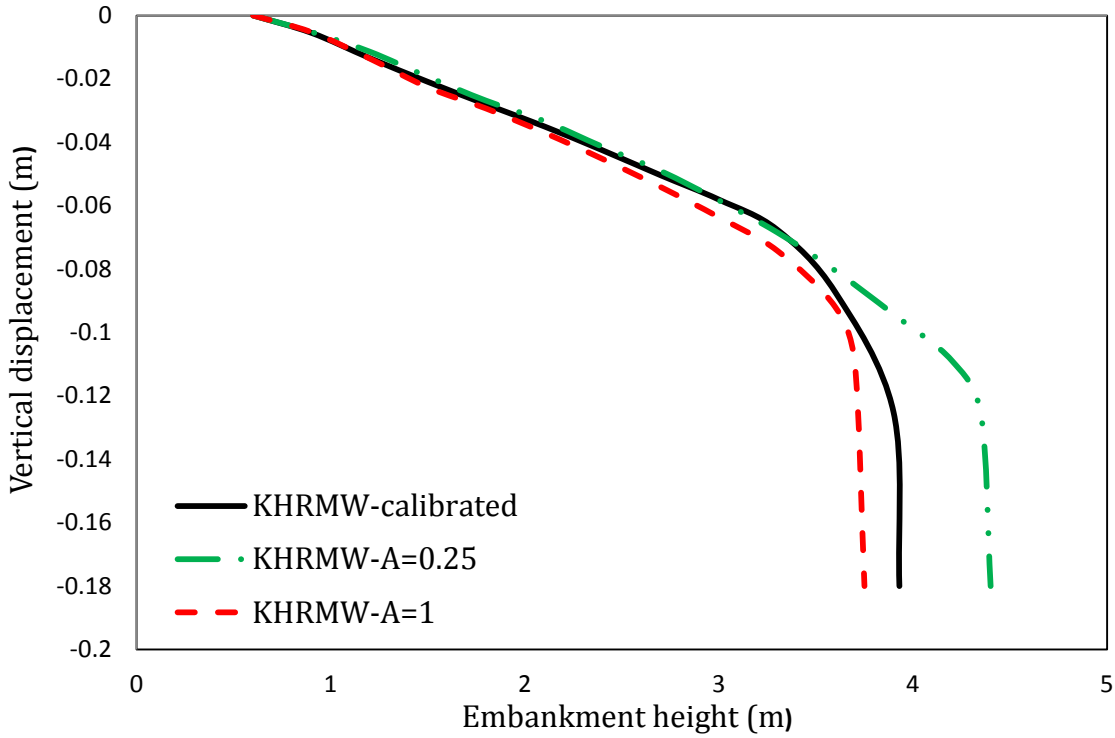

Figure 5.31: St Alban test embankment: parametric study of the effect of different values of the shear damage coefficient A on the vertical displacement at the embankment centreline

Figure 5.31 shows the effect of varying the material parameter A which influences the damage caused to the structure of the foundation soil. It can be observed that when the damage is completely distortional (A = 1) the embankment failure height is under-predicted at, 3.75 m. As the destructuration becomes increasingly volumetric (A =0.25) the predicted failure height increases to 4.4 m and the response becomes stiffer. One possible reason for this attribute is the rapid construction of the embankment. The short period of time in which the embankment was erected, lead to undrained conditions, under which the deformation is predominantly distortional.

The preceding section of this chapter, presented finite element analyses of the St Alban test embankment A, which was founded on a structured, soft clay deposit. The two dimensional finite element simulations explored the influence of a realistic modelling of initial structure or bonding in the clay together with progressive destruction of this structure by plastic straining, as encapsulated in the kinematic hardening structure model KHSM. The analyses revealed that the numerical simulations using the structured model provide a close match to field monitoring data. The correlation of the observed and predicted magnitudes of the settlements is in excellent agreement for all the embankment heights that were considered. The good agreement between the observed and measured excess pore pressures echoed the convincing comparisons in the vertical settlements. The successful prediction of the pore pressures is especially significant when we consider that the two piezometers under consideration were situated either very close to or possibly on the failure surface. In the simulations with the reduced the bubble model (KHM), was adopted-in which the destructuration was ignored-, the numerical simulations predict a stiffer behaviour of the foundation soil which resulted in an overestimation of the embankment failure height.

As it was mentioned in the first section of this chapter, a number of previous finite element studies had been carried out on the St Alban embankment. Although the general features of the embankment failure were successfully modelled (failure height, displacement at various points, excess pore water pressures etc.), using plane strain two dimensional models, one particular observation was not captured. The extent of the failure surface in the soft clay foundation soil was never matched. The trend was always an underestimation of the depth of the failure surface, with the three-dimensionality of the boundary problem analysed under plane strain conditions (Zdravkovic, 2002), identified as the probable cause of this discrepancy. It was therefore decided that a three dimensional analysis would be carried out in order to firstly validate the KRMW model in a three dimensional software and secondly to assess the behaviour of the embankment under these conditions.

5.10 Assessment of three-dimensional analysis

5.10.1 *Introduction*

Qu *et* al. (2009) conducted a two and three dimensional analyses of three full scale test embankments were carried out to evaluate the accuracy of the two approaches. This study highlighted that as a whole three dimensional analysis agree better with field behaviour and that overestimation of soil strength is likely to be observed when considering 2D/plane strain conditions. The first study covered an analysis of the Laval University test embankment which is subject to this research. The two and three dimensional finite element analyses which were carried out on models using the precise geometry of the test embankments provided failure heights of 3.6 and 4.0m respectively. The actual height of failure that the embankment achieved was 4.0m. The conservative result of failure height derived from a 2D analysis is further portrayed in the examination of a Malaysia trial embankment. In this case the actual failure height achieved was 5.4m with the 2 and 3 dimensional analyses returning results of 4.2 and 5.2m.

The paper highlighted that whilst a three dimensional analysis does indeed provide a more realistic simulation of field behaviour as displayed in the Malaysia case, the results may not prove to be 100% accurate. A significant limitation within the method of the above work which is likely to be accountable for this statement was the choice of constitutive model that was adopted for the simulations.

A view that not in all cases does a three dimensional analysis produce superior results to that of a two dimensional was put forward. Again a comparative analysis was performed, in this case to simulate displacement and deformation behaviour of two full scale reinforced embankments. The analysis process employed a combination of models: Mohr-Coulomb to represent the topmost layer of the foundation soil which was described as overconsolidated soil, and then modified Cam-clay for subsequent underlying layers.

When considering a long embankment (with a length to width ratio of 3) it was discovered that the three dimensional analysis significantly underestimated long term settlement in comparison to field data. Similar error could also be observed within simulations of excess pore water pressures. Conversely however two dimensional analyses yielded substantial overestimations with both methods greatly underestimating lateral displacements. The shorter embankment (with a length to width ratio of 1) yielded vaguely similar results for all parameters except for settlement; where in this case the three dimensional analysis provided more precise findings.

5.10.2 *Revised KHSM material parameters*

La Rochelle et al. (1974) reported the soil sensitivity varying from 8 to 22 for foundation soils. In the two dimensional analyses a value for the initial structure of 2.1 was adopted, based on the available experimental data. In order to investigate the possible effect of the initial measure of structure could have on the finite element simulations a similar calibration process as in the plane strain analyses was carried out. All the optimised parameters retained their values, with the focus being on the parameters that control the size and the destructuration process. In that respect, the effort was to obtain the same peak strengths as in the calibration with r_0=2.1 for all three triaxial tests. An average value of r_0=15 was assigned to the foundation soils. The calibration process yielded a value of destructuration parameter k of 13, in order to achieve the observed peak strengths. The results from these revised parameters for the KHSM model can be seen in figure 5.32. It is evident that the general trend is again very well predicted by the gauss point simulations, both in terms of peak strengths and strain paths.

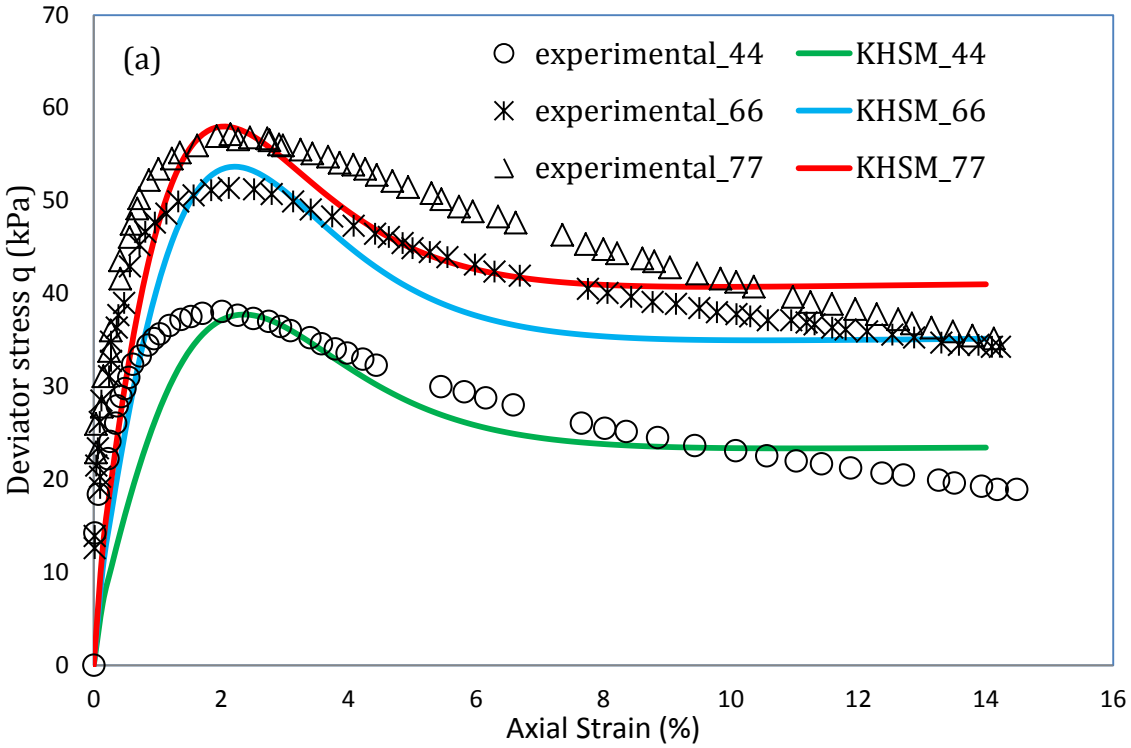

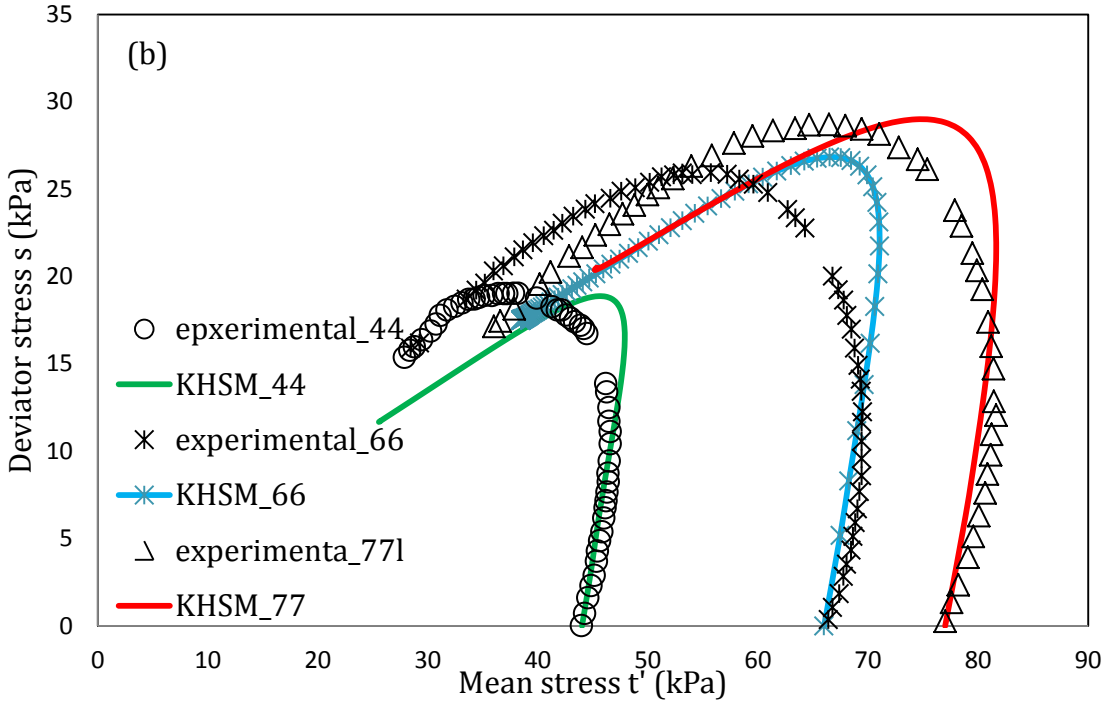

Figure 5.32: (a) Revised stress-strain curves and (b) stress paths for CIU normally consolidated tests taken at a depth of 3m

5.10.3 *Finite element model*

For all analyses 30,806 fifteen node wedge elements were used. The global coarseness for both the vertical and horizontal elements was set at fine with cluster refinements made on and around the embankment. Because of the symmetrical nature of the structure only half of the embankment was analysed, thus saving hard disk space and time. Figure 5.33 displays the finite element mesh that was adopted. The software (PLAXIS) automatically creates boundary fixities, in this case fixed supports were generated for the bottom horizontal boundary. Roller supports were used for vertical boundaries allowing movement in the vertical direction whilst resisting movement in the horizontal. The required length of the boundary in each direction was taken as a width equal to 90m, a length of 180m and a depth of 40m.

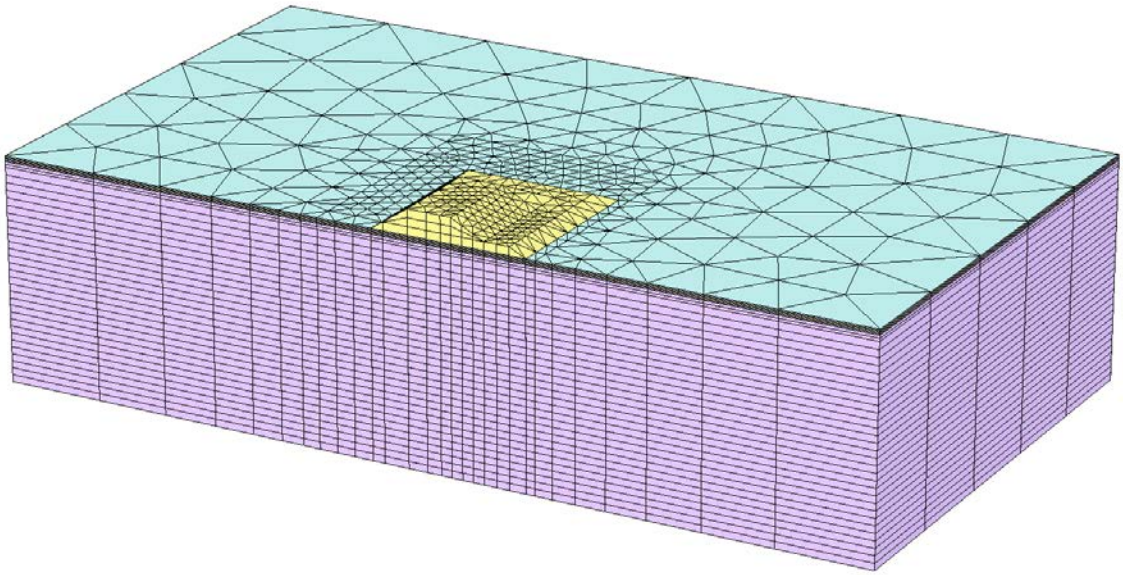

Figure 5.33: St Alban test embankment: finite element mesh and boundary conditions

5.11 Results and discussion

5.11.1 *Embankment deformations*

The following two figures show a comparison of the observed vertical displacements on site and the calculated settlements from the finite element analysis, at the settlement plates R23 and R18. It can be seen that the numerical

response agrees very well with the observed settlements at both locations. The plots confirm the observations of Tavenas et al. (1974) and also reported results from other finite element studies on the embankment (Zdravkovic et al. 2002) concerning the critical height of 2.4 m, which marks the onset of more rapid deformations as the embankment height is increased and local yielding within the clay starts to have a significant effect on the overall foundation stiffness. A failure height of 3.90 m was calculated which agrees well with the actual failure height for embankment A.

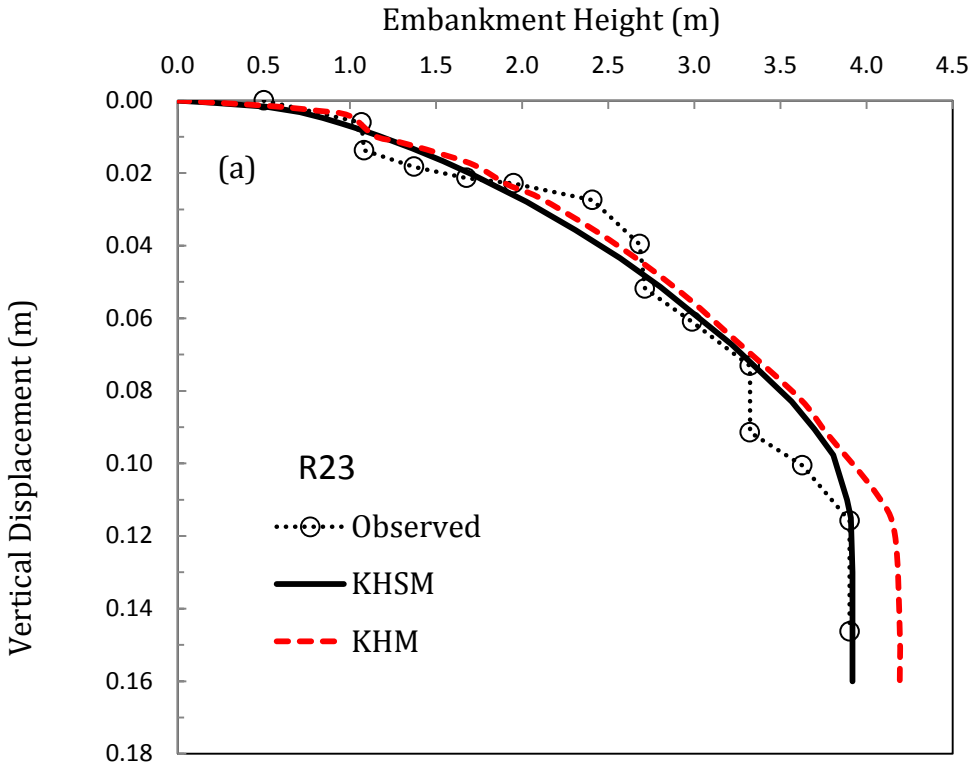

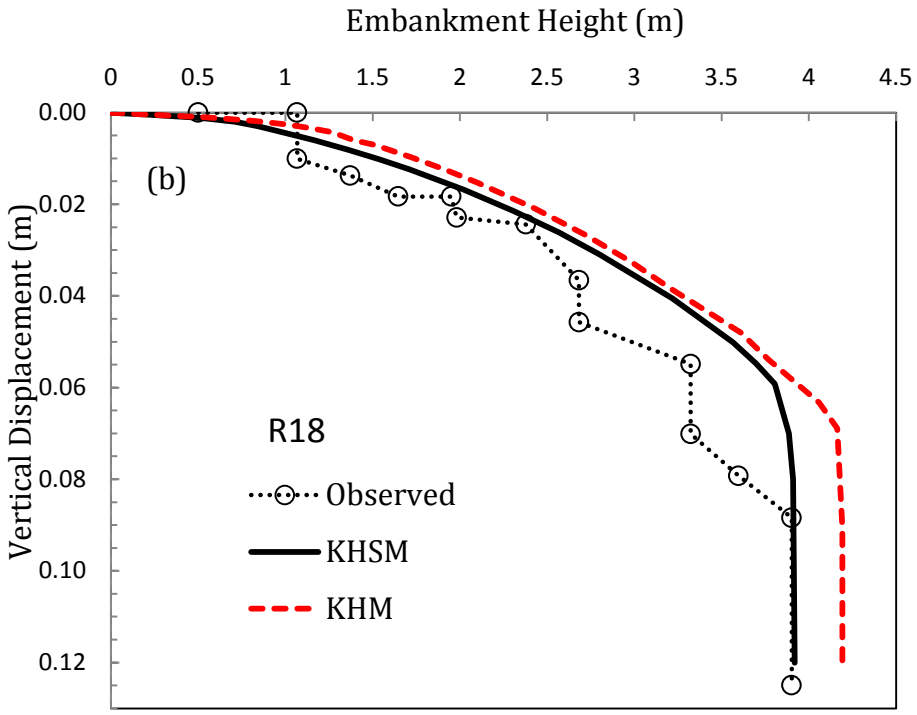

Figure 5.34: St Alban test embankment: measured and calculated vertical displacement at (a) the settlement plate R23 and (b) the settlement plate R18.

In figure 5.34a, the comparison between the numerical results for a node situated on the clay surface directly underneath the centreline of the embankment and the observed movement of settlement plate R23 shows excellent agreement. It can be seen that when the failure height is approached the KHSM model calculates a total displacement very close to the observed total settlement at failure. It can be deduced that this numerical analysis describes the pre-failure deformation behaviour of the soils very well around the centreline of the embankment. Fig. 5.34a also shows the predicted vertical settlement at R23 obtained without destructuration and by matching the observed initial shear strength profile. It can be seen that the bubble model without destructuration (KHM) predicts smaller settlement than the structure model up to an embankment height of approximately 3.3 m. Thereafter the response becomes stiffer, leading to an embankment failure height of 4.35 m. The difference is due to significant softening attributed to loss of structure which was accounted for in the predictions by the KHM.

The comparison between the simulated and observed settlements at R18, at the surface of the clay below the crest of the embankment also shows a good

agreement (figure 5.34b). From an embankment height of 2.4 m onwards, more rapid deformations were observed with the numerical prediction using the KHSM converging to the settlements that occurred on site. However, for the bubble model (KHM) it can be seen that a stiffer behaviour is predicted after an embankment height of approximately 3.35 m, which resulted in overestimating the embankment failure height by 0.42 m. This is again due to the significant influence of destructuration.

Figure 5.35 displays an observation that in plane strain analyses could not be examined, this is the horizontal movement at plate R6. As can be seen, the numerical simulation is in excellent agreement with the field observations. The drawback to this comparison however, is that data is only available from field observations up to a failure height of 3.58m and so the final horizontal displacement may well have been much higher than what was recorded.

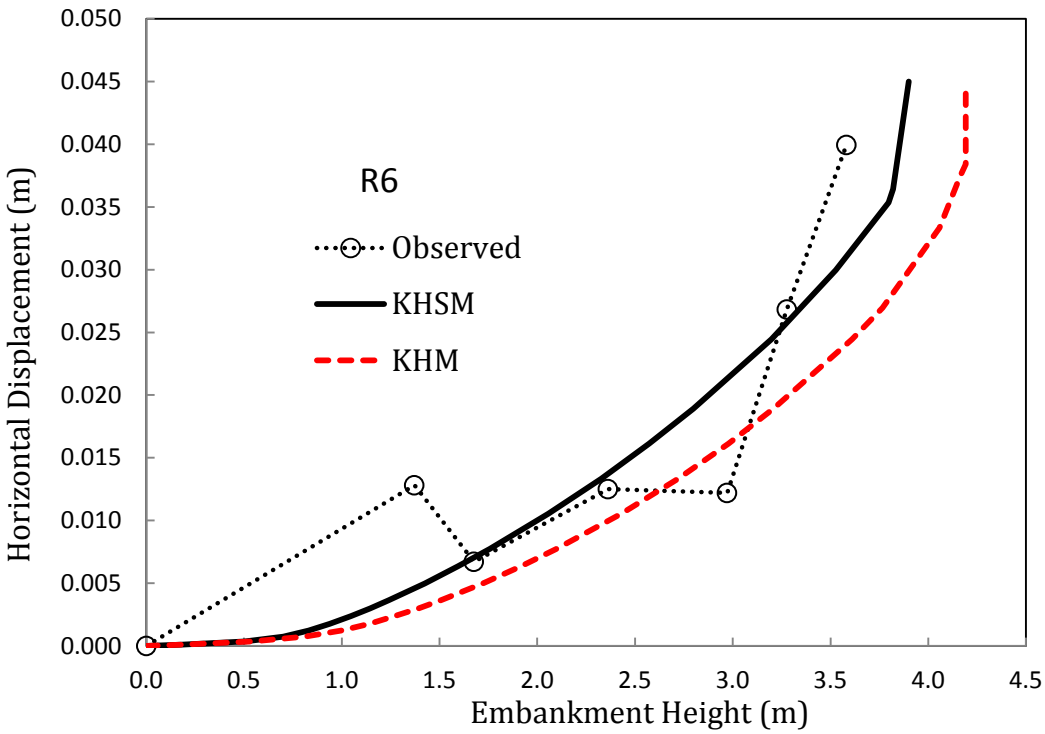

Figure 5.35: St Alban test embankment: measured and calculated horizontal displacement at the settlement plate R6

Profiles of the observed and simulated vertical movements of the soil surface in section A-A are plotted in figure 5.36. Overall, the numerical results predict a very similar distribution of vertical movements. The heave observed at the toe of the embankment was also successfully modelled. There is a tendency of the KHSM model to overpredict the heave at the toe (R13) and at the points corresponding to R8 and R3 for fill thicknesses of 2.4 m up to 3.3 m. The magnitude of the heave at the toe, for the failure height, is correctly estimated. As can be seen in Fig. 5.36, at a height of 3.9m the R8 plate exhibited a larger vertical displacement than the toe, which contradicts the experimental data from all lower fill heights. This irregularity may be explained by the description of the failure provided by La Rochelle et al. (1974), where it is stated that the toe heaved, forming a roll up to 1.2m high. In contrast, the finite element analysis maintains the trend predicting a smaller magnitude for the heave at that point (R8) for all embankment heights. For the node corresponding to settlement plate R23, the KHSM model suggests a softer behaviour when compared with the observed data at an embankment height of 2.4 m. The observed data for fill thicknesses of 3.3 m has a slightly higher magnitude than the simulated results. A final vertical movement of 0.137 is estimated by the KHSM as the embankment failure height of 3.93 m is approached.

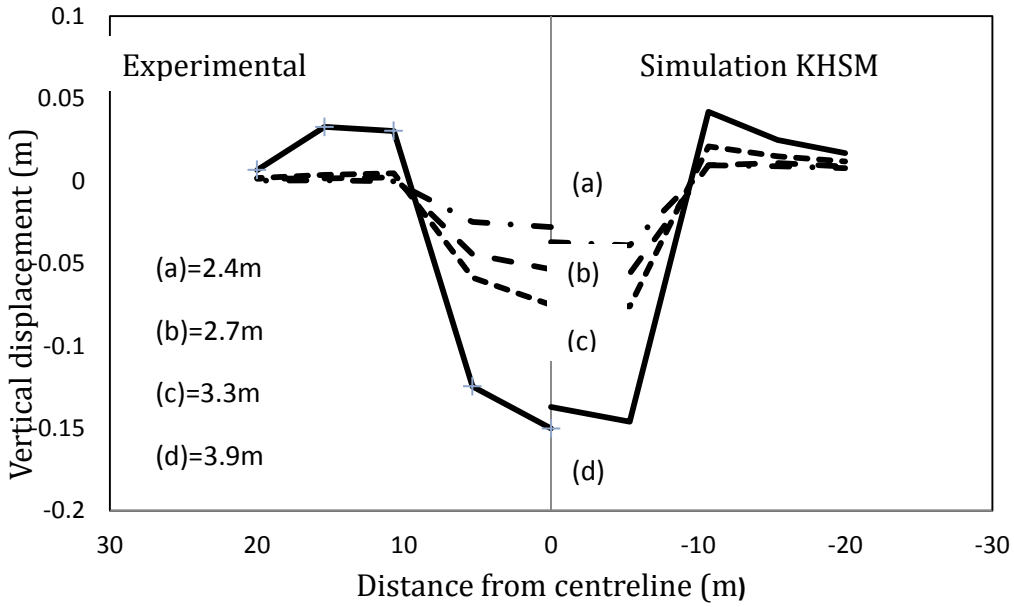

Figure 5.36: St. Alban test embankment: measured and predicted vertical displacements profile at different embankment heights

5.11.2 *Position of failure surface*

As reported by La Rochelle (1974) the failure surface of the St Alban test embankment was found to extend to 3.8m below the ground surface. Experiments using the KHSM within the PLAXIS 2D framework provided a slip plane with its lowest point 2.9m below the ground surface. From figure 5.37a it can be observed that the slip surface for the 3D models extends to a depth of approximately 3.6m, underestimating slightly the value obtained from field data.

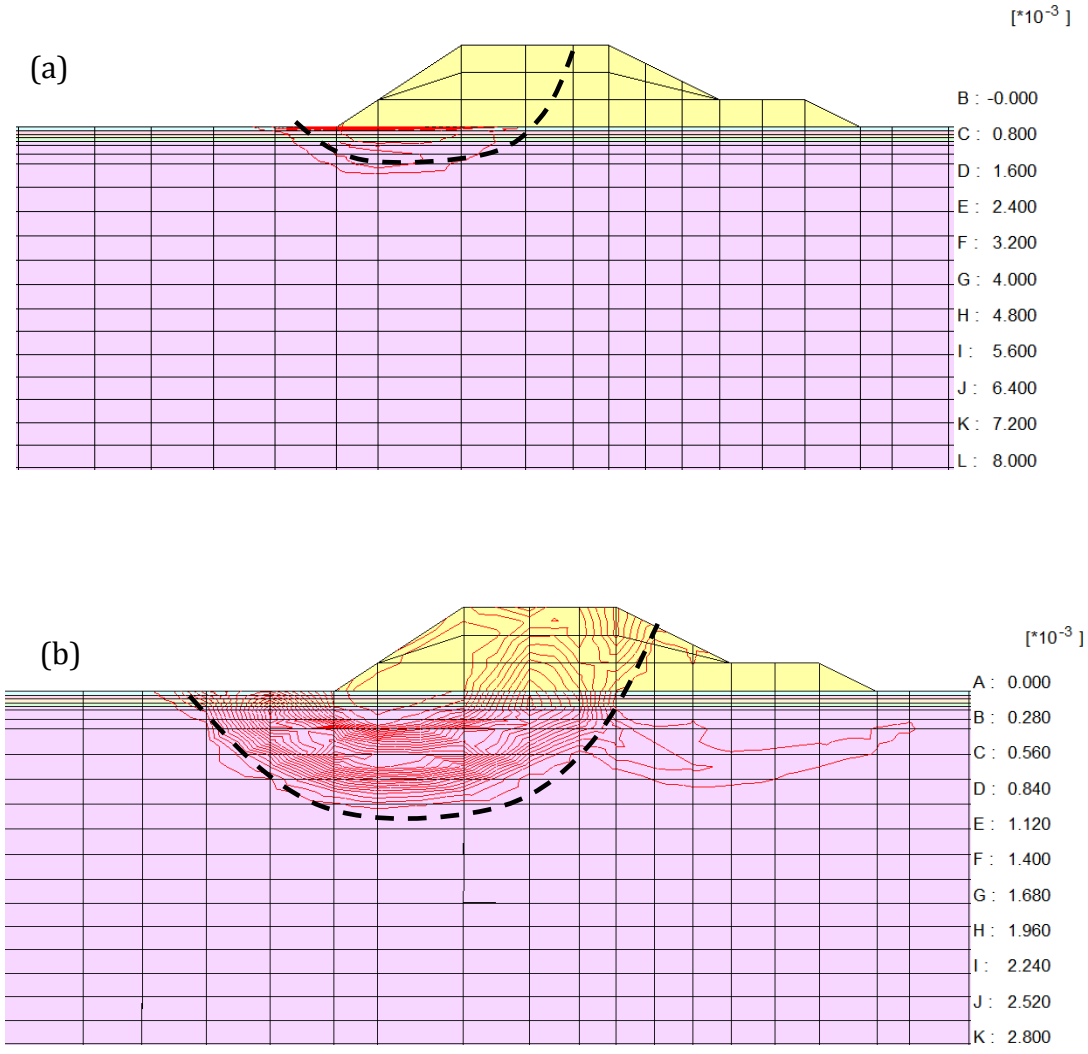

Figure 5.37: Contours of plastic shear strain increment at failure. (a) KHSM. (b) KHM

When using the KHM-bubble model a failure depth of approximately 6m can be seen in figure 5.37b In comparison to the field observations it can be clearly seen that this type of analysis grossly overestimates the volume of material mobilised with the top of the slip plane extending past the far corner of the crest. Whilst the prediction of the slip surface position when using the KHSM deviated from field data it does match well with the plane strain study by Grammatikopoulou *et al*. (2008). Similar to the outcomes of this study, when destructuration was incorporated into the analysis a shallower and narrower slip plane was observed. The analysis carried out by Zdravkovic *et al*. (2002) provided a failure surface which again did not match with that seen in the field observations. The author suggested that this could be attributed to the plane strain conditions present within analysis. One other possible explanation is that the depth has been influenced by rotation due to the presence of the access road.

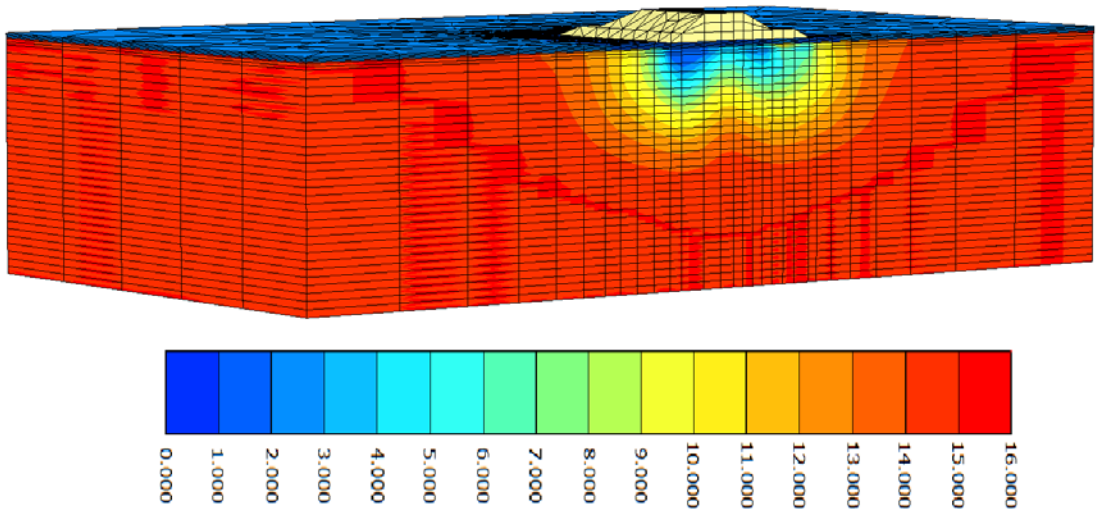

Figure 5.38: St Alban test embankment: spatial degree of structure contour at failure using the KHSM.

The above figure 5.38 shows the destructuration zones in the foundation soil at failure. It can be noticed that the initial structure has virtually been destroyed under the toe of the embankment indicating the development of potential failure. The figure also shows that the destructuration has propagated into a large zone below the located failure surface extending to an approximate depth of 11.5 m.

5.11.3 *Excess pore water pressure*

As can be seen from figure 5.39 (a & b) the KHSM managed to successfully simulate the final values of excess pore water pressure within the foundation soil. However it is observable that until failure the model tends to underestimate the stresses generated with regards to this parameter.

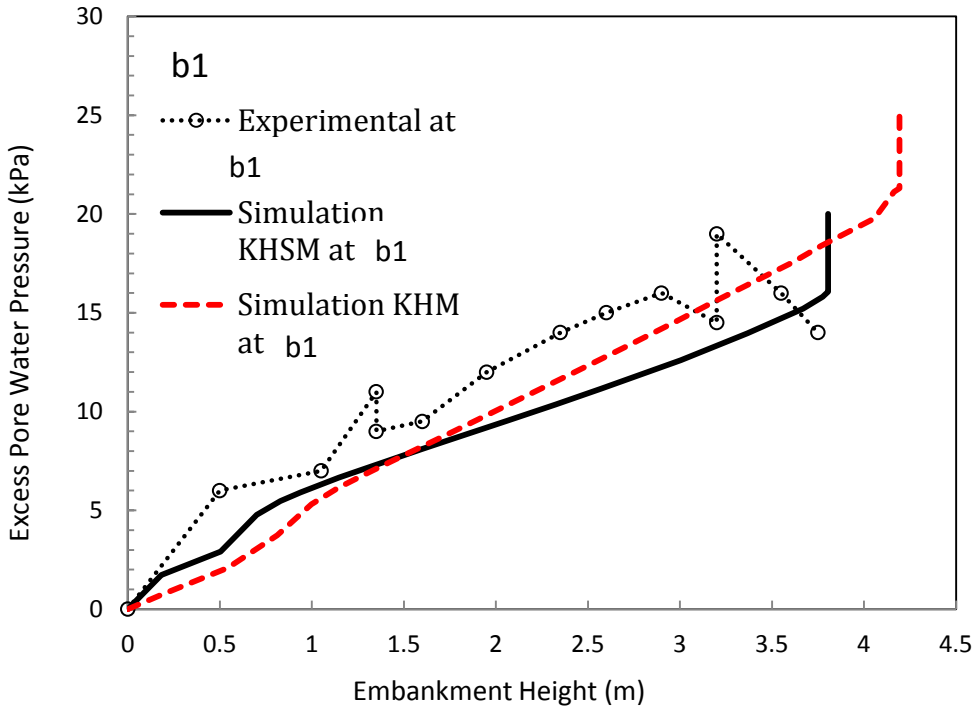

Figure 5.39: St Alban test embankment: measured and calculated excess pore water pressure at piezometers b1

This tendency to over predict excess pore water pressures (Figure 5.39) when taking no consideration of structure was also shown by Rouainia and Panayides (2011). In their plane strain analysis the KHSM was compared to the bubble model with regards to the St Alban embankment. Again at plate B1 the model without structure overestimated the final value of excess pore water pressure, however not to the extent seen in this study.

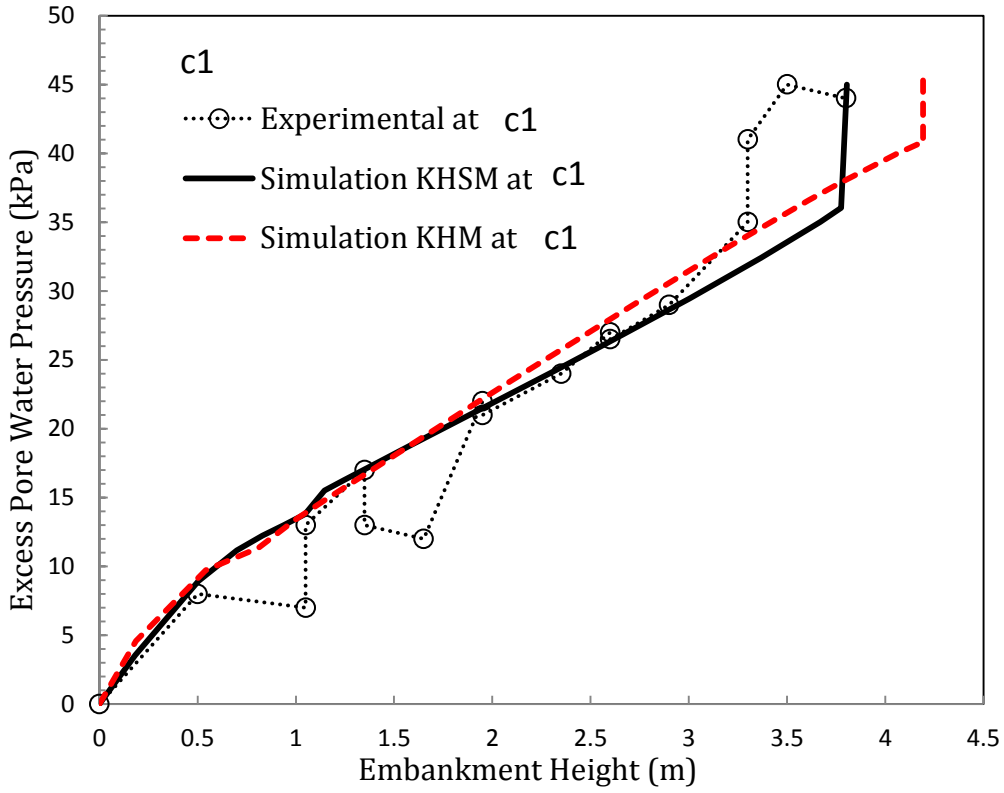

Figure 5.40: St Alban test embankment: measured and calculated excess pore water pressure at piezometers c1

The distribution of excess pore water pressure at failure in the foundation soil is shown in figures 5.41a and b. There is clear difference in the distribution between the KHSM and the KHM with higher pore pressures predicted at greater depths when no consideration is given to destructuration. Again the distribution profile bears a good comparison to what was observed in the plane strain analysis of Rouainia and Panayides (2011). A comparison between the aforementioned paper and this study also highlights how distribution varies when plane strain conditions are assumed instead of 3D. In the three-dimensional analysis any developments of

excess pore water pressure are seen to be contained below the embankment whereas two-dimensional predicts a greater lateral distribution.

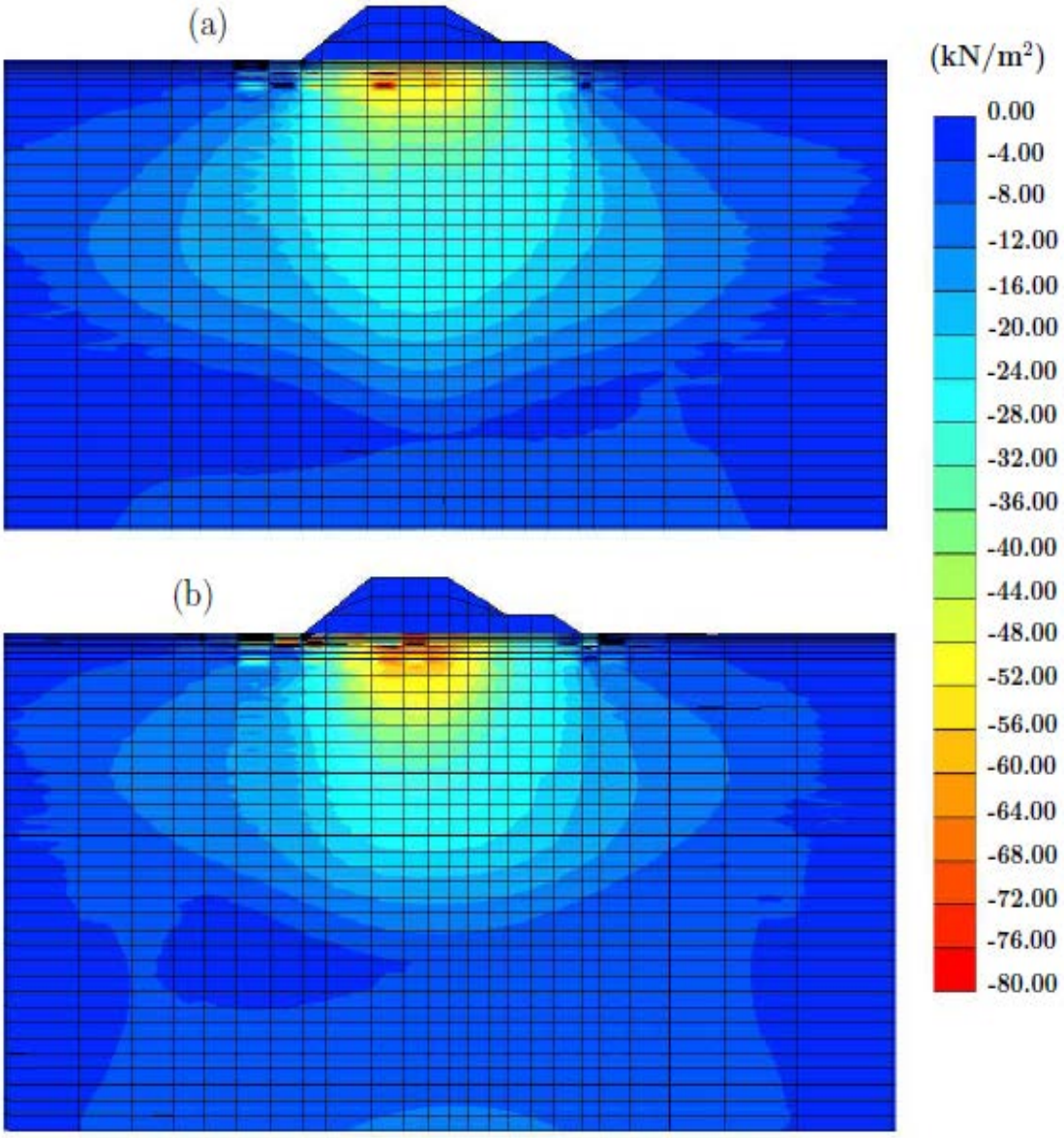

Figure 5.41: St Alban test embankment: excess pore water pressure distribution at failure:(a) with the KHSM and (b) with the KHM- bubble models

5.11.4 *Mobilised shear strength*

Figure 5.42 shows the comparison of mobilised undrained strength along the failure surface from the anisotropic KHSM analysis with that from the isotropic KHM analysis. It can be seen that this mobilised isotropic strength averages better the actual mobilised anisotropic strength.

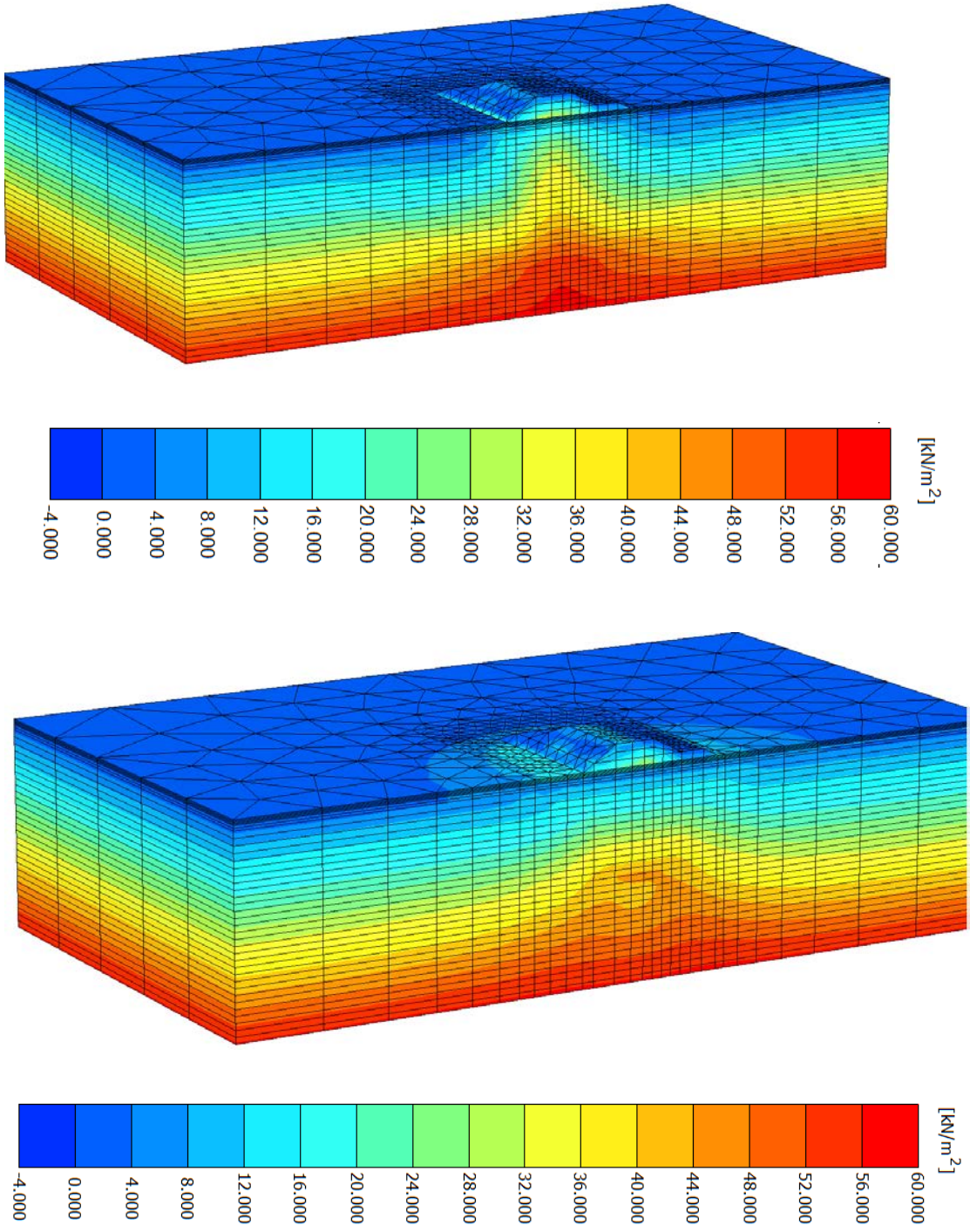

Figure 5.42: St. Alban embankment: Mobilised shear strength (a) KHSM (b) KHM-bubble models.

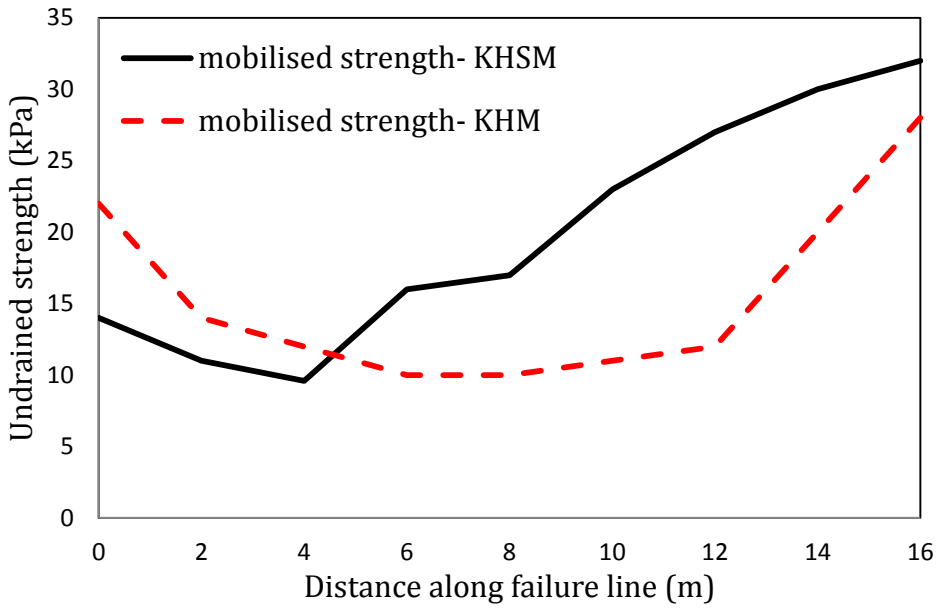

Figure 5.43: Comparison between mobilised anisotropic and isotropic strengths along failure surface for original embankment geometry.

Figure 5.43 shows the graphical representation of the comparison of mobilised undrained strength along the failure surface from the anisotropic KHSM analysis with that from the isotropic KHM-bubble simulation.

As it can be seen, this mobilised isotropic strength retains a symmetric shape under the failure surface, whereas the mobilised anisotropic strength shows significant variations as we move from the point on the failure line situated near the toe of the embankment towards the middle of the crest where the failure surface terminates. As it was evident from figure 5.24, during the two dimensional simulations, the orientation of the directions of the major principal stresses, varied significantly under the embankment. The inclination of this stress is happening along the failure surface in the three dimensional analyses as well, and hence the change in the mobilised undrained strength. The soil elements that are in proximity to the toe, are governed by the triaxial extension undrained shear strength in (see figure 5.10), whereas the clay underneath the centre of the embankment shows that the full triaxial compression strength was mobilised at failure.

5.12 Parametric analyses

As in the two dimensional finite element simulations, a parametric analysis was carried out in order to investigate the influence of the parameters controlling the initial structure and it's consequent degradation with plastic strains. The overall results follow the findings from the previous parametric study and can be summarized as follows:

- The findings for destructuration strain rate parameters (A) display that removing the volumetric strain rate (A = 1) and thus making the destructuration entirely distortional marginally reduced the failure height from 3.92m to 3.76m. Reversing the contributions from the different strain parameters (making A = 0.25) caused the height at failure to be increased to 4.36m..

- The study of varying the destructuration parameter (k) shows that as expected reducing this value leads to an increase in the failure height due to lowering the amount of strain softening with the final value of fill thickness at 4.48m.

- The final parameter which was investigated is the anisotropy of initial structure (η_0). This parameter controls the position of the centre of the structure surface of the KHSM model with respect to the reference surface. Increasing this value slightly increases failure height, however causes vertical displacements to be reduced. When the value is halved, very little difference in response can be observed with regards to the calibrated value. An examination of the effect upon horizontal movements was also performed. The findings are similar with the results from the vertical settlements, halving this value causes an almost unnoticeable change. Very little difference is also observed when this value was doubled.

5.13 Concluding remarks

The aim of this chapter was to assess the three-dimensional failure behaviour of a trial embankment founded upon structured clay, using an advanced constitutive soil model (kinematic hardening structure model - KHSM). This study has presented a number of Finite Element analyses exploring the extent to which the effects of destructuration influence the failure of a full scale embankment.

As construction in urban environments is rapidly gaining momentum due to a lack of land available for construction in both developed and developing regions of the world, engineers require the tools to accurately predict the ground movements around geotechnical structures. In most cases the interest is not solely focused on the movements at failure, but also in the stresses and movements under working loads and the effect that these may impose on adjacent structures.It was shown here that three dimensional analyses is vital when ground movements which cannot be captured by conventional two dimensional plane strain conditions and the extent of developing failure mechanisms need to be correctly assessed. In a stringent economic climate as the one the world is experiencing today, the correct design of geotechnical structures is a key factor in limiting time and costs for the construction industry.

The finite element analyses revealed that the numerical simulations using the KHSM model provided a close match to field monitoring data. The calibrated data, gave a predicted failure height of 3.93m, which is in accordance with the observed failure height of 3.9m. The embankment height of 2.4m was found to be critical in the embankment construction sequence, since it corresponds to the onset of accelerated movements in the soil mass. The correlation of the observed and predicted magnitudes of the settlements was in excellent agreement for all the embankment heights that were considered. The three dimensional analysis enabled the comparison between available data from settlement plates that were situated outside the plane at which previous two dimensional finite element models were carried out. The three dimensional effects were successfully modelled with the predicted depth of the failure surface being in close proximity with the observed value.

The good agreement between the observed and measured excess pore pressures echoed the convincing comparisons in the vertical settlements. This good agreement is especially significant when we consider that the two piezometers under consideration were situated either very close to or possibly on the failure surface. For simulations where the KHM-bubble model was used, (in which the destructuration was ignored), a stiffer behaviour of the foundation soil was predicted, which resulted in an overestimation of the embankment failure height.

Chapter 6: Finite element analysis of a deep excavation in Boston Blue Clay

This chapter analyses the behaviour of a deep excavation which forms part of a 100m wide basement excavation located in Boston, Massachusetts, USA. Two different types of tied back retaining walls were used, soldier pile tremie concrete wall and traditional reinforced concrete diaphragm wall. The glacial marine clay foundation was modelled with the kinematic hardening model for structured soils (KHSM) described in Chapter 3, the reduced version of the bubble model (KHM) as well as the very well-known modified Cam Clay models. The aim of the work conducted in this chapter is to demonstrate that the added features of the model implemented in this work such as small strain stiffness, structure and anisotropy are vital components to give a good prediction. The first part of this chapter provides a brief description of the site conditions, ground profile and construction sequences for the case study under consideration. The second part discusses the derivation of the parameters required for the model, as well as the calibration process through the numerical simulation of self-boring pressuremeter tests and constant rate of strain tests. The final section presents the comparison of the predicted wall deflection profiles for the excavation in Boston Blue Clay with observed movements taken from inclinometer readings with predicted vertical settlements also presented. Also presented are comparisons of computed and measured pore water pressures and ground movement with time.

6.1 Introduction

In recent years, the building engineering industry is becoming increasingly involved within the urban environment. The limited availability of land for construction in both developed and developing regions of the world has seen an increase in urban regeneration projects as well as construction of various types of infrastructure such as deep basements, underground train lines and associated service tunnels. In order to safely complete these deep excavations the use of appropriate retaining wall and bracing systems is required. Inadequate temporary and/or permanent designs may pose a threat to the safety and timely completion of the projects, since in the event of excessive ground movements resulting from the excavation works significant damage may be exerted to neighbouring structures. This could very well instigate litigation processes along with all te financial repercussions associated with them. In engineering terms, the issues of durability and fit-for-purpose designs associated with excessive ground movements requires a prompt and effectual management of excavation related movements. It is therefore imperative that maximum values of deformations should be carefully evaluated and compared with limiting values of the serviceability limit state. This however, can prove to be a double-edged sword as excessive conservatism may result in high-cost designs.

In geotechnical design of deep excavations, two approaches are typically employed in order to evaluate the anticipated wall deflections and soil settlements. These involve either the derivation of values from publically available date, using back-analysed cases, or alternatively results from a series of numerical simulations such as finite elements analyses. It has been well documented in this thesis that soil is a complicated, multi-phase material that inherently exhibits nonlinearity and in the case of natural, structured soils, a brittle response. An abundance of numerical models has been developed, which successfully address many features of stiffness non-linearity, as well as the effects of natural state (Gens and Nova, 1993; Asaoka et al. 2000; Liu and Carter, 2002; Kavvadas and Amorosi, 2000), however many of these models are relatively complex and the required parameters are at least, challenging to obtain.

Numerical modelling techniques are now widely used to predict the response of soil behind as well as on the walls of excavations and attempt to quantify their influence on surrounding structures. Although numerical simulations have now become the norm in addressing the design of temporary works for excavations, as well enhancing the capabilities of the back-analysing field measurements, they also receive criticism relating to their predictive capabilities (Carter et al. 2000). The origin of this criticism has been identified through the following two reasons:

- Numerical simulations adopt basic soil models which are inadequate in capturing the full suite of real soil features
- More sophisticated constitutive models are applied, however insufficient soil information result in uncertain input parameters

To address the first point above, geotechnical design on soft clays has often made use of finite element analyses employing isotropic elasto-plastic soil models formulate within the Critical State framework, such as the Modified Cam-Clay (MCC) model by Roscoe and Burland (1968) and the model extensions covered earlier. Recently formulated constitutive models have successfully replicated phenomena such as small-strain stiffness and initial degree of structure, as seen in sophisticated laboratory and in-situ tests. Test results indicated that for small strains of the order of 0.1%, which are typically encountered around excavations, a non-linear relationship with high stiffness at very small strains which decreases non-linearly as strains increase occurs. A common drawback associated with numerical analysis, however with advanced constitutive models, is that a larger number of material parameters and greater computational efforts are required.

The motivation to analyse the geotechnical problem under consideration in this chapter contains was that suitable experimental data existed and therefore provided a good opportunity to verify the proposed model in analysing the performance of the excavation retaining system. The modelling theory adopted in this work entails adequate complexity and it is focused on attempting to look at effect of initial structure on deformation predictions. It is founded on the principles of the known Cam Clay model and consequently adding the features of the models that have been developed in this thesis (history and anisotropy and structure).

Zdravkovic *et al*. (2005) examined the behaviour of a deep square excavation at Moorgate station on the Crossrail route in London by means of the Imperial College Finite Element Program (ICFEP). Their studies presented results from 2D and 3D models, utilising the Jardine small strain constitutive model for all soils. The exemption was the layer of made ground, which was modelled by means of a linear elastic Mohr-Coulomb model. The experimental data used to calibrae the Jardine model originated from the work of Addenbrook *et al*. (1997) who carried out triaxial experiments monitoring the small strain on samples of London Clay from the St James's Park area of London.

6.2 Site Location and Ground Conditions

The excavation under consideration is a 14m deep, 100m wide basement excavation above which four buildings will be constructed (Buro Happold, 2007) The complex will form the Allston Science Complex at Harvard University (see figure 6.1).

Information on ground prevalent on-site has been assembled from site investigations reports carried out as part of the project. The site investigations comprised of a suite of in-situ tests which included CPT, SCPT, pressuremeter and field vane, as well as laboratory testing comprising of consolidated undrained triaxial tests (compression and extension), direct shear tests, unconsolidated undrained triaxial tests, Atterberg limits and moisture contents.

The significant thickness of Boston Blue Clay present at the site is expected govern the response of the excavation. Boston Blue Clay was deposited in a marine environment and is characterised by a stiff crust of lightly overconsolidated clay underlain by normally consolidated clay at depth. The low degree of overconsolidation may potentially lead to substantial heave due to unloading and consequently movement of adjacent ground (Ladd *et al*. 1999). As a result, numerical modelling in conjunction with and small strain formulations for increased accuracy has been employed in an effort to predict ground movements associated with the excavation.

The stiffness and consolidation characteristics indicated that for the typical stress range associated with the excavation and construction loading the clay deposit would exhibit high stiffness. In addition, permeability testing suggested that the rate of dissipation of excess pore pressures would be very low given that typical permeability values of $3x10^{-10}$m/s were recorded on site.

The observations above suggested that the soil response would be governed by undrained conditions during the construction period, which was deemed to be significantly advantageous in terms of temporary excavation stability. This characteristic, allowed the construction of a deep supported excavation that under other circumstances would not be considered stable.

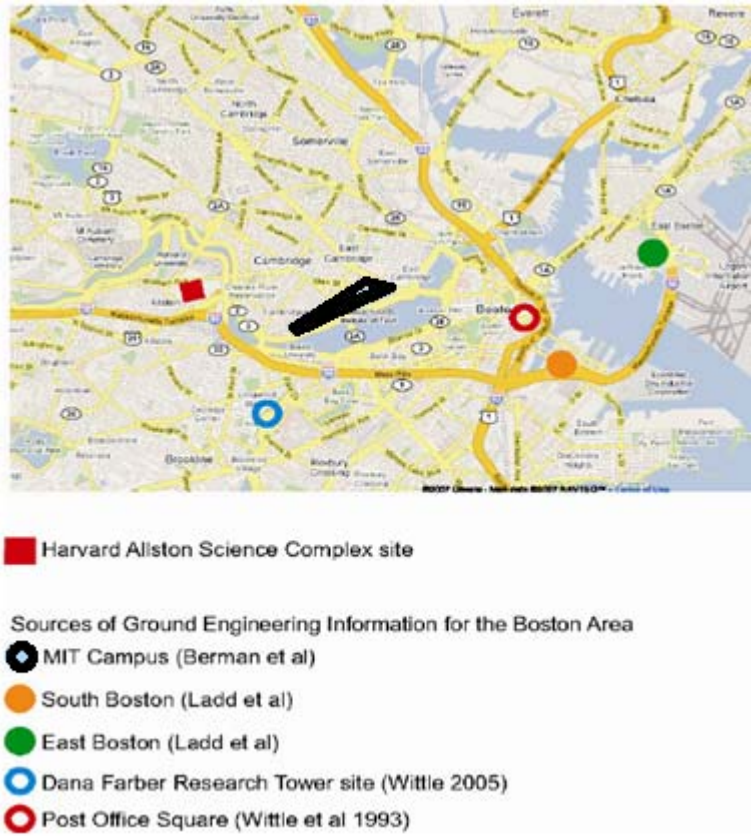

Figure 6.1: Location of Allston Sc. Comp., Boston, USA (Buro Happold, 2007)

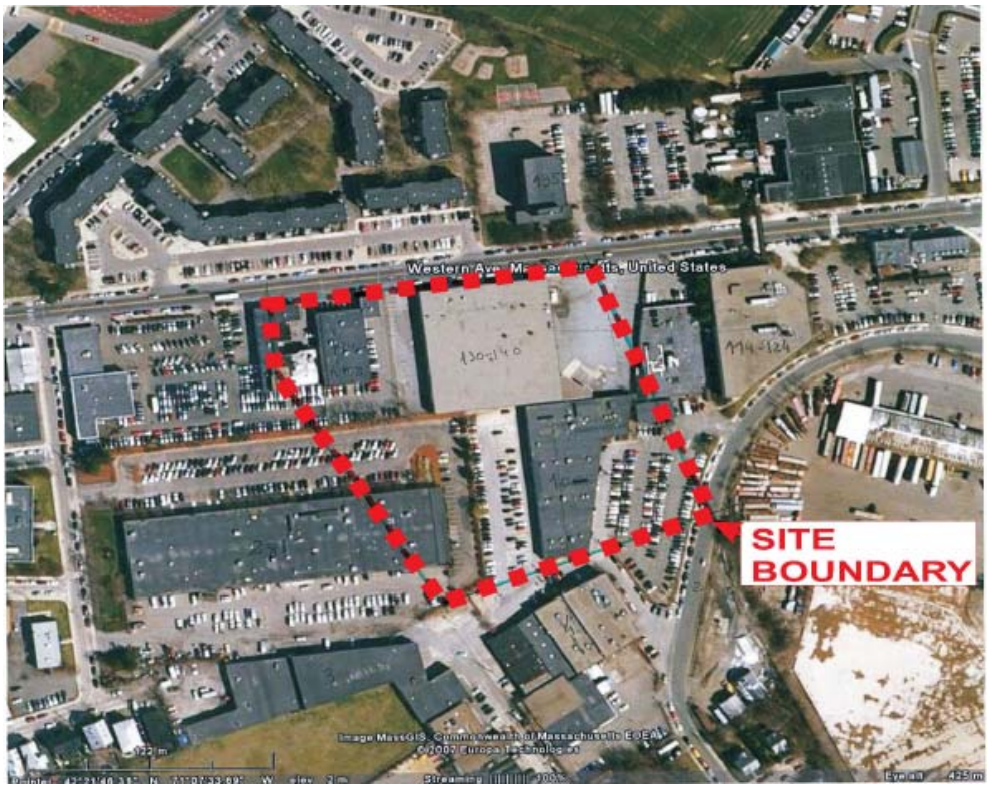

Figure 6.2: Aerial photograph of the existing site and footprint of proposed complex

6.2.1 Geology

The proximity of the proposed development (10.5km) to glacially eroded coastline, meant that the site was located geologically defined basin which was flooded durng the sea level rises of the Wisconsinan glacial era. Ensuing works such as infill and land reclamation programmes of the surrounding areas are currently ongoing, although they commenced during the 19th century Konstantakos (2005).

The greater Boston area is dominated by soils originating in post-glacial depositions as well as remains of engineered fills. The Boston Blue Clay (BBC) formation is prevalent in the majority of these areas. BBC, underlain by a layer of Glacial Till, which comprises of a mixture of clay and sandy soils containing cobbles and boulders. Areas of softer material have also been encountered within the Glacial Till.

The prevalent clay formation resulted from the depositions of fine particles separated from the till during thawing of the glacier. This process is believed to have taken place in relatively still marine waters approximately 14,000 years ago. The variability in the extent of the clay layer below surface throughout the Boston area has been well documented in literature. Another feature that was identified is the existence of thin sand band, as well as localised occurrences gravel and boulders.

The geological history of the clay deposit indicates that shallow areas of the clay were later eroded and went through a weathering process as sea level retreated approximately 12,000 to 11,000 years ago. As a result of these processes clay deposits in shallow depths appear to be fairly stiff and exhibiting a certain degree of overconsolidation, which reduces with depth, giving was to a softer and more compressible deposit at depth.

6.3 Ground investigation programme

Two Geotechnical site investigation campaigns were carried out between August 2006 and January 2007. The aim of these investigations was to establish the required engineering parameters necessary for the engineering design of the excavation and the required founding system of the proposed structure.

The geotechnical testing programme comprised of boreholes, combining Standard Penetration tests (SPT) and soil sample recovery. An additional site investigation campaign was conducted with the scope of deriving further data relating to the stiffness and strength characteristics of the clay deposit.

6.3.1 Ground conditions on site

A desk study conducted at the initial phases of the project revealed that a deposit of gravelly Sand mixed with soft compressible organic soil was underlying the Boston clay formation. It was also suggested that the Sand and Gravel deposit overlying the weathered clay was only present in some areas. The subsequent site investigation programmes served as validations of the anticipated stratigraphy as was established in the desk study. The encountered soil profile comprised of consecutive layers of Made Ground, a Sand layer occasionally containing gravel, the Boston clay formation, Glacial Till and finally Cambridge Argillite bedrock. The identified soil profile is shown in Table 6.1. The table also presents the description of the encountered strata.

Strata	Thickness (m)	Description
Made Ground	1.2 – 2.7	Granular silty sand fill with fragments of gravel, concrete, clay, brick, ash and wood
Fluvial Sands and Gravels	2.1- 5.5	Medium – dense to very dense sands and gravels
Boston Blue Clay	23.8 – 36.5	Stiff to very stiff olive grey clay with occasional discontinuous sand and silt partings, becoming softer with depth
Glacial Till	1.5 – 6.4	Very dense grey silty, clayey sand with gravels
Cambridge Argillite (bedrock)	Encountered at 33.8-45.7	Medium to moderately hard fresh to slightly weathered thinly bedded grey mudstone

Table 6.1: Strata encountered during site investigation at the Harvard Allston Science Complex site (Buro Happold, 2007).

Groundwater levels were determined with the use of ten vibrating wire piezometers. The instruments were distributed in the boreholes drilled for this purpose. The boreholes extended deep enough to facilitate the observation of porewater pressures within the cohesive layers. The hydrostatic groundwater table was encountered at 2.0m below the surface.

Figure 6.3 provides the geotechnical profile assumed for the Finite Element simulations used in this chapter.

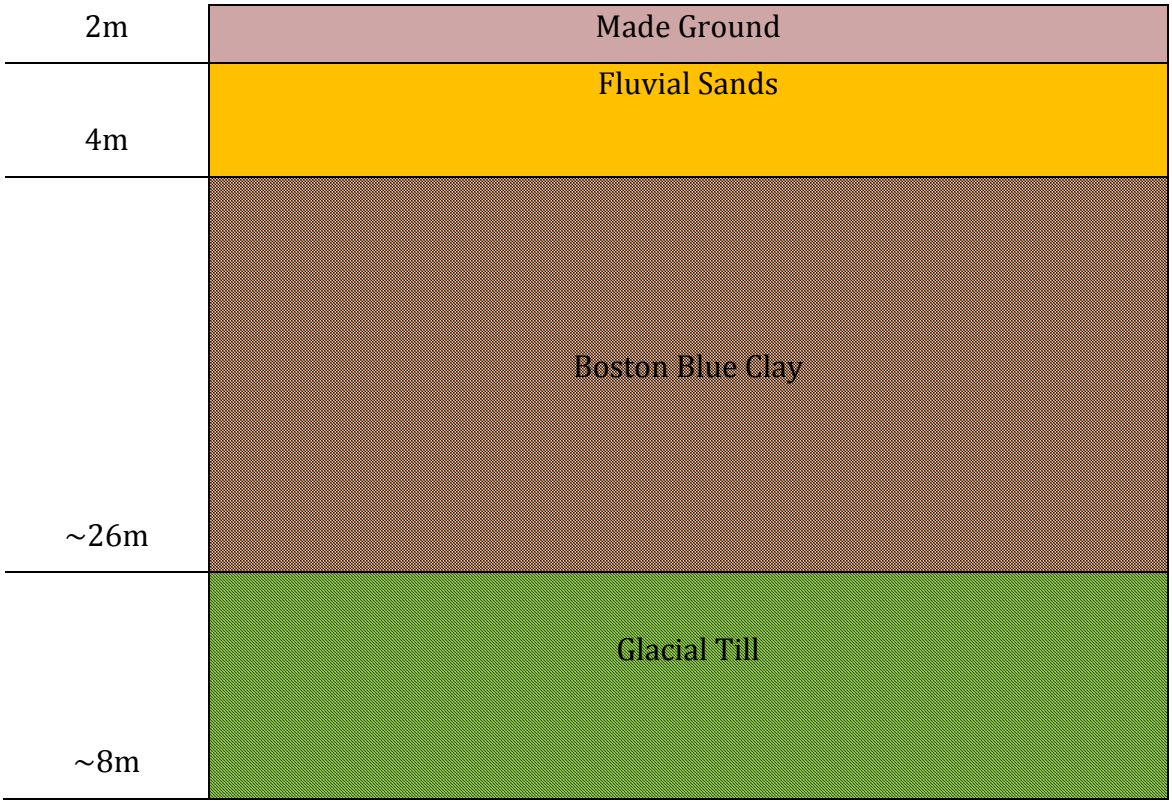

Figure 6.3: Geotechnical Profile adopted in the FE simulations

6.3.2 In situ Testing

The suite of in situ tests chosen for the site investigations had the aim of deriving engineering parameters such as strength, stiffness and permeability, in conjunction with an effort to prescribed test which were able to provide reliable information about the soil stratigraphy in order to validate the assumed ground model. It was believed that in situ testing methods would bear preliminary engineering parameters in the minimal amount of time.

6.4 Excavation retaining systems

Detailed design resulted in the adoption of two distinct types of retaining systems for the proposed excavations. It was decided that the peripheral retaining wall would take the following forms:

- Diaphragm wall (or reinforced concrete slurry wall)
- Soldier Pile Tremie Concrete slurry wall

The retaining systems which extended 13m and 17m below ground surface included four rows of ground anchors at selected elevations. The walls served the purpose of providing support the of the excavation during construction of the basement.

The first retaining system comprised of a reinforced concrete wall with a thickness of 0.91m. This option was utilised in areas of the peripheral wall where the wall would illustrate a substantial cantilever state was required The ground anchors incorporated the in the diaphragm wall were placed at a fixed interval of 1.22m centre to centre

The second system chosen for the proposed development, the SPTC slurry wall consisted of a continuous concrete outer frame which contained steel soldier piles. The soldier piles were assembled with W24x76 elements spaced at 1.53m centre to centre. Contrary to the diaphragm wall, this type of retaining system was installed in areas where the ground anchors were in relatively shallow depths. The

first row of ground anchors was installed with a spacing of 1.22m centre to centre, whereas the remaining levels made use of a 1.8 m centre to centre spacing.

Figure 6.4: SPTC wall and conventional diaphragm wall

6.5. Monitoring strategy and instrumentation

As discussed previously, the potential repercussions from the potential ground movements in the surrounding structures and infrastructure can come at a significant cost. This was more than true for the proposed development, due the large dimensions and extent of the excavation. As a result the decision was made to incorporate a monitoring system with a view to minimise the risk of damaging the adjacent buildings. The elements of the development which were continuously observed comprised first and foremost of the wall displacements and pore water pressures. For benchmarking purposes the measurements were frequently plotted

along with predictions of excavation behaviour from soil/structure interaction numerical simulations carried out as part of the detailed design stage.

In order to monitor the movement of the retaining systems, two types of inclinometers were installed as part of the monitoring programme. The manually read inclinometers were installed with the intention of being used as a contingency measure, especially at positions where it at best challenging to fit the automated In-Place Inclinometers (IPIs).The automated equipment was intended to register the bulk of deformation information, thus providing much more steady flow of data at prescribed time intervals of one hour. This automated system was inserted within the slurry wall at sixteen locations.

A review of the registered measurements suggested that the IPI probes suffered a series of malfunctions in the course of a 1-day period. Indications of movements in the range of ~ 1.3 cm were seen at certain locations. This was further investigated by means of independent surveys of the retaining systems, which indicated that the equipment had registered erroneous wall deformations.

Significant movements were observed during installation of the ground anchors. It was advocated (Buro Happold, 2009) that the use of pressurized drilling fluid with external flush and pressured grout without packers caused hydraulic fracturing of the cohesive soils retained by the excavation walls. As previously mentioned, the horizontal tieback spacing at Sections A and B were generally 1.22 m and 1.83 m, respectively. It is hypothesized that the closer tieback spacing at Section A significantly increased the amount of wall movement that occurred during the tieback installation process by exacerbating disturbance of the cohesive soils behind the slurry wall from tieback drilling and/or grouting activities.

6.6. Behaviour of Boston Blue Clay

Over the last 30 years considerable amount of research has been conducted by the Massachusetts Institute of Technology on re-sedimented Boston Blue Clay, organic clay created in the laboratory from natural Boston Blue Clay. It was found that RBBC displayed uniform properties, and exhibited behaviour that bore close resemblance to that of the natural parent material and of other low-sensitivity marine clays, including stress–strain–strength anisotropy, low to medium sensitivity, and significant strain rate dependence (Santagata and Germaine, 2002).

The behaviour of RBBC is noticeably different from that of reconstituted soils documented in the literature, despite the fact that it is a laboratory prepared soil. Findings from the extensive MIT research indicate that RBBC is described by features, such as stress– strain–strength anisotropy, rate dependency, and medium sensitivity that are typical of many natural marine types of clay, such as Boston Blue Clay (BBC), which is the natural parent material. Santagata (1998) and Santagata and Germaine (2002) provided extensive data illustrating the behaviour of RBBC. The authors advocated that the re-sedimentation procedure adopted, granted the soil, with structure which is consistent with that of natural soils characterized by a “sedimentation structure” (Cotecchia and Chandler, 2000), and therefore which chemical and aging processes have not played a significant role.

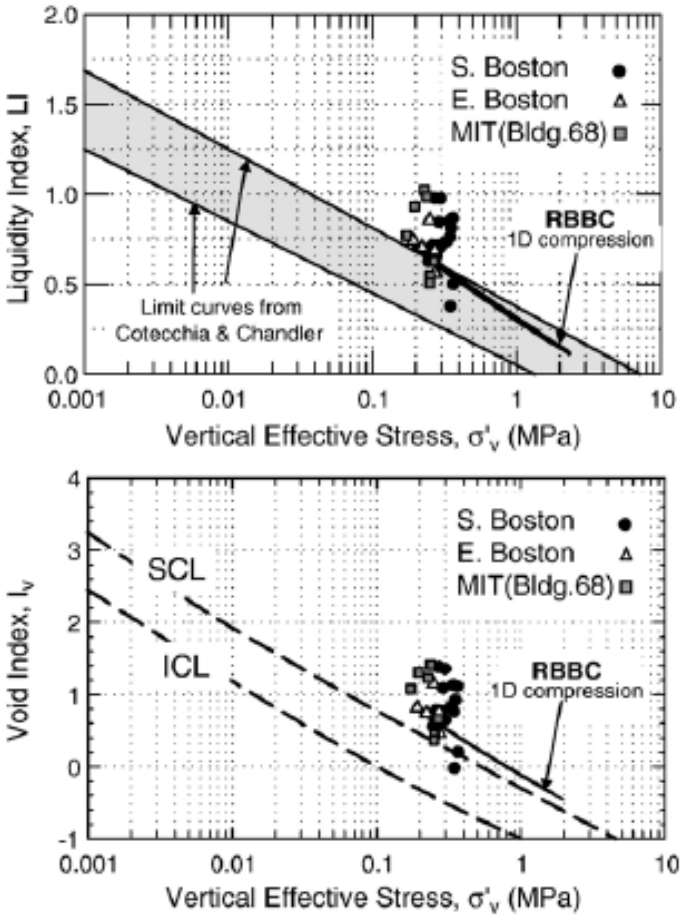

Figure 6.5: Comparison of the structure of RBBC and natural BBC to that of natural normally consolidated sedimentary clays: (a) LI–σ_v' and (b) Iv–σ_v' spaces (Santagata and Kang, 2007)

The features of RBBC described previously are evident in figure 6.5a, in which curves depicting the typical one-dimensional compression behaviour of RBBC in the normally consolidated region are plotted in terms of liquidity index versus effective stress (Santagata and Kang, 2007). The plot of experimental data in this space facilitates the comparison of the behaviour of clays of different compositions. It can be seen that compression curves for the clay have their origin at the upper end of the shaded band. Skempton (1970) proposed that the area delimited by the two lines, depicted the in situ state of natural normally consolidated clays which were defined by *'sedimentation'* structure and possess a sensitivity ranging from 1 to 10. In addition, figure 6.5a plots data for natural Boston Blue Clay in the close to normally consolidated state (OCR <1.5) from three different sites in the Boston

area: the South Boston and East Boston part of the Central Artery/Tunnel project and the MIT campus location (figure 6.1).

Burland (1990) extended the work of Skempton (1970), to further investigate the correlation between the properties of naturally sedimented clays and one-dimensionally consolidated reconstituted clays. His findings led him to the proposal of the void index (Iv) framework, which is defined by following equation:

$$I_v = \frac{e - e^*_{100}}{e^*_{100} - e^*_{1000}} \tag{6.1}$$

where e^*_{100} and e^*_{1000} are the void ratios of the reconstituted material at a vertical effective stress of 100 and 1000 kPa respectively. Burland concluded that the in situ stress state of a variety of natural sedimentary clays in normally consolidated state, which were characterised by sensitivity as large as nine formed a very narrow cluster when plotted in I_v–logσ_v' space (figure 6.5b).

In addition to the void index concept the *sedimentation compression line* (SCL), was also proposed. This limit plots above the line formed by the data for reconstituted clays- designated *intrinsic compression line* (ICL), and referred to the inherent properties of clays which are independent of its natural state. The offset between the two lines (figure 6.5b) illustrates the enhanced resistance of the structure of natural clays compared to their reconstituted counterparts. It is evident from figure 6.5b, that one dimensional compression curves for RBBC originate slightly above the SCL which indicate the likeness in the nature of the structure of RBBC to that of the majority of normally consolidated natural sedimentary clays.

6.7 Model Calibration

The focus of the work undertaken in this chapter is to present the potential of the kinematic hardening models that have been developed in this thesis and also demonstrate that the additional features incorporated in the KHSM can be easily calibrated through simple laboratory and insitu experiments. The models under consideration in this thesis were developed from the modified Cam-clay plasticity model, which has been firmly established over the past four decades. The modified Cam clay model is considered to be an accurate constitutive model in predicting the most important features of clays, such as stiffness variation with stress, volumetric change accompanying distortion and a critical state at which unlimited shear strain takes place without further change in effective stress.

However, kinematic hardening has been shown to provide a convenient framework to model a number of observed aspects of behaviour of laboratory and natural soils such as hysteretic response in cyclic loading, memory of recent stress history, smooth degradation of stiffness during loading, small strain stiffness and early onset of plastic strains. The bubble model adopted this framework with a single kinematic recording only a limited amount of recent history. A natural way of introducing progressive loss of initial structure was to prescribe that the size of the yield surface is influenced by the amount of damage.

This following section discusses and provides the recommended design soil properties and parameters for the encountered strata based on the results of the geotechnical site investigations available at the Allston Science Complex site.

6.7.1 Made Ground

As detailed earlier, parameters for the made ground were taken from work carried in the area of Boston previously. Ladd et al., (1999) classified the bulk density of made ground depending on the type of soil. For granular fill the recommended a bulk density of 19 kN/m^3, whereas for cohesive material the range of 16.5 kN/m^3 to 17.3 kN/m^3 was suggested. Given the granular nature of the made gournd at the proposed development a bulk density of 19kN/m^3 was assumed considered (Buro Happold, 2007).

Measurements of SPT 'N' values in this layer plotted between 4 and 99. The review of the data resulted in a characteristic value of 15 which was subsequently adopted for design purposes. This value alluded friction angle (φ') of 30° with no cohesion i.e. c'=0. A value of K_0=0.5 for the at rest earth pressure coefficient was specified corresponding to the recommended friction angle.

The relationship proposed by Stroud (1989) provided the basis for the derivation of the Young's Modulus for made ground:

$$E' = f_2 N_{60} \tag{6.2}$$

Where E' = Young's Modulus (MPa) and N is the blow count on SPT tests. Literature recommends that variable f_2 can be is in the range of 1.0 to 2.0 for strain levels representative of foundation loading. As a result, the recommended range of Young's Modulus between 2.25 MPa and 4.5 MPa and a characteristic value of 2.9MPa was adopted for design purposes.

6.7.2 Fluvial Sands

SPT measurements alluded to a layer of high density. Based on data from Berman, et al. (1993) and Ladd et al. (1999) a bulk density of 19kN/m^3 was adopted for design. A range of SPT values between 15 and 160 was recorded for this layer. A characteristic value 60 was selected, which led to the determination of a friction angle of φ'= 35°. The same considerations as for the made ground layer were valie with regards to the Young's Modulus derivation. A value of E'=7.5 MPa was adopted for the simulations. The at rest earth pressure coefficient (K_0) was set to a value of 0.43 during the simulations.

6.7.3 Glacial Till

Similarly to the preceding layer, SPT measurements suggested that the Glacial Till layer was generally dense to very dense. Given the nature of some dubious results in this layer, engineering properties were derived based on previously published information by Whittle et al. (1993) and O'Rourke and O'Donnell (1997). Consequently a bulk density of 21.5kN/m^3 was adopted for the simulations. Considering data from Whittle et al. (1993) a friction angle of 37° was specified for this material. Based on equation 6.1 a Young's Modulus of 100MPa was employed in this work.

6.7.4 Boston Blue Clay

Since it is anticipated that the Boston Blue Clay deposit would govern the response of the excavation, a comprehensive testing programme was put into place, examining the engineering properties of this layer. Previous studies on this material suggested the existence of a stiff crust which was underlain by a material exhibiting a normally to low overconsolidation ratios. Given this layering, it is anticipated that in the event of loading of this deposit, it is likely that substantial ground deformation can be anticipated.

Measurements of moisture content on clay specimens exhibited a moderate increase of this quantity with depth indicated. Reported values were in the range 25% to 44%. Atterberg limit tests suggested a Plasticity Index (PI) between 13% and 29% and the deposit could be described as low plasticity clay (CL). A characteristic value of 20% was used for the derivation of associated parameters for the Viggiani elastic model (figure 2.12).

In order to derive the bulk density of the Boston Blue Clay deposit, in addition to the values of 18.2kN/m^3 to 19kN/m^3, determined during the geotechnical site investigations, information collated from previous studies at the neighbouring MIT campus were also consulted. The MIT studies displayed a characteristic bulk density of 18.4kN/m^3 for the overconsolidated portion and 19.3kN/m^3 for the normally consolidated material. On review of the available information above, a bulk density of 19kN/m^3 was adopted in the finite element simulations.

A series of anisotropic undrained tests undertaken with pore pressure measurements facilitated the selection of friction angle. Reported values of 28.6°, 27.8° and 27.9° corresponding to DSS, TC and TE were taken into consideration. Given the comprehensive academic research on this material, design friction angles of φ' = 28^o and c'=0 for the normally consolidated portion and φ' = 22° for the overconsolidated BBC were recommended for design purposes. Subsequent calculation of the slope of the critical state line under triaxial compression ***M*** (equation 6.3), based on the above friction angles yielded results of ***1.11*** and ***0.856*** for NC and OC BBC respectively. Note that for the purposes of the numerical simulations a valie of **M=1.11** was used for both portions of the BBC.

$$M = \frac{6\sin\varphi'}{3 - \sin\varphi'} \tag{6.3}$$

BBC compressibility parameters $\boldsymbol{\lambda^* = 0.028}$ and $\boldsymbol{\kappa^* = 0.004}$ (Fasano, 2007) were evaluated parametrically from the results of constant rate of strain consolidation (CRSC) tests for appropriate ranges of void ratio (e). The parameters characterise the stress dependent soil stiffness within the elastic domain (κ^*) and when plastic strains are concerned (λ^*).

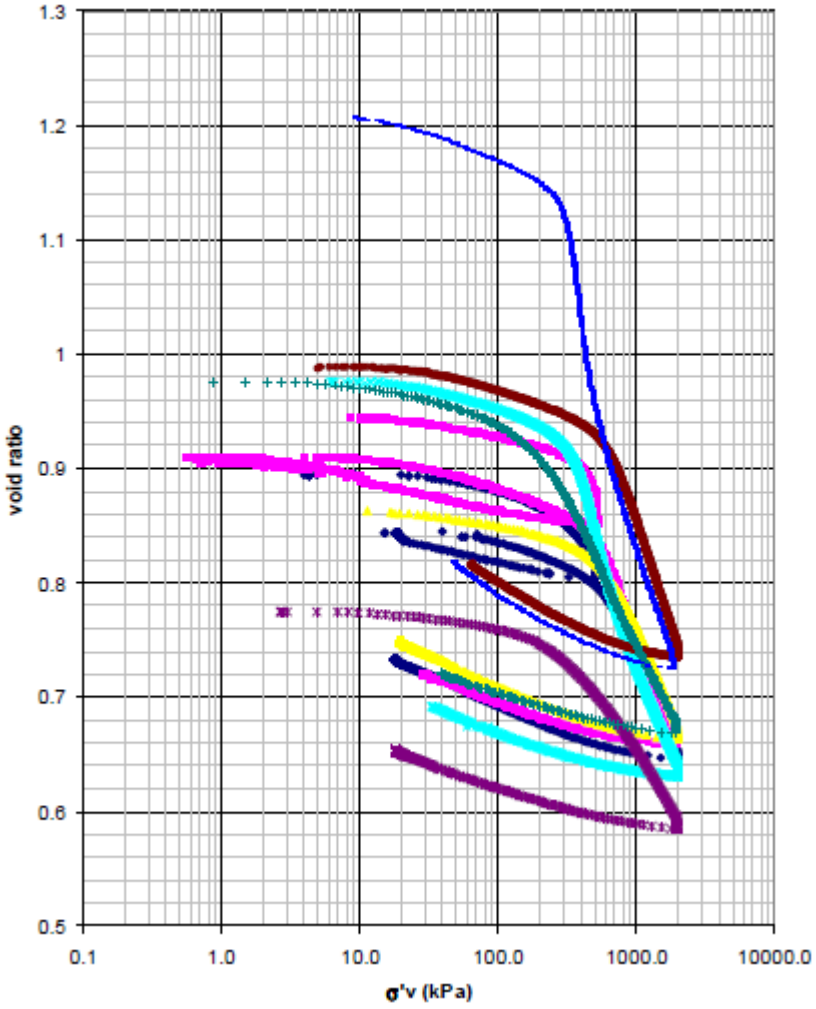

Figure 6.6: Constant Rate of Strain Compression tests in BBC

Since no test data was available with measurements of strains in the very small and small strain region, a value of R equal to 0.08 was assumed for both kinematic hardening models (KHM and KHSM). Finally, the parameters B and, ψ which are the parameters in the hardening modulus and control the decay of stiffness, cannot be measured directly from the experimental data and can only be determined by curve fitting of experimental data. This was achieved by simulations of a triaxial test on a K_0-consolidated undrained triaxial compression (CK_0 UTC) specimen of natural BBC. The specimen was reconsolidated with the SHANSEP technique to a normally consolidated state.

The SHANSEP procedure (Ladd & Foot (1974)) is based on the experimental evidence that for many clays, the undrained shear strength for a particular shearing mode is related to the stress history of the material. The following testing stages are followed:

- Consolidation of the sample to a stress level beyond the preconsolidation pressure (i.e. the maximum stress the sample has ever experienced in situ).
- Sample unloading to define a specific overconsolidation ratio (OCR).
- Testing the sample following a particular mode of shearing.

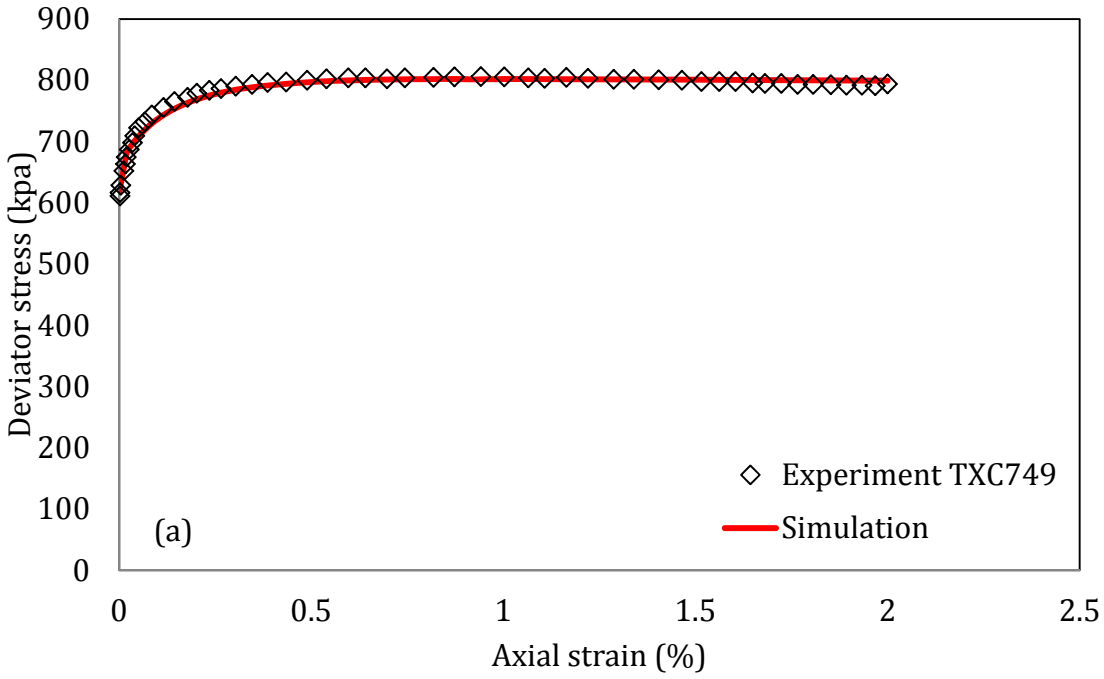

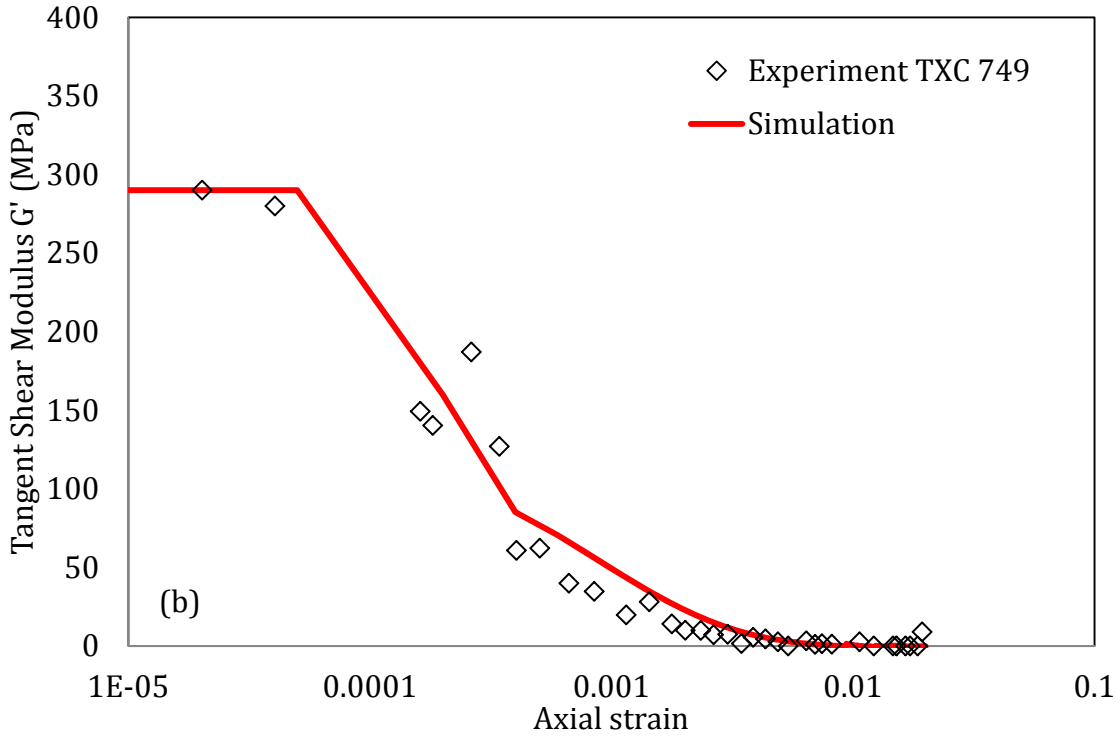

Figure 6.7: Comparison of model predictions and experimental results for undrained triaxial compression tests on anisotropically consolidated natural Boston Blue Clay clay: (a) stress:strain curve; (b) stiffness:strain curve

Burland (1990) investigated the behaviour of a North Sea clay deposit, in which two distinctive layers existed. The different deposition conditions and associated material structures resulted in significant effect on the in situ stress state and mechanical properties. On the basis of the material response in one dimensional compression, the author proposed that for normally consolidated clays for which the in situ stress state lies on or above the SCL, the SHANSEP test procedure caused modification of the structure of the clay consequently underestimates both the peak strength and the brittleness of the clay. According to the above observation, parameter r_0 was set 1, so that no inter-particle bonding was assumed for this test. Figures 6.6a and 6.6b plot comparison of the numerical results with the experimental data, for values of parameters ***B=2.0*** and ***ψ=1.35.*** The stress–strain curves predicted by the model are in good agreement with the experimental data (figure 6.7a) In terms of the stiffness–strain curves (figure 6.7b) the simulation successfully captures the degradation of stiffness with increasing strain.

The next step in the calibration procedure, involved the determination of the structure related parameters. The stress sensitivity approach as detailed in Burland (1990) and adopted in Chapters 4 and 5 for the determination on the initial structure of sensitive clays was employed here.

No available data for reconstituted and natural samples were available from the Allston Science complex site and therefore, Figure 6.5b was utilised to facilitate the evaluation of the initial measure of bonding in natural BBC. As it can be seen in figure 6.8, the corresponding value of vertical effective stress for samples with the same void index were compared for a total number of six samples. The ratio of σ'_{vNBBC} / σ'_{vRBBC}, (stress sensitivity) was assumed to represent the range of initial structure due to bonding of the soil r_0; where the first term refers to the vertical stress of the natural samples and the latter to the equivalent for the resedimented cases.

Table 6.2 shows the values obtained from this procedure using the above approach. The values formed the basis in the subsequent stage of the calibration process.

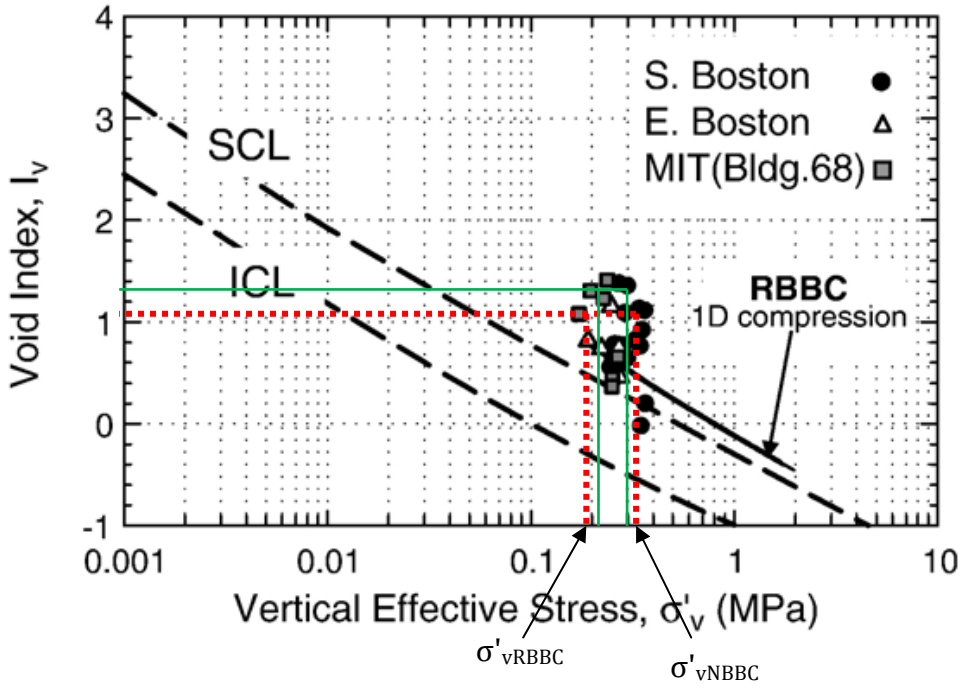

Figure 6.8: Evaluation of the post sedimentation structure of RBBC and natural BBC

Specimen Number	Stress Sensitivity
1	1.68
2	1.55
3	1.2
4	1.58
5	1.46
6	2.08

Table 6.2: Range of estimated values for post-sedimentation structure for Boston Blue Clay

CRSC test loading curves are plotted in Figure 6.9a for normally consolidated and figure 6.8b for overconsolidated BBC (Nikolic et al. 2010), together with ICL and SCL, in e-σ'_v space. The indicative range of possible SC curves is also included in both of the figures. In addition figure 6.9 also plots in situ stress states for the two samples, which point towards a substantial agreement between in situ stress levels and yield stress for the normally consolidated BBC. This observation confirms that the yield stress ratio (YSR= σ'_v / σ'_{v0}) as defined by Burland (1990), is in the same order of the OCR. This is in good agreement with previous results reported by Sheahan (2005) for deep BBC.

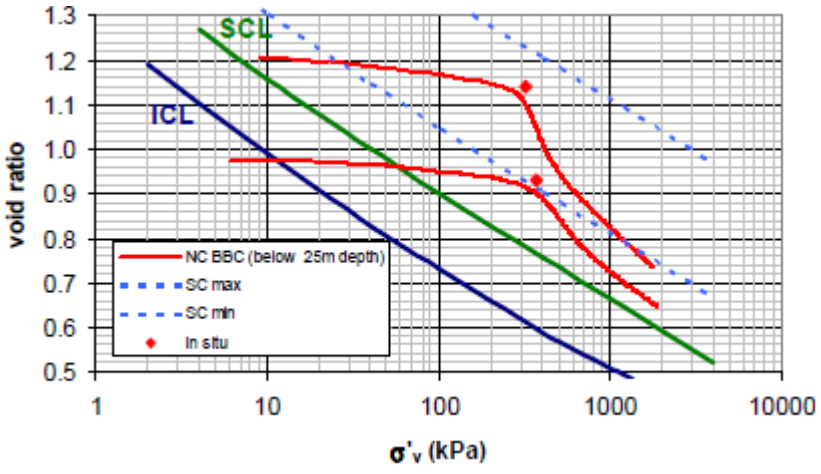

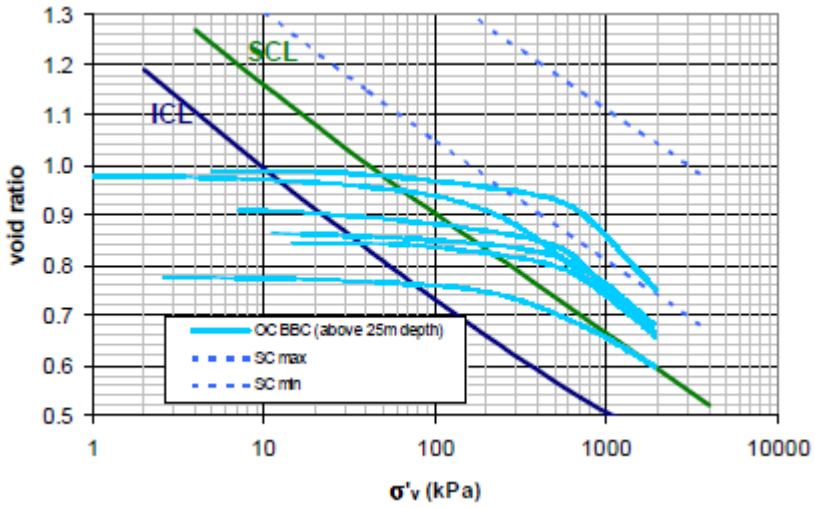

Figure 6.9: Results from CRSC tests (a) natural NC and (b) natural OC BBC (Nikolic et al. 2010)

The compression curves for the normally consolidated samples exhibit a fairly abrupt drop in stiffness once the yield stress is reached. This can be attributed to the high void ratio and consequently a more open structure that the sample has at its in situ condition. After the initial post-yield drop in stiffness (more or less abrupt), the curves fall more gently towards the SCL, however are still relatively far from crossing it.

The overconsolidated samples in figure 6.8 exhibit a more gradual fall in stiffness at yielding. This behaviour corroborates with observations from Burland et al. (1996), who stated that for stiff, overconsolidated clays, the gross yield stress is often not well defined because the destructuration in compression occurs gradually (and, in some cases, very high stresses are needed to complete the yielding). Another possible explanation is that the lower void ratio of the overconsolidated clay makes it essentially less susceptible to the sharper drop in stiffness observed with the normally consolidated material. The observations for the different behaviour of NC and OC samples served as the starting point for the assessment of the rate of destructuration ***k***. The values that have been used in the simulations of laboratory and in situ tests maintain the relationship between the two distinct zones of the BBC deposit.

However, the figures above show that once the yield pressure is surpassed, the natural compression curves continue to the right of the ICL, with the difference between the natural compression curve and the intrinsic compression line maintained at constant ratio even at high stresses. If this stress difference was attributed entirely to the structure due to interparticle bonding, progressive structural degradation would not be justified. To be more precise, the disparity was believed to result from significant differences in fabric between the natural and reconstituted soil, which will contribute to these effects. Therefore the BBC deposit was assumed to have a significant inherent anisotropy of fabric, which provided the starting point for the determination of parameter $\boldsymbol{\eta_0}$. In the absence of adequate laboratory test data to investigate their relative importance in detail, it was assumed that both plastic volumetric and shear strains influence the degradation of structure equally, and therefore the scaling parameter $\boldsymbol{A}$=**0.5** was adopted in the numerical simulations.

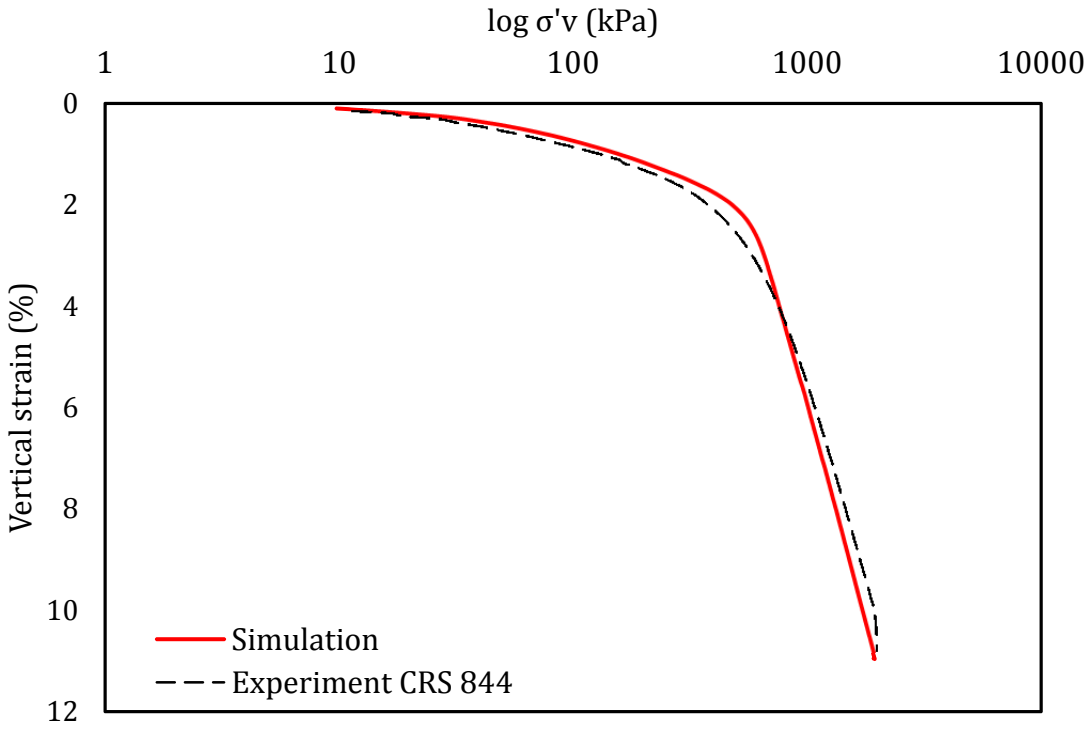

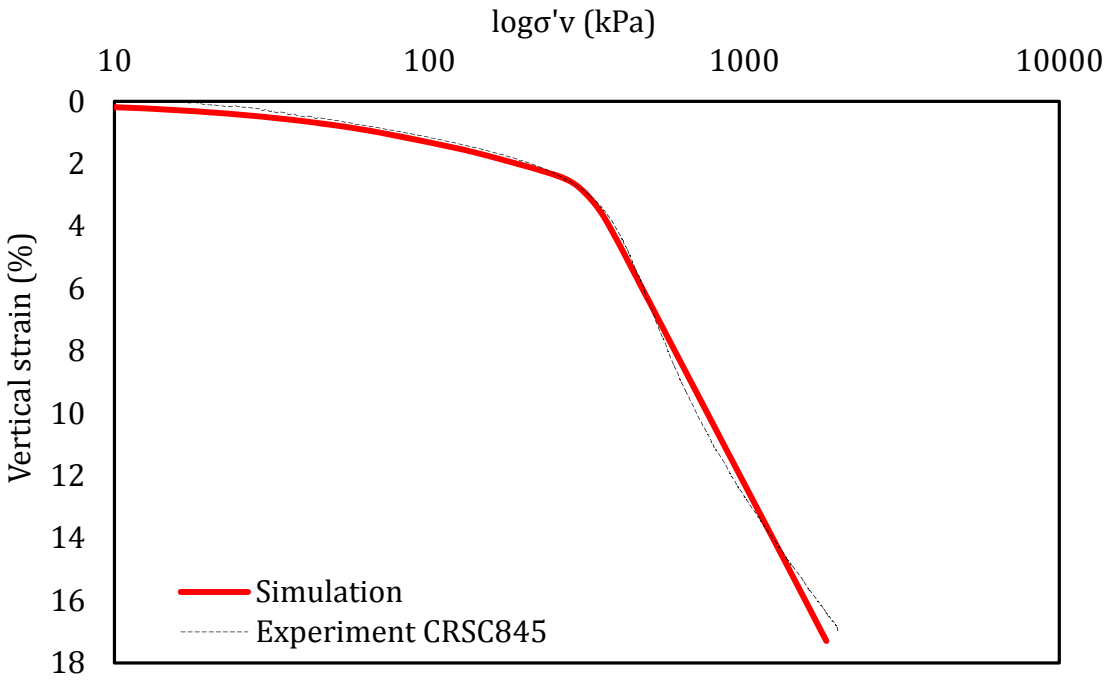

Figure 6.10: Comparison of numerical results and experiments for compression curves for natural samples of Boston Blue Clay: (a) CRS 844-depth 11m and (b) CRS 845-depth 38m

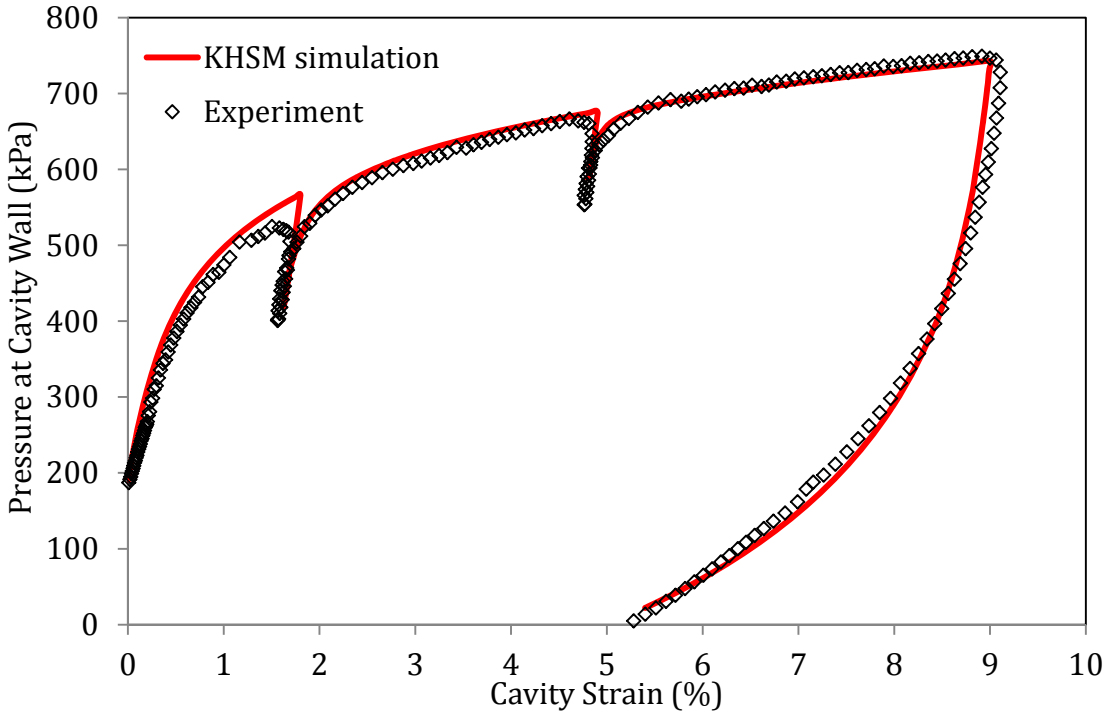

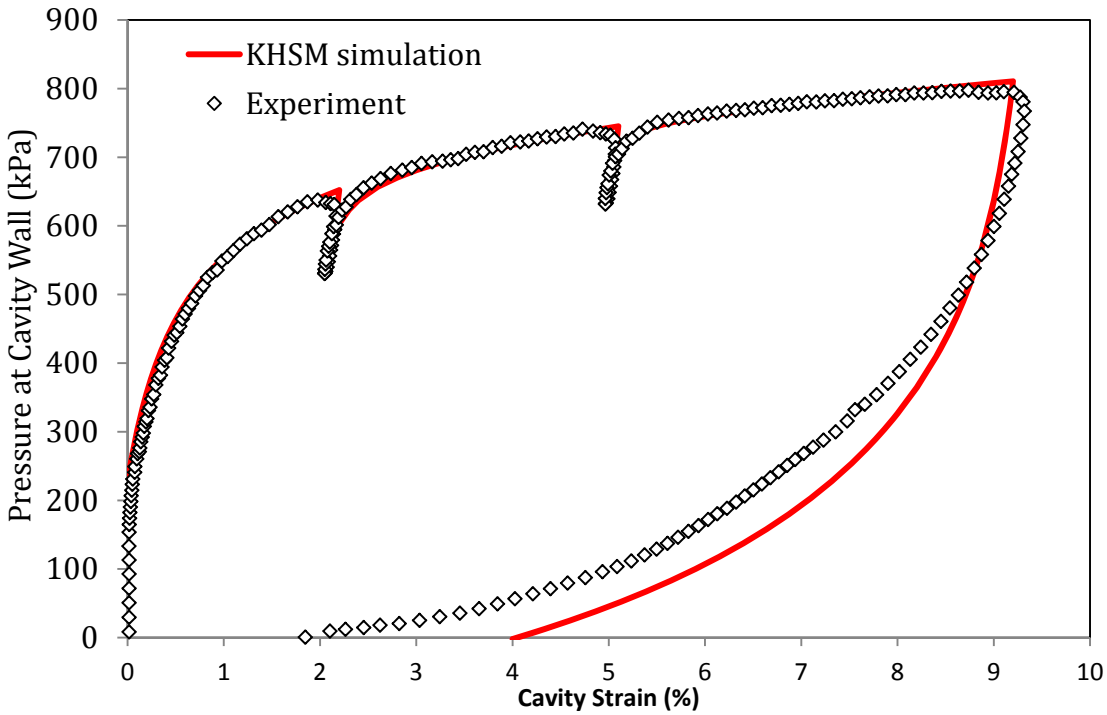

Figure 6.11: Comparison of numerical results and experiments for self boring pressuremeter test on Boston Blue Clay: (a) B106T2-depth 13m and (b) B106T10-depth 35m

Two sources of experimental data, constant rate of strain compression tests and self-boring pressuremeter, were employed in order to obtain the remaining parameters. A representative sample from the two distinctive regions (overconsolidated and normally consolidated) of the BBC deposit were selected for simulation. Stress strain curves were matched using a trial and error procedure (figures 6.10 and 6.11). Characteristics of the tests used for the calibration and the resulting fitted parameters controlling the structure are presented in the table below.

Zone	Test	Depth (m)	r_0	k	A	η_0
NC	SBPM	13	1.8	1.5	0.5	0.5
NC	CRSC	11	1.8	1.5	0.5	0.5
OC	SBPM	35	1.5	1.0	0.5	0.3
OC	CRSC	38	1.5	1.0	0.5	0.3

Table 6.3: Laboratory and field test selected for calibration and fitted structure related parameters

6.8 Numerical model

The finite element software PLAXIS 2D Version 9 was used to run a series of simulations in this study, with the KHSM introduced as a user-defined model. Following an initial mesh-sensitivity analysis, the finite element mesh with the boundary conditions for the plane strain analysis of the cross-section (figure 6.12), consisted of approximately 2200 15-noded triangular elements. No movement was permitted at the base of the foundation, and only vertical movement was permitted at the lateral boundaries. For reasons of numerical convenience, the initial location of the centre of the bubble was chosen to coincide with the initial stress.

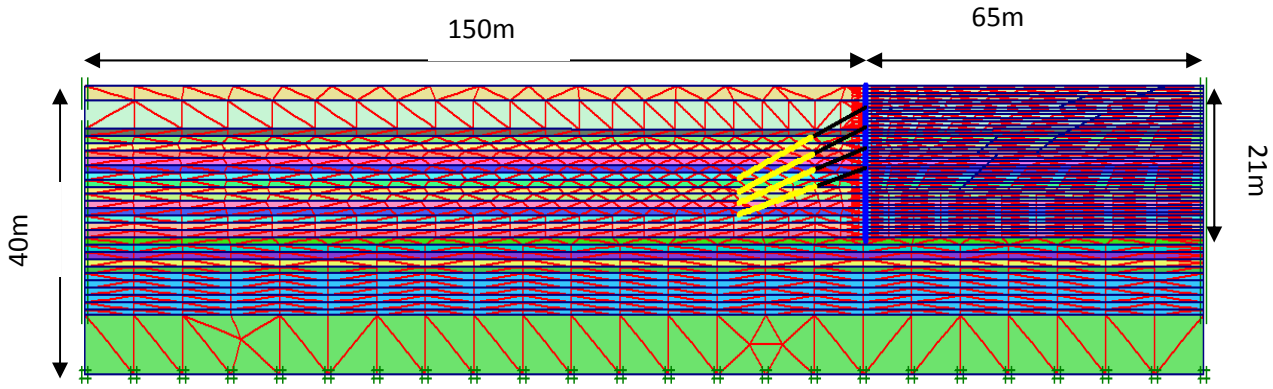

Figure 6.12: Geometry and finite element mesh of excavation

The excavation was supported by a 21m deep retaining system, with four rows of tie-back anchors. The left hand boundary of the model is set at 150m, which is over four times the depth of the excavation and thus is unlikely to interfere with the results (Kung *et al*. 2009). Table 6.4 lists the relevant characteristics of the excavation support system at the two sections.

Wall characteristics	Section A	Anchor inclination(^{0})	Section B	Anchor inclination
Thickness (m)	0.76m	-------	0.91m	--------
Tieback horizontal spacing (m)	1.22m	-------	1.83 m	--------
1st level tieback elevation (mbgl)	2.9m	22	0.3m	22
2nd level tieback elevation (mbgl)	5.7m	18	4.6m	20
3rd level tieback elevation (mbgl)	8.5m	15	7.9m	17.5
4th level tieback elevation (mbgl)	11.3m	15	11m	15

Table 6.4: Retaining system characteristics

6.7.1 Constructions sequence

The excavation sequence for both sections is listed below.

- Install slurry wall.
- Excavate to approximately 0.6m below Level 1 tiebacks.
- Install Level 1 tiebacks.
- Excavate to approximately 0.6m below Level 2 tiebacks.
- Install Level 2 tiebacks.
- Excavate to approximately 0.6m below Level 3 tiebacks.
- Install Level 3 tiebacks.

- Excavate to approximately 0.6m below Level 4 tiebacks.
- Install Level 4 tiebacks.
- Excavate to bottom of excavation

All calculations have been specified as plastic analysis calculations in the software and have a staged construction loading input.

6.8.2 Model Parameters

The made ground, sand and gravel and glacial till are modelled using the Mohr Coulomb soil model with the associated parameters provided in section 6.6. A value of poisson's ratio ***v=0.2*** was employed for these layers based on recommendations from the geotechnical report. The Boston Blue Clay layer was divided into two layers as detailed previously, in order to account for variations with depth.

6.8.3 Initial conditions and groundwater level

The K_0 profile used in the analysis is based on the design line assumed by the geotechnical report (Buro Happold, 2007) from various laboratory and field measurements. Figure 6.13 shows the K_0 values used for each stratum. Groundwater monitoring undertaken during site investigation revealed that before construction the groundwater table is at 2m and that there is a hydrostatic pore pressure increase with depth. Therefore initial pore pressures are generated using the phreatic level function in Plaxis.

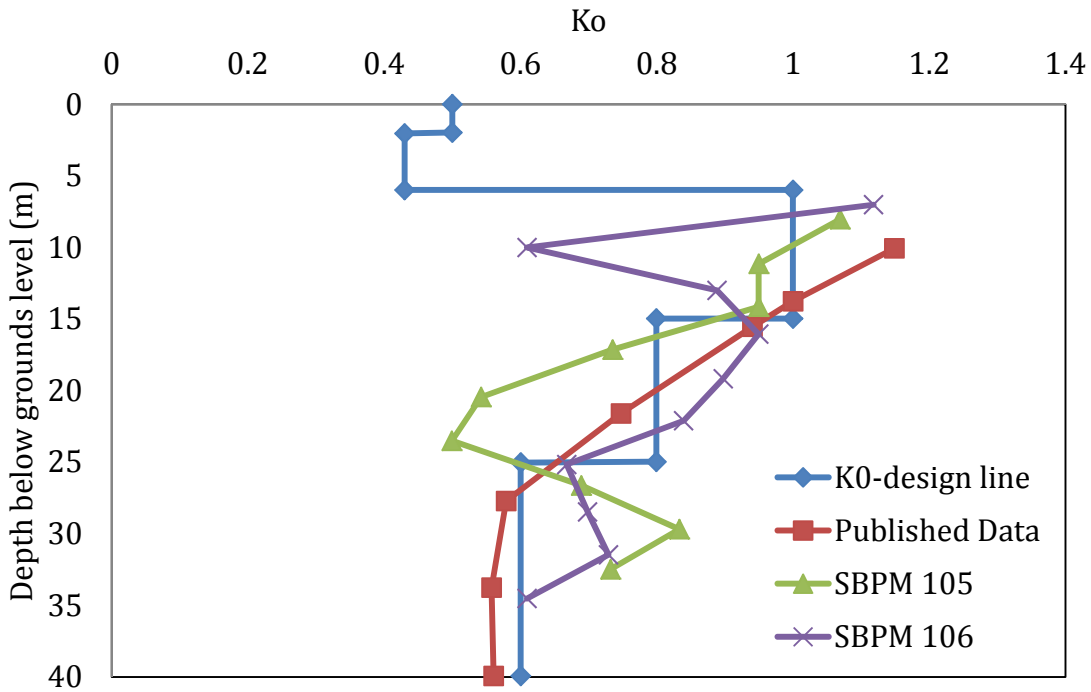

Figure 6.13: K_0 profile adopted for numerical simulations

Groundwater dewatering within the excavation was achieved by means of sump pumping. No drawdown of external water levels was permitted and as such a "water tight" temporary retaining wall was required. Since the excavation was carried out under dry, conditions excavations between 2.0m b.g.l and the base of the excavation, pore pressures were assigned using the user defined distribution function in Plaxis, based on data from Buro Happold. For each calculation phase, the groundwater table was specified by entering the level (y_{ref}) at which the magnitude of pore water pressures (p_{ref}) was zero, with the increment of pressure (p_{inc}) in the unit of stress per unit depth also specified in order to simulate the pore water distribution. Groundwater conditions for the construction sequence are given in table 6.5. This procedure resulted in a linear pore pressure distribution. The water table on the outside of the wall remains constant at 2.0m below ground level.

Excavation number	y_{ref} (mbgl)	p_{ref} (kN/m²)	p_{inc} (kN/m²/m)
1	5	0	11.44
2	7	0	13.03
3	10	0	16.5
4	13	0	22.46
5	15	0	29.6

Table 6.5: User defined pore pressure distribution during excavation (Buro Happold, 2007)

6.8.4 Undrained shear strength and overconsolidation profile for numerical simulations

As discussed in the previous chapter, undrained shear strength is not an input parameter in the formulation of the KHSM, and therefore it needs to be evaluated through simulations of tests starting from the in situ stress conditions at several points through the depth of the crust layer with varying OCR values. The profile of peak shear strength predicted by the KHSM is plotted in figure 6.14. As it can be seen the results of the numerical simulations correspond to the design profile assumed by Buro Happold. A high strength for the crust indicates a high overconsolidation ratio, which decreases with depth (fig. 6.15). This figure shows also the OCR profile obtained by matching the observed initial strength profile with the simulated response using the non-structured bubble model (KHM with r_0 = 1.0 and the KHSM-MCCM). The only difference between the structured and unstructured models is the prediction of significant softening with loss of structure as plastic strains occur.

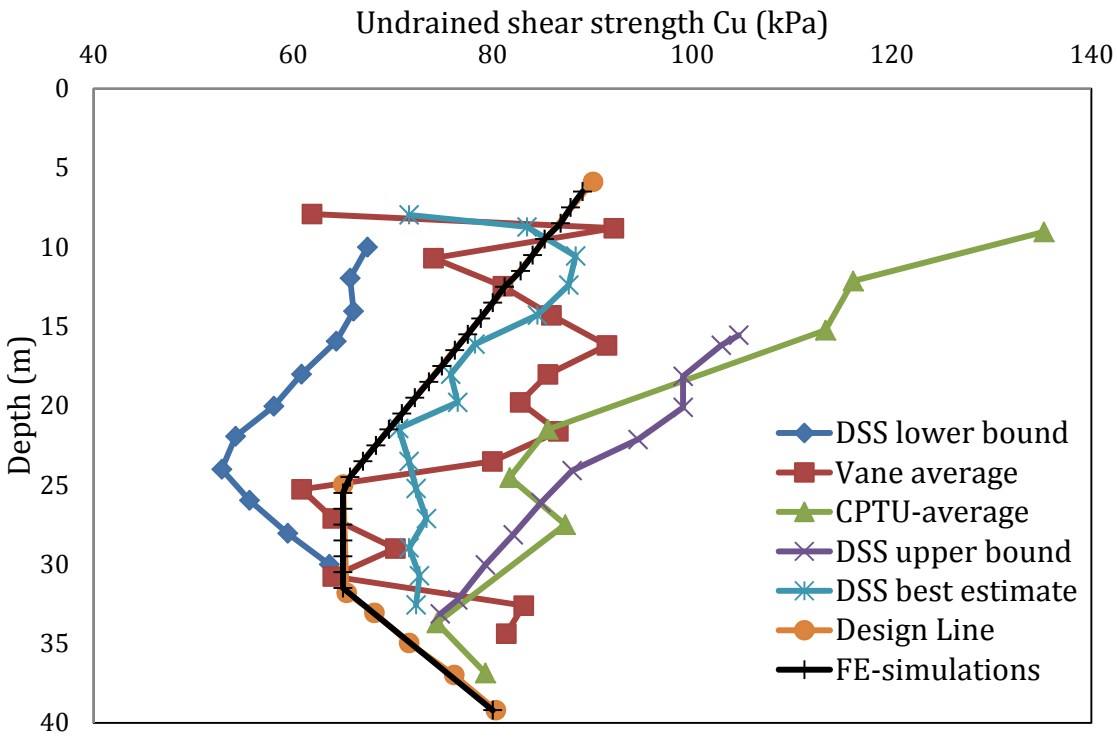

Figure 6.14: Simulated and measured undrained shear strength profile

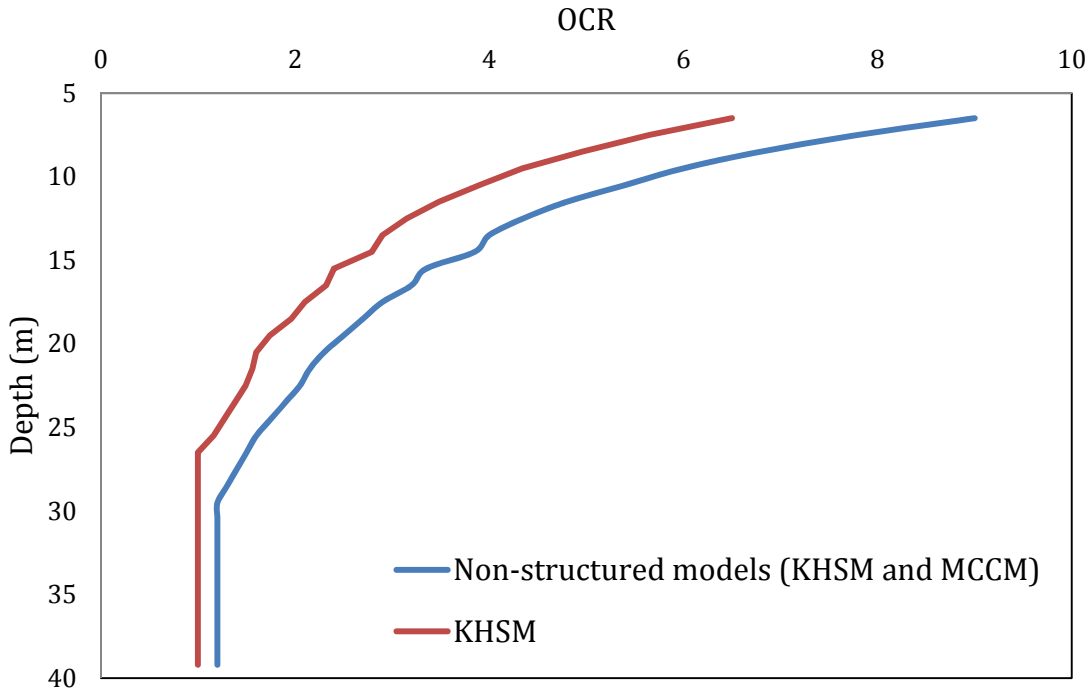

Figure 6.15: OCR profiles to fit the measured undrained shear strength profile in figure 6.11 with the models adopted in this chapter

6.8.5 Parameters for structural elements

The retaining systems were modelled using plate elements, with the tie-backs simulated with the option of node to node anchors. Material parameters for the plates include normal stiffness (EA) and flexural rigidity (EI) to relate stiffness per unit width in the out of plane direction. Properties for the two retaining systems are given in table 6.6. A geogrid was assigned to represent the grout body. Interface elements are used around the wall and are set as (R_{inter}=0.67). Geogrids are flexible elastic elements that simulate grouting or sheet of fabric. The only data required to define it is the axial stiffness as seen in table 6.7. The anchors were modelled with the aid of the node to node option in Plaxis. These are elastoplastic elements that are defined by the normal stiffness EA and a value of the pre-stress force as seen in table 6.8

Name	**Type**	**EA (kN/m)**	**EI (kN/m2)**	**Weight w (kN/m2)**	**Poisson's ratio**
Section A	Elastic	2.28e+7	1.59e+6	22	0.2
Section B	Elastic	2.13e+7	1.03e+6	22	0.15

Table 6.6: Parameters for the two retaining systems

Grout body behaviour	**Elastic**
EA (Kn/m^2)	1.12e+5

Table 6.7: Anchor grout parameters

Anchor behaviour	Elastic
EA (Kn/m^2)	1.12e+5
Spacing L (m)	1.83 (Section A) and 1.22 (Section B)
Prestress (kN/m)	383

Table 6.8: Node to node anchor parameters

Material constants	Value	
	NC	OC
Slope of swelling line κ^*	0.004	0.004
Slope of normal compression line λ^*	0.028	0.028
Critical state stress ratio M	1.11	1.11
Ratio of size of bubble and reference surface R	0.08	0.08
Stiffness interpolation parameter B	2.0	2.0
Stiffness interpolation parameter ψ	1.35	1.35
Destructuration parameter k	1.5	1.0
Destructuration strain parameter A	0.5	0.5
Initial degree of structure r_0	1.8	1.5
Aniotropy of initial structure η_0	0.5	0.3

Table 6.9: Material model paramters for Boston Blue Clay

6.9 Results and discussion

This section presents the results from the finite element simulations carried out with the different forms of the model implemented in this thesis. A sensitivity analysis to investigate the influence of the constitutive model, as well as the influence of the elastic formulation on wall movements, bending moments and surface settlements are provided. The Boston Blue Clay deposit was modelled with three different models; starting from the well-known modified Cam Clay followed by the hierarchical extensions of the KHM (bubble model) and the KHSM for structured soils. Table 6.9 provides and classifies the various analyses that have been carried out. It should be noted that in all cases, regardless of the model adopted for the BBC deposit, the made ground, fill and glacial till layers have been modelled with the Mohr Coulomb model. Based on the index properties reported in section 6.6.4 the parameters for the analyses using the small strain stiffness formulation from Viggiani and Atkinson, were estimated as ***A_g=1600, n_g=0.76 and m_g=0.22*** (figure 2.12).

Analysis classification	Constitutive model for Boston Blue Clay deposit	Elastic formulation adopted in FE simulations
A	Modified Cam Clay	Traditional elasticity
B	KHM-(bubble) model	Traditional elasticity
C	KHM-(bubble) model	Viggiani's elastic law
D	KHSM model	Viggiani's elastic law

Table 6.10: Classification of Finite element analyses

It is vital to note that the simulations have been performed in an effort to replicate the observed behaviour of the two retaining systems in a realistic manner during the excavation process. The focus was to capture the overall trends and not to attempt any exact fit with the observed value, since measurements were significantly affected by the tieback installation process. It was obvious during the monitoring, that a significant percentage of the overall horizontal wall movement was associated with the tieback installation process (Chartier et al, 2008 ; Fasano and Nikolic, 2008,2009).

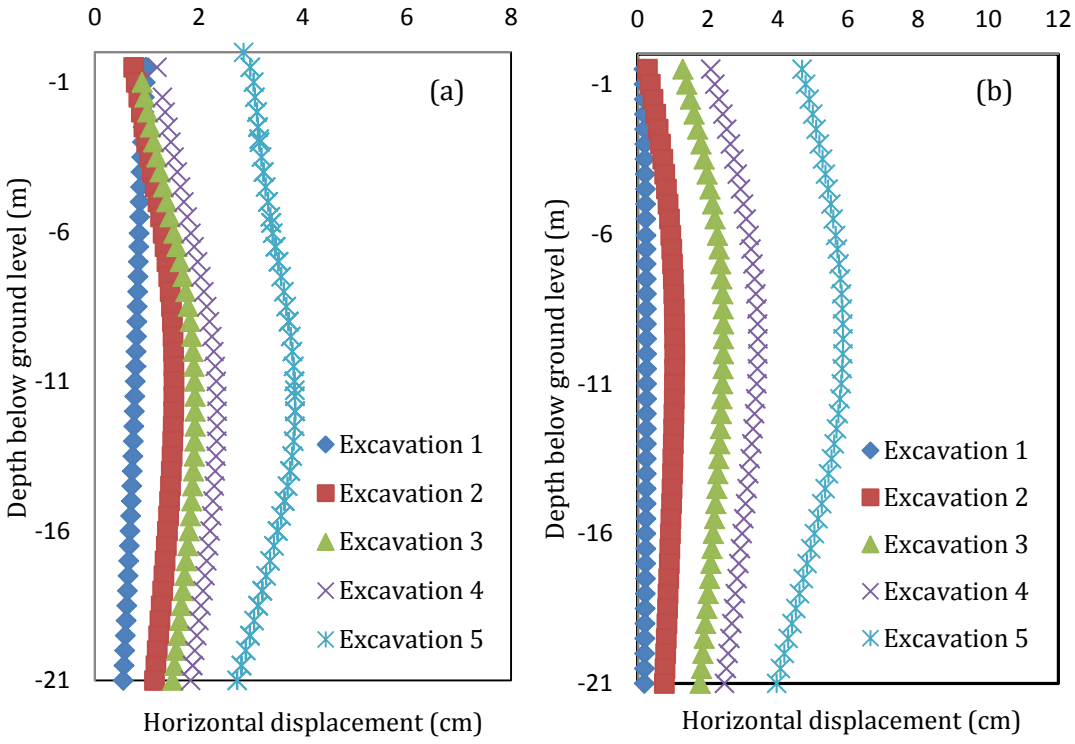

Figure 6.16: Predicted wall displacement profiles for Type A analysis (a) Section A and (b) Section B

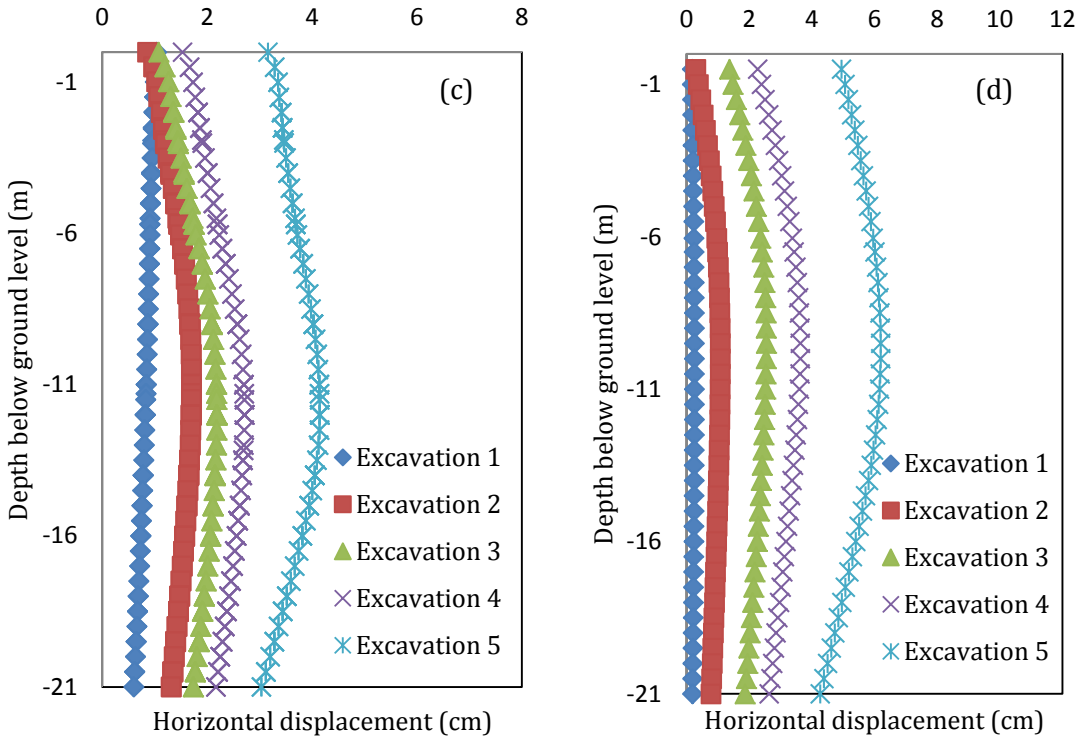

Figure 6.16 (cont.): Predicted wall displacement profile for Type B analysis (c) Section A and (d) Section B

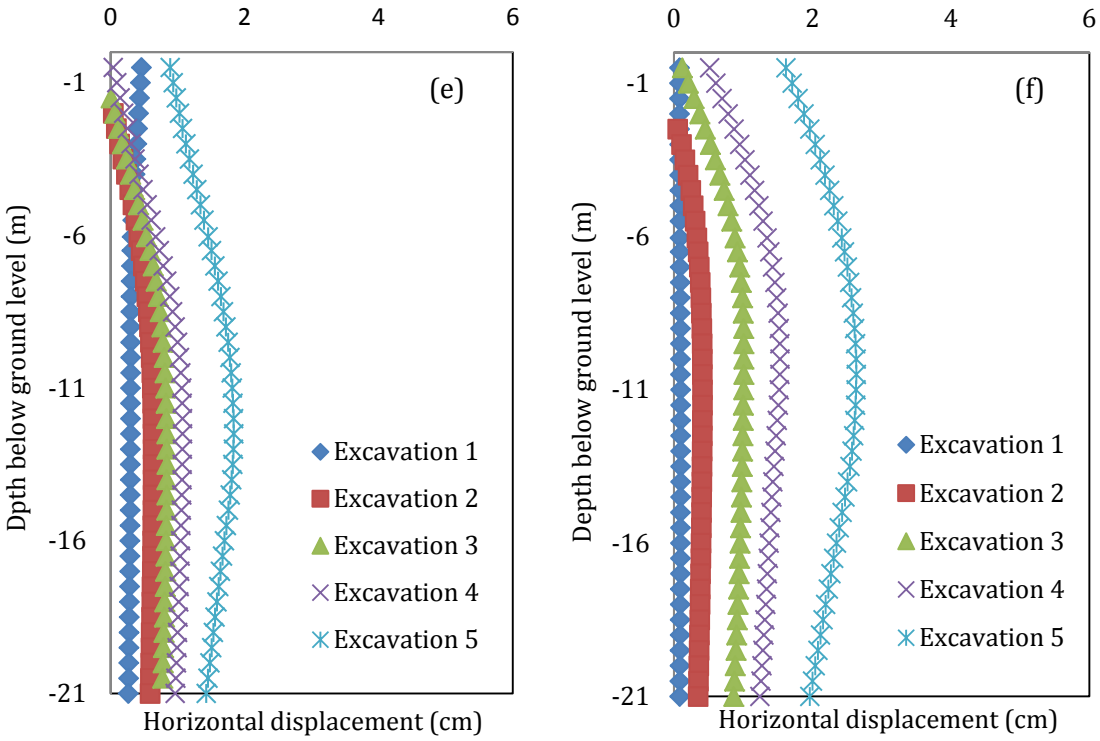

Figure 6.16 (cont.): Predicted wall displacement profile for Type C analysis (e) Section A and (f) Section B

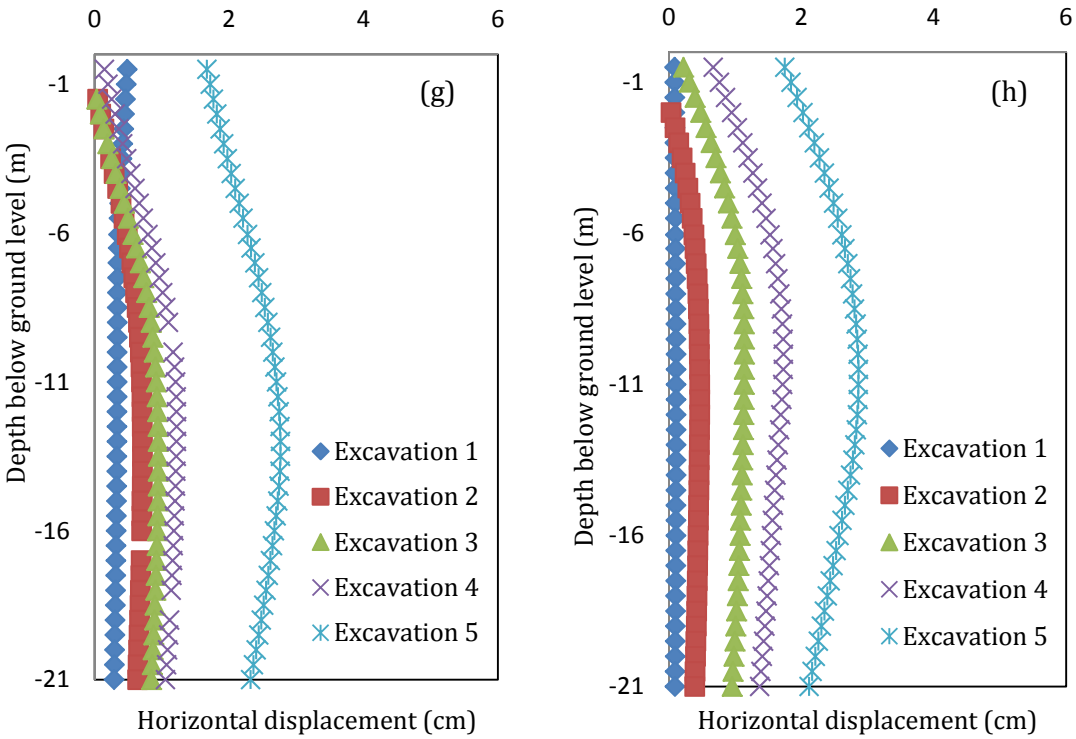

Figure 6.16 (cont.): Predicted wall displacement profiles Type D analysis; (g) Section A and (h) Section B

6.9.1 Horizontal wall displacement

Figures 6.16 (a-h) present the deflected profiles at all excavation stages for the two retaining systems employed in this project. Results for all types of analyses are depicted in the figure. The results show that analyses that employed the traditional elasticity law generate larger wall deflections during all stages of the excavation process. The flexibility of the SPTC employed in Section B relative to the reinforced concrete wall is evident by the difference in the deflected shape of Section B, where sharper curvature is predicted. The simulations suggest that top tieback in particular significantly limited top of wall movement for the SPTC wall, an observation which also made during the monitoring process on site. However, the analyses generally overestimate the wall pull-back upon initial application of the pre-stress for Section A which consequently influence the deflections at the top of the wall during excavation. During the first excavation phase –under cantilever conditions- the wall in Section A exhibits larger deflection than section B, where predictions give a significant difference between the predictions. This is attributed

to the greater depth of excavation at Section A for this stage (approximately 2.30m deeper than at Section B).

Panels 6.16a to 6.16d present the numerical results from the analyses that adopted the traditional law of elasticity. The effect of the different constitutive models employed in analyses is also clear. The introduction of the bubble, which reduces the elastic domain by introducing an inner surface allows for progressive yielding of the clay and invokes plastic deformations from the initial stages of loading. For both sections, the predicted results are not influenced by the constitutive model during the first excavation phase mainly due to the fact that this phase included excavation in the made ground and fluvial sands layer and therefore any deformations in the BBC would be contained in the very small strain regions and hence result in elastic response. The consequent excavation phases however involve the BBC layer and as it can be seen from the aforementioned figures, the application of the bubble model results in increased wall deflections at all phases of the excavation for both retaining systems with the over-prediction of the horizontal wall movement from the bubble model ranging between 5% and 9%. It should be noted that the inclusion of the smaller elastic region does not affect the shape of the deflected profile of the two retaining systems.

The remaining panels in figure 6.16 (e-h) plot the results from the numerical simulations for Type C, which adopts the Viggiani and Atkinson formulation for the small strain stiffness and Type D, which is further refined to include the initial degree of structure as calibrated in section 6.6. It is evident that the numerical predictions are strongly influenced by the elastic formulation adopted in the constitutive model, irrespective of the type of retaining system. The maximum wall deflection for Section A exhibits a reduction of 55% from 4.0cm to 1.8cm at the final level of excavation during Type C analysis. The comparison between panels (e) and (f) in figure 6.16 (Section B), indicates that the reduction of the wall deflections is of similar order to Section A (approximately 56%) as the alternative function of elasticity is employed. This noteworthy difference is credited to the high initial stiffness at small strains that is given by this formulation of the elasticity, a feature which cannot be attained by the traditional elasticity law

(constant stiffness with strain), since the strain levels likely to be relevant for retaining wall design purposes are between 0.01% and 0.1%. Panels (g) and (h) in the figure above plot the results for the full KHSM model. The influence of modelling the effects of structure degradation results in some subtle differences in the predictions between analyses of Type C and D. As it can be seen, the post peak softening that is described by the structured model, results in some small increase of the simulated wall deflections for the two types of retaining walls, with the variation being more prominent in Section A, (approximately 30%). For Section B, the difference between the predictions of the two constitutive models is limited to approximately 10%. A possible explanation for this difference is the hypothesis that the closer tieback spacing at Section A exacerbated disturbance of the cohesive soils behind the slurry wall from tieback drilling and/or grouting activities.

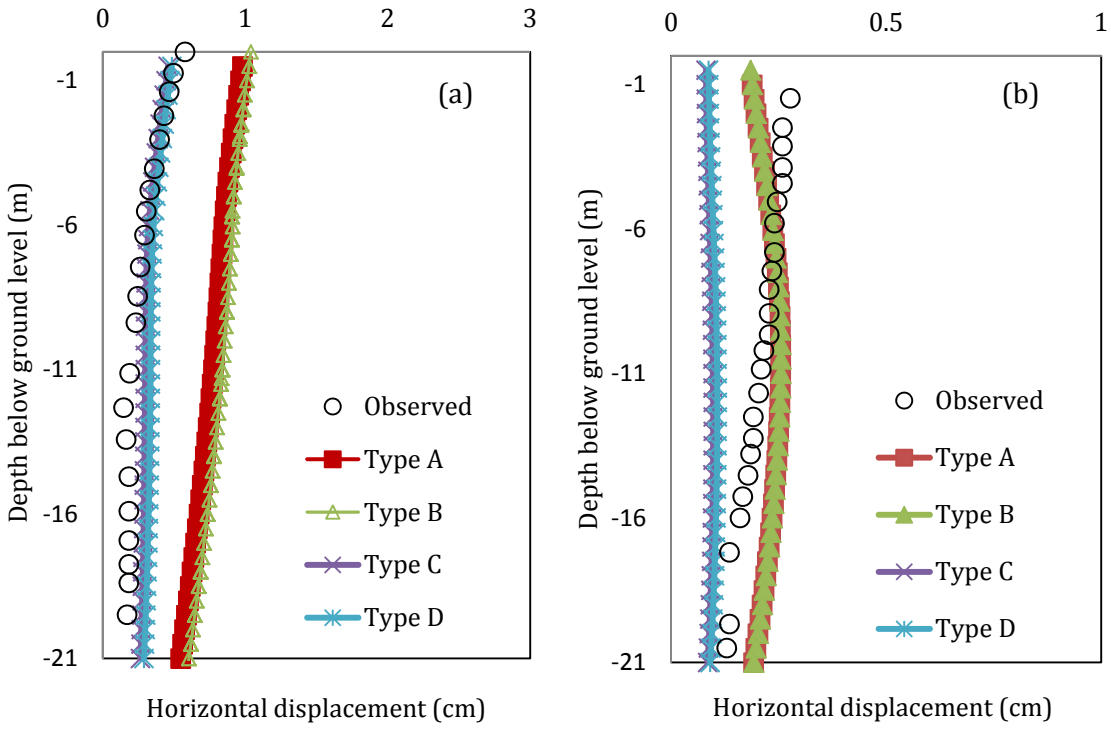

Figure 6.17: Predicted and measured wall displacement for different types of analysis at excavation level 1;(a)Section A and (b) Section B

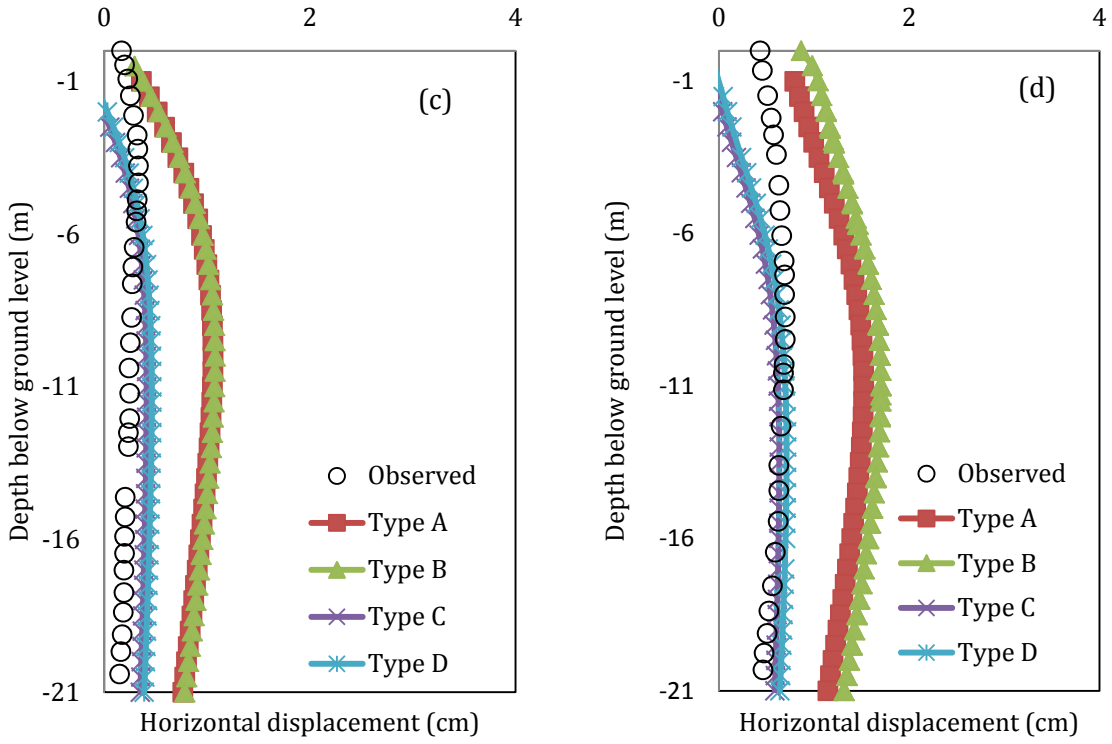

Figure 6.17: Predicted and measured wall displacement for different types of analysis at excavation level 2;(c)Section A and (d) Section B

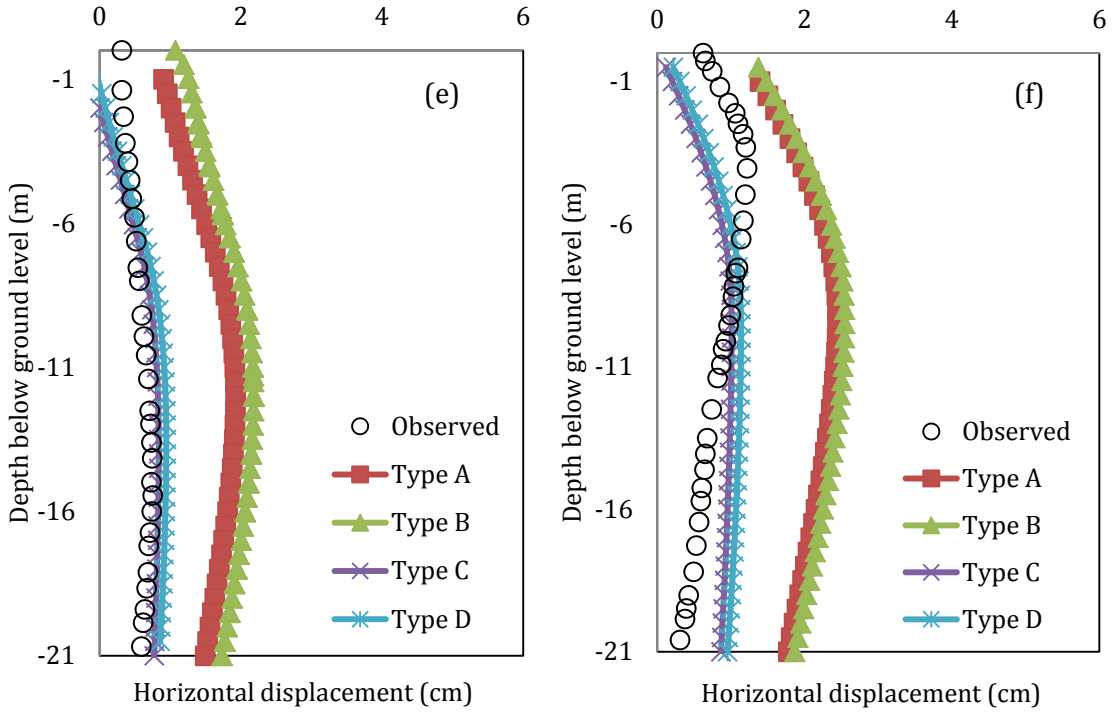

Figure 6.17: Predicted and measured wall displacement for different types of analysis; at excavation level 3 (e)Section A and (f) Section B

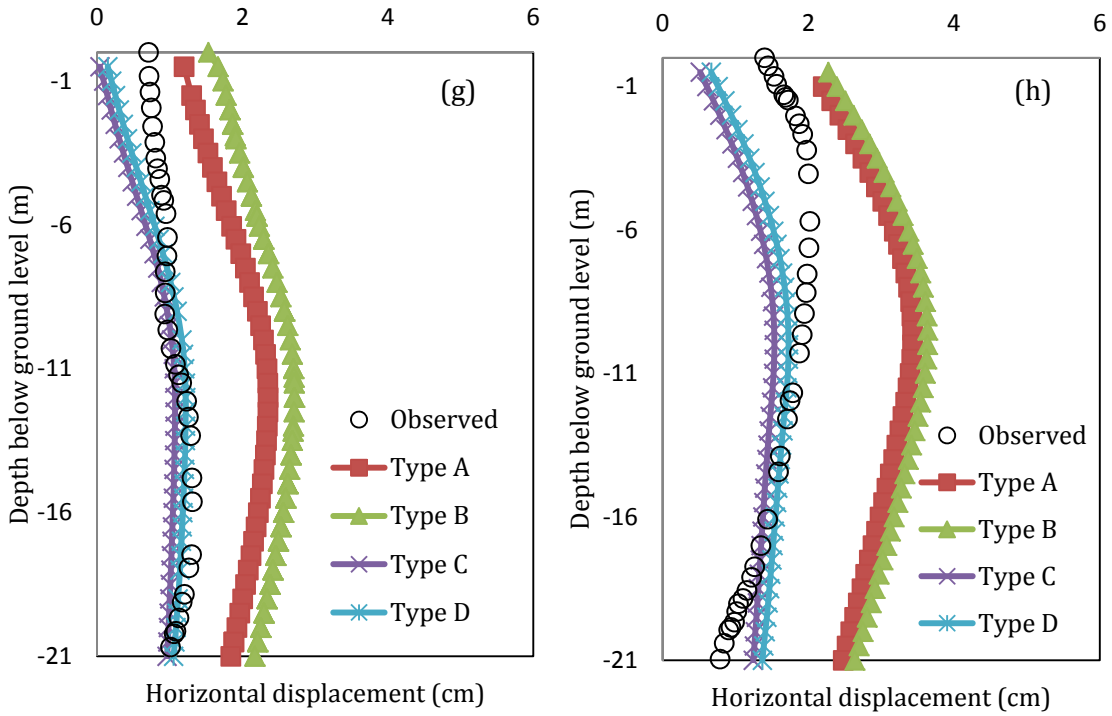

Figure 6.17: Predicted and measured wall displacement for different types of analysis at excavation level 4;(g)Section A and (h) Section B

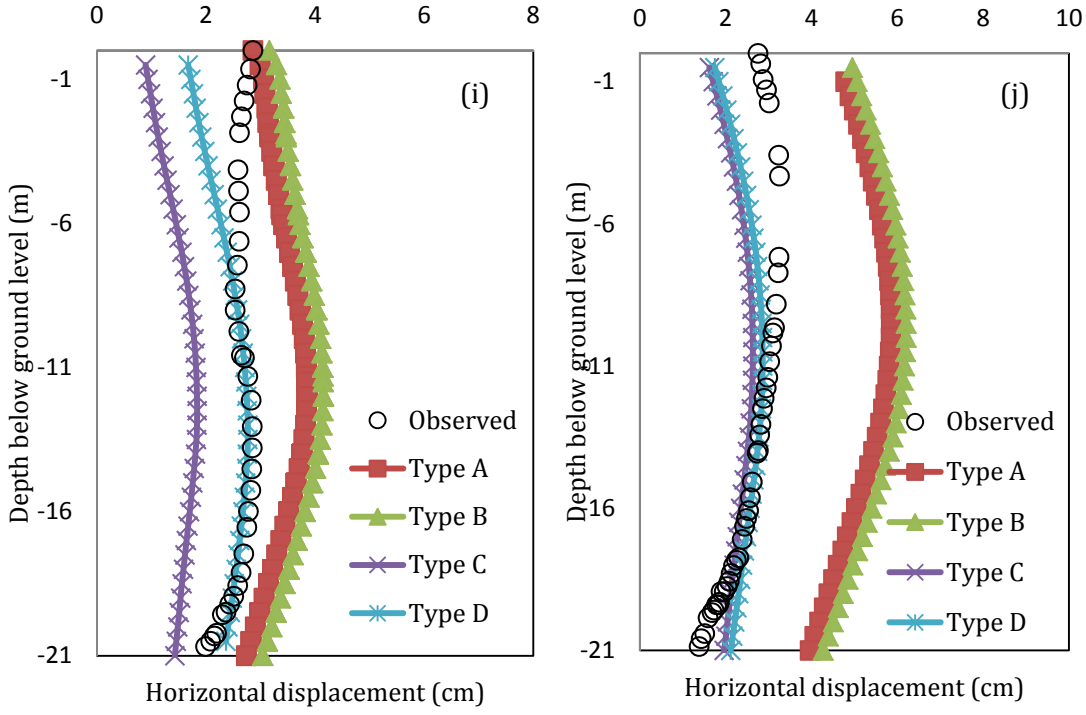

Figure 6.17: Predicted and measured wall displacement for different types of analysis at excavation level 5 ;(i)Section A and (j) Section B

Figure 6.17 (a-j) plots the comparisons of numerical simulations with the available field measurements for all excavation levels. The observations of the influence of the constitutive model adopted in each type of analysis, as described above are echoed in this plot as well. The suitability of the Viggiani elastic formulation is clearly evident, since the analyses that utilise the conventional elasticity significantly overestimate the wall deflections for all excavation stages. Therefore the discussion here will be focused on the results from Type C and Type D analyses.

At excavation level 1, the numerical predictions are in excellent agreement with the movements. For this section, the numerical predictions are in excellent agreement with the measured (top, toe and maximum) wall deflections at the final formation grade for Section A; however the numerical analyses for Section Be underestimate the maximum wall deflection by 0.12cm. Since this excavation stage is situated in the made ground and fluvial sands for Section B, the deformations are primarily due to the shear modulus of these two layers. Therefore the results in panel (b) illustrate the well known limitations of the MC model used to simulate the top two layers, which in turn imply that small strain nonlinearity should also be considered in future modelling of sands.

The finite element predictions are in fair agreement with measured lateral soil deformations at excavation level 2 for both retaining systems. The toe and maximum wall deflections at the final formation grade are well captured by the numerical simulations, although the top-of-wall deflection is somewhat underestimated. This difference is certainly not expected from the variations in support conditions but could be explained by the reported disturbance caused by the use of pressurized drilling fluid with external flush and pressured grout without packers. It was reported that this process may have caused hydraulic fracturing of the cohesive soils retained by the excavation walls.

The comparison between numerical predictions and field measurements for the remaining excavation levels is consistent with the previous two sections and hence, the underestimation of wall deflections at the top of the wall is again most

likely related to the construction activities. Furthermore the MC model is unable to differentiate between loading, reloading and unloading and predicts the same stiffness at these three different stress-paths. It is well known, that soils exhibit higher stiffness at reloading/unloading and soil stiffness increases with pressures and therefore a constitutive model which does not take into account the effects of stress levels on soil stiffness are unable to characterize actual soil behaviour during excavation. Comparison of the predictions from the KHM (Bubble) model and the KHSM with the field measurements, confirm the findings of previous research carried out on Re-sedimented and Natural Boston Blue Clay, which indicated that this type of clay possesses a structure which is consistent with that of natural soils characterized by a "sedimentation structure" (Cotecchia and Chandler, 2000), and therefore which chemical and aging processes have not played a significant role. Important features such as, stress–strain–strength anisotropy which control the performance of retaining walls in strain levels between 0.01% and 0.1% are also described by the KHSM.

6.9.2 Surface settlements

Typically, the extent of ground movement induced by earth retaining structures can be correlated with the proposed depth of excavation. In turn, the magnitude of ground movements behind earth retaining structures can be correlated with the lateral displacements of the structures concerned. The mentioned correlations and normalised relationships are directly dependent on the site geology, ground and groundwater models, construction and retaining structure details and sequencing. As part of the assessment of the 'Zone of Influence' for a 14.6m deep excavation, the likely extent of ground movement behind the proposed earth retaining structure has been investigated and evaluated by adopting the following techniques/methodology:

• Review of published papers and data relating to measurements of ground movements surrounding basement excavations in Boston.

• Review of empirical correlations between structural and ground movements subject to known ground conditions and proposed construction techniques.

In view of the site geology, ground model, basement construction details, current revised basement arrangement and proposed depth it is anticipated that the horizontal extent of ground movement is likely to be in the range of 2.5 to 4.0 times the depth of excavation. (Peck, 1969). It is noted that a series of structures and elements of infrastructure/utilities surrounding the proposed site are located within the extent of the likely 'Zone of Influence'. As the excavation proceeds to a deep layer, the ground behind retaining structures moves towards excavation side and the soils beneath excavation base will heave as the retaining walls deflect. Therefore, soil structures of the sensitive clayey soils within affected zones might be subjected to disturbance, accompanied with degradation of soil strength and stiffness.

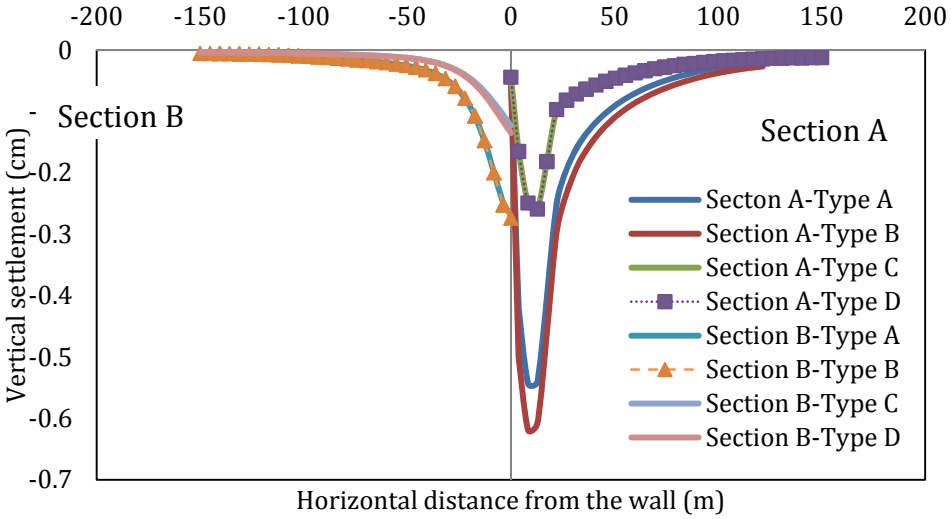

(a)

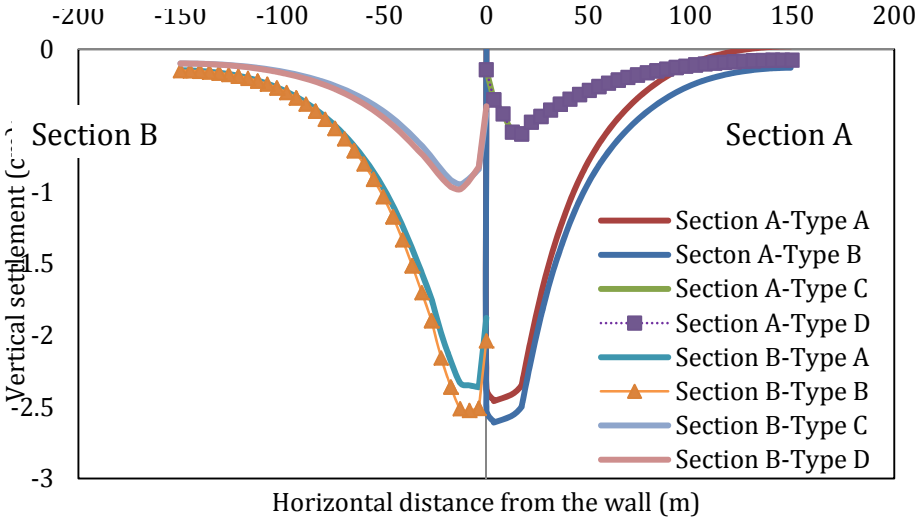

(b)

Figure 6.18: Predicted surface settlements (a) excavation level 1 and (b) excavation level 5

Figure 6.18 shows the settlement profiles produced by the four types of analyses conducted in this work. The figure looks at two different levels of excavation, (a) excavation level 1 where the tie back level differs for the two type of retaining systems and (b) excavation level 5, where the final elevation is the same. Consistent with the previous observations, the maximum settlement predicted by the analyses that adopted the conventional elasticity model exceeds those predicted by the Viggiani formulation for both Sections at the two elevations presented here.

The difference between the Type C Bubble model simulations and the KHSM analyses is negligible, especially for the first stage of the excavaton, where the removed soil is situated in the made ground and alluvium layers. As it can also be seen in panel (a), the Soldier Pile Tremie Concrete Wall (Section B) exhibits considerably smaller vertical settlements, since the first excavation level is significantly shallower (0.3m below ground level) in this part of the project, with both models showing the maximum settlement to be in a similar position behind the wall.

When the excavation level reaches the final formation grade (panel b), the results for Section A show predictions of shallower gradient to the sides of the trough and shows a slightly smaller settlement at the furthest distance from the wall, but only by 0.07 cm. Peck (1969) suggests that the width of the settlement trough behind the wall of an excavation in relatively stiff soils is usually up to two times the depth of the excavation. The troughs predicted by all analyses (Type A to Type D) are in accordance with this empirical supposition. It can also be seen that the predicted settlements in Section B for the two analyses utilising the Viggiani elastic formulation are approximately 0.4cm larger than their respective ones for Section A. This can be related to figure 6.14, where the retaining system at Section B exhibited larger horizontal movements, and therefore, as the excavation proceeded to deeper layers, the ground behind retaining structures moved towards excavation side.

6.9.3 Time dependent behaviour of the excavation

In the following section of the work the time dependent behaviour of the excavation was used in order to evaluate the performance of the KHSM model under time dependent conditions. During the excavation process in the vicinity of saturated clayey soils, negative excess pore water pressures develop in the soil below the excavation base. The assessment of time and movement dependent uplift soil pressure due to the generation of negative excess pore water pressures, which exist at the underside of a raft, is a complex finite element soil-structure interaction problem. In order to achieve a correct assessment of this behaviour, the numerical simulations should take into account the loading stages associated with the substructure construction works. The time dependent excess pore water pressure generation, dissipation and associated ground movement throughout the excavation and basement construction sequence are simulated in this section using the coupled mechanical/flow FE analyses that is available in Plaxis. It should be noted that based on the results from the previous sections of this chapter, only the KHSM model was adopted for this part of the work.

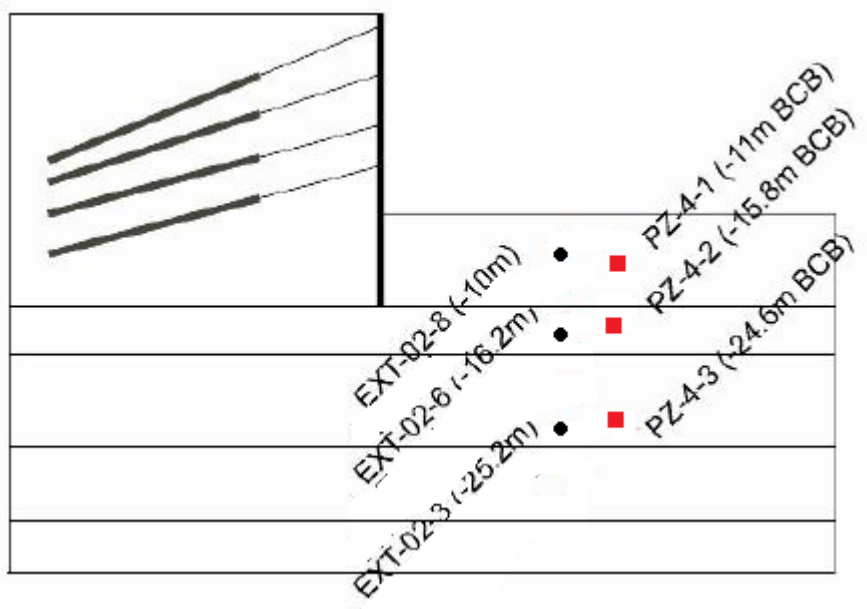

Figure 6.19: Location of vibrating wire piezometers (PZ4) and extensometers (Ext-2) for selected excavation cross section (not to scale)

The cross section that was chosen for this work was based on the retaining system for Section B. Figure 6.19 depicts the schematic diagram of the wall cross-section Also shown in the figure are the instrumentation locations of the monitoring system (vibrating wire piezometers (PZ4) and extensometers (Ext-2)) that were used to measure porewater generation and dissipation with time, as well as movements of the excavation base.

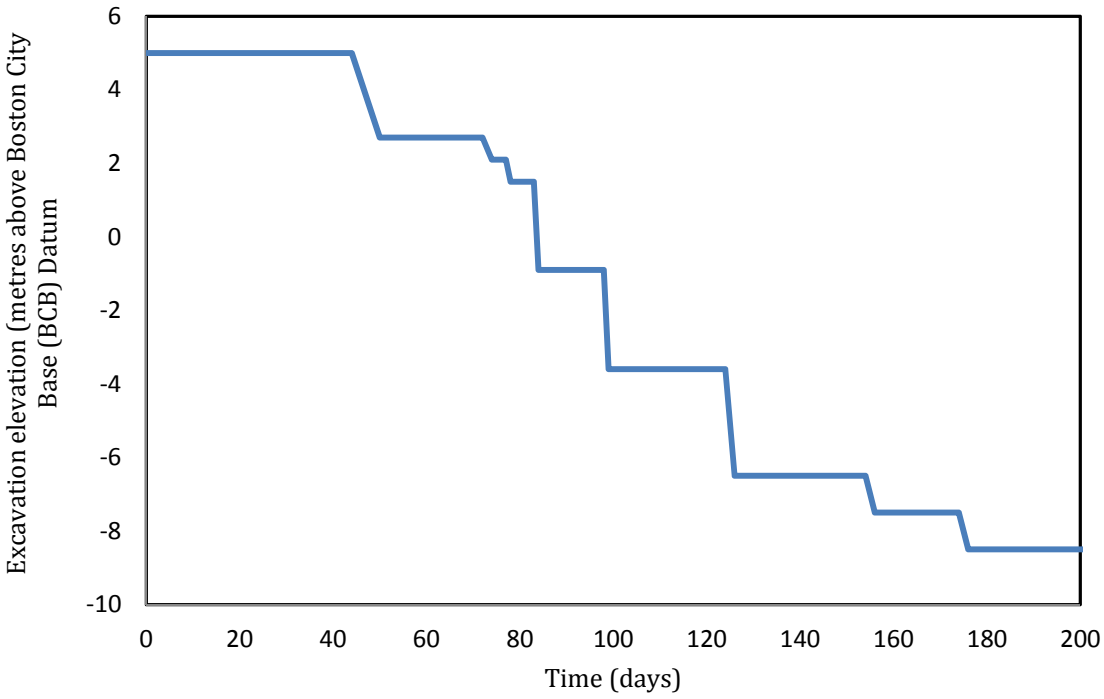

Figure 6.20: Construction sequence of the excavation process at Section B adopted for the coupled consolidation simulations.

In order to conduct the time dependent finite element simulations, appropriate construction sequence was taken into consideration (figure 6.20). It should be noted that the two different types of calculation, plastic and consolidation, which are available in the software package were employed in order to replicate the exact construction sequence. The plastic option was used in the simulations of the installations process of the four rows of tiebacks and the consolidation type was adopted during the excavation stages. The finite element simulations used an isotropic value of permeability k = 1x10-9m/s which was evaluated from the self-boring pressuremeter, cone penetration and CRSC laboratory tests. The mesh shown in figure 6.12 was also adopted in this section.

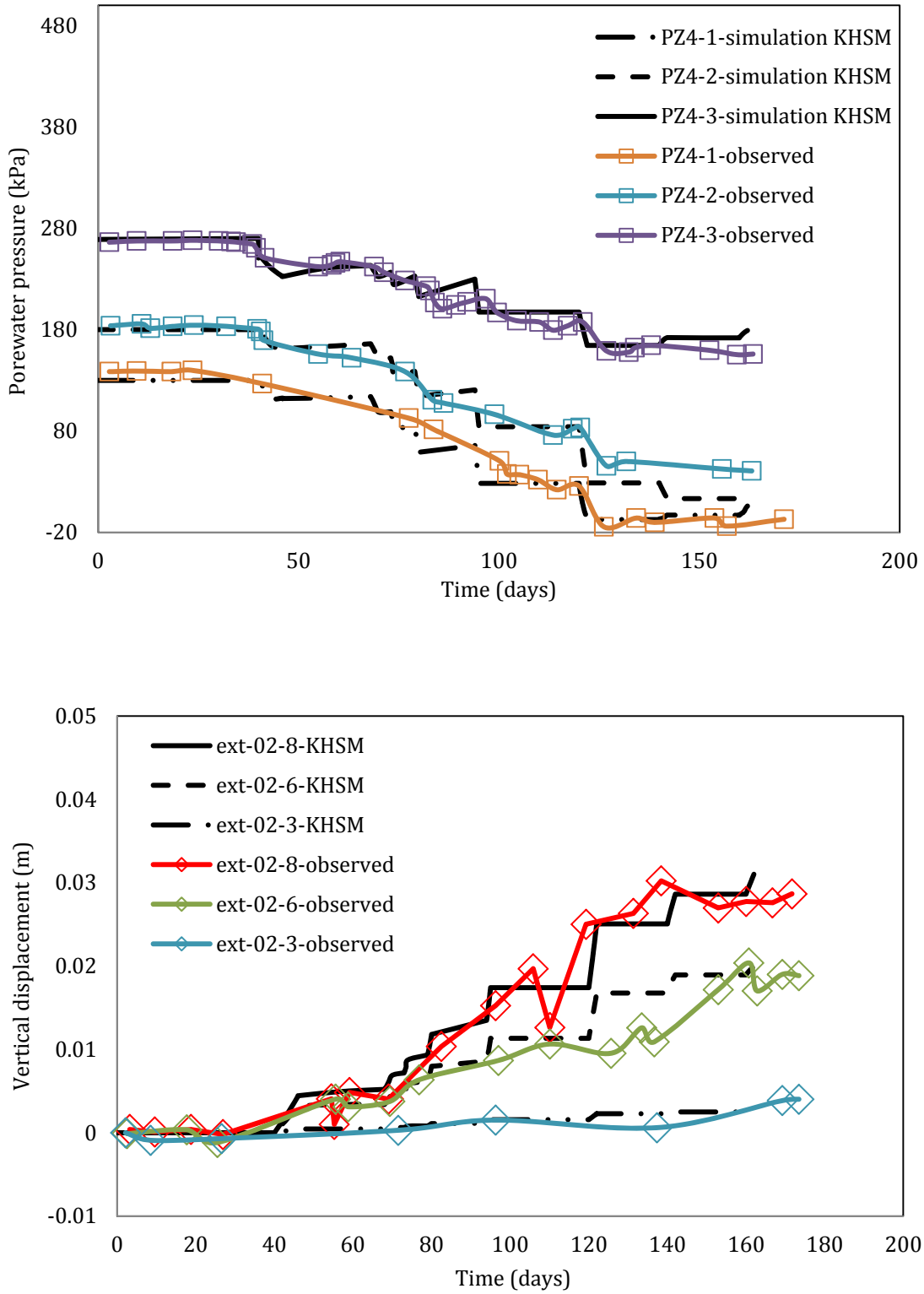

Figure 6.21: Results from Coupled finite element analysis; (a) comparison with measured pore water pressure from vibrating wire piezometers and (b) comparison with magnetic extensometer ground movement measurements.

As it can be seen from figures 6.21a and b, the numerical simulations with the structured model capture the general trend of the dissipation of pore water pressures due to the unloading and the associated ground movement of the excavation base, with time. It can be deduced that these advanced constitutive models can successfully be applied for this type of soil under the particular loading condition. These findings can benefit greatly the industry during the design of basement raft foundations. The usual practice is to base the calculations on the maximum possible uplift heave pressure, which is equal to the weight of the excavated soil, acting underneath the raft. As a consequence the partial dissipation of excess pore water pressures as seen in the field and predicated by the coupled finite element simulations is frequently ignored. Therefore the design procedure assumes entirely undrained conditions over long periods of time (up to 1 year). By taking these observations into consideration, the engineering community is likely to achieve significant gains in basement raft designs, by reducing the design loads applied on the rafts.

6.10 Summary and conclusions

This chapter examined the undrained behaviour of a deep excavation which forms part of a 100m wide basement excavation located in Boston, Massachusetts, USA. Two different types of tied back retaining walls were used, soldier pile tremie concrete wall and traditional reinforced concrete diaphragm wall. The glacial marine clay foundation was modelled with the kinematic hardening model for structured soils (KHSM) described in Chapter 3, the reduced version of the bubble model (KHM) Also investigated was the influence of the elastic formulation adopted in the simulations, by means of comparison with prediction modified Cam Clay model and the KHM model which used the traditional elasticity law (constant stiffness with strain). Also investigated were the time dependent porewater dissipation and the associated heave of the excavation base with the use of coupled finite element analyses.

A stepwise calibration procedure of the constitutive model parameters was conducted, utilising various sources of information. The calibrated parameters were evaluated by means of numerical simulations of constant rate of strain test and self-boring pressuremeters. The values for the OCR profile were meticulously selected in order to reproduce closely the design profiles of undrained shear strength. The only difference between the structured and unstructured models was the prediction of significant softening with loss of structure as plastic strains occur.

During the excavations process, it was found that significant wall movements occurred during the tieback installation phases. It was apparent that a significant percentage of the overall horizontal wall movement was associated with the tieback installation process, especially at Section A, where installation of all four tieback rows corresponded with measurable wall movement. In order to facilitate the comparison of numerical simulations and field measurements, all wall displacements that occurred during tieback installation were subtracted from subsequent excavation stages and therefore only movement associated with excavation stages was considered.

The finite element analyses reveal that the numerical simulations using the modified kinematic hardening models provide a close match to field monitoring data. The results of the undrained numerical simulations illustrate the influence of the different constitutive models employed in the analyses. The introduction of the bubble reduced the elastic domain and allowed for plastic deformations from at an earlier of loading compared with the modified Cam Clay model. As a result the application of the bubble model generates increased wall deflections at all phases of the excavation for both retaining systems. It should be noted that the inclusion of the smaller elastic region did not affect the shape of the deflected profile of the two retaining systems. The comparison of the analyses which adopted the Viggiani and Atkinson formulation for the small strain stiffness revealed that the numerical predictions are strongly influenced by the elastic formulation adopted in the constitutive model, irrespective of the type of retaining system, with wall deflection reducing to approximately half for both retaining systems. This significant change in the predictions is attributed to the high initial stiffness at small strains that is given by this formulation of the elasticity, a feature which cannot be attained by the traditional elasticity law, since the strain levels likely to be relevant for retaining wall design purposes are between 0.01% and 0.1%. The influence of modelling the effects of structure degradation produced some subtle increase of the simulated wall deflections due to the post peak softening that is described by the structured model,.

The work in this chapter went further, to examine the time dependent behaviour of the excavation by means of coupled mechanical/flow numerical analyses, adopting the actual construction sequence. During the excavation process in the vicinity of saturated clayey soils, an accumulation of negative excess pore water pressures in the soil below the excavation base is observed. The computed results of KHSM model were very successful in matching the general magnitude and rate of dissipation of the excess pore-water pressures and base heave induced in the soil during the excavation process. This observation can provide an insight in the design of raft foundations in clays, since it is customary to take into account the maximum possible uplift heave pressure acting underneath during design and assume undrained conditions for a long period of time. As it was shown from the

numerical analyses above, in this particular instance the raft design could profit from a significant reduction in design bending moments.

Chapter 7: Summary and Conclusions

7.1 Introduction

The aim of this thesis was to implement, validate and investigate the behaviour of a constitutive model that describes the initial structure, on various geotechnical problems. The kinematic hardening structured constitutive model (Rouainia and Muir Wood, 2000), formulated within a framework of kinematic hardening and bounding surface plasticity, was selected for this work. The motivation to adopt these models came from the flexibility in modelling different soil behaviours. Firstly, the model has an anisotropic general formulation, with the yield and plastic potential surfaces not necessarily circular in the deviatoric plane, secondly the model has the ability to model initial anisotropy of the structure surface and lastly contributions to destructuration of structured soil from plastic volumetric strain and distortional strain are not necessarily equal. The model was implemented into the PLAXIS Finite Element Analysis software package and validated against experimental data of drained and undrained triaxial tests on Vallericca clay. The kinematic hardening structured model was evaluated with its application in finite element analyses of a variety of geotechnical problems. The first of these simulated the Self Boring Pressuremeter test in London Clay. The second boundary value problem involved the 2D and 3D simulation of an embankment situated on soft structured clay in Saint Alban, Canada. The model developed in this work was then adopted in the study of the short term and time dependent behaviour of a deep excavation located in Boston, Massachusetts, USA. Comparison with field measurement was made where possible.

7.2 Validation and application of the KHSM model

7.2.1 Chapter 3

The hypothesis that was explored in this chapter was that the effects of structure in natural soils can be modelled through a simple, logical extension of an existing model for reconstituted, un-structured soil. The kinematic hardening structured model (KHSM) model that was implemented for this study included some modifications from the original formulation that were adopted in order to improve predictions of stiffness in the small strain region, by implementing two new elastic models in the formulation. The performance of the model was evaluated through a series of simulations on a single element finite element analysis of a number of different undrained triaxial compression tests on stiff clay from the outskirts of Rome. It was shown that the model can successfully capture the general trend in terms of stress path and peak strength observed in laboratory experiments.

In order to obtain a general indication of the influences of the key soil parameters of the model, a parametric analysis was carried out on key model parameters. Such a study could provide assistance in the search for the optimum set of parameters to match any given set of experimental observations. The conclusions reached from this study can be summarised as follows:

- Any increase in the value of the initial degree of structure r_0, resulted in higher and sharper peak in the stress-strain relationship, with the destructuration in undrained conditions largely controlled by distortional plastic strain.

- A reduction of the value controlling the destructuration rate, k resulted in increased values of both stiffness and strength. This is attributed to the fact that there is a reduction to the rate at which structure is lost and consequently a smoother peak is observed. Moreover the peak is raised at the same time, because destructuration takes place more slowly.

- The parametric analysis on A revealed that when the destructuration is produced solely by distortional strain, the loss of structure occurs faster since the undrained test is predominantly a distortional deformation. Consequently once the assumption that the destructuration process is completely governed by the volumetric component the results exhibited higher values of peak and residual strengths, and the soil showed hardening softening behaviour.

- An increase in the degree of anisotropy ($\boldsymbol{\eta 0}$) resulted in an increase in stiffness at small strains and strength (large strains).

- The variation of the plastic modulus parameters, B and ψ showed that the behaviour is considerably more sensitive to the variation of ψ, rather than parameter B. This is because the magnitude of the plastic modulus s controlled by a power function for ψ, compared to a linear relationship with B.

- The variation of the bubble size resulted in a more stiff behaviour in the small strain region, with higher peak and residual values of strength for a reduction in R. The stiffness degradation is inversely proportionate to the size of the bubble, and although a smaller value of R indicates plastic strain develop sooner, the magnitude of the plastic modulus is higher.

7.2.2 Chapter 4

The aim of this study was to analyse the performance of the KHSM in the context of the SBPM test and to characterise the degree of initial structure of London clay. A set of material parameters was produced that can be used as a benchmark for subsequent numerical models in London clay at similar depths. Overall, it can be stated that the KHSM, produced cavity pressure-cavity strain and pore pressure-cavity strain predictions that are in good agreement with the observed behaviour. The reported initial conditions on site were validated through modelling of the geological history of the London Clay deposit. The parametric study conducted on

the initial degree of structure and its degradation with strain provided a general indication of the influence of the key soil parameters on the overall response of the SBPM test. The hypothesis of disturbance of the mechanical state of the surrounding soil during the installation process was investigated in order to understand the mechanism of the disturbance effects and their influence on the subsequent pressuremeter test results. The findings indicate that the installation process caused some damage to the initial structure. The degree of initial structure will be somewhat smaller close to the cavity and retain its intact value at some distance from it.

7.2.3 Chapter 5

The aim of this chapter was to assess the pre-failure behaviour of a trial embankment founded upon structured clay, using an advanced constitutive soil model (kinematic hardening structure model - KHSM). This study has presented a number of Finite Element analyses in two and three dimensions, exploring the influence of a realistic modelling of initial structure or bonding in the clay together with progressive destruction of this structure by plastic straining, as encapsulated in the kinematic hardening structured model KHSM. The finite element analyses showed that the numerical simulations using the proposed model provided a close match to field monitoring data. The analyses using the calibrated data, predicted a failure height of 3.93 m, which was in accordance with the observed failure height of 3.9 m. It was found that the embankment height of 2.4 m was critical in the embankment construction sequence, as it corresponded to the onset of accelerated movements in the soil mass. The correlation of the observed and predicted magnitudes of the settlements was in excellent agreement for all the embankment heights that were considered in 2D and 3D. The good agreement between the observed and measured excess pore-water pressures echoed the convincing comparisons in the vertical settlements. This good agreement is especially significant when we consider that the two piezometers under consideration were situated either very close to or possibly on the failure surface. For the bubble model (KHM), where the destructuration was ignored, a stiffer behaviour of the

foundation soil was predicted, resulting in an overestimation of the embankment failure height.

The section using three dimensional analyses enabled the comparison between available data from settlement plates that are situated outside the plane at which previous two dimensional finite element models were carried out. Furthermore, the three dimensional effects were successfully modelled since the predicted depth of the failure surface being in close proximity with the observed value.

The parametric analysis was conducted with the following findings:

- The findings for destructuration strain rate parameters (A) display that removing the volumetric strain rate (A = 1) and thus making the destructuration entirely distortional marginally reduced the failure height from 3.92m to 3.76m. Whilst reversing the contributions from the different strain parameters (making A = 0.25) caused the height at failure to be increased to 4.36m..

- The study of varying the destructuration parameter (k) showed that reducing this value leads to an increase in the failure height due to lowering the amount of strain softening with the final value of fill thickness at 4.48m.

- The final parameter which was investigated is the anisotropy of initial structure (η_0). This parameter controls the position of the centre of the structure surface of the KHSM model with respect to the reference surface. Increasing this value slightly increases failure height, however causes vertical displacements to be reduced. When the value is halved, very little difference in response can be observed with regards to the calibrated value. An examination of the effect upon horizontal movements was also performed. The findings are similar with the results from the vertical settlements, halving this value causes an almost unnoticeable change. Very little difference is also observed when this value was doubled.

7.2.4 Chapter 6

This chapter analysed the behaviour of a deep excavation which forms part of a 100m wide basement excavation located in Boston, Massachusetts, USA. Two different types of tied back retaining walls were used, soldier pile tremie concrete wall and traditional reinforced concrete diaphragm wall. The aim of the work conducted in this chapter was to demonstrate that the added features and modifications of the model implemented in this work such as small strain stiffness, structure and anisotropy are vital components to give a good prediction. The results of the undrained numerical simulations illustrated the influence of the different constitutive models employed in the analyses. The introduction of the bubble reduced the elastic domain and allowed for plastic deformations from at an earlier of loading compared with the modified Cam Clay model. As a result the application of the bubble model generated increased wall deflections at all phases of the excavation for both retaining systems. It was found that the inclusion of the smaller elastic region did not affect the shape of the deflected profile of the two retaining systems.

The comparison of the analyses which adopted the Viggiani and Atkinson formulation for the small strain stiffness revealed that the numerical predictions are strongly influenced by the elastic formulation adopted in the constitutive model, irrespective of the type of retaining system, with wall deflection reducing to approximately half for both retaining systems. This significant change in the predictions is attributed to the high initial stiffness at small strains that is given by this formulation of the elasticity, a feature which cannot be attained by the traditional elasticity law, since the strain levels likely to be relevant for retaining wall design purposes are between 0.01% and 0.1%. The influence of modelling the effects of structure degradation produced some subtle increase of the simulated wall deflections due to the post peak softening that is described by the structured model,.

The comparison of the predictions from the KHM (Bubble) model and the KHSM with the field measurements, confirmed the previous research on Re-sedimented and Natural Boston Blue Clay, which indicated that this type of clay was

characterised by structure consistent with that of natural soils with "sedimentation structure" (Cotecchia and Chandler, 2000), and therefore which chemical and aging processes have not played a significant role. Therefore the inclusion of a measure of structure did not have any major impact on the numerical results. Important features such as, stress–strain–strength anisotropy which control the performance of retaining walls in strain levels between 0.01% and 0.1% were also described by the KHM.

The investigation of the time dependent behaviour of the excavation showed that by adopting the actual construction sequence, the KHSM model can successfully predict the general magnitude and rate of dissipation of the excess pore-water pressures and base heave, induced in the soil during the excavation process. This finding can provide an insight in the design of raft foundations in clays, since it is customary to take into account the maximum possible uplift heave pressure acting underneath during design and assume undrained conditions for a long period of time. As it was shown from the numerical analyses in this chapter, in this particular instance the raft design could profit from a significant reduction in design bending moments.

Critical Review of the Thesis

The kinematic hardening structured constitutive model was formulated within a framework of kinematic hardening and bounding surface plasticity, in order to improve the simulations of natural clays and the associated breakdown of their natural structure with plastic strain accumulation.

Until the development of constitutive models based on the theories of bounding surface plasticity and kinematic hardening the pre-failure behaviour of overconsolidated clays was treated as linear elastic. Although the introduction of the critical state theory provided an ideal framework for the predictions of the behaviour of normally consolidated clays, the pre-failure behaviour of overconsolidated clays was still assumed to be elastic and became non-linear only in the event the stress path engaged the yield surface before the critical state line was reached.

The KHSM model is able to successfully predict the behaviour of clays under both normally and over consolidated states. The fundamental phenomena of non-linearity and strain softening are captured through the initiation of plastic strains at an early stage and the associated gradual collapse of the structure surface due to the plastic strains. Furthermore, the model can replicate a variety of clays in their natural state, since the input parameter of r_0, maybe correlated to the sensitivity of the soil. This feature provides the flexibility to model clays ranging from low to high undrained sensitivity.

Overconsolidated clays differ from their normally consolidated counterpart in two ways. Firstly the overconsolidated soils exhibit a brittle behaviour leading to strain softening response rather than the strain hardening behaviour observed in normally consolidated clays. Secondly, the overconsolidated clays tend to have a dilatant behaviour under loading, which is in contrast to the compressive behaviour observed in normally consolidated soils. KHSM input parameter k, controls the rate at which the structure surface will degrade with plastic strains. By controlling this parameter, the model can simulate the brittle behaviour seen in the overconsolidated clays.

Chapter 2 detailed the different sources of structure in natural clays, which is a combination of fabric and bonding. It is well documented that fabric due to the sedimentation process leads to *'stable'* elements of structure. The term stable implies that this type of structure does not degrade even with significant amount of plastic straining. This type of structure has also been termed sedimentation structure based on the simple classification system proposed by Cotecchia and Chandler (2000). The formulation of the KHSM model suggests that the structure surface will collapse surface under constant loading until it coincides with the reference surface for remoulded soils. Therefore the model can only successfully replicate the behaviour of natural clays that possess meta-stable or post-sedimentation elements of structure. This issue became apparent during the simulation of the deep excavation. As shown in Chapter 6, Boston Blue Clay is a soil that is characterised by sedimentation structure and therefore chemical and ageing processes have not played a significant role during the development of the structure elements.

As such, it was observed that the results from FE simulations were not sensitive to the inclusion of the structure surface in the KHSM model.

Advanced constitutive models such as the KHSM model are advantageous in the sense that they can simulate the behaviour of soils in a far more realistic manner. However the added features that make the realistic predictions possible imply additional model parameters, as well as potential additional tests required to calibrate the constitutive model. Consequently, models such as the KHSM model will always profit from a calibration process that utilises a variety of in situ and laboratory tests in order to confidently define the required model parameters.

Certain required parameters can be easily determined from standard laboratory tests. The fundamental parameters that define the reference surface can be obtained from standard oedometer tests ($\boldsymbol{\lambda^*}$ and $\boldsymbol{\kappa^*}$), whereas the Critical State Ratio ($\boldsymbol{M}$) can be calculated from the friction angle ($\boldsymbol{\varphi'}$), which is determined by triaxial compression tests.

Triaxial compression tests with small strain measurements are required to calibrate the basic kinematic hardening parameters ***R, B*** *and* $\boldsymbol{\psi}$***.*** These parameters are not directly measured in experiments and are determined by curve fitting of the experimental data. The following staged procedure may be used for the determination of the kinematic hardening parameters.

- Step 1: Assume a size for the bubble surface.
- Step 2: Simulate the triaxial test in the small strain region.
- Step 3: Compare the extent of the plateau in the shear modulus degradation curve to the concentration of measurements and repeat Steps 1 and 2 with varying values of bubble size until the simulated stiffness begins to degrade in accordance to the experimental data.
- Step 4: Assume a combination of values for the parameters controlling the hardening modulus and the decay of stiffness.
- Step 5: Run the entire triaxial test and check if the simulated stiffness degradation curve matches the experimental data.

- Step 6: Repeat Steps 4 and 5 with different values for B and ψ (if required) until the simulated stiffness degrades in accordance to the experimental data.

The above parameters may be determined with tests that are carried out on disturbed samples and therefore are more generally available.

The staged calibration process then moves to the determination of the parameters controlling the structure surface and its degradation with plastic strains. The same stepwise approach as the one described above is employed in order to determine these parameters. The initial measure of structure $\boldsymbol{r_0}$ may be assessed based on the sensitivity value of each soil. Once the value of $\boldsymbol{r_0}$ has been established, an iterative process of varying the value of $\boldsymbol{k}$ to fit the predicted result to the experimental data may be begin.

7.3 Future Work

Although the kinematic hardening model adopted in this work models provides a substantial improvement in modelling the behaviour of natural clays through their ability to include features such as small strain stiffness and stiffness degradation with strain (Al-Tabbaa & Muir Wood, 1989; Stallebrass, 1990), it has the drawback that it does not predict a smooth transition from elastic to elasto-plastic behaviour. As mentioned in this work this is attributed to the form of the plastic modulus which exhibits a sharp transition from an infinite value to non-zero at the point of transition. The resultant non-smooth stiffness degradation curves are unable to reproduce accurately the observed pre-failure behaviour, specifically in the small strain region. As suggested by experimental observations, the stiffness degrades smoothly with increasing deformation. There have been various efforts to formulate models that predict a smooth elastic-plastic transition for example, by adding a new definition of the hardening modulus proposed by Grammatikopoulou et al. (2008).

As covered in the Literature review, natural soils usually possess a sizeable inherent anisotropy of fabric and are further differentiated from reconstituted soils, by the presence of inter-particle bonding which contributes to their strength and stiffness. The term structure therefore describes the effects of the mixture of

these two factors. Anisotropy of fabric could be *inherent* due to the depositional history of the soil, or *induced* resulting from different cases of loading and deformation. In order to model the gradual effects of anisotropic consolidation a variety of models have been proposed to account for the effects of inherent anisotropy associated with the material fabric (Sekiguchi & Ohta, 1977) and its development due to loading. The dimensionless deviatoric fabric tensor was expressed as rotational hardening since it describes the rotation, with respect to the isotropic axis, of the yield surface in stress space (Hashiguchi, 2001; Wheeler et al., 2003).

These observations have been embodied in an extension of the model adopted in this work, which provide a simple refinement of the conventional elasto-plasticity formulation without introducing any additional hardening variables. This generalization consists of an isotropic modification, whose form is independent of the choice of the yield function. This leads to an algorithmic simplification and to a more computationally efficient numerical solution of the material point integration problem (Hiley and Rouainia, 2008), with the option of making the plastic modulus discontinuous as in the conventional model. The model contains three surfaces. The reference surface controls the state of the soil in its reconstituted, structureless form and describes the intrinsic behaviour of the clay (Burland, 1990). The structure surface controls the process of destructuration which can be accompanied by significant strain-softening effects. The bubble, which encloses the elastic domain of the soil, moves within the structure surface following a kinematic hardening rule.

The equation of the kinematic hardening surface, or bubble, is:

$$F(\overline{\boldsymbol{\sigma}}, \beta\, Rrp_c) = f(\overline{\boldsymbol{\sigma}}, \beta) - (Rrp_c)^2 \qquad (7.1)$$

Where r describes the degree of structure (inter-particle bonding) of the material and β is the non-dimensional, deviatoric fabric tensor (tr β = 0), which describes the effects of inherent (structural) fabric anisotropy are introduced into the model.

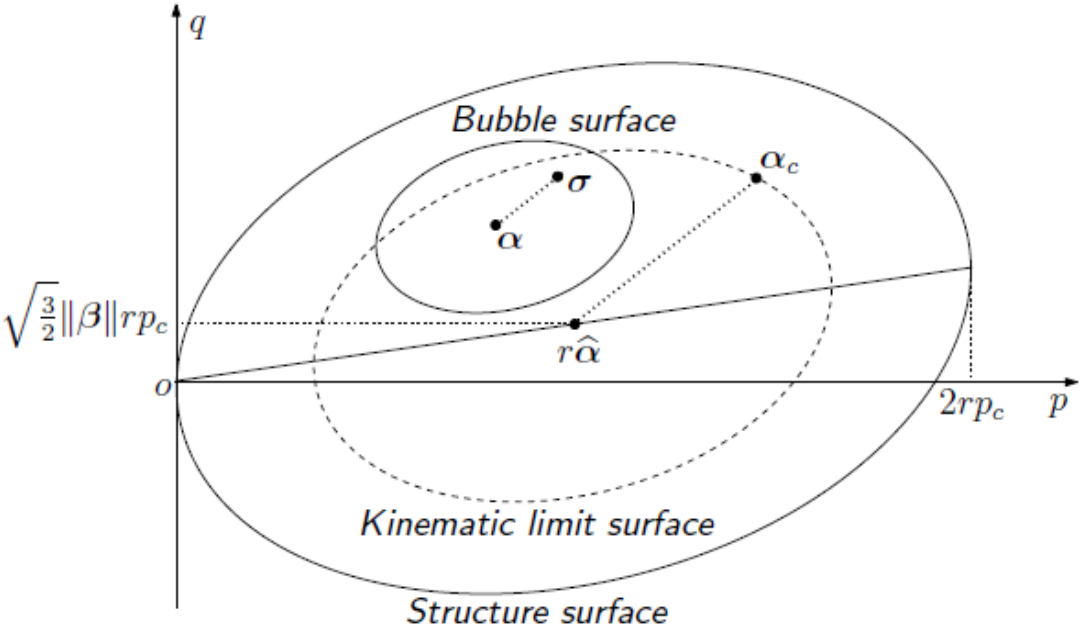

Figure 7.1: Rotated bubble model, incorporating smoothing

In order to achieve the smooth elasto-plastic transition the principle of sub-loading plasticity (Hashiguchi *et al.*, 2002) is utilised which modifies, the consistency condition so that the yield surface acts as a differential attractor rather than an algebraic constraint, and the response is elastic-plastic whenever the plastic loading condition is satisfied. This extended formulation of the KHSM model has been successfully validated against the experimental data from Vallericca Clay which were used in Chapter 3 of this thesis.

A main advantage of the kinematic hardening models over linear and non-linear elastic models is the fact that they permit the development of plastic strains from the early stages of loading and therefore are capable of capturing the hysteretic behaviour observed during cycles of unloading and reloading. The boundary value problems considered in this thesis did not investigate this feature of behaviour. Hence, it would be interesting to use these models in boundary value problems involving cyclic loading. One field that would be of great interest is the investigation of the influence of structure degradation during cyclic and repetitive loading arising from environmental factors (for example waves and storms) on offshore foundations systems, as well as the influence on the mooring lines which

secure the floating or permanent platforms to the seafloor. The behaviour of the KHSM model under static loading of suction caissons has been investigated during this work, but does not form a part of the thesis. There has been considerable work carried out in research facilities such as Oxford University and the University of Western Australia, utilising small scale and centrifuge tests, and therefore validation of the numerical models can be carried out fairly easily, before expanding the research into numerical simulations of full scale foundations.

REFERENCES

Addenbrooke T.I., Potts D.M., Puzrin A.M. (1997). The influence of pre-failure soil stiffness on the numerical analysis of tunnel construction. Géotechnique, 47(3):693-712

Amorosi, A. (1996). Il comportamento meccanico di un'argilla naturale consistente. *Doctoral thesis*, University of Rome 'La Sapienza'.

Amorosi, A. & Rampello, S. (1998). The influence of natural soil structure on the mechanical behaviour of a stiff clay. *Proc. Int. Symp. Geotech. Hard Soils – Soft Rocks, Naples 1*, 395–402

Amorosi, A. & Rampello, S. (2007). An experimental investigation into the mechanical behaviour of a structured stiff clay *Géotechnique* 57, (2), 153–166

Anderson W. F., Pyrah I. C., Haji Ali F. (*1987*) Rate effects in pressuremeter tests in clays. ASCE *Journal of Geotechnical Engineering* 113:1344–1358

Asaoka A., Nakano M., Noda T. (2000). Superloading yield surface concept for highly structured soil behavior. Soils and Foundations, 40(2):99-110

Al-Tabbaa, A. (1987). Permeability and stress-strain response of speswite kaolin, *PhD Thesis,* Cambridge University.

Al-Tabbaa, A. & Muir Wood, D. (1989). An experimentally based 'bubble' model for clay. *Numerical models in geomechanics NUMOG 3* (eds S. Pietruszczak & G. N. Pande), 91-99. London: Elsevier Applied Science.

Atkinson, J.H. (2000). Non-linear soil stiffness in routine design. *Géotechnique* 50, 487-508.

Aubeny, C., Whittle, A., and Ladd, C. (2000). "Effects of Disturbance on Undrained Strengths Interpreted from Pressuremeter Tests." *J. Geotech. Geoenviron. Eng.*, 126(12), 1133–1144

Baguelin, F., Jezequel, J., Lemee, E & Mehause, A. (1972). Expansion of Cylindrical Probe in Cohesive Soils. *Journal of the Soil Mechanics and Foundations Division, ASCE*. 98 (11), 1129-1142

Baguelin, F., Jezequel, J.F., , and Shields, D.H.,, (1978).The pressuremeter and foundation engineering*, Trans. Tech. Publications* ,Clausthall

Baldi, G., Hight, D.W. and Thomas, G.E., (1988). A re-evaluation of conventional triaxial test methods. In *Advanced triaxial testing of soil and rock.* ASTM. STP 977, 219-263.

Baudet B. and Stallebrass S. (2004). A constitutive model for structured clays, *Géotechnique*, 54(4), 269-278.

Berman D.R., Germaine J.T. and Ladd C.C. (1993) - Characterization of the Engineering Properties of Boston Blue Clay for the MIT Campus

Bishop A.W., Webb D.L. and Lewin P.I. (1965), Undisturbed samples of London Clay from the Ashford Common shaft: strength-effective stress relationships, *Géotechnique, 15, No.1, pp.1-31*

Borja, R. I., Tamagnini, C. & Amorosi, A. (1997). Coupling plasticity and energy-conserving elasticity models for clays. *J. Geotech. Engng* 123, (10), 948–956.

Boyce, H. R. (1980). A non-linear model for the elastic behaviour of granular materials under repeated loading. *Proceedings of the international symposium on soils under cyclic and transient loading,* Swansea, Vol. 1, 285–294.

Britto, A. M. and Gunn, M. J. (1987). *Critical state soil mechanics via finite elements*. Ellis - Horwood, Chichester / Halsted Press , New York, 1 - 488.

Burland, J. B. (1990). 30th Rankine Lecture: On the compressibility and shear strength of natural clays. *Geotechnique*, 40(3), 329- 378.

Burland, J. B., Rampello, S., Georgiannou, V. N. & Calabresi, G. (1996). A laboratory study of the strength of four stiff clays. *Geotechnique* 46, (3), 491-514.

Buro Happold (2007). Personal Communication

Buro Happold (2009). Personal Communication

Butterfield R. (1979). A natural compression law for soils. *Geotechnique*, 29, (4), 469-480.

Calabresi, G. & Scarpelli, G. (1985). Effects of swelling caused by unloading in overconsolidated clays. *Proc. 11th ICSMFE*, San Francisco 1, 411±414.

Callisto, L. and Calabresi, G. (1998). Mechanical behaviour of a natural soft clay, *Geotechnique 48 (*4), 495–513.

Carter, J.P., Airey, D.W., & Fahey, M. (2000). A review of laboratory testing of calcareous soils. In Engineering for calcareous sediments. Edited by K.A. Al-Shafei. A.A. Balkema, Rotterdam. Vol. 2, pp. 401–431

Chartier M., (2008), Nikolic A. and Fasano A.,. Personal Communication

Clarke, B.G. & Smith, A. (1992). Self Boring Pressuremeter Tests in Weak Rock. *Construction and Building Materials*. 6 (2), pp. 91-96.

Clarke, B.G. (1995). *Pressuremeters in Geotechnical Design*. Glasgow: Blackie Academic and Professional

Clayton, C.R.I. and Khartush, S.A. (1986). A new device for measuring local axial strains on triaxial specimens. *Geotechnique* 36, 593-597.

Clayton, C. & Heymann, G. (2001). Stiffness of geomaterials at very small strains. Géotechnique 51
(3), 245-255.

Cole, K.W and Burland, J.B (1972). Observation of retaining wall movements associated with a large excavation. *Proc 5th ECSMFE*, Madrid.

Coop M.R., Atkinson J.H. and Taylor R.N. (1995), Strength, yielding and stiffness of structured and unstructured soils, *Proc. 11th ECSMFE, Copenhagen 1,* 55-62*.*

Coop M.R. and Cotecchia F. (1995), The compression of sediments at the archeological site of Sibari. *Proc. 11th ECSMFE, Copenhagen 1, 19-26.*

Collins, I. & Yu, H. (1996). Undrained Cavity Expansion in Critical State Soils. *International Journal for Numerical and Analytical Methods in Geotechnics*. 16, 3-23.

Coecchia , F. (1996). The effects of structure on the porpoerties of an Italian Pleiostocene clay. PhD thesis, University of London.

Cotecchia, F. & Chandler, R. J. (1997). The influence of structure on the pre-failure behaviour of a natural clay. *Geotechniqu*e, 47,(3), 523-544.

Cotecchia F and Chandler R.J. (2000). A general framework for the mechanical behaviour of clay. *Géotechnique,* 50, (4) .431-447*.*

Dafalias Y.F. and Herrmann (1982). Bounding surface formulation of soil plasticity. *Soil Mechanics-Transient and Cyclic Loads*, G.N. Pande and O.C. Zienkiewicz (eds.). John Wiley and Sons Ltd.

Dafalias, Y. F. (1986). Bounding surface plasticity. I: Mathematical foundation and hypoplasticity. *J. of Engineering Mechanics*, Vol. 116, 9, 966 - 987.

De Freitas, M. H. & Mannion, W. G. (2007). A biostratigraphy for the London Clay in London. Géotechnique 57 (1), 91–99.

Drucker, D. C., Gibson, R. E. and Henkel, D. J. (1957). Soil mechanics and work hardening theories of plasticity. *Trans ASCE*, Vol. 122, 101 - 106.

Dyvik, R. and Madshus, C. (1985). Lab measurements of Gmax using bender elements. In *Advances in the art of testing soils under cyclic conditions,* 186-196, Detroit, Michigan, ASCE.

Eden, W.J & Law, K.T. (1980) Comparison of undranied shear strength results obtained by difference test methods in soft clays *Canadian Geotechnical Journal*, 2008, 17:(3) 369-381.

Fahey M. and Randolph M.F., (1984) Effect of disturbance on parameters derived from self-boring pressuremeter tests in sand. *Geotechnique*. 36 (1), p65.

Fasano A. (2007). Personal Communication

Fasano A. and Nikolic A. (2008). Personal Communication

Fasano A. and Nikoic A., (2009). Personal Communication

Fioravante, V., Jamiolkowski, M. & Lancellotta, R. (1994). An analysis of pressuremeter holding tests. Géotechnique 44(2), 227–238

Gasparre, A., Nishimura, S., Coop, M.R. & Jardine, R.J. (2007). The Influence of Structure on theBehaviour of London Clay. Géotechnique, 57 (1), pp 19-31

Gasparre, A., and Coop, M.R (2008). Quantification of the effects of structure on the compression of a stiff clay. *Canadian Geotechnical Journal*, 2008, 45:(9) 1324-1334.

Gens, A. & Nova, R. (1993). Conceptual bases for a constitutive model for bonded soils and weak rocks. *Proc. of Int. Symp. On Hard Soils-Soft Rocks*, Athens (Greece), 485-494.

Gibson, R.E. & Anderson, W.F. (1961). In situ measurement of soil properties with the pressuremeter. Civil Engineering Public Works Review, Vol. 56, 615-618.

González, N.A., Arroyo, M. and Gens, A. (2009). *Identificación of bonded clay parameters in SBPT tests: A numerical study.* Soils and foundations. Vol. 49, No.3, pp. 329-340

Gonzáles N.A., Rouainia M., Arroyo M., Gens A. (2012). Analysis of tunnel excavation in London Clay incorporating soil structure. Géotechnique, 62(12):1095-1109

Graham, J., Noonan, M.L., and Lew, K.V., (1983). Yield states and stress-strain relationships in a natural plastic clay. *Canadian Geotechnical Journal*, 20(3), 502-516

Grammatikopoulou, A. (2004). Development, implementation and application of kinematic hardening models for overconsolidated clay*. PhD Thesis, University of London, Imperial College of Science, Technology and Medicine*

Grammatikopoulou, A., Zdravkovic, L. & Potts, D. M. (2002). The effect of a kinematic yield surface on the predicted behaviour of an embankment. *Numerical models in geomechanics NUMOG 8* (eds S. Pietruszczak & G. N. Pande), 553-559. Rotterdam: Balkema.

Grammatikopoulou, A., Zdravkovic, L. & Potts, D. M. (2007). The effect of the yield and plastic potential deviatoric surfaces on the failure height of an embankment. *Geotechnique,* 50(3), 263-273.

Grammatikopoulou, A., Zdravkovic, L. & Potts, D. M. (2008). Numerical analysis of an embankment founded on soft structured clay. *12th Int. Conf. of Computer Methods and Advances in Geomechanics (IACMAG),* 1-6 October 2008, Goa, India.

Grammatikopoulou, A., Zdravkovic, L. & Potts, D.M. (2008). The Influence of Previous Stress History and Stress Path Direction on the Surface Settlement Trough Induced by Tunnelling. *Geotechnique*. 58 (4), 267-281.

Hardin B.O. and Black W.L. (1969). Closure to: Vibration modulus of normally consolidated clay. *Journal of the Soil Mechanics and Foundations Division, ASCE*, Vol. 95, No. SM3, pp. 1531-1537.

Hardin B.O. (1978). The nature of stress-strain behavior for soils. *Proceedings of Specialty Conference on Earthquake Engineering and Soil Dynamics, ASCE*, Pasadena, California, 3-90.

Hashiguchi, K. (1985). Two-and three-surface models of plasticity. *Proc. of 5th int. conf. On numerical methods in geomechanics, Nagoy*a, 285 - 292.

Hashiguchi K. (1989). Subloading surface model in unconventional plasticity. *International Journal of solids and structures*, Vol. 25, 917-945.

Hashiguchi, K. (2002). A proposal of the simplest convex-conical surface for soils. *Soils and foundations*, Vol. 42, (3), 107 - 113.

Hashiguchi, K., Saitoh, K., Okayasu, T. & Tsutsumi, S. (2002) Evaluation of typical conventional and unconventional plasticity models for prediction of softening behaviour of soils. Géotechnique 52(8), 561-578

Hight D.W., McMillan F., Powell J.J.M., Jardine R.J. and Allenou C.P. (2003). Some characteristics of London Clay. *Proc. Conf. Characterisation and Engineering*, *National University Singapore. Tan T.S., Phoon, K.K., Hight D.W., Lerouil S. (eds). Balkema, Vol. 2,851-907*.

Hiley RA, Rouainia M. (2008). Explicit Rnge0Kutta methods for the integration of rate-type constitutive equations *Computational Mechanics* 2008, **42**(1), 53-66.

Houlsby, G. T. (1985). The use of a variable shear modulus in elastic-plastic models for clays. *Comput. Geotech*. 1, (1), 3–13.

Houlsby, G.T. & Withers, N.J. (1988). Analysis of the Cone Pressuremeter Test in Clay. *Geotechnique*. 38 (4), pp. 575-587

Houlsby, G. & Carter, J. (1993). The effects of pressuremeter geometry on the results of tests in clay, Géotechnique 43(4), 567-576.

Houlsby G. T., Amorosi A. & Rojas E. (2005) Elastic moduli of soils dependent on pressure: a hyperelastic formulation, *Geotechniqu*e 55, (10), 383–392.

Hvorslev M.J. (1937). Uber die Festigkeitseigenschaften gestorter bindiger Boden. *Ingerniorvidenshabelige Skriften*, no. 45, Danmarks Naturvidenshabelige Samfund, Kopenhavn, Denmark.

Jardine R.J. (1985). *Investigations of pile-soil behaviour with special reference to the foundations of offshore structures*. PhD thesis, Imperial College, University of London, London, UK.

Jardine R.J., St John H.D., Hight D.W. and Potts D.M. (1991), Some practical applications of a non-linear ground model. *Proc. 10th ECSMFE, Florence, Vol.1, pp.223-228.*

Jezequel, J. F., Lemasson, H. & Touze, J. (1968) Le pressiomètre Louis Ménard: Quelques problèmes de mise en oeuvre et leur influence sur les valeurs pressiométriques. *Bulletin de Liaison des Laboratoires des Ponts et Chaussées,* 32 (June - July)**,** 97-120.

Karstunen, M., Krenn, H., Wheeler, S. J. Koskinen, M. & Zentar, R. (2005). Effect of anisotropy and destructuration on the behaviour of Murro test embankment. ASCE, *Internation Journal of Geomechanics,* 87-97.

Kavvadas, M. (1995). A plasticity approach to the mechanical behaviour of bonded soils. Proc. 4th Int. Conf. Computational Plasticity, Barcelona.

Kavvadas, M & Amorosi, A. (2000). A constitutive model for structured soils. *Geotechniqu*e, 50(3), 263-273.

King C. (1981), The stratigraphy of the London Basin and associated deposits. *Tertiary Research Special Paper*, Vol. 6, Backhuys, Rotterdam.

Konstantakos, D.C., Whittle, A.J. and Scharner, B. (2005). Control of ground movements for a multi-level-anchored diaphragm wall during excavation. *Plaxis Bulletin*, Issue 17.

Kung G.T.C., Ou C.Y., Juang C.H. (2009). Modelling small-strain behaviour of Taipei clays for finite element analysis of braced excavations. Computer and Geotechnics, 36(1-2):304-319

Ladd C.C. and Foott R. (1974). New design procedure for stability of soft clays. Journal of Geotechnical Engineering, 100(GT7):763-786

Ladd, C.C., Young, G.A., Kramer, S.A. and Burke, D.M., (1999). Engineering properties of Boston Blue Clay from special testing program, *Proceedings ASCE Geo-Congress 98*, GSP v91, p1-24.

Lagioia, R. & Nova, R. (1995). An experimental and theoretical study of the behaviour of a calcarenite in triaxial compression. *Geotechnique* 45, No. 4, 633±648.

Lambe T.W. and Whitman R.V. (1969), Soil Mechanics, John Wiley & Sons Inc., New York.

Lambe, T., and Whitman, R. 1979. Soil mechanics, SI version. Wiley

La Rochelle, P. Trak, B. Tavenas, F. & Roy, M. (1974). Failure of a test embankment on a sensitive Champlain clay. *Canadian Geotech. Jnl.* 11: 142-164.

Lefebvre, G., and La Rochelle, P. 1974. The analysis of two slope failures in cemented Champlain clays. Canadian Geotechnical Journal, 11(1): 89–108. doi:10.1139/t74-007.

Leroueil S. (1977). *Quelques considerations sur le comportement des argiles sensibles*. PhD thesis, University of Laval, Quebec, Canada

Leroueil S, Tavenas F, Brucy F, La Rochelle P, Marius R. Behavior of destructured natural clays. Journal of the Geotechnical Engineering Division, ASCE 1979;105(GT6):759{778.

Leroueil S., Tavenas F. and Locat J. (1984), Discussion on: Correlations between index tests and the properties of remoulded clays *Géotechnique, 35, No.2,* 223-226.

Leroueil S. & Vaughan P.R. (1990). The important and congruent effects of structure in natural soils and weak rocks. *Geotechnique*, 40(3), 467-488.

Leroueil, S., Magnan, J.P. & Tavenas, F. (1990). *Embankments on soft clays.* Ellis Horwood Limited, Chichester, England.

Liu, M., and Carter, J. 2002. A structured Cam clay model. Canadian Geotechnical Journal, 39(6): 1313–1332.

Lo, K. 1970. The operational strength of fissured clays. *Géotechnique,* 20(1): 57–74. doi:10.1680/geot.1970.20.1.57.

Lo, K., and Morin, J. 1972. Strength anisotropy and time effects of two sensitive clays. *Canadian Geotechnical Journal*, 9(3): 261– 277. doi:10.1139/t72-030

Menard, L. (1957). *An Apparatus for Measuring the Strength of Soils in Place*. Illinois: University of Illinois.

Mitchell, J.K. (1976). *Fundamentals of Soil Behaviour*, New York: Wiley

Mroz Z. (1967). On the description of anisotropic work hardening. *Journal of the Mechanics and Physics of Solids*, Vol. 15, pp. 163-175.

Mroz, Z., Norris, V. A. and Zienkiewicz, O. C. (1979). Application of an anisotropic hardening model in the analysis of elasto-plastic deformation of soils. *Géotechnique*, 29, 1 - 34.

Muir Wood, D. (1990). *Soil behaviour and critical state soil mechanics.* Cambridge: Cambridge University Press.

Muir Wood, D. (1995). Kinematic hardening model for structured soil. *Proceedings of the international symposium on numerical models in geomechanics*, Davos, 83±88.

Nikolic A. Fasano A. and Cartier M., (2010). Personal Communication

Ohtsuki, H., Nishi, K., Okomoto, T & Tanaka, S. (1981). Time Dependant Characteristics of Strength and Deformation of a Mudstone. *Proceedings of the Symposium on Weak Rock*. 1 (1), 119-124

O'Rourke T.D. and O'Donnell C.J. (1997). Field behavior of excavation stabilized by deep soil mixing. Journal of Geotechnical and Geoenvironmental Engineering, 123(6):516-524

Pantelidou, H. & Simpson, B. (2007). Geotechnical variation of London Clay across central London. Géotechnique 57 (1), 101–112

Potts D.M. & Gens A. (1985), A critical assessment of methods of correcting for drift from the yield surface in elasto-plastic finite element analysis, Int. Jnl. Num. Anal. Meth. Geomech., Vol. 9,149-159

Peck, R.B. (1969). Deep excavations and tunnelling in soft ground. *Proceedings of the 7th International Conference of Soil Mechanics and Foundation Engineering, Mexico, p225-290* Rendulic L. (1937). Ein Grundgesetz der Tonmechanik und sein experimenteller Beweis. *Der Baunginenieur*, Vol. 18, 459-467.

Prapaharan, S., Chameau, J., Altschaeffl, A., and Holtz, R. (1990). "Effect of Disturbance on Pressuremeter Results in Clays." *J. Geotech. Engrg.*, 116(1), 35–53.

Puswewala, U.G.A., Rajapakse, R.K.N.D., Domaschuk, L. & Lach, R.P.. (1992). Finite Element Modelling of Pressuremeter Tests and Footings on Frozen Soils. *International Journal for Numerical and Analytical Methods in Geotechnics*. (16), pp.351-375

Qu, G., Hinchberger, S. D and Lo, K. Y. (2009). Case studies of three-dimensional effects on the behaviour of test embankments. *Canadian Geotechnical Journal*. **46**(11): 1356-1370

Rampello, S., Georgiannou, V. N. & Viggiani, G. (1993). Strength and dilatancy of natural and reconstituted Vallericca clay. *Proc. Int. Symp. on Hard Soils – Soft Rocks*, Athens 1, 761–768.

Rangeard, D., Hicher, P. & Zentar, R. (2003), 'Determining soil permeability from pressuremeter tests', International Journal for Numerical and Analytical Methods in Geomechanics 27, 1-24.

Rendulic L. (1937). Ein Grundgesetz der Tonmechanik und sein experimenteller Beweis. *Der Baunginenieur*, Vol. 18, pp. 459-467.

Roscoe, K. H. and Schofield, A .N. and Wroth, C. P. (1958). On the yielding of soils. *Géotechnique,* 8, 22 – 53

Roscoe K.H. and Schofield A.N. (1963). Mechanical behaviour of an idealised 'wet' clay. *Proceedings of the 2nd European Conference on Soil Mechanics*, Wiesbaden, Vol.1, 47-54

Roscoe, K. H. & Burland, J. B. (1968). On the generalised stress-strain behaviour of "wet" clay. In *Engineering plasticity.* Cambridge: Cambridge University Press, pp 535-609.

Rouainia, M. & Muir Wood, D. (2000). A kinematic hardening model for natural clays with loss of structure, *Geotechnique*, 50(2), 153-164.

Santagata M.C. (1998). Factors affecting the initial stiffness and the stiffness degradation behavior of cohesive soils. Ph.D. Thesis, Dept. of Civil and Environmental Engineering, MIT, Cambridge, MA

Santagata M.C. and Germaine J.T. (2002). Sampling disturbance effects in normally consolidated clays. Journal of Geotechnical and Geoenvironmental Engineering, 128(12):997-1006

Santagata, M. C. and Kang, Y. I. (2007), "Geologic time effects on the initial stiffness of clays", *Journal of Engineering Geology* 89 (1-2), 98-111

Sciotti, A. (1992). Compressibilita` e resistenza di alcune argille sovraconsolidate dell'Italia Centrale. *Thesis, University of Rome 'La Sapienza'.*

Sekiguchi, H & Ohta, H. (1977)Induced anisotropy and tie dependency of clays. *Proc. Of Speciailty Session 9, 9th ICSMFE,* 229-238.

Sheahan T.C. (2005). A Soil Structure Index to Predict Rate Dependence of Stress Strain Behavior. In Geomechanics: Testing, Modeling and Simulation, ASCE Geotechnical Special Publication, 143:81-97

Sheng D, Sloan SW, (2001) Load stepping methods for critical state models, *International Journal for Numerical Methods in Engineering*, 50(1), 67-93.

Sides G. and Barden L. (1970), The microstructure of dispersed and flocculated samples of kaolinite, illite and montmorillonite, *Canadian Geotech. Jnl., 8* 391-399.

Silvestri, V. 1995. Determination of undrained shear strength of soft clays by pressuremeter tests. In The pressumeter and its new avenues. Balkema, Rotterdam, the Netherlands. pp. 231–237

Silvestri, V. (2004*).* Disturbance Effects in *Pressuremeter* Tests in Clay*. Canadian Geotech Jnl, 41(4), p. 738-759*

Skempton (1970), The consolidation of clays by gravitational compaction. *Q.J. Geological Soc. No.125, pp373-411*

Sloan, S.W. & Randolph, M.F., (1982). Numerical prediction of collapse loads using finite element methods, *Int. J. Num. Analy. Meth. Geomech.* 6, 47-76.

Sloan SW, Abbo AJ, Sheng D.C., (2001). Refined explicit integration of elastoplastic models with automatic error control. *Engineering Computations*, 18(1/2), 121-154

Smith, P. R., Jardine R. J. High, P. W. (1992). The yielding of Bothkanna clay. *Géotechnique,* 42, 257 - 274.

Stallebrass, S. E. (1990). Modelling the effects of recent stress history on the behaviour of overconsolidated soils, *Ph.D. thesis*, City University, London.

Stallebrass, S. E. and Taylor, R. N. (1997). The development of a constitutive model forthe prediction of ground movements in overconsolidated clay. *Géotechnique,* 47, 235 -253.

Standing J.R. & Burland J.B. (2006), Unexpected tunnelling volume losses in the Westminster area, London, *Geotechnique* 56, pp.11-26,

St. John H.D. (1975). *Field and theoretical studies of the behaviour of ground around deep excavations in London Clay*. PhD thesis, University of Cambridge, Cambridge, UK.

Stroud M.A. (1989). The Standard Penetration Test - its Application and Interpretation. Penetration Testing in the U.K., Thomas Telford, London, 29-49

Tavenas, F., Chapeau, C., La Rochelle, P. & Roy, M. (1974). Immediate settlement of three test embankments on Champlain clay. *Canadian Geotech. Jnl.* 11: 109-141.

Tavenas, F. & Leroueil, S. (1977). Effects of stresses and time on yielding of clays. *Proc. 9th Int. Conf. on Soil Mechanics and Foundation Engineering,* Vol 1, Toyko, 319-326.

Tavenas, F. A., Jean, P., Leblong, P. & Leroueil, S. (1983). The permeability of natural soft clays. Part II: Permeability characteristics. *Canadian Geotech. Jnl.* 20: 645-660

Tavenas, F. & Leroueil, S. (1990). The behaviour of embankments on clay foundations. *Canadian Geotech. Jnl.* 17, (2), 236-260.

Terzaghi K. (1943), Ends and means in Soils Mechanics, *Engineering Journal (Canada), Vol.27, p.608.*

Vermeer, P. (1978). A double hardening model for sand. *Geotechnique* 28,(4), 413–433.

Viggiani, G. & Atkinson, J. H. (1995). Stiffness of fine-grained soils at very small strains. *Geotechnique* 45, (2), 249-265.

Von Mises R., (1928): Mechanik der plastischen Form¨anderungen von Kristallen. Z. Angew. Math. Mech. 8, 161-185

Wheeler, S. J., Näätänen, A., Karstunen, M., and Lojander, M. (2003). An anisotropic elastoplastic model for soft clays. *Can. Geotech. J.*, 40(2), 403-418.

Whittle A.J., Hashash Y.M.A., Whitman R.V. (1993). Analysis of deep excavation in Boston. Journal of Geotechnical Engineering, 119(1):69-90

Whittle A.J. (1993). Evaluation of a constitutive model for overconsolidated clays. *Geotechnique*, Vol. 43, No. 2, pp. 289-313.

Whittle, A.J. & Aubeny, C.P. (1993). The Effect of Installation Disturbance on Interpretation of Insitu Tests in Clays. In: *Predictive Soil Mechanics*. Oxford: Proc. Wroth Memorial Symposium. 585-605

Whittle, A., and Kavvadas, M. (1994). Formulation of {MIT-E3} constitutive model for overconsolidated clays. Journal of Geotechnical Engineering, 120(1): 173–198. doi:10.1061/(ASCE) 0733-9410(1994)120:1(173).

Wood, D. M. (1990). *Soil Behaviour and critical state soil mechanics*. Cambridge University Press, England / New York, 1 - 462.

Wroth, C.P & Hughes, J.M.O. (1973). An Instrument for the Insitu Measurement of the Properties of Soft Clays. *Proc 8th Int. Conference SMFE*. 1.2 (2), 487-494

Wroth C.P. (1982). British Experience with the self-boring pressuremeter. *Proc. 1st Symp. Pressuremeter and its Marine Applications,* Paris. 36, 13-164.

Wroth C.P. and Houlsby G.T. (1985). Soil mechanics – property characterisation, and analysis procedures. *Proceedings of the 11th International Conference on Soil Mechanics and Foundation Engineering*, San Francisco, Vol. 1, 1-55

Yeung, S. & Carter, J. (1990). Interpretation of the pressuremeter test in clay allowing for membrane end effects and material non-homogeneity. In 'Proceedings of the 3rd International Symposium on Pressuremeters', pp. Oxford, 199-208.

Yildiz, A., Karstunen, M. & Krenn, H. (2009). Effect of anisotropy and destructuration on behaviour of Haarajoki test embankment. ASCE *International Journal of Geomechnics,* 9 (4), 153-168.

Yu, H. (1990). Cavity expansion theory and its application to the analysis of pressuremeters. PhD Thesis, University of Oxford.

Yu, H.S., & Collins, I.F. (1998). Analysis of self-boring pressuremeter tests in overconsolidated clays. *Géotechnique* 48 (5), 689-693.

Yu, H. (2004). James Mitchell Lecture: Insitu Soil Testing - from Mechanics to Interpretation. *Proceedings of the ISC-2 on Geotechnical and Geophysical Site Characterisation*. 1 (1), pp. 3-38

Yu, H., Charles, M. & Khong, C. (2005). Analysis of pressuremeter geometry effects in clay using critical state models. International Journal for Numerical and Analytical Methods in Geomechanics 29, 845-859.

Zdravkovic, L., Potts, D. M. & Hight, D. W. (2002). The effect of strength anisotropy on the behaviour of embankments on soft ground. *Geotechnique* 52, No. 6, 447-457.

Zdravkovic L., Potts D.M., St John H.D. (2005). Modelling of a 3D excavation in finite element analysis. Géotechnique, 55(7):497-513

Zentar, R., Moulin, G. & Hicher, P.Y. (1998). Numerical analysis of pressuremeter test in soil. 4th European Conference on Numerical Methods in Geomechanics (NUMGE), Udine: 593- 600.

Zhao, J., Sheng, D., Rouainia, M., and Sloan, S.W. 2005. Explicit stress integration of complex soil models. *International Journal for Numerical and Analytical Methods in Geomechanics*, 29(12): 1209–1229. doi:10.1002/nag.456.

Zytynski, M., Randolph, M., Nova, R. & Wroth, C. P. (1978). On modelling the unloading–reloading behaviour of soils*. Int. J. Numer. Anal. Methods Geomech*. 2, 87–93.

APPENDIX A

Publications

1. Panayides S, Rouainia M, Wood DM. Influence of degradation of structure on the behaviour of a full-scale embankment. *Canadian Geotechnical Journal* 2012, **49**(3), 344-356.

2. Panayides S, Rouainia M, Osman AS. A Numerical study of behaviour of suction caissons in structured soil subjected to combined loads *International Journal of Geomechanics.* (Re-submitted after comments).

3. Rouainia M., Panayides *S.* Wood DM. Assessing the three-dimensional behaviour of a trial embankment founded on structured soil *Geotechnique* (Submitted and replying to comments).

4. Panayides S, Rouainia M. Analysis of pressuremeter performance using a kinematic hardening constitutive model with structure. *In: 13th International Conference of the Association for Computer Methods and Advances in Geomechanics (IACMAG13)*. 2011, Mebourne, Australia.

5. Panayides S, Rouainia M, Osman AS. Ultimate capacity of suction anchors using an advancedconstitutive model. *In: Second International Symposium on Frontiers in Offshore Geotechnics (ISFOG)*. 2010, Perth, Australia.

6. Panayides S, Rouainia M. Ultimate capacity of suction anchors using an advanced constitutive model. *In: Second International Symposium on Frontiers in Offshore Geotechnics (ISFOG)*. 2010, Perth, Australia.

7. Panayides S, Rouainia M Undrained ultimate capacity of suction anchors using an advanced constitutive model. *In*: *Numerical Methods in Geotechnical Engineering (NUMGE)* 2010*,* Trondheim, Norway.